UNIVERSITY OF CALIFORNIA SAN DIEGO

Nonequilibrium effects of vibrational strong coupling on chemical reactions

A dissertation submitted in partial satisfaction of the
requirements for the degree Doctor of Philosophy

in

Chemistry

by

Matthew Du

Committee in charge:

Professor Joel Yuen-Zhou, Chair
Professor Richard Averitt
Professor Michael Galperin
Professor Francesco Paesani
Professor Wei Wang

2022

The dissertation of Matthew Du is approved, and it is acceptable in quality and form for publication on microfilm and electronically.

University of California San Diego

2022

EPIGRAPH

Let me be your mirror

Help you see a little bit clearer

The light that shines within

There's a hope that's waiting for you in the dark

You should know you're beautiful just the way you are

—Alessia Cara, "Scars To Your Beautiful"

TABLE OF CONTENTS

LIST OF FIGURES

LIST OF TABLES

ACKNOWLEDGMENTS

First and foremost, I would like to acknowledge my Ph. D. advisor, Prof. Joel Yuen-Zhou. I cannot thank you enough for all the patience, time, and effort you have devoted towards my scientific, professional, and personal growth.

Next, I would like to thank former and current members of the Yuen-Zhou research group: Dr. Luis Martínez-Martínez, Dr. Jorge Campos-Gonzalez-Angulo, Gerardo Soriano, Dr. Raphael Ribeiro, Etienne Palos, Garret Wiesehan, Sindhana Pannir-Sivajothi, Juan Pérez-Sánchez, Kai Schwennicke, Deepak Vinod, Kunyang (Oliver) Sun, Arghadip Koner, Dr. Stephan van den Wildenberg, and Dr. Borna Zandkarimi.

I am grateful for the many others that I have worked with throughout my graduate studies: Prof. Wei Xiong, Dr. Bo Xiang, Dr. Tengteng Chen, Prof. V. Ara Apkarian, Prof. Jennifer Shumaker-Perry, and Dr. Peter Stevenson.

I would like to thank friends from UCSD, undergrad, and extracurricular activities. These people helped make graduate school an enjoyable experience for me.

I also thank my undergraduate research advisors, Profs. SonBinh Nguyen and Toru Shiozaki, for providing me the opportunity to experience research and learn skills that turned out to be invalulable for my graduate studies.

There are other teachers for which I would like to express gratitude: math professors at Northwestern University, as well as math and science teachers from middle and high schools.

Finally, I am indebted to my family for supporting my academic pursuits since my childhood years.

Chapter 2, in full, is adapted from the material as it appears in "Nonequilibrium effects of cavity leakage and vibrational dissipation in thermally-activated polariton chemistry," M. Du, J. A. Campos-Gonzalez-Angulo, J. Yuen-Zhou, *J. Chem. Phys.* **154**, 084108 (2021). The dissertation author was the primary investigator and author of this paper.

Chapter 3, in full, is adapted from the material as it appears in "Catalysis by Dark States in Vibropolaritonic Chemistry," M. Du, J. Yuen-Zhou, *Phys. Rev. Lett.* **128**, 096001 (2022). The

dissertation author was the primary investigator and author of this paper.

Chapter 4, in full, is adapted from the material as it appears in "Remote Control of Chemistry in Optical Cavities," M. Du, R. F. Ribeiro and J. Yuen-Zhou, *Chem* **5**, 1167 (2019). The dissertation author was the primary investigator and author of this paper.

Chapter 5, in full, is adapted from the material as it appears in "Theory for polariton-assisted remote energy transfer," M. Du, L. A. Martínez-Martínez, R. F. Ribeiro, Z. Hu, V. M. Menon and J. Yuen-Zhou, *Chem. Sci.* **9**, 6659 (2018). The dissertation author was the primary investigator and author of this paper.

VITA

2016 Bachelor of Arts in Chemistry, Northwestern University

2016-2017 Teaching Assistant, University of California San Diego

2022 Doctor of Philosophy in Chemistry, University of California San Diego

PUBLICATIONS

M. Du, J. Yuen-Zhou, "Catalysis by Dark States in Vibropolaritonic Chemistry," *Phys. Rev. Lett.* **128**, 096001 (2022).

R. Pandya, R. Y. S. Chen, Q. Gu, J. Sung, C. Schnedermann, O. S. Ojambati, R. Chikkaraddy, J. Gorman, G. Jacucci, O. D. Onelli, T. Willhammar, D. N. Johnstone, S. M. Collins, P. A. Midgley, F. Auras, T. Baikie, R. Jayaprakash, F. Mathevet, R. Soucek, M. Du, A. M. Alvertis, A. Ashoka, S. Vignolini, D. G. Lidzey, J. J. Baumberg, R. H. Friend, T. Barrisien, L. Legrand, A. W. Chin, J. Yuen-Zhou, S. K. Saikin, P. Kukura, A. J. Musser, A. Rao, "Microcavity-Like Exciton-Polaritons can be the Primary Photoexcitation in Bare Organic Semiconductors," *Nat. Commun.* **12**, 6519 (2021).

R. Collison, J. B. Pérez-Sánchez, M. Du, J. Travino, J. Yuen-Zhou, S. O'Brien, V. M. Menon, "Purcell Effect of Plasmonic Surface Lattice Resonances and its Influence on Energy Transfer," *ACS Photonics* **8**, 2211 (2021).

M. Du, J. A. Campos-Gonzalez-Angulo, J. Yuen-Zhou, "Nonequilibrium effects of cavity leakage and vibrational dissipation in thermally-activated polariton chemistry," *J. Chem. Phys.* **154**, 084108 (2021).

P. R. Stevenson, M. Du, C. Cherqui, M. Bourgeois, K. Rodriguez, J. R. Neff, E. Abreu, I. Meiler, V. A. Tamma, V. A. Apkarian, G. C. Schatz, J. Yuen-Zhou, J. S. Shumaker-Parry, "Active Plasmonics and Active Chiral Plasmonics Through Orientation-Dependent Multipolar Interactions," *ACS Nano* **14**, 11518 (2020).

B. Xiang, R. F. Ribeiro, M. Du, L. Chen, Z. Yang, J. Wang, J. Yuen-Zhou, W. Xiong, "Intermolecular Vibrational Energy Transfer Enabled by Microcavity Strong Light-Matter Coupling," *Science* **368**, 665 (2020).

B. Xiang, R. F. Ribeiro, L. Chen, J. Wang, M. Du, J. Yuen-Zhou and W. Xiong, "State-Selective Polariton to Dark State Relaxation Dynamics," *J. Phys. Chem. A* **123**, 5918 (2019).

M. Du, "Theory Reveals Novel Chemistry of Photonic Molecules," *Chem* 5, 1009 (2019).

M. Du, A. M. Agrawal, S. Chakraborty, S. J. Garibay, R. Limvorapitux, B. Choi, S. T. Madrahimov and S. T. Nguyen, "Matching the Activity of Homogeneous Sulfonic Acids: The Fructose-to-HMF Conversion Catalyzed by Hierarchically Porous Sulfonic-Acid-Functionalized Porous Organic Polymer (POP) Catalysts," *ACS Sustainable Chem. Eng.* **7**, 8126 (2019).

M. Du, R. F. Ribeiro and J. Yuen-Zhou, "Remote Control of Chemistry in Optical Cavities," *Chem* **5**, 1167 (2019).

M. Du, L. A. Martínez-Martínez, R. F. Ribeiro, Z. Hu, V. M. Menon and J. Yuen-Zhou, "Theory for polariton-assisted remote energy transfer," *Chem. Sci.* **9**, 6659 (2018).

R. F. Ribeiro, L. A. Martínez-Martínez, M. Du, J. Campos-Gonzalez-Angulo and J. Yuen-Zhou, "Polariton chemistry: controlling molecular dynamics with optical cavities," *Chem. Sci.* **9**, 6325 (2018).

L. A. Martínez-Martínez, M. Du, R. F. Ribeiro, S. Kéna-Cohen and J. Yuen-Zhou, "Polariton-Assisted Singlet Fission in Acene Aggregates," *J. Phys. Chem. Lett.* **9**, 1951 (2018).

ABSTRACT OF THE DISSERTATION

Nonequilibrium effects of vibrational strong coupling on chemical reactions

by

Matthew Du

Doctor of Philosophy in Chemistry

University of California San Diego, 2022

Professor Joel Yuen-Zhou, Chair

An ongoing goal in chemistry is to develop cheaper and greener methods of catalysis. Recent experiments show modified reaction kinetics when placing molecules inside an optical cavity and achieving vibrational strong coupling (VSC). VSC occurs when $N \gg 1$ molecular vibrations strongly interact with a cavity photon mode to form two hybrid light-matter modes called polaritons, as well as $N-1$ optically dark vibrational modes. Since the aforementioned changes in reactivity occur without external pumping, VSC holds promise as a future tool in industrial catalysis. However, VSC-modified chemistry is not well understood. Initial theoretical efforts demonstrate that transition-state theory (TST), the most commonly used reaction-rate theory, predicts negligible

changes in reaction rate due to VSC for typical experimental conditions. Subsequent works have begun to consider how VSC influences reactions for which the assumptions of TST break down.

In this dissertation, we theoretically explore how VSC affects reactions where thermalization occurs on a similar or longer time scale compared to reactive events. Such reactions, which include photochemical processes, can violate the TST assumption that internal thermal equilibrium is maintained throughout the reaction.

First, we study thermally activated electron transfer. For two molecules under VSC, we find that thermalization can be accelerated by cavity decay, a dissipative channel available to polaritons but not the uncoupled molecular vibrations. As a result, nonequilibrium effects that impact the reaction rate are suppressed. For a disordered ensemble of many molecules, VSC yields dark modes that are delocalized across several molecules. We reveal an unconventional mechanism by which this delocalization suppresses reactive events but not vibrational decay, thus speeding up the reaction.

We then investigate photochemistry under VSC. Specifically, we propose a "remote control" of chemistry, where photoexcitation of molecules in one optical cavity enhances the photoisomerization of molecules in another optical cavity. This idea challenges the standard paradigm that a catalyst must bind its substrate to change reactivity.

Finally, we develop a comprehensive theory for a related phenomenon: polariton-assisted energy transfer between spatially separated molecules. This theory not only sheds light on experimental observations but even predicts a number of intriguing effects, including the role reversal of donor and acceptor chromophores.

Chapter 1

Introduction

The manufacturing of everyday products involves chemical reactions. The reactions are often carried out away from room temperature, using catalysts not found in nature, under artificial lighting, and/or with electricity running through the reaction mixture. These conditions enable reactions to occur fast enough, or have high enough yield of the desired product, to meet the demands of society. However, maintaining non-ambient temperatures, synthesizing catalysts, and applying optical/electrical stimuli contribute to the cost of production, as well as detrimental effects on the environment. Finding cheaper and greener ways of carrying reactions has been, and continues to be, an important goal in chemistry research.

A recent wave of experiments has shown that simply placing a reaction mixture inside an optical microcavity can significantly change chemical reactivity [1]. An optical microcavity [2] consists of two highly reflective mirrors that are parallel and separated by a microscopic length, ranging from hundreds of nanometers to tens of micrometers. The cavity can support standing waves of light, analogous to the standing waves of vibration on the string of a violin or the standing waves of sound in a flute. Like that in the musical instruments, each standing-wave mode of the cavity has a frequency that is inversely proportional to the cavity length (i.e., distance between the cavity mirrors).

The cavity length can be tuned such that a cavity mode is resonant with electronic or vi-

brational transitions of molecules inside the cavity. Such resonance allows the cavity mode to favorably interact with the molecules. If the interaction is made strong enough, e.g., by increasing the molecular concentration, the cavity mode will hybridize with an optically bright superposition of molecular transitions to form hybrid light-matter states called polaritons [3, 4]. This phenomenon is known as strong light-matter coupling (or simply, strong coupling). In typical experiments [1, 3, 5, 6], a cavity mode collectively couples to $N \gg 1$ molecular transitions, where each transition resides in a different molecule. In this case, two polaritons and $N-1$ optically dark superpositions are formed [3, 4].

Besides their partial photonic character, the polaritons have different energies than the bare molecular states. Thus, polariton formation can potentially serve as a general tool for modifying chemical reactivity. Indeed, the past decade has witnessed the emergence of polariton chemistry, i.e., chemistry under strong light-matter coupling [1, 3–16]. Notably, the strong coupling of molecular vibrations [17–19], or vibrational strong coupling (VSC), has been observed to modify reaction kinetics for a wide range of reactions [1], ranging from organic [20–23] to inorganic [24] to enzymatic [25, 26]. That the investigated reactions are thermally activated (i.e., are carried out in the absence of external pumping, such as laser and electrical excitation) raises the possibility of using VSC in industrial applications.

To better understand the experimental changes in reactivity due to VSC, several studies [27–30] have applied transition-state theory (TST) [31], one of the simplest and most commonly used reaction-rate theories, to the case of molecules inside an optical cavity. However, these theoretical efforts find that reaction rates should change negligibly when many molecules collectively undergo VSC to a cavity mode, as in the experiments. This discrepancy can be attributed to the fact that there are only 2 polaritons compared to $N-1 \gg 1$ dark states, where the latter states have the same energy as the bare (i.e., outside the cavity) vibrational states. Only for a single molecule (or a small number of molecules) does TST predict a change of reaction rate due to VSC [27, 28, 32].

Other works have focused on modeling reactions for which the assumptions of TST break down. The key assumptions of TST are [31]

1. no recrossing of reactive trajectories,

2. no quantum tunneling (on a single electronic potential energy surface),

3. no nonadiabatic transitions (i.e., transitions between different electronic surfaces),

4. internal thermal equilibrium [i.e., thermal equilibrium within the states of each chemical species (e.g., reactant, product)] is maintained throughout the reaction.

Significant changes in reactivity due to VSC have been theoretically revealed for reactions where assumptions 1 [33–37], 2 [35], and 3 [38, 39] break down. However, it is still unclear how VSC can modify reaction kinetics under typical experimental conditions [13, 15, 40]. In the context of VSC chemistry, reactions where TST assumption 4 breaks down have not been previously explored theoretically (to our knowledge; note that several perspective articles [15, 40] have suggested that nonequilibrium effects could be important in VSC chemistry).

To this end, this dissertation is focused on how VSC affects reactions where thermalization occurs on a similar or longer time scale compared to reactive events. For such reactions, internal thermal equilibrium may not be maintained—even approximately—at all times (i.e., TST assumption 4 may break down). First, we consider thermally activated electron transfer. We reveal two different mechanisms by which VSC can accelerate thermalization and suppress nonequilibrium effects that influence the reaction rate. In the first mechanism, which is more likely when a few molecules undergo VSC [$N \sim O(1)$], the polaritons enable modified reactivity [41]. In the second mechanism, which relies on energetic disorder and is entropically favorable when many molecules undergo VSC ($N \gg 1$), the reaction kinetics is altered by the dark states [42]. Then, we turn our focus to a photochemical reaction, where molecules are driven out of thermal equilibrium by a laser. Using VSC, we theoretically engineer a "remote control" of chemistry, where excitation of molecules in one optical cavity can boost the reaction efficiency of molecules in a second optical cavity [43]. Lastly, we study a related phenomenon, polariton-assisted remote energy transfer

(PARET), in which strong coupling of molecular electronic transitions enables energy transfer between spatially separated dye molecules [44].

1.1 Summary of contents

In Chapter 2, which is adapted from [41], we investigate how VSC affects thermally activated electron transfer where thermalization and reactive transitions occur on similar time scales. We employ an electron-transfer model based on Marcus-Levich-Jortner theory [45–47]. For $N = 2$ molecules coupled to a cavity mode, we show that the reaction kinetics can altered by dissipative processes (in particular, cavity decay) that are available to polaritons but not to molecular states outside a cavity.

In Chapter 3, which is adapted from [42], we study a disordered ensemble of $N \gg 1$ molecules under VSC. When static disorder (i.e., inhomogeneous broadening) is present in the molecules, VSC creates dark states that are delocalized across $2-3$ molecules, in contrast to the localized molecular states outside a cavity. Using the aforementioned model of electron transfer, we reveal an unconventional mechanism by which dark-state delocalization suppresses the backward reaction of vibrationally hot product while leaving vibrational decay unchanged, thereby increasing the net rate of product formation.

In Chapter 4, which is adapted from [43], we propose a device involving two optical cavities, one containing a "remote catalyst" and the other containing a reactant. Featuring VSC between each compound and its host cavity, the device enables excitation of the remote catalyst to alter the photochemical reactivity of the reactant, even though the two compounds are spatially separated. We demonstrate such "remote control" for the infrared-induced *cis* $\rightarrow$ *trans* conformational isomerization of nitrous acid (HONO).

In Chapter 5, which is adapted from [44], we focus on PARET. We develop a comprehensive theory for energy transfer between spatially separated chromophores, whose electronic

transitions are strong coupled to surface plasmons. Applying the theory, we shed light on experiments reporting PARET when both donor and acceptor chromophores undergo strong coupling. We also predict PARET (or lack thereof) for cases where one chromophore undergoes strong coupling, including a "carnival effect" where donor and acceptors reverse roles.

In Chapter 6, we summarize the research presented in this dissertation and present an outlook on the field of polariton chemistry.

Chapter 2

Electron transfer under vibrational strong coupling: effect of polaritons

2.1 Introduction

Strong light-matter interaction, or simply strong coupling (SC), occurs when an optical cavity mode and a material excitation coherently exchange energy faster than either species decays [2, 48–50]. This interaction results in light-matter eigenstates called polaritons. In addition to inheriting both photonic and material properties, the hybrid states have different energies than their constituents.

These features make polaritons a promising platform for modifying the physicochemical properties of molecular systems [4, 9]. Typically, SC in such systems is achieved by the interaction between a cavity mode and $N \gg 1$ quasidegenerate excitations in a molecular ensemble. This collective SC produces two polariton states and $N-1$ dark states. At light-matter resonance, the so-called lower and upper polaritons are respectively redshifted and blueshifted from the bare molecular (photonic) excitations by the collective light-matter coupling strength $g\sqrt{N}$, where g is the single-molecule light-matter coupling strength and $\Omega = 2g\sqrt{N}$ is the so-called Rabi splitting.

In contrast, the dark states remain unchanged in energy. Nevertheless, the polaritons can dissipate into the dark states [51–57], enriching the relaxation dynamics of the SC regime.

In light of the considerable impact that polariton formation has on molecular excited states [58–61], and of the photonic character of polaritons, it is not surprising that SC is emerging as a versatile tool for manipulating photochemistry. It has been shown that, in organic materials, polaritons can lower the activation barrier of spin-conversion processes [62–66], enhance conductivity [67–71], change the dynamics of photoinduced charge transfer [72–77], and alter photoisomerization yield [78–83]. In some situations, dissipation associated with SC plays a key role in the modification of photochemical processes. Notably, cavity decay (photon leakage from the cavity) can enable the suppression of photodegradation by diverting population from polaritons to the electronic ground state instead of to the product [84–86]. The effect of cavity decay on photochemical reactivity has also been demonstrated theoretically for photodissociation [87, 88], and photoisomerization [82, 83]. Another contributor to the suppression of photodegradation is the relaxation between polaritons and dark states [84, 86]. This dissipative coupling can even mediate polariton-assisted remote energy transfer [44, 89–92]. Moreover, relaxation from polaritons to dark states can be harnessed to realize remote control of photoisomerization (see Chapter 4) [43].

Much less is understood about the ability to modify thermally activated reactions using SC [17, 19] of molecular vibrations, commonly known as vibrational SC (VSC). Recent experiments [1] demonstrate that reactions can be enhanced or suppressed by VSC without external pumping (e.g., laser excitation). Reactions affected by VSC include organic substitution [20–22], organic rearrangement [23], and hydrolysis [24]. However, the intriguing VSC reaction kinetics still lacks a theoretical underpinning. Transition-state theory, the most commonly used reaction-rate theory, has been unsuccessful at explaining the VSC reactions [27–30]. While a model of nonadiabatic electron transfer under VSC captures some of the observed trends [38], additional connections to experiments have yet to be made. Common to the attempted theoretical approaches is the following assumption: internal thermalization (i.e., within the states of each chemical species) is much faster than reactive transitions (i.e., between the states of different chemical species). Said differently,

states of each chemical species are assumed to remain at internal thermal equilibrium throughout the reaction.

Nonequilibrium effects may therefore be relevant in thermally activated reactions modified by VSC. In the context of adiabatic reactions, recent findings [33] reveal that non-Markovian dynamics along the cavity-mode coordinate can induce trapping of population in a high-energy region of the potential energy surface, preventing internal thermalization and promoting backward reactive transitions. Alternatively, it would be interesting to explore how VSC affects reactions with significant nonequilibrium effects outside the cavity. For instance, some organic reactions involve the formation of vibrationally hot intermediate species that react before they fully thermalize [93–95]. This may happen in desilylation reactions, which feature reactive intermediates [96] and appear in studies reporting suppression of product formation [20, 21, 97] and rise in product selectivity [21] using VSC. If nonequilibrium effects are indeed relevant to the VSC reactions, then another intriguing topic is the role of dissipation, which is what enables thermal equilibrium to be reached.

Here, we carry out a kinetic study of how the dissipative processes that VSC introduces to the chemical system—specifically, cavity decay plus incoherent energy exchange among polaritons and dark states—affects thermally activated reactions with significant nonequilibrium effects. The class of reactions we consider is electron transfer, which is modeled using Marcus-Levich-Jortner (MLJ) theory [45–47]. We examine reactions where vibrational relaxation and reactive transitions occur on similar timescales. For the case of VSC, we use a generalization of the MLJ model to calculate rates of reactive transitions. Rates associated with internal thermalization are calculated using a standard treatment [53] of polariton relaxation. By comparing reaction kinetics under VSC with those in the bare case and under weak light-matter coupling, we show that dissipation associated with VSC can alter reaction kinetics by suppressing nonequilibrium effects. It follows that the presence of nonequilibrium effects in the bare reaction can be important in determining the influence of VSC on reactivity. Before concluding this paper, we discuss our results in the context of the aforementioned experiments.

2.2 Theory

2.2.1 Hamiltonian

Consider N identical molecules inside an optical cavity. Each molecule can undergo a series of nonadiabatic electron transfer reactions. Such reactions occur via transitions between diabatic electronic states, each representing a different reactive species (e.g., reactant, intermediate, product). In the spirit of MLJ theory, the electronic states experience vibronic coupling to high-frequency intramolecular vibrational modes and low-frequency solvent vibrational modes [47], i.e., electron transfer is coupled to high- and low-frequency vibrations. Both types of modes are hence reactive degrees of freedom. For simplicity, suppose that each molecule has only one high-frequency reactive mode (hereafter conveniently referred to as vibrational mode), and assume that VSC takes place between this mode and a single cavity mode. Already, we can see that the role of VSC is to modify the dynamics of a reactive mode.

The Hamiltonian describing the electron-transfer molecules under VSC is

$$H = H_{\mathrm{S}} + H_{\mathrm{B}} + H_{\mathrm{S-B}}. \tag{2.1}$$

The first term,

$$H_{\mathrm{S}} = H_{\mathrm{e}} + H_{\mathrm{v}} + H_{\mathrm{e-v}} + H_{\mathrm{c}} + H_{\mathrm{c-v}} + V_{\mathrm{ET}}, \tag{2.2}$$

characterizes the "system", the subspace whose evolution we are interested in. Comprising the system are the electronic, vibrational, and cavity degrees of freedom. Electronic states are given by

$$H_{\mathrm{e}} = \sum_{i=1}^{N} \sum_{\phi} E_{\phi} |\phi^{(i)}\rangle\langle\phi^{(i)}|, \tag{2.3}$$

where $|\phi^{(i)}\rangle$ has energy E_ϕ and represents the molecule i belonging to reactive species ϕ. Next,

$$H_{\mathrm{v}} = \hbar\omega_{\mathrm{v}} \sum_{i=1}^{N} a_i^\dagger a_i \tag{2.4}$$

characterizes the vibrational modes, where the mode belonging to molecule i is represented by creation (annihilation) operator $a_i^\dagger$ (a_i). Vibronic coupling involving the high-frequency vibrational modes is described by

$$H_{\mathrm{e-v}} = \hbar\omega_{\mathrm{v}} \sum_{i=1}^{N} \sum_{\phi} |\phi^{(i)}\rangle\langle\phi^{(i)}| \left[\lambda_\phi \left(a_i^\dagger + a_i\right) + \lambda_\phi^2\right]. \tag{2.5}$$

For any molecule of reactive species ϕ, λ_ϕ is the dimensionless displacement of the corresponding vibrational mode. The following two terms of H_{S} [Eq. (2.2)] are the cavity Hamiltonian

$$H_{\mathrm{c}} = \hbar\omega_{\mathrm{c}} a_0^\dagger a_0, \tag{2.6}$$

and the light-matter interaction

$$H_{\mathrm{c-v}} = \hbar g \sum_{i=1}^{N} \left(a_i^\dagger a_0 + a_0^\dagger a_i\right). \tag{2.7}$$

The cavity mode has frequency ω_{c} and is represented by creation (annihilation) operator $a_0^\dagger$ (a_0). In writing Eq. (2.7), we have assumed that molecules of all reactive species undergo VSC. Presumably, this condition has been realized in studies showing that organic desilylation [21] and TPPK-acetone cyclization [24] can be modified by VSC, namely that involving a vibrational mode which is optically bright and nearly identical in energy for both reactant and product species. For cases where only one of reactant and product experiences VSC, theoretical modeling [38, 39] predicts interesting effects such as autocatalysis [38]; we do not focus here on situations where different reactive species couple unequally to the cavity. Finally, the electron-transfer interaction

reads

$$V_{\mathrm{ET}} = \sum_{i=1}^{N} \sum_{\phi \neq \varphi} \left(J_{\phi\varphi} |\varphi^{(i)}\rangle\langle\phi^{(i)}| + J_{\varphi\phi} |\phi^{(i)}\rangle\langle\varphi^{(i)}| \right), \tag{2.8}$$

where $J_{\phi\varphi} = J_{\varphi\phi}$ is the diabatic coupling between reactive species ϕ and φ. The remaining degrees of freedom, which constitute the "bath", are captured in H_{B}. The bath includes the low-frequency solvent modes that participate in electron transfer, as well as modes that induce decay and incoherent energy exchange among the polaritons and dark states. The system-bath coupling responsible for these relaxation processes is characterized by $H_{\mathrm{S-B}}$. For the sake of brevity, we will not explicitly define H_{B} and $H_{\mathrm{S-B}}$ here.

The eigenstates of the system, treating the electron-transfer interaction (V_{ET}) as perturbative, can be found by diagonalizing the zeroth-order Hamiltonian

$$H_0 = H_{\mathrm{e}} + H_{\mathrm{e-v}} + H_{\mathrm{CV}}, \tag{2.9}$$

where $H_{\mathrm{CV}} = H_{\mathrm{v}} + H_{\mathrm{c}} + H_{\mathrm{c-v}}$ governs the subsystem that includes cavity and vibrational modes. Two polariton and $N-1$ dark modes make up the eigenmodes of H_{CV}. Let operators $\alpha_q = \sum_{i=0}^{N} c_{qi} a_i$ for $q = \pm, 2, \ldots, N$ represent the eigenmodes. The polariton modes respectively have frequencies $\omega_{\pm} = \frac{1}{2}\left(\omega_{\mathrm{c}} + \omega_{\mathrm{v}} \pm \sqrt{(\omega_{\mathrm{c}} - \omega_{\mathrm{v}})^2 + 4g^2 N}\right)$ and are given by

$$\alpha_+ = (\cos\theta) a_0 + (\sin\theta) \frac{1}{\sqrt{N}} \sum_{i=1}^{N} a_i, \tag{2.10a}$$

$$\alpha_- = (\sin\theta) a_0 - (\cos\theta) \frac{1}{\sqrt{N}} \sum_{i=1}^{N} a_i, \tag{2.10b}$$

where $\theta = \frac{1}{2}\tan^{-1}[2g\sqrt{N}/(\omega_{\mathrm{c}} - \omega_{\mathrm{v}})]$. The dark modes all have frequency ω_{v}, and each one is represented by α_q for $q = 2, \ldots, N$. Due to the degeneracy of the dark states, there exist multiple ways to express the dark modes in terms of the bare modes (e.g., see Refs. [38] and [98]). We now define multiparticle states for the various system degrees of freedom. Define $|\boldsymbol{\phi}\rangle \equiv |\phi_1, \phi_2, \ldots, \phi_N\rangle$ as the multiparticle electronic state where molecule i belongs to reactive species ϕ_i. For the cavity-

vibrational modes, we define $|\mathbf{m}\rangle \equiv |m_+, m_-, m_2, \ldots, m_N\rangle$, which is an eigenstate of H_{CV} with m_q excitations in mode q and with energy $\sum_{q=\pm,2,\ldots,N} m_q \hbar\omega_q$. Moving to this multiparticle representation and carrying out some additional rearrangements, we can write the zeroth-order system Hamiltonian [Eq. (2.9)] in the diagonal form

$$H_0 = \sum_{\boldsymbol{\phi}} \sum_{\mathbf{m}} E_{\boldsymbol{\phi};\mathbf{m}} |\boldsymbol{\phi};\mathbf{m}\rangle\langle\boldsymbol{\phi};\mathbf{m}|. \tag{2.11}$$

The eigenstates

$$|\boldsymbol{\phi};\mathbf{m}\rangle \equiv |\boldsymbol{\phi}\rangle \otimes |\tilde{\mathbf{m}}_{(\boldsymbol{\phi})}\rangle \tag{2.12}$$

are expressed as products of an electronic state and a displaced cavity-vibrational state. The latter is given by

$$|\tilde{\mathbf{m}}_{(\boldsymbol{\phi})}\rangle \equiv \left[\prod_{q=\pm,2,\ldots,N} \mathcal{D}_q^\dagger(\lambda_{\boldsymbol{\phi}q})\right] |\mathbf{m}\rangle, \tag{2.13}$$

where $\mathcal{D}_q(\lambda) = \exp\left(\lambda\alpha_q^\dagger - \lambda^*\alpha_q\right)$ is the displacement operator for eigenmode q. The displacement of mode q, when the system is in electronic state $|\boldsymbol{\phi}\rangle$, is

$$\lambda_{\boldsymbol{\phi}q} \equiv \sum_{i=1}^{N} \lambda_{\phi_i q}^{(i)}, \tag{2.14}$$

where

$$\lambda_{\phi_i q}^{(i)} \equiv c_{qi} \frac{\omega_{\mathrm{v}}}{\omega_q} \lambda_{\phi_i} \tag{2.15}$$

is the contribution due to the vibronic coupling in molecule i (when this molecule belongs to reactive species ϕ_i). From Eqs. (2.14)-(2.15), it is evident that VSC redistributes the displacements of the bare modes among the polariton and dark modes. How displaced each eigenmode is depends on its frequency and its overlap with the bare modes [Eq. (2.15)]. Returning to the electronic-

cavity-vibrational eigenstates $|\boldsymbol{\phi};\mathbf{m}\rangle$, the corresponding energies are

$$E_{\boldsymbol{\phi};\mathbf{m}} = \sum_{i=1}^{N} E_{\phi_i} + \sum_{q=\pm,2,\ldots,N} m_q \hbar\omega_q + \left(\hbar\omega_{\mathrm{v}} \sum_{i=1}^{N} \lambda_{\phi_i}^2 - \sum_{q=\pm,2,\ldots,N} \hbar\omega_q \left|\lambda_{\boldsymbol{\phi}q}\right|^2 \right). \tag{2.16}$$

We see that VSC does not only change the energies of states containing vibrational character [second summation in the first line of Eq. (2.16)], but it also induces an energy shift equal to the difference in high-frequency reorganization energy before and after VSC [second line of Eq. (2.16)].

2.2.2 Kinetic model: VSC

Having obtained the system eigenstates and energies, we proceed to discuss the kinetic model for simulating thermally activated nonadiabatic electron transfer under VSC. We are interested in reactions where nonequilibrium effects are significant outside the cavity. To focus on how the reactions are impacted by VSC, including dissipation brought about by VSC, we limit ourselves to the case of $N = 2$ and neglect multiply excited cavity-vibrational states; the state-space truncation is a good approximation in our simulations (Sec. 2.3), where we choose parameters such that (1) virtually all initial population resides in the zero- and first-excitation manifolds of the cavity-vibrational subspace and (2) such that transitions within these lower manifolds are much faster than transitions into higher manifolds. With these simplifications, we keep the dynamics tractable enough for physical interpretation while still working in the regime of collective VSC (i.e., $N > 1$). In Sec. 2.4, we discuss the case of many-molecule VSC.

We now present the kinetic model. The evolution of the system is governed by the master

equation

$$\frac{dp_{(\boldsymbol{\phi};\mathbf{m})}(t)}{dt} = -\left[\sum_{(\boldsymbol{\phi}';\mathbf{m}')\neq(\boldsymbol{\phi};\mathbf{m})} k(\boldsymbol{\phi}';\mathbf{m}'|\boldsymbol{\phi};\mathbf{m})\right] p_{(\boldsymbol{\phi};\mathbf{m})}(t) + \sum_{(\boldsymbol{\phi}';\mathbf{m}')\neq(\boldsymbol{\phi};\mathbf{m})} k(\boldsymbol{\phi};\mathbf{m}|\boldsymbol{\phi}';\mathbf{m}') p_{(\boldsymbol{\phi}';\mathbf{m}')}(t). \tag{2.17}$$

The quantity $p_{(\boldsymbol{\phi};\mathbf{m})}$ represents the population of $|\boldsymbol{\phi};\mathbf{m}\rangle$, and $k(\boldsymbol{\phi}';\mathbf{m}'|\boldsymbol{\phi};\mathbf{m})$ denotes the rate of transition $|\boldsymbol{\phi};\mathbf{m}\rangle \to |\boldsymbol{\phi}';\mathbf{m}'\rangle$. Processes of three types are included in the kinetic model: reactive transitions; cavity-vibrational loss and gain; and relaxation among polaritons and the dark state (there is only one dark state for $N = 2$). The latter two sets of processes occur within the same electronic state and contribute to internal thermalization.

A reactive transition occurs between states $|\boldsymbol{\phi};\mathbf{m}\rangle$ and $|\boldsymbol{\phi}';\mathbf{m}'\rangle$ if the initial state is converted to the final state by the electron-transfer reaction of molecule i from reactive species φ to reactive species $\varphi' \neq \varphi$ (i.e., $|\boldsymbol{\phi}\rangle \neq |\boldsymbol{\phi}'\rangle$, $\phi_i = \varphi$, $\phi_i' = \varphi'$, $\phi_j = \phi_j'$ for $j \neq i$). The corresponding transition rate, derived in analogy to the MLJ electron-transfer rate [99], is

$$k(\boldsymbol{\phi}';\mathbf{m}'|\boldsymbol{\phi};\mathbf{m}) = \sqrt{\frac{\pi}{\lambda_{\mathrm{s}}^{(\varphi\varphi')} k_B T}} \frac{|J_{\varphi\varphi'}|^2}{\hbar} \left|\langle \tilde{\mathbf{m}}'_{(\boldsymbol{\phi}')} | \tilde{\mathbf{m}}_{(\boldsymbol{\phi})} \rangle\right|^2 \times \exp\left[-\frac{\left(E_{\boldsymbol{\phi}';\mathbf{m}'} - E_{\boldsymbol{\phi};\mathbf{m}} + \lambda_{\mathrm{s}}^{(\varphi\varphi')}\right)^2}{4\lambda_{\mathrm{s}}^{(\varphi\varphi')} k_B T}\right], \tag{2.18}$$

where $\lambda_{\mathrm{s}}^{(\varphi\varphi')} = \lambda_{\mathrm{s}}^{(\varphi'\varphi)}$ is the low-frequency reorganization energy for the reaction between species φ and φ', k_B is the Boltzmann constant, and T is the temperature. The rate depends on a generalized Franck-Condon factor, $\langle \tilde{\mathbf{m}}'_{(\boldsymbol{\phi}')} | \tilde{\mathbf{m}}_{(\boldsymbol{\phi})} \rangle$, for the cavity-vibrational states, where

$$\left|\langle \tilde{\mathbf{m}}'_{(\boldsymbol{\phi}')} | \tilde{\mathbf{m}}_{(\boldsymbol{\phi})} \rangle\right|^2 = \left| \prod_{q=\pm,\mathrm{d}} \langle m'_q | \mathcal{D}_q \left(\lambda_{\varphi' q}^{(i)} - \lambda_{\varphi q}^{(i)}\right) | m_q \rangle \right|^2. \tag{2.19}$$

We have relabeled the single dark mode of the two-molecule system as $q = \mathrm{d}$. The undisplaced

cavity-vibrational state $|m_q\rangle$ is the single-particle eigenstate of H_{CV} with m_q excitations in mode q. Matrix elements of the displacement operator $\mathcal{D}_q(\lambda)$ with respect to the undisplaced cavity-vibrational states are evaluated according to the property [100]

$$\langle m_q'|\mathcal{D}_q(\lambda)|m_q\rangle = \sqrt{\frac{m_q!}{(m_q')!}} e^{-|\lambda|^2/2} \lambda^{m_q'-m_q} L_{m_q}^{m_q'-m_q}(|\lambda|^2)$$
$$\text{for } m_q' \geq m_q, \tag{2.20}$$

where $L_n^k(x)$ is an associated Laguerre polynomial; for $m_q' < m_q$, the matrix element is evaluated using the same expression except with $m_q' \leftrightarrow m_q$ and $\lambda \to -\lambda^*$.

We next discuss cavity-vibrational loss and gain. First consider loss. For the optical cavities used in previous experiments of VSC reactions, bare cavity states decay via the leakage of photons out into free space. In contrast, bare vibrational states decay through dissipation into solvent and intermolecular modes. In VSC, the cavity-vibrational states can decay through a combination of cavity and vibrational channels. The decay of $|\boldsymbol{\phi}, \hat{\mathbf{e}}_q\rangle$, where $\hat{\mathbf{e}}_q$ is the unit vector representing a single excitation of mode $q = \pm, \mathrm{d}$, has rate [53, 62]

$$k(\boldsymbol{\phi}; \mathbf{0}|\boldsymbol{\phi}; \hat{\mathbf{e}}_q) = |c_{q0}|^2 \kappa + \left(\sum_{i=1}^{2} |c_{qi}|^2 \right) \gamma. \tag{2.21}$$

The bare cavity decay rate is κ, and the bare vibrational decay rate is γ. For nonzero temperatures, the reverse process, gain, can occur. The corresponding rate is determined by detailed balance: $k(\boldsymbol{\phi}; \hat{\mathbf{e}}_q|\boldsymbol{\phi}; \mathbf{0}) = k(\boldsymbol{\phi}; \mathbf{0}|\boldsymbol{\phi}; \hat{\mathbf{e}}_q) \exp(-\hbar\omega_q / k_B T)$.

Lastly, we have relaxation among polaritons and the dark state. Processes of this type originate from anharmonic coupling between vibrational states and low-frequency molecular modes of the local environment [53, 55, 56, 101]. The relaxation from $|\boldsymbol{\phi}, \hat{\mathbf{e}}_q\rangle$ to $|\boldsymbol{\phi}, \hat{\mathbf{e}}_{q'}\rangle$ (where $q, q' = \pm, \mathrm{d}$

and $q \neq q'$) has rate [53, 62]

$$k(\boldsymbol{\phi};\hat{\mathbf{e}}_{q'}|\boldsymbol{\phi};\hat{\mathbf{e}}_q) = 2\pi \left(\sum_{i=1}^{2} |c_{q'i}|^2 |c_{qi}|^2 \right) \times \{\Theta(-\omega)\,[\bar{n}(-\omega)+1]\,\mathcal{J}(-\omega) + \Theta(\omega)\bar{n}(\omega)\mathcal{J}(\omega)\}\,, \tag{2.22}$$

where $\Theta(\omega)$ is the Heaviside step function, $\bar{n}(\omega) = [\exp(\hbar\omega/k_B T) - 1]^{-1}$ is the Bose-Einstein distribution function, and $\mathcal{J}(\omega)$ is the spectral density of the anharmonically coupled low-frequency bath modes. For the simulations in Sec. 2.3, we assume an Ohmic spectral density [53]: $\mathcal{J}(\omega) = \eta\,\omega \exp\left[-(\omega/\omega_{\text{cut}})^2\right]$, where η is a dimensionless parameter representing the anharmonic system-bath interaction, and ω_{cut} is the cutoff frequency of the low-frequency bath modes.

Now that we have presented the various processes captured by our kinetic model, we note, for completeness, that $k(\boldsymbol{\phi}';\mathbf{m}'|\boldsymbol{\phi};\mathbf{m}) = 0$ for any transition $|\boldsymbol{\phi};\mathbf{m}\rangle \to |\boldsymbol{\phi}';\mathbf{m}'\rangle$ not induced by these processes, i.e., not described by Eqs. (2.18), (2.21), and (2.22).

To conclude this section, we summarize how VSC influences reactive transitions and internal thermalization within our kinetic model. We do so in the context of reactions with nonequilibrium effects, which arise when internal thermalization is not fast compared to reactive transitions. First, recall that VSC alters energies and redistributes the vibronic coupling of localized bare modes among the delocalized eigenmodes (Sec. 2.2.1). In view of this, Eq. (2.18) says that VSC affects the rate of reactive transitions by changing activation energy—which is related to the energies of the initial and final states—and the Franck-Condon factor between initial and final states. These rate changes can lead to modified reactivity when reactive species are at internal thermal equilibrium and when they are not. On the other hand, the additional relaxation channels created by VSC, i.e., cavity loss and gain for polaritons [Eq. (2.21)] and relaxation among polaritons and the dark state [Eq. (2.22)], help thermalize the vibrational states and only change populations when reactive species are not at internal thermal equilibrium. Thus, if creating these additional relaxation channels is the dominant effect of VSC, then nonequilibrium effects will be suppressed, as we will

see in Sec. 2.3.

2.2.3 Kinetic model: no light-matter coupling

For the kinetic model of reactions in the bare case (i.e., light-matter coupling strength $g = 0$), we write the zeroth-order system eigenstates [i.e., the eigenstates of H_0, Eq. (2.9)] in the basis of localized vibrational and cavity modes [see Eqs. (2.4) and (2.6), respectively] instead of the basis of the polariton and dark modes. In the chosen basis, the eigenstates are still of the form $|\boldsymbol{\phi};\mathbf{m}\rangle \equiv |\boldsymbol{\phi}\rangle \otimes |\tilde{\mathbf{m}}_{(\boldsymbol{\phi})}\rangle$ [Eq. (2.12)], except that the displaced cavity-vibrational states are given by

$$|\tilde{\mathbf{m}}_{(\boldsymbol{\phi})}\rangle = \left[\prod_{i=1}^{N} \mathcal{D}_i^{\dagger}(\lambda_{\phi_i})\right] |\mathbf{m}\rangle, \tag{2.23}$$

where $|\mathbf{m}\rangle \equiv |m_0, m_1, , \ldots, m_N\rangle$ represents the state where mode $i = 0, 1, , \ldots, N$ has m_i excitations, and $\mathcal{D}_i(\lambda) = \exp\left(\lambda a_i^{\dagger} - \lambda^* a_i\right)$ is the displacement operator for mode i. The zeroth-order energy of $|\boldsymbol{\phi};\mathbf{m}\rangle$ is

$$E_{\boldsymbol{\phi};\mathbf{m}} = \sum_{i=1}^{N} E_{\phi_i} + m_0 \hbar \omega_{\mathrm{c}} + \hbar \omega_{\mathrm{v}} \sum_{i=1}^{N} m_i. \tag{2.24}$$

The bare system is evolved under the same assumptions (including $N = 2$) as in the case of VSC (Sec. 2.2.2). The master equation of the bare dynamics takes the general form of Eq. (2.17). For the reaction of molecule $i = 1, 2$ from reactive species φ to reactive species $\varphi' \neq \varphi$, the reactive-transition rate is calculated with Eq. (2.18), where the generalized Franck-Condon factors are evaluated using

$$\left|\langle \tilde{\mathbf{m}}'_{(\boldsymbol{\phi}')} | \tilde{\mathbf{m}}_{(\boldsymbol{\phi})} \rangle\right|^2 = \left|\delta_{m'_0 m_0} \langle m'_i | \mathcal{D}_i(\lambda_{\varphi'} - \lambda_{\varphi}) | m_i \rangle \delta_{m'_j m_j}\right|^2 \tag{2.25}$$

for $j = 2\delta_{i1} + \delta_{i2} \neq i$ (here, δ_{ik} is the Kronecker delta) and the analog of Eq. (2.20) with $q \to i$. The undisplaced single-particle state $|m_i\rangle$ represents m_i excitations in mode i. The decay transitions

have rates

$$k(\boldsymbol{\phi};\mathbf{0}|\boldsymbol{\phi};\hat{\mathbf{e}}_i) = \begin{cases} \kappa, & i = 0, \\ \gamma, & i \neq 0. \end{cases} \tag{2.26}$$

The reverse rates are governed by detailed balance:

$$k(\boldsymbol{\phi};\hat{\mathbf{e}}_i|\boldsymbol{\phi};\mathbf{0}) = \begin{cases} k(\boldsymbol{\phi};\mathbf{0}|\boldsymbol{\phi};\hat{\mathbf{e}}_i)\exp(-\hbar\omega_{\mathrm{c}}/k_B T), & i = 0, \\ k(\boldsymbol{\phi};\mathbf{0}|\boldsymbol{\phi};\hat{\mathbf{e}}_i)\exp(-\hbar\omega_{\mathrm{v}}/k_B T), & i \neq 0. \end{cases} \tag{2.27}$$

Among the singly excited vibrational states, there are no transitions of the same nature as the relaxation among polaritons and dark states, i.e., $k(\boldsymbol{\phi};\hat{\mathbf{e}}_j|\boldsymbol{\phi};\hat{\mathbf{e}}_i) = 0$. As mentioned in Sec. 2.2.2, this incoherent energy exchange is caused by local system-bath interactions, which do not couple different local vibrational modes. All rates $k(\boldsymbol{\phi}';\mathbf{m}'|\boldsymbol{\phi};\mathbf{m})$ that have not been discussed in this section are taken to be 0.

2.2.4 Kinetic model: weak light-matter coupling

In this section, we derive the kinetic model that we use to simulate reactions where the light-matter interaction strength is $g = (3\times10^{-4})\omega_{\mathrm{v}}/\sqrt{2}$ and the cavity decay rate is $\kappa = 1\mathrm{ps}^{-1} \gg g\sqrt{N}$ (where $N = 2$). Together, these parameters signify the regime of weak light-matter coupling. In this regime, the light-matter coupling can be treated as a perturbation to the system. Thus, the zeroth-order system eigenstates are those of the bare case (Sec. 2.2.3). However, the light-matter coupling does change the population dynamics of the system. Below we follow a textbook approach (see Ref. [99], pp. 103-106 and 413) to show that, when the cavity and/or vibrational excitations decay on a timescale much shorter than that of the reaction dynamics, the effect of weak light-matter coupling is to induce incoherent energy exchange between the excitations. Essentially, the employed approach is a perturbative correction to the non-Hermitian dynamics of the bare case.

Formally, the dynamics of the bare system can be given by the quantum master equation

[99]

$$\frac{d\rho(t)}{dt} = -i(\mathcal{L}_0 - i\mathcal{R})\rho(t), \tag{2.28}$$

where $\rho(t)$ is the reduced density operator of the system, and the superoperator $\mathcal{L}_0 - i\mathcal{R}$ generates the bare dynamics. The Liouvillian superoperator $\mathcal{L}_0(\cdot) = [H_0, \cdot]/\hbar$ generates the coherent (Hermitian) dynamics of the bare system. Here, H_0 is the zeroth-order system Hamiltonian without light-matter interaction. The superoperator $\mathcal{R}$ represents system-bath interaction and generates the incoherent (non-Hermitian) dynamics of the system, i.e., all reaction and relaxation dynamics of the bare case. If we act on Eq. (2.28) with $\langle \boldsymbol{\phi}; \mathbf{m}|$ from the left and $|\boldsymbol{\phi}; \mathbf{m}\rangle$ from the right, we recover the master equation governing the bare population dynamics (see Sec. 2.2.3):

$$\begin{aligned}\frac{dp_{(\boldsymbol{\phi};\mathbf{m})}(t)}{dt} = &-k^{(\mathrm{out})}_{(\boldsymbol{\phi};\mathbf{m})} p_{(\boldsymbol{\phi};\mathbf{m})}(t) \\ &+ \sum_{(\boldsymbol{\phi}';\mathbf{m}')\neq(\boldsymbol{\phi};\mathbf{m})} k(\boldsymbol{\phi};\mathbf{m}|\boldsymbol{\phi}';\mathbf{m}') p_{(\boldsymbol{\phi}';\mathbf{m}')}(t),\end{aligned} \tag{2.29}$$

where, for convenience, we have defined $k^{(\mathrm{out})}_{(\boldsymbol{\phi};\mathbf{m})} \equiv \sum_{(\boldsymbol{\phi}';\mathbf{m}')\neq(\boldsymbol{\phi};\mathbf{m})} k(\boldsymbol{\phi}';\mathbf{m}'|\boldsymbol{\phi};\mathbf{m})$ as the outgoing rate of population transfer from state $|\boldsymbol{\phi};\mathbf{m}\rangle$. If we instead act on Eq. (2.28) with $\langle \boldsymbol{\phi};\mathbf{m}|$ from the left and $|\boldsymbol{\phi}';\mathbf{m}'\rangle \neq |\boldsymbol{\phi};\mathbf{m}\rangle$ from the right, we arrive at

$$\begin{aligned}\frac{d\rho_{(\boldsymbol{\phi};\mathbf{m}),(\boldsymbol{\phi}';\mathbf{m}')}(t)}{dt} = -i\Big[&(E_{\boldsymbol{\phi};\mathbf{m}} - E_{\boldsymbol{\phi}';\mathbf{m}'})/\hbar \\ &- ik^{(\mathrm{out})}_{(\boldsymbol{\phi};\mathbf{m})}/2 - ik^{(\mathrm{out})}_{(\boldsymbol{\phi}';\mathbf{m}')}/2\Big]\rho_{(\boldsymbol{\phi};\mathbf{m}),(\boldsymbol{\phi}';\mathbf{m}')}(t),\end{aligned} \tag{2.30}$$

where $\rho_{(\boldsymbol{\phi};\mathbf{m}),(\boldsymbol{\phi}';\mathbf{m}')}(t) = \langle \boldsymbol{\phi};\mathbf{m}|\rho(t)|\boldsymbol{\phi}';\mathbf{m}'\rangle$ is a coherence. In writing Eq. (2.30), we have assumed that each coherence is decoupled from populations and other coherences. We have also, for simplicity, neglected pure dephasing.

For the system under weak light-matter coupling, the light-matter interaction $H_{\mathrm{c-v}}$ [Eq. (2.7)] is added to the Hamiltonian (H_0) of the bare system. To account for this change in the quantum master equation, we simply add the superoperator $\mathcal{L}_{\mathrm{c-v}}(\cdot) = [H_{\mathrm{c-v}}, \cdot]/\hbar$ to the superoperator $(\mathcal{L}_0 - i\mathcal{R})$ that generates the bare dynamics. In doing so, we implicitly ignore the effect of light-

matter coupling on system-bath interaction; this approximation should hold for sufficiently small values of light-matter interaction strength. Quantum master equation (2.28) now reads

$$\frac{d\rho(t)}{dt} = -i(\mathcal{L}_0 - i\mathcal{R})\rho(t) - i\mathcal{L}_{\mathrm{c-v}}\rho(t). \tag{2.31}$$

With this transformation, states with a single vibrational excitation (i.e., $|\boldsymbol{\phi}, \hat{\mathbf{e}}_i\rangle$, $i = 1,2$) evolve as

$$\begin{aligned}\frac{dp_{(\boldsymbol{\phi};\hat{\mathbf{e}}_i)}(t)}{dt} = &-k^{(\mathrm{out})}_{(\boldsymbol{\phi};\hat{\mathbf{e}}_i)} p_{(\boldsymbol{\phi};\hat{\mathbf{e}}_i)}(t) \\ &+ \sum_{(\boldsymbol{\phi}';\mathbf{m}')\neq(\boldsymbol{\phi};\hat{\mathbf{e}}_i)} k(\boldsymbol{\phi};\hat{\mathbf{e}}_i|\boldsymbol{\phi}';\mathbf{m}') p_{(\boldsymbol{\phi}';\mathbf{m}')}(t) \\ &+ 2g\mathrm{Im}\rho_{(\boldsymbol{\phi};\hat{\mathbf{e}}_0),(\boldsymbol{\phi};\hat{\mathbf{e}}_i)}(t),\end{aligned} \tag{2.32}$$

and states with a single cavity excitation (i.e., $|\boldsymbol{\phi}, \hat{\mathbf{e}}_0\rangle$) evolve as

$$\begin{aligned}\frac{dp_{(\boldsymbol{\phi};\hat{\mathbf{e}}_0)}(t)}{dt} = &-k^{(\mathrm{out})}_{(\boldsymbol{\phi};\hat{\mathbf{e}}_0)} p_{(\boldsymbol{\phi};\hat{\mathbf{e}}_0)}(t) \\ &+ \sum_{(\boldsymbol{\phi}';\mathbf{m}')\neq(\boldsymbol{\phi};\hat{\mathbf{e}}_0)} k(\boldsymbol{\phi};\hat{\mathbf{e}}_0|\boldsymbol{\phi}';\mathbf{m}') p_{(\boldsymbol{\phi}';\mathbf{m}')}(t) \\ &- 2g\mathrm{Im}\sum_{j=1}^{2} \rho_{(\boldsymbol{\phi};\hat{\mathbf{e}}_0),(\boldsymbol{\phi};\hat{\mathbf{e}}_j)}(t).\end{aligned} \tag{2.33}$$

To arrive at Eqs (2.32)-(2.33), we have used the general relation $\rho_{(\boldsymbol{\phi}';\mathbf{m}'),(\boldsymbol{\phi};\mathbf{m})} = \rho^*_{(\boldsymbol{\phi};\mathbf{m}),(\boldsymbol{\phi}';\mathbf{m}')}$. For states with no vibrational or cavity excitations, the equations of motion remain the same as in the bare case. From Eqs. (2.32) and (2.33)—in particular, the last line of each equation—it is clear that the evolution of vibrational and cavity populations now depends on the light-matter coherence $\rho_{(\boldsymbol{\phi};\hat{\mathbf{e}}_0),(\boldsymbol{\phi};\hat{\mathbf{e}}_i)}$. In the presence of weak light-matter coupling, this light-matter coherence evolves

according to

$$\begin{aligned}
&\frac{d\rho_{(\boldsymbol{\phi};\hat{\mathbf{e}}_0),(\boldsymbol{\phi};\hat{\mathbf{e}}_i)}(t)}{dt} \\
&= -i\left(\Delta - ik^{(\mathrm{out})}_{(\boldsymbol{\phi};\hat{\mathbf{e}}_0)}/2 - ik^{(\mathrm{out})}_{(\boldsymbol{\phi};\hat{\mathbf{e}}_i)}/2\right)\rho_{(\boldsymbol{\phi};\hat{\mathbf{e}}_0),(\boldsymbol{\phi};\hat{\mathbf{e}}_i)}(t) \\
&\quad - igp_{(\boldsymbol{\phi};\hat{\mathbf{e}}_i)}(t) + igp_{(\boldsymbol{\phi};\hat{\mathbf{e}}_0)}(t) \\
&\quad - ig\rho_{(\boldsymbol{\phi};\hat{\mathbf{e}}_j),(\boldsymbol{\phi};\hat{\mathbf{e}}_i)}(t),
\end{aligned} \tag{2.34}$$

where $j = 2\delta_{i1} + \delta_{i2} \neq i$. We have defined $\Delta \equiv \omega_{\mathrm{c}} - \omega_{\mathrm{v}}$. Notice the appearance of $\rho_{(\boldsymbol{\phi};\hat{\mathbf{e}}_j),(\boldsymbol{\phi};\hat{\mathbf{e}}_i)}$, a coherence involving different vibrational states, in the last line of Eq. (2.34). In the weak-coupling regime, the evolution of this purely vibrational coherence is given by

$$\begin{aligned}
\frac{d\rho_{(\boldsymbol{\phi};\hat{\mathbf{e}}_j),(\boldsymbol{\phi};\hat{\mathbf{e}}_i)}(t)}{dt} &= -\left(k^{(\mathrm{out})}_{(\boldsymbol{\phi};\hat{\mathbf{e}}_j)}/2 + k^{(\mathrm{out})}_{(\boldsymbol{\phi};\hat{\mathbf{e}}_i)}/2\right)\rho_{(\boldsymbol{\phi};\hat{\mathbf{e}}_j),(\boldsymbol{\phi};\hat{\mathbf{e}}_i)}(t) \\
&\quad - ig\left[\rho_{(\boldsymbol{\phi};\hat{\mathbf{e}}_0),(\boldsymbol{\phi};\hat{\mathbf{e}}_i)}(t) - \rho_{(\boldsymbol{\phi};\hat{\mathbf{e}}_j),(\boldsymbol{\phi};\hat{\mathbf{e}}_0)}(t)\right].
\end{aligned} \tag{2.35}$$

It is apparent that the coherence $\rho_{(\boldsymbol{\phi};\hat{\mathbf{e}}_j),(\boldsymbol{\phi};\hat{\mathbf{e}}_i)}$ does not directly couple to populations. In other words, the coupling of populations to the purely vibrational coherence is higher-order in g, the strength of the perturbative light-matter interaction. We are interested in the lowest-order correction to the population dynamics due to light-matter interaction. Hence, we neglect the contribution of $\rho_{(\boldsymbol{\phi};\hat{\mathbf{e}}_j),(\boldsymbol{\phi};\hat{\mathbf{e}}_i)}$ in Eq. (2.34). This truncation, followed by formal integration of Eq. (2.34), leads to

$$\begin{aligned}
&\rho_{(\boldsymbol{\phi};\hat{\mathbf{e}}_0),(\boldsymbol{\phi};\hat{\mathbf{e}}_i)}(t) \\
&= -ig\int_0^t dt' \exp\left[-i\left(\Delta - ik^{(\mathrm{out})}_{(\boldsymbol{\phi};\hat{\mathbf{e}}_0)}/2 - ik^{(\mathrm{out})}_{(\boldsymbol{\phi};\hat{\mathbf{e}}_i)}/2\right)t'\right] \\
&\quad \times \left[p_{(\boldsymbol{\phi};\hat{\mathbf{e}}_i)}(t-t') - p_{(\boldsymbol{\phi};\hat{\mathbf{e}}_0)}(t-t')\right],
\end{aligned} \tag{2.36}$$

where we have made the change of variable $(t - t') \to t'$. For our simulations, we are interested in how populations change over times much longer than cavity and vibrational decay. Since these two processes are included in $k^{(\mathrm{out})}_{(\boldsymbol{\phi};\hat{\mathbf{e}}_0)}$ and $k^{(\mathrm{out})}_{(\boldsymbol{\phi};\hat{\mathbf{e}}_i)}$, respectively, then the exponential term will decay

on a timescale much shorter than the timescales of interest. We therefore make a Markovian approximation—i.e., the substitutions $p_{(\boldsymbol{\phi};\hat{\mathbf{e}}_i)}(t-t') \to p_{(\boldsymbol{\phi};\hat{\mathbf{e}}_i)}(t)$ and $p_{(\boldsymbol{\phi};\hat{\mathbf{e}}_0)}(t-t') \to p_{(\boldsymbol{\phi};\hat{\mathbf{e}}_0)}(t)$, as well as extending the integral to infinity—to obtain

$$\begin{aligned}
&\rho_{(\boldsymbol{\phi};\hat{\mathbf{e}}_0),(\boldsymbol{\phi};\hat{\mathbf{e}}_i)}(t) \\
&= -ig\left[p_{(\boldsymbol{\phi};\hat{\mathbf{e}}_i)}(t) - p_{(\boldsymbol{\phi};\hat{\mathbf{e}}_0)}(t)\right] \\
&\quad \times \int_0^\infty dt' \exp\left[-i\left(\Delta - ik^{(\mathrm{out})}_{(\boldsymbol{\phi};\hat{\mathbf{e}}_0)}/2 - ik^{(\mathrm{out})}_{(\boldsymbol{\phi};\hat{\mathbf{e}}_i)}/2\right)t'\right].
\end{aligned} \tag{2.37}$$

Evaluating the integral and plugging Eq. (2.37) into Eqs. (2.32)-(2.33), we arrive at

$$\begin{aligned}
\frac{dp_{(\boldsymbol{\phi};\hat{\mathbf{e}}_i)}(t)}{dt} &= -k^{(\mathrm{out})}_{(\boldsymbol{\phi};\hat{\mathbf{e}}_i)} p_{(\boldsymbol{\phi};\hat{\mathbf{e}}_i)}(t) \\
&\quad + \sum_{(\boldsymbol{\phi}';\mathbf{m}')\neq(\boldsymbol{\phi};\hat{\mathbf{e}}_i)} k(\boldsymbol{\phi};\hat{\mathbf{e}}_i|\boldsymbol{\phi}';\mathbf{m}') p_{(\boldsymbol{\phi}';\mathbf{m}')}(t) \\
&\quad - \gamma'_{\boldsymbol{\phi} i} p_{(\boldsymbol{\phi};\hat{\mathbf{e}}_i)}(t) + \gamma'_{\boldsymbol{\phi} i} p_{(\boldsymbol{\phi};\hat{\mathbf{e}}_0)}(t),
\end{aligned} \tag{2.38}$$

$$\begin{aligned}
\frac{dp_{(\boldsymbol{\phi};\hat{\mathbf{e}}_0)}(t)}{dt} &= -k^{(\mathrm{out})}_{(\boldsymbol{\phi};\hat{\mathbf{e}}_0)} p_{(\boldsymbol{\phi};\hat{\mathbf{e}}_0)}(t) \\
&\quad + \sum_{(\boldsymbol{\phi}';\mathbf{m}')\neq(\boldsymbol{\phi};\hat{\mathbf{e}}_0)} k(\boldsymbol{\phi};\hat{\mathbf{e}}_0|\boldsymbol{\phi}';\mathbf{m}') p_{(\boldsymbol{\phi}';\mathbf{m}')}(t) \\
&\quad - \left(\sum_{j=1}^{2} \gamma'_{\boldsymbol{\phi} j}\right) p_{(\boldsymbol{\phi};\hat{\mathbf{e}}_0)}(t) + \sum_{j=1}^{2} \gamma'_{\boldsymbol{\phi} j} p_{(\boldsymbol{\phi};\hat{\mathbf{e}}_j)}(t),
\end{aligned} \tag{2.39}$$

where

$$\gamma'_{\boldsymbol{\phi} i} = \frac{4g^2\left(k^{(\mathrm{out})}_{(\boldsymbol{\phi};\hat{\mathbf{e}}_0)} + k^{(\mathrm{out})}_{(\boldsymbol{\phi};\hat{\mathbf{e}}_i)}\right)}{4\Delta^2 + \left(k^{(\mathrm{out})}_{(\boldsymbol{\phi};\hat{\mathbf{e}}_0)} + k^{(\mathrm{out})}_{(\boldsymbol{\phi};\hat{\mathbf{e}}_i)}\right)^2}. \tag{2.40}$$

Eq. (2.40) is in line with standard expressions for the Purcell factor [2, 102]. Eqs. (2.38)-(2.39) reveal that the dynamics under weak light-matter coupling is identical to the bare dynamics [Eq. (2.29)], except that vibrational mode i incoherently exchanges energy with the cavity at rate $\gamma'_{\boldsymbol{\phi} i}$. Thus, the master equation for the weak coupling regime is that of the bare case but with the fol-

lowing rates for relaxation between vibrational and cavity excitations:

$$k(\boldsymbol{\phi};\hat{\mathbf{e}}_i|\boldsymbol{\phi};\hat{\mathbf{e}}_0) = k(\boldsymbol{\phi};\hat{\mathbf{e}}_0|\boldsymbol{\phi};\hat{\mathbf{e}}_i) = \gamma'_{\boldsymbol{\phi}i}, \qquad i = 1,2. \tag{2.41}$$

We reiterate that this result rests on the condition that at least one of cavity and vibrational excitations decays on a timescale faster than that of the reaction dynamics. In all our simulations involving weak light-matter coupling, we only consider cases where this separation of timescales is satisfied, and so we use the kinetic framework described by Eq. (2.41) and the immediately preceding text.

2.3 Simulations

In this section, we perform kinetic simulations of thermally activated nonadiabatic electron transfer under VSC. We simulate a set of representative reactions whose reactive transitions are comparable in timescale to internal thermalization. As discussed in Sec. 2.1, we are interested in understanding how such reactions are affected by VSC-induced dissipative processes. To this end, we choose reaction parameters that highlight the impact of cavity decay, as well as relaxation among polaritons and the dark state. In addition, parameters are chosen such that the dynamics of states with more than one cavity-vibrational excitation are insignificant compared to the dynamics of states with one or zero of such excitation (Sec. 2.2.2). Parameters specific to each reaction are listed in Table 2.1. Throughout the simulations, we use $\hbar\omega_\mathrm{v} = 2000$ cm^{-1} and assume a resonant cavity mode (i.e., $\omega_\mathrm{c} = \omega_\mathrm{v}$). We also fix the temperature at $T = 298$ K. Unless otherwise stated, we use the following parameters to characterize internal thermalization: $\gamma = 0.01$ ps^{-1} , $\kappa = 1$ ps^{-1}, $\eta = 0.001$, and $\omega_\mathrm{cut} = 0.1\omega_\mathrm{v}$. We note that the chosen cavity decay rate (κ) is much faster than the chosen vibrational decay rate (γ) and that both rates are similar to those found in VSC experiments [55, 56, 92]. In calculations of reactions under VSC, we choose $g = (0.03\omega_\mathrm{v})/\sqrt{2}$, which yields a Rabi splitting of $\Omega = 0.06\omega_\mathrm{v}$.

For comparison, we also simulate the reactions in the bare case (see Sec. 2.2.3 for kinetic

Table 2.1: Reaction parameters.

Reaction	Figure	Reaction type	Parameters[a]
1	2.1	$A \to B$	$E_B = -0.6$, $\lambda_B = 1.5$, $J_{AB} = 0.01$, $\lambda_s^{(AB)} = 0.08$
2	2.2	$A \to B$	$E_B = 0.95$, $\lambda_B = 1$, $J_{AB} = 0.002$, $\lambda_s^{(AB)} = 0.05$
3	2.3	$A \to B \to C$	$E_B = -1.05$, $E_C = -1.35$, $\lambda_B = 1.5$, $\lambda_C = 4.5$, $J_{AB} = 0.0003$, $J_{BC} = 0.02$, $\lambda_s^{(AB)} = 0.05$, $\lambda_s^{(BC)} = 0.3$

[a]For all reactions, $E_A = 0$ and $\lambda_A = 0$. All $J_{\phi\varphi}$ not listed here are equal to 0. All parameters, except λ_ϕ (dimensionless), have units $\hbar\omega_v$.

model) and in the case of weak light-matter coupling (see Sec. 2.2.4 for kinetic model and its derivation). In the latter, we set the light-matter coupling to 1% of the value used for VSC. For all simulations in the weak-coupling regime, cavity decay is fast compared to the overall reaction dynamics (which can have a different timescale than the reactive transitions; see Sec. 2.4 for further discussion). Therefore, the weak light-matter coupling effectively induces relaxation between vibrational and cavity states (Sec. 2.2.4) [103, 104].

In all simulations, the initial population is a thermal distribution of reactant eigenstates. The distribution is determined by the Boltzmann probability function [i.e., $p_{(\boldsymbol{\phi};\mathbf{m})} \propto \exp(-E_{\boldsymbol{\phi};\mathbf{m}}/k_BT)$] and normalized to 1. In accordance with our truncation of the cavity-vibrational subspace (Sec. 2.2.2), the initial distribution consists only of states with ≤ 1 excitation in this subspace.

After calculating the population evolution for each state in the system, the total population $N_\varphi(t)$ of each reactive species φ at time t is computed according to

$$N_\varphi(t) = \sum_{(\boldsymbol{\phi};\mathbf{m})} p_{(\boldsymbol{\phi};\mathbf{m})}(t) \langle \boldsymbol{\phi};\mathbf{m}|\mathcal{P}_\varphi|\boldsymbol{\phi};\mathbf{m}\rangle. \tag{2.42}$$

The projection operator

$$\mathcal{P}_\varphi = \sum_{i=1}^{2} |\varphi^{(i)}\rangle\langle\varphi^{(i)}| \tag{2.43}$$

counts the number of molecules belonging to reactive species φ.

We first simulate a reaction where the vibrationally hot product undergoes the reverse reaction as fast as it decays (Fig. 2.1a). The main reactive transition involves a $0 \to 1$ vibrational

excitation upon going from reactant to product. The vibrationally hot product either returns to the reactant via the reverse transition or relaxes to the ground state, with both processes occurring at similar rates. This scenario represents a nonequilibrium effect where the product does not fully thermalize before it undergoes the reverse reaction. Under VSC, the reaction is enhanced compared to the bare case (Fig. 2.1c, blue solid line vs black dashed line). The observed modification is consistent with the following mechanism: dissipative processes associated with VSC speed up internal thermalization and thereby force the product to decay instead of transforming back into reactant. To test this mechanism, we carry out simulations for various values of cavity decay rate κ (Fig. 2.1d) and anharmonic system-bath coupling parameter η (Fig. 2.1e). The latter determines the rates of relaxation among polaritons and the dark state (Fig. 2.1b, red dotted arrows). As cavity decay rate κ is lowered to zero, most of the reaction enhancement goes away (Figs. 2.1e). In contrast, the modification largely survives as η is decreased. These trends reveal not only that the reaction is enhanced by accelerated internal thermalization, but also that cavity decay plays the main role in speeding up the thermalization. Specifically, cavity decay of the polaritons (Fig. 2.1b, yellow dashed arrows) enables the vibrationally hot product to cool much faster than it can undergo a reverse reactive transition. Relaxation from the dark state to polaritons (Fig. 2.1b, red dotted arrows) plays a supporting role: it transfers population to the (polariton) states that decay via cavity leakage.

The second reaction we investigate has a reactive transition that starts from a vibrational excited state and occurs on the same timescale as vibrational decay (Fig. 2.2a). Although thermodynamically unfavorable, this reaction can serve as an instructional example for thermodynamically favorable situations where the most reactive channel involves a vibrational excited state in the reactant. Due to a large energy difference between reactant and product electronic states, there is only one reactive transition, which is accompanied by a $1 \rightarrow 0$ vibrational deexcitation. This transition happens at a rate comparable to the decay of the initial vibrational state. Since vibrational decay is extremely fast compared to its reverse process, the timescale of reactant internal thermalization is that of vibrational decay, i.e., that of the reactive transition. Intuitively speaking, the population

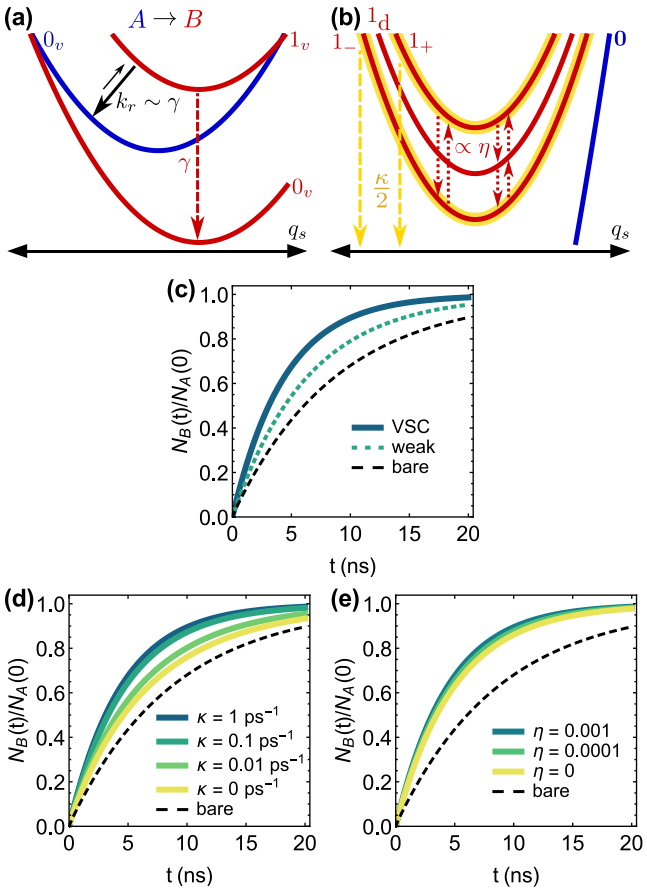

Figure 2.1: (a) Scheme of reaction where a reverse reactive transition (rate k_r) from the vibrationally hot product occurs on the same timescale as vibrational decay (rate γ). Reactant (blue) and product (red) potential energy surfaces are plotted against effective solvent coordinate q_s. Noteworthy transitions are shown. (Non)reactive transitions are represented with (dashed) solid arrows. (b) Scheme depicting VSC-induced internal thermalization of the product. Potential energy surfaces and nonreactive transitions, shown here for the system under VSC, follow the formatting style used in (a), with the additional attribute that polaritonic surfaces are drawn with yellow outline. Polaritons can decay via cavity leakage (rate $\kappa/2$, where κ is the decay rate of the bare cavity), and polaritons and dark state incoherently exchange energy (rates $\propto \eta$, where η represents the system-bath interaction that gives rise to this relaxation). (c-e) Product population kinetics for various (c) regimes of light-matter coupling, (d) κ, and (e) η.

of the reactive vibrational excited state does not reach its fully replenished (thermalized) value prior to subsequent reactive transitions. In the presence of VSC, the reaction experiences an enhancement (Fig. 2.2c, blue solid line vs black dashed line). By varying κ (Fig. 2.2d) and η (Fig. 2.2e), we again find that the reaction modification is attributed mostly to cavity decay and less so to relaxation among polaritons and the dark state. Cavity decay facilitates rapid thermalization between the ground state and polaritons (Fig. 2.2b, yellow dashed arrows), while the dark state quickly reaches thermal equilibrium through incoherent energy transfer with the polaritons (Fig. 2.2b, blue dotted arrows). As a result of these relaxation dynamics, the excited cavity-vibrational states are refilled with population before the next reactive transition takes place.

While the first two reactions are enhanced by VSC, suppression is found for the third reaction, which involves a vibrationally hot intermediate that reacts before it can fully thermalize (Fig. 2.3a) [93–95]. The first reactive transition is from reactant to intermediate and involves a $0 \rightarrow 1$ vibrational excitation. Next, the vibrationally hot intermediate can either make a reactive transition to product or relax to the ground state, with similar rates for both processes. The former process is followed by vibrational decay, while the latter is followed by an intermediate-to-product reactive transition that is much slower than vibrational decay. Overall, a significant amount of intermediate population first makes a fast reactive transition and then cools, and the remaining intermediate population first cools and then makes a slow reactive transition. With VSC, the population kinetics of the reactant is unchanged (Fig. 2.3c, blue solid line vs black dashed line) because the vibrationally hot intermediate, with or without VSC, is transformed into a different state much quicker than it can transition back to reactant. However, there is greater accumulation of the intermediate (Fig. 2.3d, blue solid line vs black dashed line) and suppressed formation of the product under VSC (Fig. 2.3e, blue solid line vs black dashed line). Carrying out the same analysis as done with the previous two reactions (see Figs. 2.3f-2.3i), we conclude that the rapid decay of polaritons via cavity leakage (Fig. 2.3b, yellow dashed arrows), assisted by the relaxation from the dark state to polaritons (Fig. 2.3b, green dotted arrows), causes the intermediate to reach thermal equilibrium

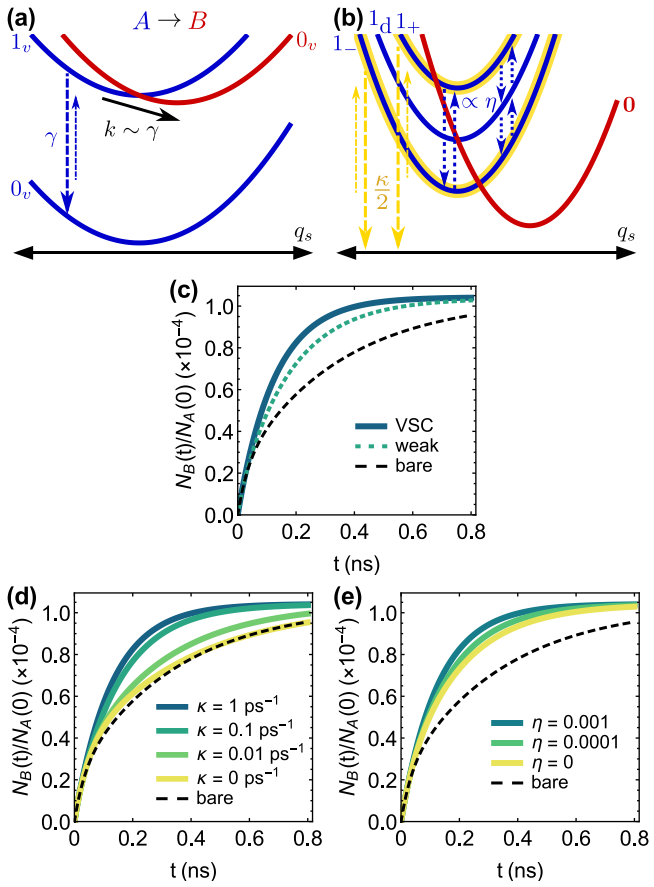

Figure 2.2: (a) Scheme of reaction where a reactive transition (rate k) from a vibrational excited state occurs on the same timescale as vibrational decay (rate γ). Reactant (blue) and product (red) potential energy surfaces are plotted against effective solvent coordinate q_s. Noteworthy transitions are shown. (Non)reactive transitions are represented with (dashed) solid arrows. (b) Scheme depicting VSC-induced internal thermalization of the reactant. Potential energy surfaces and nonreactive transitions, shown here for the system under VSC, follow the formatting style used in (a), with the additional attribute that polaritonic surfaces are drawn with yellow outline. Polaritons can gain energy from the ground cavity-vibrational state via photon absorption from the surroundings into the cavity, and polaritons and dark state incoherently exchange energy. See caption of Fig. 2.1 for explanation of κ, η, and labels containing these symbols. (c-e) Product population kinetics for various (c) regimes of light-matter coupling, (d) κ, and (e) η.

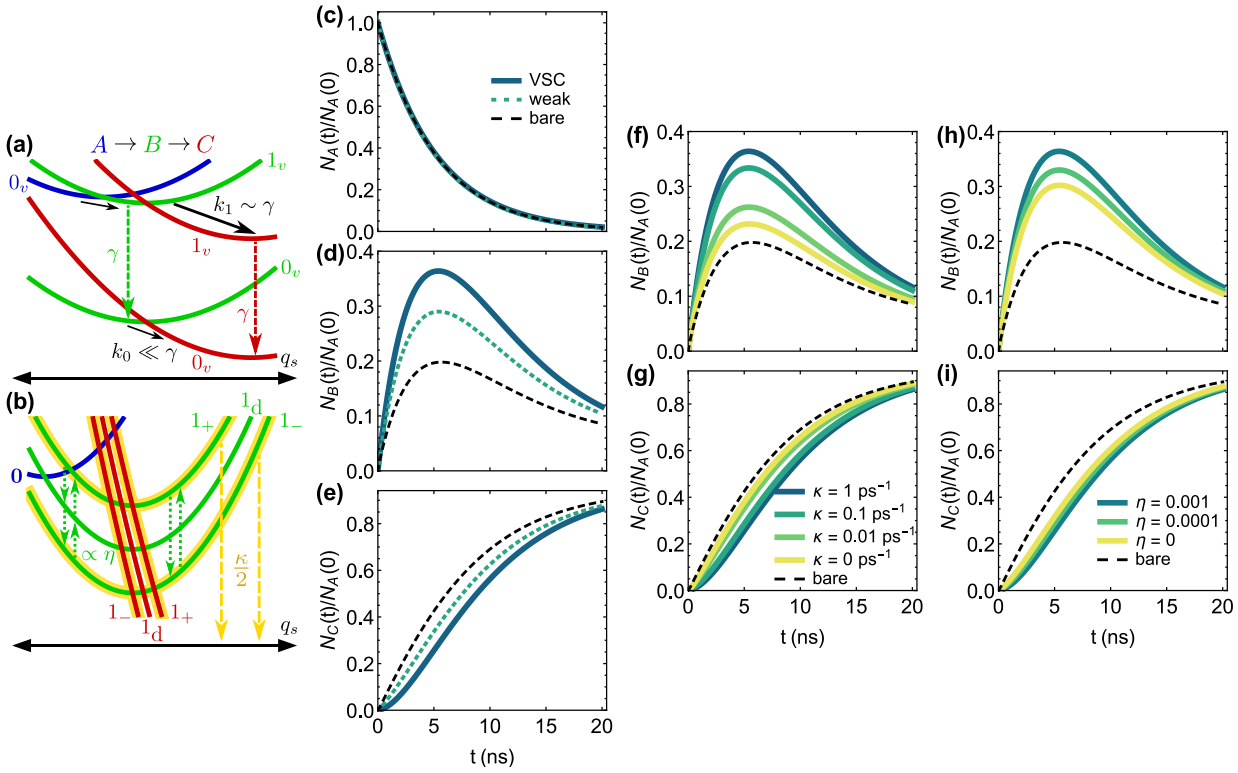

Figure 2.3: (a) Scheme of reaction where a reactive transition (rate k_1) from a vibrationally hot intermediate occurs on the same timescale as vibrational decay (rate γ). Reactant (blue), intermediate (green), and product (red) potential energy surfaces are plotted against effective solvent coordinate q_s. Noteworthy transitions are shown. (Non)reactive transitions are represented with (dashed) solid arrows. The rate k_0 describes a reactive transition from the intermediate in its vibrational ground state. Note: $k_0 \neq k_1$ because the corresponding reactive transitions are associated with different Franck-Condon factors [Eq. (2.25)]. (b) Scheme depicting VSC-induced internal thermalization of the intermediate. Potential energy surfaces and nonreactive transitions, shown here for the system under VSC, follow the formatting style used in (a), with the additional attribute that polaritonic surfaces are drawn with yellow outline. Polaritons can decay via cavity leakage, and polaritons and dark state incoherently exchange energy. See caption of Fig. 2.1 for explanation of κ, η, and labels containing these symbols. (c-e) Population kinetics of (c) reactant, (d) intermediate, and (e) product for various regimes of light-matter coupling. (f-i) Population kinetics of (f, h) intermediate and (g, i) product for various (f, g) κ, and (h, i) η.

before it can go through the faster reactive transition.

To obtain additional insight regarding nonequilibrium effects and how VSC alters reactivity, we study the reactions under weak light-matter coupling. Figs. 2.1c, 2.2c, 2.3d-2.3e show population kinetics for VSC (blue solid line), weak light-matter coupling (aquamarine dotted line), and the bare case (black dashed line). For all reactions, weak light-matter coupling leads to significantly modified kinetics. The direction of change is the same as that of VSC. This finding is consistent with the fact that, similar to VSC, weak light-matter coupling opens up relaxation between vibrations and the cavity, and enables internal thermalization of the reactive species to be sped up by cavity decay. It also makes sense that the magnitude of change is less than that of VSC, since the vibration-cavity relaxation resulting from weak light-matter interaction is not as fast as cavity decay [103]. Nevertheless, it is interesting that one only needs to enter the weak-coupling regime to manipulate reactivity. The same conclusion has been reached in a study of how cavity decay allows light-matter coupling to protect molecules from photodegradation [85].

The simulations discussed so far suggest that the VSC-induced modifications to the above reactions arise mainly from the suppression of nonequilibrium effects. To strengthen this claim, we simulate the same reactions except the vibrational decay rate is made 100 times larger (i.e., $\gamma = 1$ ps$^{-1} = \kappa$). With this condition, we find that the VSC and bare kinetics (Fig. 2.4, blue solid line vs black dashed line) are either virtually identical or much more similar than in the case of slow vibrational decay. Thus, the changes in reactivity due to VSC are considerably reduced when, outside the cavity, internal thermalization is already rapid compared to reactive transitions.

While our focus has been on nonequilibrium effects and their suppression by VSC-related dissipation, we should note that the calculated reaction kinetics do exhibit some changes as a consequence of VSC modifying activation energies and redistributing vibronic coupling among the cavity-vibrational eigenmodes (Sec. 2.2.2). Because cavity decay has been identified as the major contributor to the altered kinetics in the above reactions, the impact of the minor contributors could be revealed by comparing simulations for VSC and no cavity decay (i.e., $\kappa = 0$ ps^{-1}) with those for the bare case. For the reaction of Fig. 2.1, the kinetics is noticeably different for the

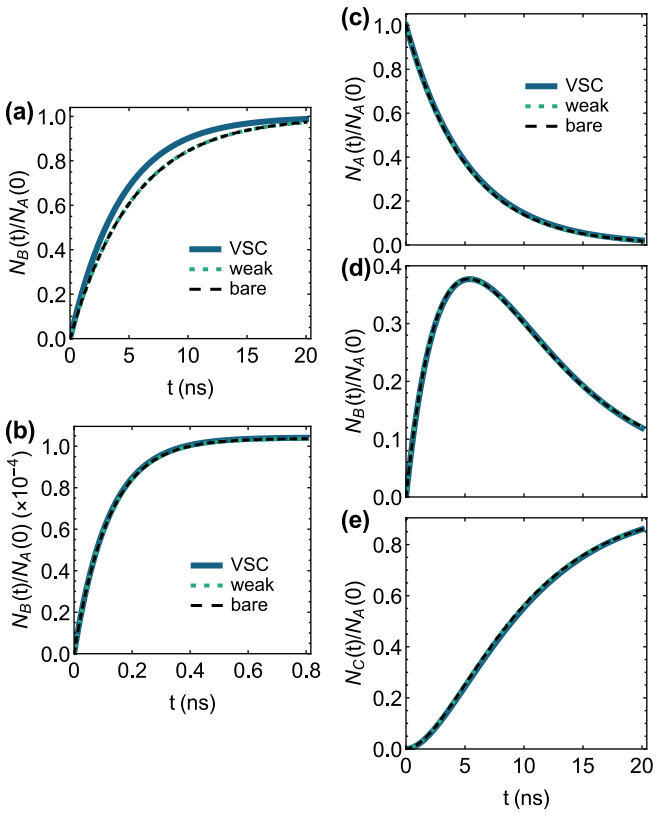

Figure 2.4: Population kinetics with fast vibrational decay rate $\gamma = 1$ ps^{-1}. Plots correspond to the following figures showing population kinetics with vibrational decay rate $\gamma = 0.01$ ps^{-1} but otherwise same conditions: (a) Fig. 2.1c, (b) Fig. 2.2c, and (c-e) Figs. 2.3c–2.3e.

two conditions (Fig. 2.1d, yellow solid line vs black dashed line). It seems that the difference cannot be fully accounted for by the presence of relaxation among polaritons and dark state (Fig. 2.1e). Hence, modified energy differences and Franck-Condon factors likely impart a small but appreciable influence on the reaction. This conclusion is corroborated by the slight enhancement observed for the VSC reaction when vibrational decay is made faster than all reactive transitions (Fig. 2.4a, blue solid line vs black dashed line); in this regime, dissipative processes introduced by VSC should have no effect. For further discussion of how changes in energetics and Franck-Condon factors due to VSC manifest as changes in reactivity, we refer the reader to Refs. [38] and [39] (see also Ref. [105], which discusses these topics but in the context of SC to electronic states).

2.4 Connection to experiments

A noteworthy difference between our simulations and the experiments of VSC reactions is the number N of molecules involved in VSC. In our simulations $N = 2$. In the experiments, N is estimated to be 10^6 to 10^{12} [38, 53, 106].

For such large N, the particular reactions studied here are unlikely to be modified by VSC. To understand this statement and to identify reactions that would be significantly affected by many-molecule VSC, we present the following argument. Without loss of generality, consider a reaction featuring a single forward reactive transition, which involves a $0 \rightarrow 1$ vibrational excitation. This hypothetical reaction resembles that depicted in Fig. 2.1a. Assuming the steady-state approximation (SSA) for the vibrationally excited product and ignoring vibrational gain (i.e., the reverse process of vibrational decay), the reaction rate can be written as $k_{R\rightarrow P} = k_f[k_d/(k_r+k_d)]$, where k_f is the rate of the forward reactive transition, k_r is the rate of the reverse reactive transition, and k_d is the decay rate of the vibrationally excited product. The quantity in square brackets, $k_d/(k_r+k_d)$, is the efficiency with which the vibrationally excited product decays rather than returns to reactant. In the reaction with VSC, there are $N+1$ forward reactive transitions, each involving the $0 \rightarrow 1$ excitation of a polariton or dark state; there are two and $N-1$ such transitions, respectively.

We first focus on the two polaritonic forward reactive transitions. Recall that the Franck-Condon factor for a 0-1 vibronic transition is proportional to the displacement between initial and final vibrational states [Eq. (2.20) with $m'_q = 1$ and $m_q = 0$]. Since the overlap between a polariton mode and each bare vibrational mode is $O(N^{-1/2})$ [Eq. (2.10)], the displacements—and therefore the 0-1 Franck-Condon factors—associated with the polaritons are $O(N^{-1/2})$ times the corresponding bare values [Eqs. (2.14)-(2.15)]. Then the polaritonic reactive transitions have rates that scale as $O(N^{-1})$ because the rate of a reactive transition depends on the square of a Franck-Condon factor [Eq. (2.18)]. Suppose that cavity decay is much faster than all other transitions from the polaritons, including reverse reactive transitions and relaxation to dark states. This scenario, which has been observed for cavity-coupled $W(CO)_6$ in nonpolar solvents [107], results in a decay efficiency of 1 for product states with an excitation in a polariton mode. By applying the SSA to such states and neglecting cavity gain (i.e., the reverse process of cavity decay), we arrive at the following effective rate for the polaritonic reactive transitions: $k^{(p)}_{R\to P} = \varepsilon k_f/N$, where ε is a dimensionless constant that accounts for changes in the reaction rate caused by the polaritons having modified energies. In contrast, we assume that the reactive transitions involving the dark states do not afford changes in the reaction rate, given that the dark states have similar decay dynamics to the bare vibrations [51, 53, 55, 56, 101, 107, 108]. Furthermore, relaxation from dark states to polaritons should be negligible: this dissipative process is mediated by local system-bath interactions (see Sec. 2.2.2) and has rates scaling as $O(N^{-1})$ [44, 53, 62], corresponding to the probability of each molecule in either polariton [Eq. (2.10)]. So, in order for the reaction to be modified by VSC, the reaction rate ($k^{(p)}_{R\to P}$) due to the polaritonic reactive transitions should be, at least, comparable to the bare reaction rate ($k_{R\to P}$), i.e.,

$$\frac{\varepsilon}{N} \gtrsim \frac{k_d}{k_r + k_d}. \tag{2.44}$$

With arbitrary reactions in mind, criterion (2.44) says that for systems with experimentally relevant values of N, VSC can change the kinetics of thermally activated reactions if

1. the polaritons give rise to $\varepsilon \gg 1$, which means that activation energies are significantly reduced compared to the bare case (this scenario is discussed in Ref. [38]), and/or

2. in the bare case, reverse reactive transitions are extremely fast compared to internal thermalization, i.e., populations are efficiently trapped in the reactants.

When at least one of these two conditions is satisfied, a large-N generalization of the kinetic model presented in Sec. 2.2.2 should predict altered reactivity under VSC. Indeed, Ref. [38] theoretically demonstrates the ability for condition 1 to enable VSC catalysis of ground-state reactions when $N = 10^7$. While such a demonstration has not been carried out for condition 2, Ref. [109] (see Fig. 6a of that work) has shown that condition 2 enables electronic SC to boost the efficiency of harvesting triplet excitons into singlet polaritons, ultimately leading to enhanced photoluminescence compared to the bare organic material (in this case, the reverse reactive transition is the very rapid fission of singlets into triplets).

Despite the above and other differences between this theoretical work and the experiments, the suppression of nonequilibrium effects is a general phenomena and could be relevant to the mechanism by which VSC modifies reaction kinetics in the latter. According to our calculations, the suppression of nonequilibrium effects can lead to significant increase or decrease in reactivity, depending on the specific properties of the reaction. Both types of modifications have been found experimentally [1]. The resemblance does not stop there. Recall the experimental studies showing that the desilylation of PTA using TBAF is suppressed by VSC [20, 97]. This reaction involves an intermediate species [96]. Based on kinetic measurements, the authors propose that VSC forces the reaction to go through a new pathway, which involves a different intermediate. Compared to the intermediate of the bare reaction, the intermediate in the VSC reaction forms more easily but reacts less readily. We would like to propose an alternative mechanism based on our results. In the bare case, there could be nonequilibrium effects that cause slow conversion of reactant to intermediate (similar to the reaction of Fig. 2.2) and fast conversion of intermediate to product (like in the reaction of Fig. 2.3; see Refs. [93], [94], and [95]). Under VSC, the intermediate would be

the same as in the bare case, but nonequilibrium effects would be suppressed, thereby accelerating the reactant-to-intermediate transformation and decelerating the intermediate-to-product transformation. This mechanism is consistent with the experimentally proposed one. Future works should test the possibility of VSC-induced suppression of nonequilibrium effects in the desilylation and other reactions.

When evaluating this possibility, it is important to keep in mind that nonequilibrium effects can affect reactivity even if internal thermalization occurs on a much shorter timescale than the reaction. Whether or not nonequilibrium effects are present is determined by how fast internal thermalization is relative to reactive transitions, which may be faster than the (overall) reaction. These guiding principles are supported by our simulations. For the bare reactions shown in Figs. 2.1 and 2.3, internal thermalization occurs on a 100 ps timescale while the reaction occurs on a 10 ns timescale (Figs. 2.1a, 2.1c, 2.3a, 2.3c). Nevertheless, as already discussed in Sec. 2.3, the ability of VSC—in particular, the associated relaxation processes—to change the reaction kinetics relies on having (in the bare case) reactive transitions with similar rates as internal thermalization. The above principles, when made specific to adiabatic reactions, can be stated as follows [110]: regardless of the actual reaction rate or that predicted by transition-state theory, the influence that nonequilibrium effects have on reactivity depends on how the rate of internal thermalization compares to the reactive flux (i.e., the rate of product formation per unit population) at the transition-state barrier.

2.5 Conclusions

In this work, we study how reactions with significant nonequilibrium effects are influenced by the dissipative channels that VSC introduces to the chemical system. By using the MLJ formalism of electron transfer as our reaction model, we present a kinetic framework that captures reactive transitions, vibrational decay, cavity decay, and relaxation among polaritons and dark states. We

then simulate reactions where internal thermalization and reactive transitions occur on the same timescale. The considered reactions respectively exhibit three representative nonequilibrium effects: vibrationally hot product transforming back to reactant while thermalizing (Fig. 2.1), slow replenishing of reactive vibrational excited state after a reactive transition (Fig. 2.2), and vibrationally hot intermediate reacting before it can fully thermalize (Fig. 2.3). Under VSC, the first two reactions are enhanced whereas the last reaction is suppressed. These modifications largely occur because nonequilibrium effects are suppressed by VSC-induced dissipative processes. The suppression of nonequilibrium effects is driven by cavity decay, which causes polaritons to thermalize much faster than reactive transitions occur. Relaxation between polaritons and dark states allows the latter to indirectly experience accelerated thermalization due to cavity decay. When we substantially increase the vibrational decay rate, i.e., make internal thermalization much faster than reactive transitions (for the cavity-free case), the bare and VSC reactivities become much closer (Fig. 2.4). Finally, we discuss our work in the context of recent experiments [1], which demonstrate that thermally activated reactions can be enhanced or suppressed by the collective VSC of a large number of molecules. We identify types of reactions for which our theory would predict modified kinetics induced by many-molecule VSC. We also highlight resemblances between our results and experimental observations. These resemblances suggest that VSC-triggered suppression of nonequilibrium effects could play a role in the experiments.

Chapter 2, in full, is adapted from the material as it appears in "Nonequilibrium effects of cavity leakage and vibrational dissipation in thermally-activated polariton chemistry," M. Du, J. A. Campos-Gonzalez-Angulo, J. Yuen-Zhou, *J. Chem. Phys.* **154**, 084108 (2021). The dissertation author was the primary investigator and author of this paper.

Chapter 3

Electron transfer under vibrational strong coupling: effect of dark states

3.1 Introduction

The past decade has seen much interest in the control of chemical phenomena via the strong coupling of matter to confined electromagnetic modes [3–11, 59, 61, 76, 83, 89, 111–114]. An exciting prospect in this direction is vibropolaritonic chemistry, that is, the use of collective vibrational strong coupling (VSC) [17–19] to modify thermally-activated chemical reactivity without external pumping (*e.g.*, laser excitation) [1]. While collective VSC involves a large number of molecules per photon mode, it has been observed to substantially alter the kinetics of organic substitution [20, 21], cycloaddition [23], hydrolysis [24], enzyme catalysis [25, 26], and crystallization [115], among other electronic ground-state chemical processes.

However, such modified reactivity under VSC is still not well understood. Studies [27–30] show that the observed kinetics cannot be explained with transition state theory (TST) [31], the most commonly used framework to predict and interpret reaction rates. Breakdowns of TST, including recrossing the activation barrier [33], deviation from thermal equilibrium [29, 41], and

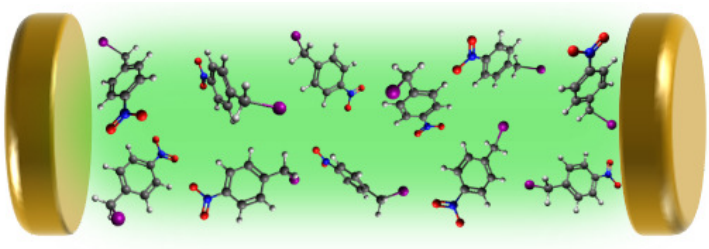

Figure 3.1: Schematic of the model setup. Inside an optical cavity, an energetically disordered ensemble of molecular vibrations, each belonging to a separate molecule, collectively interacts with a cavity mode. When a molecule reacts, its cavity-coupled vibrational mode concomitantly experiences a displacement in equilibrium geometry. Depicted here are molecules that undergo intramolecular electron transfer, the reaction studied in this work.

quantum/nonadiabatic phenomena [29, 32, 38, 39, 41], have also been considered. The aforementioned works regard all N vibrations coupled to the cavity mode to be identical. Under this assumption, VSC forms two polaritons and $N-1$ optically dark vibrational modes, where the latter remain unchanged from the cavity-free system. It follows that VSC-induced changes to thermally-activated reactivity must arise from the polaritons. In fact, one study from our group highlighted the molecular parameter space where polaritons dominate the kinetics [38] with respect to dark modes; however, this hypothesis has been questioned as entropically unlikely [106].

Disorder, despite its ubiquity in molecular systems, has often been ignored when modeling molecules under strong light-matter coupling. Only recently has it been shown that the strong coupling of disordered chromophores to an optical cavity mode can produce dark states which are delocalized on multiple molecules [116, 117] (hereafter, referred as semilocalized). This semilocalization is predicted to improve or even enable coherent energy transport [116, 118]. Other findings hint at adding sample impurities to help strong coupling modify local molecular properties [119].

In this work, we demonstrate that the VSC of a disordered molecular ensemble (Fig. 3.1) can significantly modify the kinetics of a thermally-activated chemical reaction. The altered reactivity is attributed to the semilocalized dark modes. The semilocalization affects the reaction rate

by changing the efficiency with which a reactive mode dissipates energy.

3.2 Hamiltonian H

Consider a disordered ensemble of N molecular vibrations, respectively corresponding to N independent molecules, inside an optical cavity (Fig. 3.1). The system is described by the Hamiltonian $H = \hbar\omega_c a_0^\dagger a_0 + \hbar\sum_{i=1}^N \omega_i a_i^\dagger a_i + \hbar\sum_{i=1}^N g_i(a_i^\dagger a_0 + \text{h.c.})$. Vibrational mode i is represented by annihilation operator a_i and has frequency $\omega_i = \overline{\omega}_v + \delta\omega_i$, where $\overline{\omega}_v$ is the mean vibrational frequency and $\delta\omega_i$ is the frequency offset of mode i. Reflecting inhomogeneous broadening (static diagonal disorder), $\delta\omega_i$ is a normally distributed random variable with mean zero and standard deviation σ_v. The cavity mode is represented by annihilation operator a_0, has frequency ω_c, and couples to vibration i with strength g_i. For simplicity, we hereafter take $g_i = g$ for all i.

Using H, we investigate the physicochemical properties of a disordered molecular system under VSC. Unless otherwise noted, calculations assume that the cavity is resonant with the average vibration, $\omega_c = \overline{\omega}_v$, and couples to the vibrations with collective strength $g\sqrt{N} = 8\sigma_v$ (for all N). Numerical values reported below are obtained by averaging over 5000 disorder realizations, *i.e.*, sets $\{\omega_i\}_{i=1}^N$. In plots versus the H eigenfrequencies, each data point is an average over the H eigenmodes—from all disorder realizations—whose frequency lies in the bin $\left(\Delta\omega(l-\frac{1}{2}), \Delta\omega(l+\frac{1}{2})\right]$ for $\Delta\omega = 10^{-1}\sigma_v$ and $l \in \mathbb{Z}$.

3.3 Properties of the eigenmodes of H

We first study the eigenmodes of H. Formally, mode $q = 1, \ldots, N+1$ is represented by operator $\alpha_q = \sum_{i=0}^N c_{qi} a_i$ and has frequency ω_q. Figs. 3.2a and 3.2b show the probability distribution and photon fraction ($|c_{q0}|^2$), respectively, of the eigenmodes with respect to eigenfrequency. The majority of modes form a broad distribution in frequency around $\overline{\omega}_v$ and are optically dark. A minority of modes are polaritons, which have frequency $\overline{\omega}_v \pm 8\sigma_v$, photon fraction ≈ 0.5, and

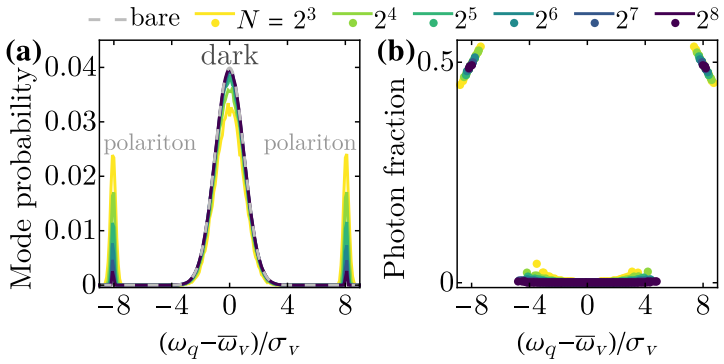

Figure 3.2: (a) Probability distribution and (b) photon fraction of the eigenmodes of H. Values are plotted versus eigenfrequency ω_q for various N. In (a), the gray dashed line is the probability density function $[P(\omega_q) = (\sigma_v\sqrt{2\pi})^{-1}\exp\left(-(\omega_q-\overline{\omega}_v)^2/(2\sigma_v^2)\right)$, displayed in units of $1/\Delta\omega$] of the bare vibrational modes.

a lineshape minimally affected by inhomogeneous broadening [120]. As N rises, the eigenmodes become increasingly composed of dark modes, whose probability distribution approaches that of the bare ($g = 0$) vibrational modes (Fig. 3.2a, gray dashed line).

Next, we examine the delocalization of the dark modes. For the purpose of studying chemical reactions, it is useful to compute the molecular participation ratio (PR) [117, 121]. This measure, defined as

$$\text{molecular PR} = 1/\sum_{i=1}^{N}\left|\frac{c_{qi}}{\sqrt{\sum_{i=1}^{N}|c_{qi}|^2}}\right|^4 \tag{3.1}$$

and analogous to the usual PR [122], estimates the number of molecules over which eigenmode q is delocalized. According to Fig. 3.3a, the average dark mode has molecular PR ∼2-3, and this semilocalization persists as N increases. These phenomena were first noted independently by Scholes [117] and Schachenmayer and co-workers [116]. For additional insight, we plot the squared overlap ($|c_{qi}|^2$, Fig. 3.3b) and frequency difference ($|\omega_{qi}|$, where $\omega_{qi} = \omega_q - \omega_i$; Fig. 3.3c) between each dark mode and each bare vibrational mode. The typical dark mode has sizable overlap with the bare modes that are nearest to it in frequency. The frequency difference between

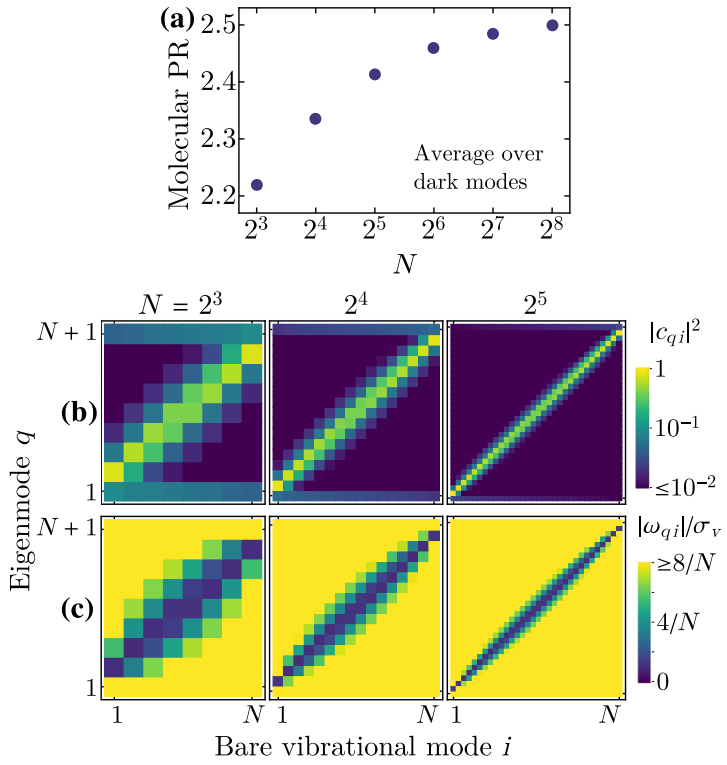

Figure 3.3: (a) Average molecular PR of the dark modes as a function of N. (b) Squared overlap $|c_{qi}|^2$ ($\log_{10}$ scale) and (c) frequency difference $|\omega_{qi}|$ between each eigenmode q and each bare vibrational mode i. Each group of modes is ordered from low to high frequency, *i.e.*, dark (polariton) modes have index $q = 2,\ldots,N$ ($q = 1, N+1$). The quantities in (b)-(c) are plotted for various N.

the dark mode and any of its major constituents is $O(\sigma_v/N)$, *i.e.*, negligible for large N.

3.4 Chemical reaction

We now explore how VSC influences the kinetics of a thermally-activated chemical reaction. Consider a reactive molecule under collective VSC (Fig. 3.1). The molecule undergoes nonadiabatic intramolecular electron transfer, and a cavity mode interacts collectively with a reactive vibrational mode and $N-1$ nonreactive vibrational modes. The model here considered is general enough that it should also be applicable to the case of "solvent-assisted VSC" [22, 123–125].

3.4.1 Hamiltonian

To model the reaction of one molecule in the ensemble, we employ the Hamiltonian $H_{\text{rxn}} =$

$H + \sum_{X=R,P} |X\rangle\langle X| \{E_X + \hbar\omega_r[\lambda_X(a_r + a_r^\dagger) + \lambda_X^2]\} + V + H_s^{(l)}$. Note that vibrational and cavity modes are still described by H. In writing H_{rxn}, we have changed the numerical index of the bare vibrational mode ($i = 1$) involved in the reaction to the letter r (*i.e.*, $\omega_1 \to \omega_r$, $a_1 \to a_r$); hereafter, we refer to this mode as v_r. The electronic subspace consists of reactant $|R\rangle$ and product $|P\rangle$ states. Electronic state $|X\rangle$ has energy E_X and couples to v_r with dimensionless strength λ_X. As a result of the vibronic coupling, v_r experiences a displacement in its equilibrium position upon electron transfer. The interaction between $|R\rangle$ and $|P\rangle$ is represented by $V = J_{RP}(|P\rangle\langle R| + \text{h.c.})$, where J_{RP} is the interaction strength. The last term of H_{rxn} is

$$H_s^{(l)} = \hbar \sum_j \omega_j^{(l)} b_j^\dagger b_j + \hbar \sum_j \omega_j^{(l)} \sum_{X=R,P} |X\rangle\langle X| \left[\lambda_{Xj}^{(l)}(b_j + b_j^\dagger) + (\lambda_{Xj}^{(l)})^2\right], \tag{3.2}$$

where the jth low-frequency mode has frequency $\omega_j^{(l)}$ and couples to electronic state $|X\rangle$ with dimensionless strength $\lambda_{Xj}^{(l)}$. The contribution of the low-frequency modes to the reaction rate is characterized by reorganization energy $\lambda_s = \sum_j \left(\lambda_{Pj}^{(l)} - \lambda_{Rj}^{(l)}\right)^2 \hbar\omega_j^{(l)}$. Through $H_s^{(l)}$, Hamiltonian H_{rxn} also accounts for low-frequency vibrational modes of the solvent that help mediate electron transfer. There is no direct coupling, though, of the cavity mode to the $|R\rangle \rightleftharpoons |P\rangle$ electronic transitions, which we assume are dipole-forbidden.

3.4.2 Kinetic model

Since we are considering a nonadiabatic reaction, we treat V perturbatively and calculate rates of reactive transitions between the zeroth-order electronic-vibrational-cavity eigenstates of H_{rxn}. These states take the form $|X, \boldsymbol{\chi}\rangle = |X\rangle \otimes |\tilde{\boldsymbol{\chi}}_{(X)}\rangle$. Belonging to the subspace of vibrational and cavity modes, $|\tilde{\boldsymbol{\chi}}_{(X)}\rangle = \left(\prod_{q=1}^{N+1} D_q^\dagger(\lambda_{Xq})\right)|\boldsymbol{\chi}\rangle$ is a displaced Fock state with $m_q^{(\chi)}$ excitations in H eigenmode q. The undisplaced Fock state $|\boldsymbol{\chi}\rangle$ is an eigenstate of H, and $D_q(\lambda) = \exp(\lambda\alpha_q^\dagger - \lambda^*\alpha_q)$ is a displacement operator. Mode q has equilibrium (dimensionless) position $\lambda_{Xq} = \lambda_X c_{qr}(\omega_r/\omega_q)$ when the system is in electronic state $|X\rangle$. Returning to the electronic-vibrational-cavity state $|X, \boldsymbol{\chi}\rangle$, we can write its energy as $E_{(X,\boldsymbol{\chi})} = E_X + \sum_{q=1}^{N+1} m_q^{(\chi)}\hbar\omega_q + \Delta_X$, where

$\Delta_X = \lambda_X^2 \hbar\omega_r - \hbar\sum_{q=1}^{N+1} |\lambda_{Xq}|^2 \omega_q$ is the difference in reorganization energy—namely, that due to vibronic coupling between v_r and $|X\rangle$—with and without VSC.

Following extensions [38, 39, 41] of Marcus-Levich-Jortner theory [45–47] to electron transfer under VSC, the rate of the reactive transition from $|R,\chi\rangle$ to $|P,\chi'\rangle$ can be expressed as

$$k_{(R,\chi)\to(P,\chi')} = \mathcal{A} F_{\chi,\chi'} \exp\left(-\beta E_a^{\chi,\chi'}\right), \tag{3.3}$$

where $\mathcal{A} = \sqrt{\pi\beta/\lambda_s}|J_{RP}|^2/\hbar$, and β is the inverse temperature For this transition, the activation energy is $E_a^{\chi,\chi'} = (E_{(P,\chi')} - E_{(R,\chi)} + \lambda_s)^2/(4\lambda_s)$. Through the Franck-Condon (FC) factor $F_{\chi,\chi'} = |\langle\tilde{\chi}_{(R)}|\tilde{\chi}'_{(P)}\rangle|^2$, the transition rate depends on the overlap between initial and final vibrational-cavity states $|\tilde{\chi}_{(R)}\rangle$ and $|\tilde{\chi}'_{(P)}\rangle$, respectively. It can be shown that the rate $k_{(P,\chi')\to(R,\chi)}$ corresponding to the backward transition, $|P,\chi'\rangle \to |R,\chi\rangle$, is related to Eq. (3.3) by detailed balance [99].

We specifically study a reaction where, in the absence of light-matter coupling, reactive transitions occur on the same timescale as internal thermalization (*i.e.*, thermalization of states having the same electronic component). In such cases, internal thermal equilibrium is not maintained throughout the reaction, and the reaction rate (*i.e.*, net rate of reactant depletion) may not be approximated by a thermal average of reactant-to-product transition rates. Instead, the reaction rate can also depend on, *e.g.*, backward reactive transitions (from product to reactant) or vibrational relaxation.

With this in mind, we numerically simulate the bare and VSC reactions using a kinetic model. The population $p_{(X,\chi)}$ of state $|X,\chi\rangle$ evolves according to the master equation

$$\frac{dp_{(X,\chi)}}{dt} = -\sum_{(X',\chi')\neq(X,\chi)} k_{(X,\chi)\to(X',\chi')} p_{(X,\chi)} + \sum_{(X',\chi')\neq(X,\chi)} k_{(X',\chi')\to(X,\chi)} p_{(X',\chi')}. \tag{3.4}$$

State-to-state transitions ($|X,\chi\rangle \to |X',\chi'\rangle$), which are either reactive ($X' \neq X$) or nonreactive ($X' = X$), include forward and backward reactive transitions [Eq. (3.3)], vibrational and cavity decay, and energy exchange among dark and polariton states [53, 55, 107]. The third set of processes results from vibrational dephasing interactions (i.e., homogeneous broadening) of the molecular

system [53]. The reaction parameters (Sec. 3.4.3) are such that the population dynamics proceeds almost completely through states $|X,\chi\rangle$ with zero or one excitation in the vibrational-cavity modes. To reduce computational cost, the kinetic model includes only these states, which are denoted by $\chi = 0$ and $\chi = 1_q$, respectively, where q is an eigenmode of the vibrational-cavity subspace. Master equation (3.4) is numerically solved (Sec. A.1) with the initial population being a thermal distribution of reactant states ($|R,\chi\rangle$). Then, the *apparent* reaction rate is obtained by fitting the reactant population as a function of time (Sec. A.2).

We now present expressions for the rates of transitions within the truncated state space. Rates ($k_{(X,\chi)\to(X',\chi')}$ for $X' \neq X$) of reactive transitions are given by Eq. (3.3) and depend on FC factor $F_{\chi,\chi'}$. To evaluate $F_{\chi,\chi'}$, recall the standard identity [100]

$$\langle m'|D(\lambda)|m\rangle = \sqrt{\frac{m!}{(m')!}} e^{-|\lambda|^2/2} \lambda^{m'-m} L_m^{(m'-m)}(|\lambda|^2), \quad m' \geq m, \tag{3.5}$$

where $D(\lambda) = \exp(\lambda a^\dagger - \lambda^* a)$ is the displacement operator corresponding to bosonic annihilation operator a, $|m\rangle$ is a number state of the mode represented by a, and $L_n^k(x)$ is an associated Laguerre polynomial. Using Eq. (3.5), we obtain

$$F_{\chi,\chi'} = \begin{cases} e^{-S}, & (\chi',\chi) = (0,0), \\ e^{-S} S_q, & (\chi',\chi) = (1_q,0),(0,1_q). \\ e^{-S}(1-S_q)^2, & (\chi',\chi) = (1_q,1_q). \\ e^{-S} S_{q'} S_q, & (\chi',\chi) = (1_{q'},1_q), \quad q' \neq q, \end{cases} \tag{3.6}$$

where $S = \sum_{q=1}^{N+1} S_q$ and $S_q = |\lambda_{Pq} - \lambda_{Rq}|^2$.

Regarding the nonreactive transitions, an excitation in mode q decays at rate

$$k_{(X,1_q)\to(X,0)} = |c_{q0}|^2 \kappa + \left(\sum_{i=1}^{N} |c_{qi}|^2 \right) \gamma, \tag{3.7}$$

where κ is the decay (leakage) rate of the bare cavity and γ is the decay rate of all bare vibrations. Detailed balance governs the rate of the reverse process: $k_{(X,0)\to(X,1_q)} = k_{(X,1_q)\to(X,0)} \exp(-\beta\hbar\omega_q)$. Following theories [51, 53, 126] of relaxation dynamics for molecules under VSC, the transition from a polariton or dark state to another has rate

$$k_{(X,1_q)\to(X,1_{q'})} = \left(\sum_{i=1}^{N} |c_{q'i}|^2 |c_{qi}|^2 \right) \mathcal{R}(\omega_{q'} - \omega_q), \tag{3.8}$$

where $q' \neq q$,

$$\mathcal{R}(\omega) = 2\pi \left[\Theta(-\omega) \left(n(-\omega) + 1 \right) J(-\omega) + \Theta(\omega) n(\omega) J(\omega) \right], \tag{3.9}$$

and $\Theta(\omega)$ is the Heaviside step function. The environmental modes are characterized by spectral density $J(\omega)$ and the Bose-Einstein distribution function, $n(\omega) = (\exp(\beta\hbar\omega) - 1)^{-1}$.

3.4.3 Reaction parameters

Unless otherwise stated, calculations of reaction rates are carried out using the parameters described in this section.

For the bare molecular vibrations, we choose a mean frequency of $\overline{\omega}_v = 2000\ \text{cm}^{-1}$, which is representative of experimental studies on VSC [22, 23, 55, 101, 107, 127]. Since these studies do not report values of inhomogeneous broadening, we simply take the vibrational frequencies to have a standard deviation of $\sigma_v = 10\ \text{cm}^{-1}$. This choice of σ_v yields a spectral linewidth of $\approx 24\ \text{cm}^{-1}$, which is consistent with vibrational lineshapes measured in some of the cited works [22, 23, 107, 127]. For the cavity frequency and cavity-vibration interaction, we use $\omega_c = \overline{\omega}_v$ and $g\sqrt{N} = 8\sigma_v$ (for all N), respectively. Regarding the electronic degree of freedom and its coupling to other degrees of freedom, we select parameters employed in the reaction simulations of [41]: $E_R = 0$, $E_P = -0.6\overline{\omega}_v$, $\lambda_R = 0$, $\lambda_P = 1.5$, $J_{RP} = 0.01\overline{\omega}_v$, $\lambda_s = 0.08\overline{\omega}_v$.

Next, we describe the parameters governing the relaxation of vibrational and cavity modes.

The temperature T is set to 298 K. We choose $\kappa = 1$ ps^{-1} as the bare cavity decay rate and $\gamma = 0.01$ ps^{-1} for the decay rate of all bare vibrational modes [107]. To model the relaxation among dark and polariton states [Eq. (3.8)], we use the super-Ohmic spectral density

$$J(\omega) = \eta \omega_0^{-1} \omega^2 \exp[-(\omega/\omega_{\text{cut}})^2], \tag{3.10}$$

where $\eta = 1 \times 10^{-3}$ is the interaction strength between each bare vibrational mode and its local chemical environment, $\omega_{\text{cut}} = 50$ cm^{-1} is the cutoff frequency of the environmental modes, and $\omega_0 = \omega_{\text{cut}}$. The spectral density resembles those in models of condensed-phase systems in general [128], while the cutoff frequency is similar to those in liquid-phase molecular systems [129–131].

Our choice of spectral density is motivated by a number of other factors. First, $J(\omega)$ of Eq. (3.10) allows for relaxation from polaritons to dark states that occurs on a timescale of 20-25 ps for $g\sqrt{N} \approx 20$ cm^{-1}. This value is estimated by calculating the corresponding rate constant [Eq. (3.8)] as $\mathcal{R}(\mp 20 \text{ cm}^{-1})/2$ (Fig. 3.4), which applies when the initial state is the upper/lower polariton [53]. Measurements of vibrational polaritons using ultrafast 2D IR spectroscopy have revealed that, by 25 ps (but not less than 5 ps) after polaritons are excited, the dark states significantly contribute to the transient absorption signal [55, 132].

Second, we choose $J(\omega)$ such that the rate of relaxation between dark states decreases as the frequency between the states approaches zero [see Fig. 3.4, namely $\mathcal{R}(\mp\omega)$ as $\omega \to 0$]. We do this so that the associated decay linewidths of dark states do not exceed their energy spacing, maintaining the validity of the kinetic model in this work (Sec. 3.4.4). For the same reason, we set $N \leq 32$ throughout this work (Sec. 3.4.4).

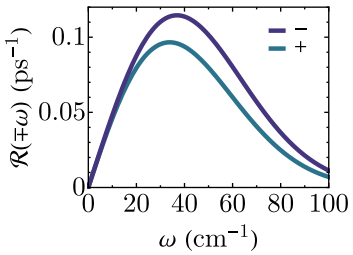

Figure 3.4: $\mathcal{R}(\mp\omega)$ [Eq. (3.9)] for $J(\omega)$ of Eq. (3.10) and $T = 298$ K.

3.4.4 Validity of the kinetic model

Note that, for large enough N, the energy spacing between dark modes becomes smaller than their decay linewidths. Under this condition, our kinetic model is not valid. In this section, we discuss the validity of the model, as well as estimate the range of N for which the model holds.

At the core of our kinetic model is master equation (3.4), which is an example of the Pauli master equation (PME) [99, 133]. The PME is a Markovian master equation that describes the exchange of population among the eigenstates of a quantum system, which interacts with an environment. Let H_{tot} be the total Hamiltonian governing the system and environment. Make the partition $H_{\text{tot}} = H_{0,S} + (H_{\text{tot}} - H_{0,S})$, where $H_{0,S}$ is a zeroth-order system Hamiltonian and $H_{\text{tot}} - H_{0,S}$ acts perturbatively on the $H_{0,S}$ eigenstates $\{|n\rangle\}$, which have frequencies $\{\omega_n\}$. While $H_{0,S}$ is not necessarily the full Hamiltonian of the system in the absence of the bath, we assume that $H_{\text{tot}} - H_{0,S}$ gives rise to purely dissipative dynamics. Then the PME can be written as

$$\frac{d\rho_{nn}(t)}{dt} = \sum_m k_{nn,mm}\rho_{mm}(t), \tag{3.11}$$

where ρ is the reduced density matrix of the system, ρ_{nn} (ρ_{mm}) is the population of $H_{0,S}$ eigenstate $|n\rangle$ ($|m\rangle$), and $k_{nn,mm}$ is the rate constant for population transfer from $|m\rangle$ to $|n\rangle$. Notice that the populations are not coupled to coherences, which are the off-diagonal elements ρ_{lm}, where $|l\rangle$ and $|m\rangle$ are different eigenstates of $H_{0,S}$. In general, such coupling exists and cannot be ignored.

To understand when this decoupling is acceptable, consider the Redfield equation (RE) [99], a Markovian quantum master equation that is more general than the PME. For the proceeding analysis, it is convenient to first move to the interaction picture where the reduced density matrix evolves as

$$\rho_{lm}^{(I)}(t) = \langle l|e^{iH_{0,S}t}\rho(t)e^{-iH_{0,S}t}|m\rangle = e^{i\omega_{lm}t}\rho_{lm}(t), \tag{3.12}$$

where $\omega_{lm} = \omega_l - \omega_m$. With this transformation, the RE, for populations of $H_{0,S}$ eigenstates, can

be written as

$$\frac{d\rho_{nn}(t)}{dt} = \sum_m k_{nn,mm}\rho_{mm}(t) + \sum_{l\neq m} k_{nn,lm}e^{-i\omega_{lm}t}\rho^{(I)}_{lm}(t), \tag{3.13}$$

where l, m run over the eigenstates of $H_{0,S}$. In writing Eq. (3.13), we have used $\rho^{(I)}_{nn}(t) = \rho_{nn}(t)$ [Eq. (3.12)]. Compared to the PME [Eq. (3.11)], the RE [Eq. (3.13)] additionally includes coupling of populations to coherences through the constants $k_{nn,lm}$. To see when we can ignore this coupling, formally integrate Eq. (3.13):

$$\rho_{nn}(t) = \rho_{nn}(0) + \sum_m k_{nn,mm}\int_0^t dt'\,\rho_{mm}(t') + \sum_{l\neq m} k_{nn,lm}\int_0^t dt'\,e^{-i\omega_{lm}t'}\rho^{(I)}_{lm}(t'). \tag{3.14}$$

Focus on the second summation, which runs over the coherences. If $e^{-i\omega_{lm}t'}$ oscillates much faster than the (relaxation) timescale $\tau_{\mathrm{rel},lm}$ over which $\rho^{(I)}_{lm}(t')$ evolves, then the integral in term lm approximately vanishes for $t = O(\tau_{\mathrm{rel},lm})$. Then a good approximation is to neglect all terms lm that satisfy this condition, which can be concisely expressed as

$$\frac{\omega_{lm}\tau_{\mathrm{rel},lm}}{2\pi} \gg 1. \tag{3.15}$$

This approximation, which falls under the secular approximation (also known as the rotating wave approximation) of the theory of open quantum systems [99, 133], can be heuristically interpreted as follows: if the energy gap between two states is larger than their decay linewidths [Eq. (3.15)], then the two states are “good eigenstates" of the (reduced) system, and population will remain in these states in the presence of decoherence processes. Applying the secular approximation to all coherence terms, *i.e.*, dropping all terms in the second summation of Eq. (3.13), converts the RE to the PME. In other words, the PME is valid when the secular approximation [Eq. (3.15)] holds for all coherences. Thus, one should be careful when using the PME to model systems with (near) degeneracies.

In light of this, we reflect on the appropriateness of our kinetic model. Here, a system of N molecules features a quasidegenerate manifold of $N-1$ dark states, whose frequencies are approx-

imately normally distributed with mean $\overline{\omega}_v$ and standard deviation σ_v. In our kinetic simulations, we vary N while fixing σ_v. As N increases, the frequency spacing between dark states decreases. At the same time, the rates of relaxation processes—which include the electron transfer reaction, vibrational/cavity decay, and scattering among polariton and dark states—do not change as much. These relaxation rates determine the timescales over which coherences between dark states evolve [in the interaction picture of Eq. (3.12)]. So, the secular approximation, and therefore our kinetic model, will be invalid for large enough N.

Given the default parameters used in our reaction-rate calculations (Sec. 3.4.3), let us estimate the values of N for which the secular approximation holds. Motivated by the previous paragraph, we introduce a simplified version of the secular-approximation criterion [Eq. (3.15)]:

$$\frac{\Delta\omega_{\text{dark}}\,\tau_{\text{rel, dark}}}{2\pi} \gg 1, \tag{3.16}$$

where $\Delta\omega_{\text{dark}}$ is the characteristic frequency spacing between consecutive dark states, and $\tau_{\text{rel, dark}}$ is the characteristic timescale for the evolution of dark-state coherences [in the interaction picture of Eq. (3.12)]. Since the vast majority of dark states have frequency within $2\sigma_v$ of the mean (ω_v), we take $\Delta\omega_{\text{dark}} = 4\sigma_v/(N-1)$. Accounting for only the aforementioned relaxation processes (*i.e.*, ignoring pure dephasing [99]), we evaluate $\tau_{\text{rel, dark}}$ as the sum of characteristic rate constants for the population decay of a single dark state (the corresponding quantity for population gain is smaller; see Sec. 3.5):

$$\tau_{\text{rel, dark}}^{-1} = \frac{k_b}{2} + \gamma + k_{\text{scat, dark}}. \tag{3.17}$$

The right-hand side is a sum of major decay rates, where $k_b/2$ represents the rate of a backward reactive transition for a dark state with 50% character of the reactive mode, γ is the (bare) vibrational decay rate, and $k_{\text{scat, dark}}$ is a characteristic rate at which a dark state decays into other dark states. From the default parameters (Sec. 3.4.3), we have $k_b \approx \gamma = 0.01$ ps^{-1}. To estimate $k_{\text{scat, dark}}$, we consider three dark states ($q = 1,2,3$) that are consecutive in frequency and let $k_{\text{scat, dark}}$ be the sum of rates [Eq. (3.8)] of decay from dark state $q = 2$ to each dark state

$q' \neq 2$ (including states with $q' \neq 1,3$). For simplicity and based on the results of Sec. 3.3, we assume that dark states $q = 1,2,3$ are equally delocalized across two of four bare vibrational states ($i = 1,2,3,4$), such that the expansion coefficients c_{qi} (see Sec. 3.3) satisfy $|c_{qi}|^2 = 0.5$ for $(q,i) = (1,1),(1,2),(2,2),(2,3),(3,3),(3,4)$ [and $|c_{qi}|^2 = 0$ for all other (q,i) where $q = 1,2,3$]. Also, we set $\Delta\omega_{\text{dark}}$ as the frequency difference between states $q = 1,2$ and between states $q = 2,3$. With $J(\omega)$ of Eq. (3.10) as the spectral density and $T = 298$ K as the temperature, Eq. (3.8) yields

$$k_{\text{scat, dark}} = 0.25\mathcal{R}(-\Delta\omega_{\text{dark}}) + 0.25\mathcal{R}(\Delta\omega_{\text{dark}}) \tag{3.18a}$$

$$\approx 0.5\frac{0.05 \text{ ps}^{-1}}{10 \text{ cm}^{-1}}\Delta\omega_{\text{dark}}. \tag{3.18b}$$

In obtaining the second line, we have used Fig. 3.4 to approximately linearize $\mathcal{R}(\mp\omega)$ [Eq. (3.9)] as $(0.05 \text{ ps}^{-1})\omega/(10 \text{ cm}^{-1})$ for $\omega \in [0,10]$ cm^{-1}. Using the above rates, $\sigma_v = 10$ cm^{-1} (Sec. 3.4.3), and Eq. (3.16), we estimate that the secular approximation holds for $N \ll 74$. In all numerical kinetic simulations, we set $N \leq 32$.

3.5 Approximate kinetic models for chemical reaction

Even though we run the full numerical kinetic simulations as explained above (see also Secs. A.1-A.2), we now introduce approximate models that shed conceptual intuition on the calculated kinetics.

3.5.1 Bare reaction

The bare reaction can be essentially captured by Fig. 3.5a, described as follows. Starting from its vibrational ground state, the reactant converts to product mainly by a $0 \rightarrow 1$ vibronic

transition, which excites the reactive mode and has rate $k_f \equiv k_{(R,0)\to(P,1_r)}$, where

$$k_f = \mathcal{A} F_{0,1_r} \exp\left(-\beta E_a\right), \tag{3.19}$$

$E_a \equiv E_a^{0,1_r}$. The vibrationally hot product either reverts to the reactant at rate $k_b \equiv k_{(P,1_r)\to(R,0)} \gg k_f$, where

$$k_b = k_f \exp\left[\beta\left(E_P + \hbar\omega_r - E_R\right)\right], \tag{3.20}$$

or decays to its vibrational ground state at rate $\gamma \approx k_b$. Once the product reaches its vibrational ground state, it effectively stops reacting due to the high reverse activation energy.

This kinetic scheme can be represented by a simplified kinetic model:

$$\frac{dp_{(R,0)}}{dt} = -k_f p_{(R,0)} + k_b p_{(P,1_r)}, \tag{3.21}$$

$$\frac{dp_{(P,1_r)}}{dt} = -(k_b + \gamma) p_{(P,1_r)} + k_f p_{(R,0)}. \tag{3.22}$$

The first and second equations describe how the populations of $|R,0\rangle$ and $|P,1_r\rangle$ evolve, respectively. Since $k_f \ll k_b, \gamma$, $p_{(P,1_r)}$ does not accumulate, and so we apply the steady-state approximation (SSA) [134] to this population: $dp_{(P,1_r)}/dt \approx 0$. Solving the resulting equation for $p_{(P,1_r)}$ and plugging the solution into Eq. (3.21) leads to $dp_{(R,0)}/dt \approx -k_{\text{bare}}^{(\text{analytical})} p_{(R,0)}$, where

$$k_{\text{bare}}^{(\text{analytical})} = k_f \left(\frac{\gamma}{\gamma + k_b}\right) \tag{3.23}$$

is an effective rate for the bare reaction.

3.5.2 VSC reaction

Under VSC, the primary reaction pathway of the bare case is split into multiple pathways, each involving the (de)excitation of a dark or polariton eigenmode q. For the VSC reaction chan-

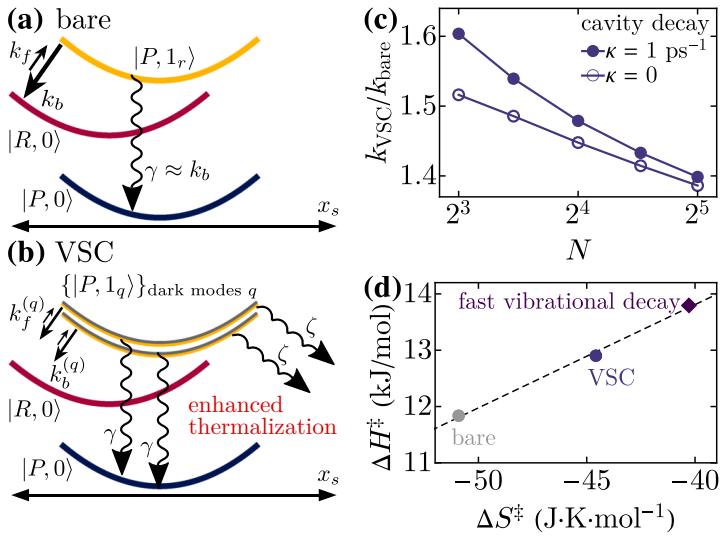

Figure 3.5: (a) Schematic of the bare reaction kinetics. Parabolas represent potential energy surfaces with respect to the effective low-frequency coordinate x_s. After the main reactive transition ($|R,0\rangle \to |P,1_r\rangle$) with rate k_f (the transition $|R,0\rangle \to |P,0\rangle$ is not shown), the product either reverts to the reactant ($|P,1_r\rangle \to |R,0\rangle$) at rate k_b or vibrationally decays to its stable form ($|P,1_r\rangle \to |P,0\rangle$) at rate $\gamma \approx k_b$. (b) Schematic of the reaction kinetics under VSC. The half-yellow half-gray parabolas qualitatively represent potential energy surfaces of product states with one excitation in a dark mode ($|P,1_q\rangle$). The reaction proceeds via multiple reaction channels, each involving a reactive transition ($|R,0\rangle \to |P,1_q\rangle$) with rate $k_f^{(q)} < k_f$ to the product with one excitation in a dark mode. The total forward rate is approximately the bare rate k_f. In contrast, the vibrationally hot product formed from each reaction channel either returns to the reactant ($|P,1_q\rangle \to |R,0\rangle$) at rate $k_b^{(q)} < k_b$ or cools ($|P,1_q\rangle \to |P,0\rangle$) at the *bare* molecular rate γ. There is also scattering (at effective rate ζ) from dark modes with $c_{qr} \not\approx 0$ to those with $c_{qr} \approx 0$. Overall, VSC accelerates product thermalization, suppressing backward reactive transitions, and thus enhancing the net reaction rate. (c) $k_{\text{VSC}}/k_{\text{bare}}$ as a function of N for fixed $g\sqrt{N}$ and various cavity decay rates κ. (d) Activation enthalpy $\Delta H^\ddagger$ versus activation entropy $\Delta S^\ddagger$ for reactions with $N = 32$: bare (gray circle), VSC (purple circle, $\kappa = 1$ ps^{-1}), and bare with vibrational decay rate γ made 100 times faster (purple diamond). The black dashed line is a fit to the points shown. In (c) and (d), the individual rates (k_{VSC}, k_{bare}) and thermodynamic parameters ($\Delta H^\ddagger$, $\Delta S^\ddagger$) are averages over 5000 disorder realizations.

nels, the forward and backward rates take the form

$$k_f^{(q)} = \mathcal{A} F_{0,1_q} \exp\left(-\beta E_a^{(q)}\right), \tag{3.24}$$

$$k_b^{(q)} = k_f^{(q)} \exp\left\{\beta\left[E_P + \hbar\omega_q + \Delta_P - (E_R + \Delta_R)\right]\right\}, \tag{3.25}$$

respectively, where $k_f^{(q)} \equiv k_{(R,0)\to(P,1_q)}$, $k_b^{(q)} \equiv k_{(P,1_q)\to(R,0)}$, and $E_a^{(q)} \equiv E_a^{0,1_q}$. Now, consider the following argument, which holds strictly for large N. As N increases, the average bare mode

becomes localized on dark modes that have essentially the same frequency as it (Figs. 3.3b-3.3c), and its overlap with the polariton modes vanishes (*i.e.*, $c_{qr} \propto \frac{1}{\sqrt{N}} \to 0$ for $q = 1, N+1$; see Fig. 3.3b). These observations suggest that $c_{qr} \not\approx 0$ only for modes q that are dark and have frequency $\omega_q \approx \omega_r$. It is then straightforward to show that $E_a^{(q)}\Big|_{c_{qr}\not\approx 0} \approx E_a$, $F_{0,1_q} \approx |c_{qr}|^2 F_{0,1_r}$, and

$$k_{f/b}^{(q)} \approx |c_{qr}|^2 k_{f/b}. \tag{3.26}$$

Thus, VSC leads to reaction channels that have lower rates of reactive transitions, due to changes not in activation energies but in FC factors, which are smaller as a result of the semilocalization of dark modes. From Eq. (3.26), it is evident that the total forward rate is approximately that of the bare reaction ($\sum_{q=1}^{N+1} k_f^{(q)} \approx k_f$, since $\sum_{q=1}^{N+1} |c_{qr}|^2 = 1$). However, once a forward reactive transition happens—and a dark mode is excited—the product either returns to the reactant at a *reduced rate* ($k_b^{(q)} < k_b$) or, due to the almost fully vibrational nature of the dark modes, vibrationally decays to its stable form ($|P,0\rangle$) at essentially the same *bare rate* (γ). In other words, VSC suppresses reverse reactive transitions by promoting the cooling of the reactive mode upon product formation.

This kinetic scheme can be represented by the following simplified model. In this model, polaritons are decoupled from the reaction, and the reaction proceeds through multiple reaction channels, each involving the (de)excitation of a dark mode. Define $\mathcal{D}$ as the set of dark modes. The populations of $|R,0\rangle$ and $|P,1_q\rangle$, where $q \in \mathcal{D}$, evolve according to

$$\frac{dp_{(R,0)}}{dt} = -\sum_{q\in\mathcal{D}} k_f^{(q)} p_{(R,0)} + \sum_{q\in\mathcal{D}} k_b^{(q)} p_{(P,1_q)}, \tag{3.27}$$

$$\frac{dp_{(P,1_q)}}{dt} = -\left(k_b^{(q)} + \gamma\right) p_{(P,1_q)} + k_f^{(q)} p_{(R,0)}, \tag{3.28}$$

respectively. In analogy to the derivation of Eq. (3.23), we can apply the SSA to each $p_{(P,1_q)}$ to arrive at

$$\frac{dp_{(R,0)}}{dt} \approx -k_f \left(\sum_{q\in\mathcal{D}} |c_{qr}|^2 \frac{\gamma}{\gamma + |c_{qr}|^2 k_b}\right) p_{(R,0)}, \tag{3.29}$$

where we have used Eq. (3.26). Eq (3.29) can be rewritten as $dp_{(R,0)}/dt \approx -k_{\mathrm{VSC}}^{(\mathrm{analytical})} p_{(R,0)}$, where

$$k_{\mathrm{VSC}}^{(\mathrm{analytical})} = k_f \left\langle \frac{\gamma}{\gamma + |c_{qr}|^2 k_b} \right\rangle_{\text{dark modes } q} \tag{3.30}$$

is an effective rate for the VSC reaction, and $\langle \cdot \rangle_{\text{dark modes } q}$ is a weighted average over all dark modes q, each with weight $|c_{qr}|^2$. Since $|c_{qr}|^2 < 1$ for all q, then $k_{\mathrm{VSC}}^{(\mathrm{analytical})} > k_{\mathrm{bare}}^{(\mathrm{analytical})}$. We emphasize that the major contributions to the average in Eq. (3.30) come from dark modes which are closest in frequency to the bare reactive mode (see above). Further enhancement of the VSC reaction, beyond that given by $k_{\mathrm{VSC}}^{(\mathrm{analytical})}$, occurs via dissipative scattering from these dark modes to those with $c_{qr} \approx 0$. Said differently, the product is protected from reversion to reactant when dark modes with relatively more reactive character lose their energy to those with relatively less. Importantly, this scattering requires dark modes to be delocalized. The VSC reaction kinetics, as described above, is summarized in Fig. 3.5b.

3.6 Numerical kinetic simulations of chemical reaction

Fig. 3.5c shows the ratio of VSC reaction rate to bare reaction rate, as determined from numerical kinetic simulations. As we have shown analytically, VSC significantly accelerates the reaction compared to the bare case. For $8 \leq N \leq 32$ (and $g\sqrt{N}$ held constant), the rate enhancement is roughly 50%. Notably, the effect of cavity decay on the reaction is minor and diminishes with N (Fig. 3.5c). This behavior supports that the reaction proceeds mainly through the dark modes. The present scenario is quite generic and contrasts with our previous model where extreme geometric parameters are needed for polaritons to dominate the VSC kinetics [38].

We next look at the dependence on cavity detuning, $\delta = \omega_c - \overline{\omega}_v$, of the reaction rate and reactive-mode delocalization. The lattermost quantity is defined as $1/\sum_{q=1}^{N+1} |c_{qr}|^4$ (the PR of v_r when the mode is expressed in the eigenbasis of H). We find, for various light-matter coupling strengths, that the reactive-mode delocalization is maximum close to resonance and eventually

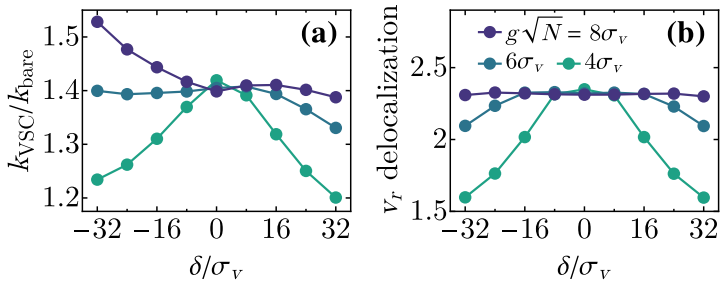

Figure 3.6: (a) k_{VSC}/k_{bare} and (b) v_r delocalization, as a function of cavity detuning δ, for various collective light-matter coupling strengths $g\sqrt{N}$ and fixed $N = 32$. In (a), k_{VSC} and k_{bare} are averages over 5000 disorder realizations.

decreases with detuning (Fig. 3.6a). The rate enhancement due to VSC mostly follows the same trend (Fig. 3.6b). Deviation from this trend at large negative detunings and collective light-matter couplings is attributed to polariton contributions to the rate which, as discussed in [38], decrease as N increases (Fig.). The observed correlation between reactivity under VSC and delocalization of the reactive mode corroborates that the reaction is sped up by dark-mode semilocalization.

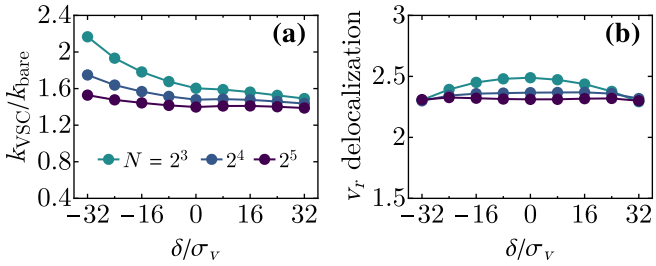

Figure 3.7: (a) k_{VSC}/k_{bare} and (b) v_r delocalization, as a function of cavity detuning δ, for various N and fixed collective light-matter coupling strength $g\sqrt{N} = 8\sigma_v$. In (a), k_{VSC} and k_{bare} are averages over 5000 disorder realizations. For $\delta \ll 0$, k_{VSC}/k_{bare} has a significant positive contribution from the reduced activation energy afforded by the lower polariton [38], whose overlap with v_r scales as $O(N^{-1})$. As N increases, this polaritonic contribution diminishes, and the δ-dependence of k_{VSC}/k_{bare} becomes more similar to that of v_r delocalization.

For additional mechanistic insight into VSC catalysis and following the procedures in [20, 22, 23], we plot in Fig. 3.5d the activation enthalpy ($\Delta H^{\ddagger}$) versus activation entropy ($\Delta S^{\ddagger}$) for multiple cases of VSC and bare reactions. The thermodynamic parameters of activation are computed by calculating the apparent reaction rate for additional temperatures and fitting the obtained values to the Eyring-Polanyi equation (Sec. A.3). This fit indicates that changes in effective parameters $\Delta H^{\ddagger}$ and $\Delta S^{\ddagger}$ can result from dynamical effects such as accelerated vibrational decay,

rather than from potential energy changes.

3.7 Conclusions

In conclusion, we show that, by forming semilocalized dark modes, the VSC of a disordered molecular ensemble can modify the kinetics of a thermally-activated chemical reaction. For a reactive molecule under collective VSC, we find that the electron transfer rate is significantly increased. The spreading of reactive character across dark modes, as well as the dissipative scattering among these modes, allows the reactive mode to thermalize more efficiently once the product is formed, suppressing dynamical effects, such as reversion to reactant. Although experimental characterization of dark states remains a challenge, the phenomena proposed here might be verified using nonlinear infrared spectroscopy to measure populations [55, 56] and spatially resolved energy transport measurements to detect delocalization [116]. The main mechanisms operating in our model do not seem to be limited to nonadiabatic reactions and might have generalizations in adiabatic reactions; these will be explored in future work. Given that these mechanisms only rely on collective VSC, they should also be operative in the cavity-free polaritonic architectures [135], although experiments along this front have so far not been reported. More broadly, our work highlights that the previously overlooked dark states are the entropically likely channels through which collective light-matter interaction can control chemistry.

Chapter 3, in full, is adapted from the material as it appears in "Catalysis by Dark States in Vibropolaritonic Chemistry," M. Du, J. Yuen-Zhou, *Phys. Rev. Lett.* **128**, 096001 (2022). The dissertation author was the primary investigator and author of this paper.

Chapter 4

Remote control of infrared-induced chemistry using vibrational strong coupling

4.1 Introduction

In photochemistry, energy transfer from light to matter produces nonequilibrium distributions of molecular states, therefore enabling selective initiation of reactive trajectories. For a given reaction, tuning of yields is commonly achieved by surveying a series of chemical analogs. These compounds undergo the same process but on different potential energy surfaces. The ability to synthesize substrates with sufficiently varying energetics, though, limits the range of accessible yields.

More facile chemical control of photoinduced reactivity is attainable in the *strong coupling* [48] limit. In this regime, energy coherently oscillates between light and matter faster than the rates at which their respective excitations decay, and the photonic and molecular states hybridize into *polariton states* [5]. To reach sufficiently strong interaction between light and matter, ensembles of molecules can be placed in optical microcavities (Fig. 4.1) [5]. These nano- or microstructures support electromagnetic modes that form polaritons with molecular superpositions

of the same symmetry as the spatial profile of the electric field. Importantly, the majority of linear combinations of matter energy states do not possess the right symmetry to mix with light (in realistic systems, slight mixing occurs due to symmetry-breaking environments; for example, see Ref. [54]) and constitute the reservoir of *dark states*, which remains centered at the original molecular transition energy and plays a crucial role in the relaxation dynamics of polaritons [3–5]. The energetic consequences and resulting reactivity of molecular polaritons have seen a surge in interest over the past several years [3, 4, 7, 9, 136]. Since the observation of suppressed conversion between spiropyran and merocyanine organic dyes [78], modified kinetics upon polariton formation have been demonstrated in a wide variety of photochemical processes by experimental (reverse intersystem crossing [63], photobleaching [84], triplet-triplet annihilation [109], water splitting [137]), theoretical (charge transfer [72, 73], dissociation [59, 138], isomerization [79], singlet fission [62]), or both types of studies (energy transfer [44, 68, 90, 91, 139]). In addition to detuning the cavity from molecular resonances, polaritonic systems offer a robust control knob of energetics: reactant concentration N/V (more precisely, N is the total number of cavity-coupled reactant transitions and V is the cavity mode volume) [3, 4, 7, 9]. Indeed, the dependence of light-matter coupling strength, and the concomitant polaritonic energy splittings (Fig. 4.2), on $\sqrt{N/V}$ has enabled concentration-controlled tuning of a number of the aforementioned processes [63, 78, 90]. Although more robust than substituting the reactant species, changing the concentration is still prone to issues of unfavorable intermolecular interactions, particularly insolubility.

Another convenient way to modulate the light-matter coupling is laser-driven ultrafast population of the dark-state reservoir [55, 56, 101, 108]. In pump-probe spectroscopy of vibrational polaritons, the pump excitation (timescale $\sim$ 0.1 ps [108]) of the polaritons is followed by subsequent relaxation into the dark-state reservoir within $\sim$10-100 ps of delay time [55, 108]. This excited-state reservoir, as a result of its large density of almost purely vibrational states, acts as a very efficient energy sink for the polaritons [53]; the energy transfer is mediated by the interaction between the molecular component of the hybrid states and solvent or other intramolecular modes. Due to vibrational anharmonicity, the $1 \rightarrow 2$ transitions are detuned from the $0 \rightarrow 1$ transitions and

therefore do not couple as well to cavity modes that are resonant with the latter. In other words, the concentration N/V of molecular transitions that can strongly couple to the cavity mode is effectively reduced on an ultrafast timescale. The reduction is tuned by varying the intensity of the pump and detected in the frequency-resolved transient transmission of the proceeding probe pulse [55, 108].

Here we theoretically demonstrate ultrafast and remote tuning of reaction yields of the infrared-induced *cis* $\rightarrow$ *trans* fast isomerization channel of nitrous acid (HONO) [140]. Observed in solid Kr matrices using ultrafast spectroscopy, this reaction is initiated by excitation of the OH stretch vibration of the *cis* (reactant) conformer. Product formation happens on a 20 ps timescale with an appreciable quantum yield of 10%. Therefore, this isomerization should serve as an ideal candidate to study photoinduced processes involving vibrational polaritons, given that typical infrared-optical microcavities are sufficiently long-lived (cavity photon lifetime $\sim$ 1-10 ps) [55, 101, 108] to accommodate the described photochemical transformation. We propose a polaritonic device (Fig. 4.1) that consists of two connected microcavities containing, respectively, the "remote catalyst"[1] (RC) *trans-cis* conformer [141, 142] of glyoxylic acid and the reactant (R) *cis*-HONO [143]. Strong coupling exists between the OH stretch ensembles of the molecules and their corresponding host microcavities. Also strongly coupled are the microcavities themselves; this effect is made possible by light transmission through their shared mirror [144]. The resulting polaritonic eigenstates are delocalized among both RC and R molecules [145]. It follows that without any direct interaction between the two molecular species, pump-driven population of the RC dark-state reservoir can modify the energetics of R and thereby its reactivity in probe-driven conversion to product (P) *trans*-HONO (Fig. 4.1, cf. A and B). Specifically, under thermal equilibrium conditions, the lowest-energy polariton is off-resonant with a probe pulse (Fig. 4.2A), impinging

[1] In this work, "remote catalyst" appropriately describes the *trans-cis* conformer of glyoxylic acid. The definition of a catalyst is a species that participates in a chemical reaction and accelerates it without being consumed (for example, see: D.W. Oxtoby, H.P. Gillis, and L.J. Butler [2011]. Principles of Modern Chemistry [Cengage Learning]). Here, the glyoxylic-acid conformer constitutes a component of the reacting polariton state, enhances HONO isomerization efficiency when its first excited state is populated, and is not consumed.

on the R cavity (Fig. 4.1A). This state also has reduced character of R and its cavity due to delocalization (Fig. 4.2A). After pumping—with a pulse impinging on the RC cavity (Fig. 4.1B)—and subsequent relaxation, the polariton becomes resonant with the proceeding probe pulse (Fig. 4.2B) and has increased R and R-cavity characters (Fig. 4.2, cf. A and B). Employing higher pump field intensities, this nonlocal strategy can turn up reaction efficiency by an order of magnitude.

4.2 Theoretical framework: bare reaction

4.2.1 Hamiltonian

To model ultrafast tuning of the photoinitiated R $\rightarrow$ P conversion, we first describe the bare reaction (*i.e.*, that without strong light-matter coupling) as comprising three steps. The first is absorption of light to create a single OH stretch excitation in R, which we label with $|\mathrm{R}\rangle$. The second step is intramolecular vibrational redistribution (IVR, [146]) transition from $|\mathrm{R}\rangle$ to the near-resonant seventh overtone mode of the torsional coordinate. Given the proximity of this highly excited state to the barrier of the torsional double-well potential energy surface and its consequent delocalization across R and P [140], the third step is relaxation into the R and P local wells via interaction with environment degrees of freedom. For simplicity of notation, we hereby refer to the product-yielding overtone state as $|\mathrm{P}\rangle$, although it should be clear that it has mixed character of R and P. This mechanism is in line with that first proposed for the reaction induced by pulsed [140] and continuous-wave [147] excitation, and is in qualitative agreement with mechanisms suggested by later studies [148].

Following the first mechanism [140], we take $|\mathrm{P}\rangle$ to be 40 cm^{-1} lower in energy than $|\mathrm{R}\rangle$. This energy gap (illustrated by the difference between the minima of potential energy curves 3 and 4 in Fig. 7 of [140]) was obtained by adjusting the barrier height of the torsional double well to a value (3610 cm^{-1}) that allows the potential energy curves of $|\mathrm{R}\rangle$ and $|\mathrm{P}\rangle$ to cross [140]. Here, IVR from $|\mathrm{R}\rangle$ to $|\mathrm{P}\rangle$ is treated as a coupling between the two states, while the other reaction steps (*e.g.*,

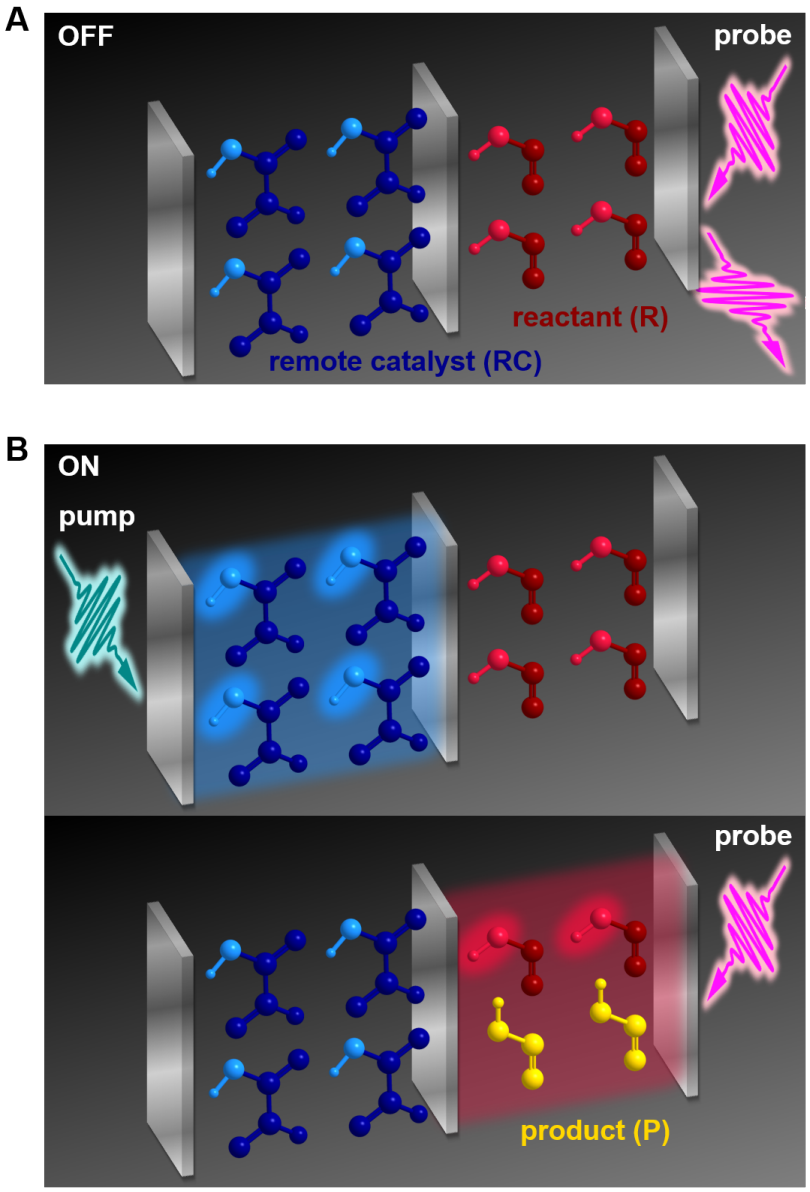

Figure 4.1: Optical microcavities enable remote control of infrared-induced conformational isomerization of HONO (A) The reaction is off. Without excitation of the "remote catalyst" (RC, blue molecule) *trans-cis* conformer of glyoxylic acid, a "probe" laser pulse impinging on the cavity containing reactant (R, red molecule) *cis*-HONO is off-resonant with polaritons and thereby reflected; no reaction occurs. (B) The reaction is on. First, a "pump" laser pulse impinging on the mirror of the RC cavity excites a polariton whose character is predominantly the RC cavity and the strongly coupled OH stretch (light-blue bond) of RC. Next, the probe pulse is now able to efficiently excite a polariton whose character is predominantly the R cavity and the strongly coupled OH stretch (light-red bond) of R; R subsequently converts into the product molecule (P, yellow molecule) *trans*-HONO.

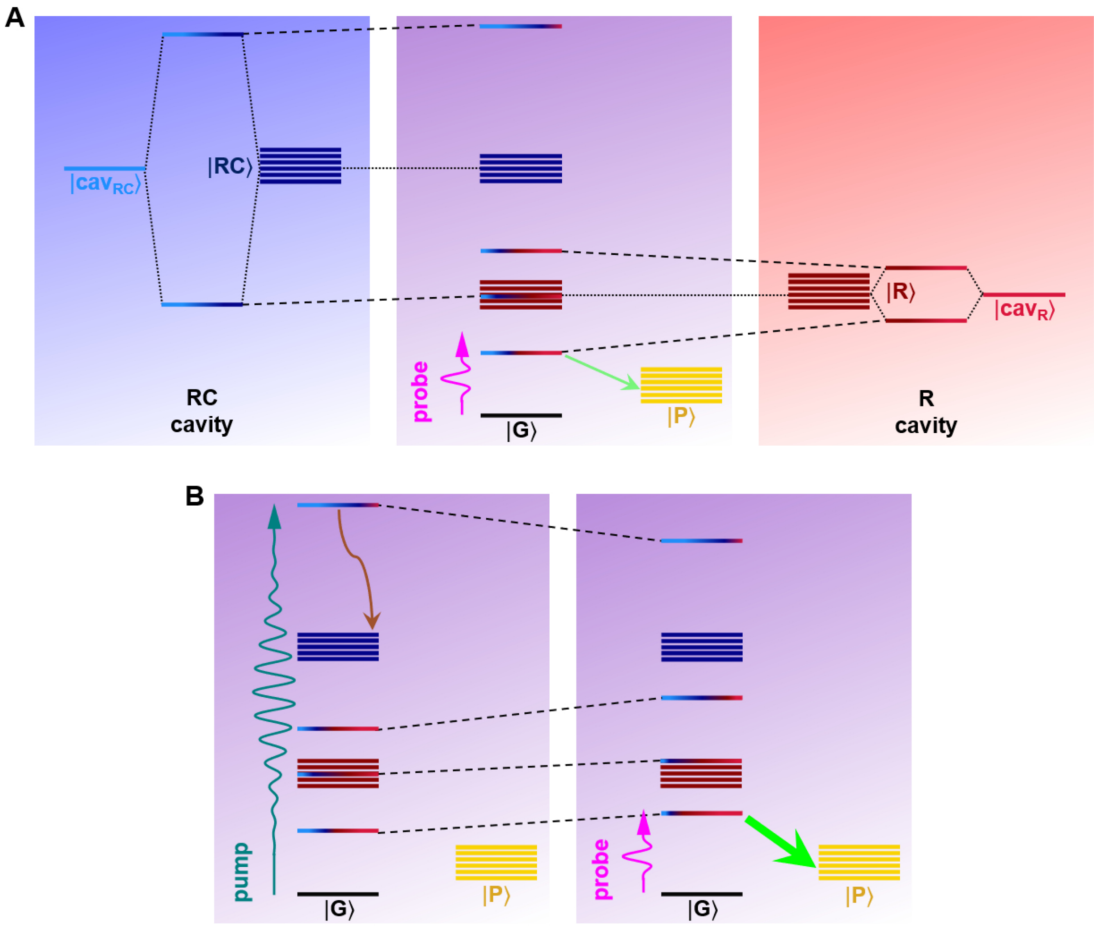

Figure 4.2: Pumping of the RC modifies energetics (A) (Left and right) For each of RC and reactant (R), strong coupling between N molecules and the photon of their host cavity produces two polaritons and $N-1$ dark states; $N=6$ is depicted here for illustration. (Middle) Intercavity coupling hybridizes the polaritons of the noninteracting cavities into polaritons of the entire light-matter device. Because of this delocalization of character across R and RC sides of the device, the lowest polariton is off-resonant with a probe excitation and has reduced mixing fraction of R and its cavity, affording inefficient transfer into product-yielding state $|\mathrm{P}\rangle$. (B) (Left) Pump excitation of the highest polariton is followed by relaxation into the RC dark states during a $\sim$10-100 ps delay time. As a result of anharmonicities, the collective RC light-matter interaction is reduced, modifying the polaritons within an ultrafast timescale. (Right) Now, the lowest polariton is resonant with the proceeding probe excitation and has increased mixing fraction of R and its cavity, affording efficient transfer into $|\mathrm{P}\rangle$. In both (A) and (B), $|\mathrm{G}\rangle$ is the molecular and photonic vacuum ground state (energy not drawn to scale), and the polariton vertical positions (color gradients) qualitatively represent their energies (mixing fractions).

absorption, relaxation into *trans* torsional potential well) are assumed to occur via coupling to a continuum of bath modes under the wide-band [149] approximation. Understanding that photonic bath modes induce excitation but nonradiative bath modes are the main contributors to relaxation of $|\mathrm{R}\rangle$ [149], we write the Hamiltonian for the bare reaction as $H_0 = H_{\mathrm{system},0} + H_{\mathrm{bath},0} + H_{\mathrm{system-bath},0}$. Specifically (hereafter, $\hbar = 1$),

$$H_{\mathrm{system},0} = H_{\mathrm{R}} + H_{\mathrm{P}} + H_{\mathrm{R-P}}, \tag{4.1a}$$

$$H_{\mathrm{bath},0} = \sum_{x=\mathrm{rad,nonrad}} \sum_{i=1}^{N_{\mathrm{R}}} \int_{-\infty}^{\infty} d\omega\, \omega B_{x,i}^{\dagger}(\omega) B_{x,i}(\omega) + \sum_{y=cis,trans} \sum_{i=1}^{N_{\mathrm{R}}} \int_{-\infty}^{\infty} d\omega\, \omega |B_{y,i}(\omega)\rangle\langle B_{y,i}(\omega)|, \tag{4.1b}$$

$$H_{\mathrm{system-bath},0} = \sum_{x=\mathrm{rad,nonrad}} \frac{\sqrt{\gamma_x}}{\sqrt{2\pi}} \sum_{i=1}^{N_{\mathrm{R}}} \int_{-\infty}^{\infty} d\omega [a_{\mathrm{R},i}^{\dagger} B_{x,i}(\omega) + \mathrm{h.c.}] + \sum_{y=cis,trans} \frac{\sqrt{\Gamma_y}}{\sqrt{2\pi}} \sum_{i=1}^{N_{\mathrm{R}}} \int_{-\infty}^{\infty} d\omega [|\mathrm{P}_i\rangle\langle B_{y,i}(\omega)| + \mathrm{h.c.}]. \tag{4.1c}$$

where

$$H_{\mathrm{R}} = \omega_{\mathrm{R}} \sum_{i=1}^{N_{\mathrm{R}}} a_{\mathrm{R},i}^{\dagger} a_{\mathrm{R},i}, \tag{4.2}$$

$$H_{\mathrm{P}} = \omega_{\mathrm{P}} \sum_{i=1}^{N_{\mathrm{R}}} |\mathrm{P}_i\rangle\langle \mathrm{P}_i|, \tag{4.3}$$

$$H_{\mathrm{R-P}} = V_{\mathrm{R-P}} \sum_{i=1}^{N_{\mathrm{R}}} (|\mathrm{P}_i\rangle\langle \mathrm{G}| a_{\mathrm{R},i} + \mathrm{h.c.}) \tag{4.4}$$

describe $|\mathrm{R}\rangle$, $|\mathrm{P}\rangle$, and the $|\mathrm{R}\rangle$-$|\mathrm{P}\rangle$ IVR coupling, respectively. Here, $a_{\mathrm{R},i}^{\dagger}$ ($a_{\mathrm{R},i}$) is the bosonic creation (annihilation) operator for an OH stretch excitation at the ith molecule of the R species. The OH stretch has frequency $\omega_{\mathrm{R}} = 3402\ \mathrm{cm}^{-1}$. Next, $|\mathrm{P}_i\rangle$ is the seventh overtone (eighth excited state) of HONO molecule i, where this state has mixed *cis-trans* character and energy $\omega_{\mathrm{P}} = 3362\ \mathrm{cm}^{-1}$. Finally, $|\mathrm{G}\rangle$ is the molecular and photonic vacuum ground state. The various interactions between $|\mathrm{R}_i\rangle = a_{\mathrm{R},i}^{\dagger}|\mathrm{G}\rangle$, $|\mathrm{P}_i\rangle$, and their baths are summarized in Fig. 4.3. The $|\mathrm{R}\rangle$-$|\mathrm{P}\rangle$ coupling

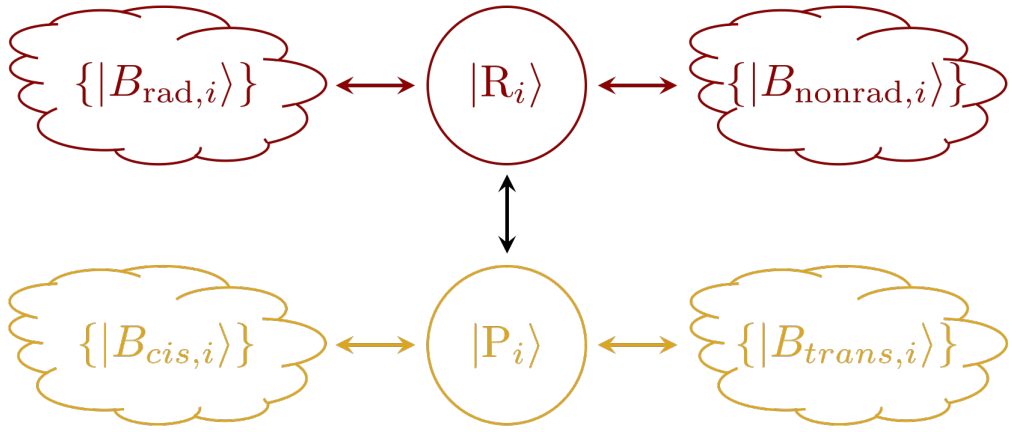

Figure 4.3: Schematic of the system and bath interactions of the R → P fast isomerization channel in the absence of strong light-matter coupling See Eq. (4.1) for the Hamiltonian H_0. The ith R molecule has an OH stretch $|\mathrm{R}_i\rangle$ (dark red circle) which is coupled to a set $|B_{\mathrm{rad},i}\rangle$ of radiative bath states (left dark red cloud) that contribute to its excitation and a set $|B_{\mathrm{nonrad},i}\rangle$ of nonradiative bath states (right dark red cloud) that contribute to its decay. $|\mathrm{R}_i\rangle$ is coupled to the torsional overtone state $|\mathrm{P}_i\rangle$ (yellow circle), which can decay into either the *cis* or *trans* potential wells of HONO via coupling to $|B_{cis,i}\rangle$ (left yellow cloud) or $|B_{trans,i}\rangle$ (right yellow cloud), respectively.

has strength $V_{\mathrm{R-P}}$. The bath modes, which are described by $H_{\mathrm{bath},0}$ and $H_{\mathrm{system-bath},0}$, are taken to be linearly coupled to $\{|\mathrm{R}_i\rangle\}$ and $\{|\mathrm{P}_i\rangle\}$ and are written in a form convenient for application of input-output theory [150]. In particular, the operator $B^{\dagger}_{x,i}(\omega)$ ($B_{x,i}(\omega)$) creates (annihilates) an $|\mathrm{R}\rangle$ bath mode of type x and frequency ω on R molecule i and satisfies the bosonic commutation relations $[B_{x,i}(\omega), B^{\dagger}_{x',i'}(\omega')] = \delta_{x,x'}\delta_{i,i'}\delta(\omega-\omega')$ and $[B_{x,i}(\omega), B_{x',i'}(\omega')] = 0$, where $\delta_{x,x'}, \delta_{i,i'}$ are Kronecker deltas and $\delta(\cdot)$ is the Dirac delta function. The label $x = \mathrm{rad}$ ($x = \mathrm{nonrad}$) indicates a radiative (nonradiative) bath mode that excites (relaxes) R due to coupling to $|\mathrm{R}\rangle$ with strength γ_{rad} (γ_{nonrad}). Similarly, the state $|B_{y,i}(\omega)\rangle$, representing a $|\mathrm{P}\rangle$ bath mode of type y and frequency ω, satisfies the relation $\langle B_{y,i}(\omega)|B_{y',i'}(\omega')\rangle = \delta_{y,y'}\delta_{i,i'}\delta(\omega-\omega')$. The label $y = cis$ ($y = trans$) indicates a bath that relaxes $|\mathrm{P}\rangle$ into the *cis* (*trans*) well via coupling to $|\mathrm{P}\rangle$ with strength Γ_{cis} (Γ_{trans}).

We use state representation for $|\mathrm{P}\rangle$ in Eqs. (4.1b) and (4.1c) because this state is the seventh overtone of the torsional coordinate, *i.e.*, $|\mathrm{P}_i\rangle = \sum_{m=1}^{\infty}[c_{cis,m}(a^{\dagger}_{\tau,cis,i})^m/\sqrt{m!} + c_{trans,m}(a^{\dagger}_{\tau,trans,i})^m/\sqrt{m!}]|\mathrm{G}\rangle$. The creation (annihilation) operator $a^{\dagger}_{\tau,x,i}$ ($a_{\tau,x,i}$) is associated with the diabatic torsional state $x = cis, trans$ for the ith HONO molecule . The mth state of this mode has expansion coefficient $c_{x.m}$. If $|\mathrm{P}\rangle$ overlaps most with the seventh localized overtones of

each conformational isomer, we can write $|\mathrm{P}_i\rangle \approx [c_{cis,8}(a^\dagger_{\tau,cis,i})^8/\sqrt{8!} + c_{trans,8}(a^\dagger_{\tau,trans,i})^8/\sqrt{8!}]|\mathrm{G}\rangle$. Likewise, the use of state representation for the bath modes of $|\mathrm{P}\rangle$ is motivated by the fact they are also likely to be combination/overtone modes, given that they must be high in energy to efficiently couple to the torsional state and induce relaxation.

4.2.2 Input-output theory

We next use input-output theory [150–152] to calculate the reaction efficiency. For notational convenience, we define $\beta_x(\omega) = \sum_{i=1}^{N_\mathrm{R}} B_{x,i}(\omega)/\sqrt{N_\mathrm{R}}$ and $\beta_y(\omega) = \sum_{i=1}^{N_\mathrm{R}} |\mathrm{G}\rangle\langle B_{y,i}(\omega)|/\sqrt{N_\mathrm{R}}$, and use $\frac{d\mathcal{O}(t)}{dt} = -i[\mathcal{O}, H_0]$ for any operator $\mathcal{O}$ which is time-independent in the Schrödinger picture. Then we obtain the following Heisenberg equations of motion:

$$\frac{dP_\mathrm{R}(t)}{dt} = -i\omega_\mathrm{R} P_\mathrm{R}(t) - iV_{\mathrm{R-P}}P_\mathrm{P}(t) - i\sum_{x=\mathrm{rad,nonrad}} \frac{\sqrt{\gamma_x}}{\sqrt{2\pi}} \int_{-\infty}^{\infty} d\omega \beta_x(\omega)(t), \tag{4.5}$$

$$\frac{dP_\mathrm{P}(t)}{dt} = -i\omega_\mathrm{P} P_\mathrm{P}(t) - iV_{\mathrm{R-P}}P_\mathrm{R}(t) - i\sum_{y=cis,trans} \frac{\sqrt{\Gamma_y}}{\sqrt{2\pi}} \int_{-\infty}^{\infty} d\omega \beta_y(\omega)(t), \tag{4.6}$$

$$\frac{d\beta_x(\omega)(t)}{dt} = -i\omega\beta_x(\omega)(t) - i\frac{\sqrt{\gamma_x}}{\sqrt{2\pi}} P_\mathrm{R}(t), \tag{4.7}$$

$$\frac{d\beta_y(\omega)(t)}{dt} = -i\omega\beta_y(\omega)(t) - i\frac{\sqrt{\Gamma_y}}{\sqrt{2\pi}} P_\mathrm{P}(t), \tag{4.8}$$

for polarization operators $P_\mathrm{R} = \sum_{i=1}^{N_\mathrm{R}} a_{\mathrm{R},i}/\sqrt{N_\mathrm{R}}$ and $P_\mathrm{P} = \sum_{i=1}^{N_\mathrm{R}} |\mathrm{G}\rangle\langle \mathrm{P}_i|/\sqrt{N_\mathrm{R}}$. Notice that

$$\frac{d[\beta_x(\omega)(t)e^{i\omega t}]}{dt} = -i\frac{\sqrt{\gamma_x}}{\sqrt{2\pi}} P_\mathrm{R}(t)e^{i\omega t}, \tag{4.9}$$

$$\frac{d[\beta_y(\omega)(t)e^{i\omega t}]}{dt} = -i\frac{\sqrt{\Gamma_y}}{\sqrt{2\pi}} P_\mathrm{P}(t)e^{i\omega t}. \tag{4.10}$$

Defining $t_\mathrm{in} < t$ and $t_\mathrm{out} > t$, we integrate Eq. (4.9) and obtain the relations

$$\beta_x(\omega)(t) = \beta_x(\omega)(t_\mathrm{in})e^{-i\omega(t-t_\mathrm{in})} - i\frac{\sqrt{\gamma_x}}{\sqrt{2\pi}} \int_{t_\mathrm{in}}^{t} dt' P_\mathrm{R}(t')e^{-i\omega(t-t')}, \tag{4.11a}$$

$$\beta_x(\omega)(t) = \beta_x(\omega)(t_\mathrm{out})e^{-i\omega(t-t_\mathrm{out})} + i\frac{\sqrt{\gamma_x}}{\sqrt{2\pi}} \int_{t}^{t_\mathrm{out}} dt' P_\mathrm{R}(t')e^{-i\omega(t-t')}. \tag{4.11b}$$

Plugging in Eq. (4.11) for $x = \text{rad}$ into Eq. (4.5) yields [150]

$$\frac{dP_{\text{R}}(t)}{dt} = -i\omega_{\text{R}}P_{\text{R}}(t) - iV_{\text{R-P}}P_{\text{P}}(t) - i\frac{\sqrt{\gamma_{\text{nonrad}}}}{\sqrt{2\pi}}\int_{-\infty}^{\infty} d\omega\beta_{\text{nonrad}}(\omega)(t) - \sqrt{\gamma_{\text{rad}}}P_{\text{R,in,rad}}(t) - (\gamma_{\text{rad}}/2)P_{\text{R}}(t), \tag{4.12a}$$

$$\frac{dP_{\text{R}}(t)}{dt} = -i\omega_{\text{R}}P_{\text{R}}(t) - iV_{\text{R-P}}P_{\text{P}}(t) - i\frac{\sqrt{\gamma_{\text{nonrad}}}}{\sqrt{2\pi}}\int_{-\infty}^{\infty} d\omega\beta_{\text{nonrad}}(\omega)(t) - \sqrt{\gamma_{\text{rad}}}P_{\text{R,out,rad}}(t) + (\gamma_{\text{rad}}/2)P_{\text{R}}(t), \tag{4.12b}$$

where the input and output polarizations are

$$P_{\text{R,in},z}(t) = \frac{i}{\sqrt{2\pi}}\int_{-\infty}^{\infty} d\omega\beta_z(\omega)(t_{\text{in}})e^{-i\omega(t-t_{\text{in}})}, \tag{4.13}$$

$$P_{\text{R,out},z}(t) = \frac{i}{\sqrt{2\pi}}\int_{-\infty}^{\infty} d\omega\beta_z(\omega)(t_{\text{out}})e^{-i\omega(t-t_{\text{out}})}, \tag{4.14}$$

respectively, for $z = \text{rad}, \text{nonrad}, cis, trans$. Subtracting the second from the first row of Eq. (4.12) gives

$$P_{\text{R,out,rad}}(t) - P_{\text{R,in,rad}}(t) = \sqrt{\gamma_{\text{rad}}}P_{\text{R}}(t). \tag{4.15}$$

This is an example of *input-output relation*. We analogously obtain relations for the $x = \text{nonrad}$ and $y = cis, trans$ baths,

$$P_{\text{R,out,nonrad}}(t) - P_{\text{R,in,nonrad}}(t) = \sqrt{\gamma_{\text{nonrad}}}P_{\text{R}}(t), \tag{4.16}$$

$$P_{\text{P,out},y}(t) - P_{\text{P,in},y}(t) = \sqrt{\Gamma_y}P_{\text{P}}(t). \tag{4.17}$$

Eqs. (4.16) and (4.17) will prove useful below.

We want to express the output polarizations above in terms of $P_{\text{R,in,rad}}$. To proceed, we first substitute Eq. (4.11a) for $x = \text{nonrad}$ into Eq. (4.12a) [150],

$$\frac{dP_{\mathrm{R}}(t)}{dt} = -i\omega_{\mathrm{R}}P_{\mathrm{R}}(t) - iV_{\mathrm{R-P}}P_{\mathrm{P}}(t) - \sum_{x=\mathrm{rad,nonrad}} \sqrt{\gamma_x}P_{\mathrm{R,in},x}(t) - \sum_{x=\mathrm{rad,nonrad}} (\gamma_x/2)P_{\mathrm{R}}(t). \quad (4.18)$$

The analogous equation for P_{P} is

$$\frac{dP_{\mathrm{P}}(t)}{dt} = -i\omega_{\mathrm{P}}P_{\mathrm{P}}(t) - iV_{\mathrm{R-P}}P_{\mathrm{R}}(t) - \sum_{y=cis,trans} \sqrt{\Gamma_y}P_{\mathrm{P,in},y}(t) - \sum_{y=cis,trans} (\Gamma_y/2)P_{\mathrm{P}}(t). \quad (4.19)$$

Recalling that $|\mathrm{R}\rangle$ is only excited by the photonic bath via *weak* light-matter coupling and $|\mathrm{P}\rangle$ is only excited by IVR coupling to $|\mathrm{R}\rangle$, we hereafter take $P_{\mathrm{R},1,\mathrm{in,nonrad}}(t), P_{\mathrm{P,in},y}(t) = 0$ and $\gamma_{\mathrm{rad}} \ll \gamma_{\mathrm{nonrad}}$ to arrive at the Heisenberg-Langevin equations:

$$\frac{dP_{\mathrm{R}}(t)}{dt} = -i(\omega_{\mathrm{R}} - i\gamma_{\mathrm{nonrad}}/2)P_{\mathrm{R}}(t) - iV_{\mathrm{R-P}}P_{\mathrm{P}}(t) - \sqrt{\gamma_{\mathrm{rad}}}P_{\mathrm{R,in,rad}}(t) \quad (4.20)$$

$$\frac{dP_{\mathrm{P}}(t)}{dt} = -i[\omega_{\mathrm{P}} - i(\Gamma_{cis} + \Gamma_{trans})/2]P_{\mathrm{P}}(t) - iV_{\mathrm{R-P}}P_{\mathrm{R}}(t). \quad (4.21)$$

We now solve for P_{R} and P_{P} in the frequency domain to calculate the (frequency-resolved) absorption of R and the reaction efficiency. Taking the Fourier transform $\mathcal{F}[f(t)] = \int_{-\infty}^{\infty} dt\, e^{i\omega t} f(t)$ of Eqs. (4.20) and (4.21), we obtain

$$P_{\mathrm{R}}(\omega) = S_{\mathrm{R},0}(\omega)P_{\mathrm{R,in,rad}}(\omega), \quad (4.22)$$

$$P_{\mathrm{P}}(\omega) = S_{\mathrm{P},0}(\omega)P_{\mathrm{R,in,rad}}(\omega), \quad (4.23)$$

where

$$S_{\mathrm{R},0}(\omega) = \frac{-i\sqrt{\gamma_{\mathrm{rad}}}[\omega - \omega_{\mathrm{P}} + i(\Gamma_{cis} + \Gamma_{trans})/2]}{(\omega - \omega_{\mathrm{R}} + i\gamma_{\mathrm{nonrad}}/2)[\omega - \omega_{\mathrm{P}} + i(\Gamma_{cis} + \Gamma_{trans})/2] - V_{\mathrm{R-P}}^2}, \quad (4.24)$$

$$S_{\mathrm{P},0}(\omega) = S_{\mathrm{R},0}(\omega)\frac{V_{\mathrm{R-P}}}{\omega - \omega_{\mathrm{P}} + i(\Gamma_{cis} + \Gamma_{trans})/2}. \quad (4.25)$$

We proceed to calculate the absorption of R and the reaction efficiency. The steady-state absorbance of R, *i.e.*, the fraction of the input energy that is dissipated by the nonradiative bath coupled to R, is

$$\text{absorbance}_{\text{R},0}(\omega) = \frac{\langle P^{\dagger}_{\text{R,out,nonrad}}(\omega) P_{\text{R,out,nonrad}}(\omega)\rangle}{\langle P^{\dagger}_{\text{R,in,rad}}(\omega) P_{\text{R,in,rad}}(\omega)\rangle} \tag{4.26a}$$

$$= \gamma_{\text{nonrad}} |S_{\text{R},0}(\omega)|^2 \tag{4.26b}$$

$$= \frac{\gamma_{\text{rad}}\gamma_{\text{nonrad}}}{\left|\omega - \omega_{\text{R}} + i\gamma_{\text{nonrad}}/2 - \frac{V^2_{\text{R-P}}}{\omega - \omega_{\text{P}} + i(\Gamma_{cis}+\Gamma_{trans})/2}\right|^2} \tag{4.26c}$$

where we have used input-output equation (4.16), as well as Eqs. (4.22) and (4.24). In agreement with physical intuition, Eq. (4.26c) says that the absorption of R peaks near ω_{R} but is slightly offset by an IVR-induced energy correction represented by the fraction in the denominator. Analogous to the absorbance of R, the steady-state reaction efficiency η_0 is the fraction of the input energy whose bath-induced dissipation relaxes $|\text{P}\rangle$ into the *trans* localized potential well. Thus,

$$\eta_0(\omega) = \frac{\langle P^{\dagger}_{\text{P,out},trans}(\omega) P_{\text{P,out},trans}(\omega)\rangle}{\langle P^{\dagger}_{\text{R,in,rad}}(\omega) P_{\text{R,in,rad}}(\omega)\rangle} \tag{4.27a}$$

$$= \Gamma_{trans} |S_{\text{P},0}(\omega)|^2 \tag{4.27b}$$

$$= \frac{\text{absorbance}_{\text{R},0}(\omega)}{\gamma_{\text{nonrad}}} \gamma_{\text{R}\to\text{P}}(\omega). \tag{4.27c}$$

We have used input-output equation (4.17), as well as Eqs. (4.23), (4.25), and (4.26b). We also recognized that

$$\gamma_{\text{R}\to\text{P}}(\omega) = \frac{V^2_{\text{R-P}}\Gamma_{trans}}{(\omega - \omega_{\text{P}})^2 + [(\Gamma_{cis}+\Gamma_{trans})/2]^2} \tag{4.28}$$

is exactly the (quantum mechanical) steady-state rate of transition from the (energy-broadened) $|\text{R}\rangle$ state of frequency ω into the *trans* well [149, 153]. Then the bare reaction efficiency can be intuitively expressed as

$$\eta_0(\omega) = \text{absorbance}_{\text{R},0}(\omega)\text{QY}_{\text{R}\to\text{P}}(\omega), \tag{4.29}$$

where $\mathrm{QY}_{\mathrm{R}\to\mathrm{P}} = \gamma_{\mathrm{R}\to\mathrm{P}}(\omega)/\gamma_{\mathrm{nonrad}}$ is an isomerization quantum yield, though defined differently than in the experimental report of fast-channel HONO isomerization [140]. Satisfyingly, Eq. (4.29) says that the reaction efficiency depends on how well R first absorbs at ω into $|\mathrm{R}\rangle$ and then isomerizes by IVR coupling into $|\mathrm{P}\rangle$ at this same frequency. In the simulations shown in Figs. 4.5 and 4.6, we use [see Eq. (4.60)] $\eta_0(\omega_\mathrm{R}) \approx 0.0023$, calculated from Eq. (4.27c) with the previously reported $\mathrm{absorbance}_{\mathrm{R},0}(\omega_\mathrm{R}) \approx 0.07$ [140], absorption linewidth $\gamma_{\mathrm{nonrad}} \approx 5\ \mathrm{cm}^{-1}$ [140], and isomerization rate $\gamma_{\mathrm{R}\to\mathrm{P}}(\omega_\mathrm{R}) \approx 0.167\ \mathrm{cm}^{-1}$ (or $5\ \mathrm{ns}^{-1}$) [140].

For $\omega \neq \omega_\mathrm{R}$, computing $\eta_0(\omega)$ requires [see Eq. (4.27c)] explicit evaluation of $\gamma_{\mathrm{R}\to\mathrm{P}}(\omega)$, Eq. (4.28), and $\mathrm{absorption}_{\mathrm{R},0}(\omega)$, Eq. (4.26c). For calculating $\gamma_{\mathrm{R}\to\mathrm{P}}(\omega)$, in both this and polaritonic (Sec. 4.3.2) cases, we assign values to $\Gamma_{cis} + \Gamma_{trans}$ and $V^2_{\mathrm{R}-\mathrm{P}}\Gamma_{trans}$. First, we set $\Gamma_{cis} + \Gamma_{trans}$ to the rate of $|\mathrm{P}\rangle$ population relaxation. Treating the process as one-phonon emission of the diabatic eighth-excited torsional state of *cis*-HONO in the harmonic limit, $\Gamma_{cis} + \Gamma_{trans}$ is 8 times the population relaxation rate of the singly excited torsion of *cis*-HONO [149]. We make this harmonic approximation because the population decay rate of $|\mathrm{P}\rangle$ is not reported (to the best of our knowledge), but that of the $v = 1$ torsional state of *cis*-HONO can be estimated. Specifically, we assume that this single excitation relaxes at the same rate ($1.67\ \mathrm{cm}^{-1}$, or $(20\ \mathrm{ps})^{-1}$ [140]) as $|\mathrm{R}\rangle$, in analogy to the similarity of their absorption linewidths [154]. While anharmonicity, other relaxation channels (*e.g.*, multiphonon processes), and pure dephasing may significantly contribute to the decay of $|\mathrm{P}\rangle$, these contributions are not well-characterized (to the best of our knowledge). Furthermore, modeling these contributions is difficult and should not change the main conclusions of this work. Having set $\Gamma_{cis} + \Gamma_{trans} = 8 \times 1.67\ \mathrm{cm}^{-1}$, we assign $V^2\Gamma_{trans} \approx 275\ \mathrm{cm}^{-3}$ to afford the experimentally observed value $\gamma_{\mathrm{R}\to\mathrm{P}}(\omega_\mathrm{R}) = 0.167\ \mathrm{cm}^{-1}$ [140] from Eq. (4.28).

Like $\gamma_{\mathrm{R}\to\mathrm{P}}(\omega)$, explicit calculation of $\mathrm{absorption}_{\mathrm{R},0}(\omega)$ using Eq. (4.26c) requires an unknown (to the best of our knowledge) parameter, namely $V_{\mathrm{R}-\mathrm{P}}$. Since the reported value [140] is incorrect [148], we evaluate $\mathrm{absorbance}_{\mathrm{R},0}(\omega)$ [Eq. (4.26c)] by assuming $V_{\mathrm{R}-\mathrm{P}}$ is small,

$$\mathrm{absorbance}_{\mathrm{R},0}(\omega) \approx \frac{\gamma_{\mathrm{rad}}\gamma_{\mathrm{nonrad}}}{(\omega-\omega_\mathrm{R})^2 + (\gamma_{\mathrm{nonrad}}/2)^2}, \tag{4.30}$$

which intuitively is the Lorentzian lineshape for $|\mathrm{R}\rangle$ in the absence of IVR. The criterion to justify Eq. (4.30) can be derived as follows. From Eqs. (4.26b) and (4.24), the poles of the absorption are given by

$$\omega_{\text{average}} \pm \frac{\sqrt{\omega_{\text{squared difference}}}}{2}, \tag{4.31}$$

as well as their complex conjugates. The frequency

$$\omega_{\text{average}} = \frac{\omega_{\mathrm{R}} + \omega_{\mathrm{P}} - i(\gamma_{\text{nonrad}} + \Gamma_{cis} + \Gamma_{trans})/2}{2} \tag{4.32}$$

is the average of the complex-valued energies $\omega_{\mathrm{R}} - i\gamma_{\text{nonrad}}/2$ and $\omega_{\mathrm{P}} + i(\Gamma_{cis} + \Gamma_{trans})/2$ of $|\mathrm{R}\rangle$ and $|\mathrm{P}\rangle$, respectively. When $V_{\mathrm{R-P}} = 0$, the squared difference of these energies is

$$\begin{aligned}\omega_{\text{squared difference}} = (\omega_{\mathrm{R}} - \omega_{\mathrm{P}})^2 - (\gamma_{\text{nonrad}} - \Gamma_{cis} - \Gamma_{trans})^2/4 - i(\omega_{\mathrm{R}} - \omega_{\mathrm{P}})(\gamma_{\text{nonrad}} - \Gamma_{cis} - \Gamma_{trans}) \\ - V_{\mathrm{R-P}}^2. \end{aligned} \tag{4.33}$$

By analogy with the criteria for strong interaction [48], the IVR energy correction in Eq. (4.26c) can be neglected if the square of the IVR coupling is less than the "linewidth" of $\omega_{\text{squared difference}}$:

$$V^2 < |(\omega_{\mathrm{R}} - \omega_{\mathrm{P}})(\gamma_{\text{nonrad}} - \Gamma_{cis} - \Gamma_{trans})|. \tag{4.34}$$

Using the values for $\Gamma_{cis} + \Gamma_{trans}$ and $V^2\Gamma_{trans}$ from the previous paragraph, this inequality is satisfied if the probability $\Gamma_{trans}/(\Gamma_{cis} + \Gamma_{trans})$ of decaying into the *trans* potential well is greater than ≈ 0.06. This range of probabilities is reasonable, given that the measured isomerization quantum yield (as defined in [140]) is 10% [140].

4.3 Theoretical framework: reaction in polaritonic device

4.3.1 Hamiltonian

We next describe the reaction in the proposed polaritonic device (Sec. 4.1 and Fig. 4.1), where the probe absorption into the polariton states triggers IVR onto $|\mathrm{P}\rangle$. Both absorption and IVR are treated with a version of input-output theory [151, 152, 155] adapted to pump-probe spectroscopy for vibrational polaritons [56]. The major qualitative and quantitative features of experimental transient spectra are captured within this theory [55, 56], including the frequencies and intensities of the resonances exhibited by the transient transmission of the probe. In this work, we disregard electrical anharmonicity [56] (and fine-structure contributions such as molecular rotations [60, 156]), whose inclusion should not qualitatively change our main findings.

The Hamiltonian for the proposed polaritonic setup (Fig. 4.1) is $H = H_{\mathrm{system}} + H_{\mathrm{bath}} + H_{\mathrm{system-bath}}$. The first term on the right-hand side reads

$$\begin{aligned} H_{\mathrm{system}} = {} & H_{\mathrm{RC}} + H_{\mathrm{cav_{RC}}} + H_{\mathrm{cav_{RC}-RC}} \\ & + H_{\mathrm{cav_{RC}-cav_R}} + H_{\mathrm{R}} + H_{\mathrm{cav_R}} + H_{\mathrm{cav_R-R}} \\ & + H_{\mathrm{P}} + H_{\mathrm{R-P}}, \end{aligned} \tag{4.35}$$

from which Hamiltonian $H_{\mathrm{system}}^{(\mathrm{no\ pump})}$, Eq. (4.61), follows in the perturbative limit of $H_{\mathrm{R-P}}$. From left to right and top to bottom, the terms of Eq. (4.35) respectively represent the contributions of $|\mathrm{RC}\rangle$ (the OH stretch excitation in RC), RC cavity, their coupling, intercavity coupling, R cavity, $|\mathrm{R}\rangle$, cavity-$|\mathrm{R}\rangle$ coupling, $|\mathrm{P}\rangle$, and the $|\mathrm{R}\rangle$-$|\mathrm{P}\rangle$ IVR coupling. The terms H_{R}, H_{P}, and $H_{\mathrm{R-P}}$ have

been defined in Sec. 4.2.1. The other terms read

$$H_{\mathrm{RC}} = \omega_{\mathrm{RC}} \sum_{i=1}^{N_{\mathrm{RC}}} a^{\dagger}_{\mathrm{RC},i} a_{\mathrm{RC},i} \tag{4.36a}$$

$$+ \Delta \sum_{i=1}^{N_{\mathrm{RC}}} a^{\dagger}_{\mathrm{RC},i} a^{\dagger}_{\mathrm{RC},i} a_{\mathrm{RC},i} a_{\mathrm{RC},i}, \tag{4.36b}$$

$$H_{\mathrm{cav_{RC}}} = \omega_{\mathrm{cav_{RC}}} c^{\dagger}_{\mathrm{RC}} c_{\mathrm{RC}}, \tag{4.37}$$

$$H_{\mathrm{cav_{RC}-RC}} = g_{\mathrm{RC}} \sum_{i=1}^{N_{\mathrm{RC}}} (a^{\dagger}_{\mathrm{RC},i} c_{\mathrm{RC}} + \mathrm{h.c.}), \tag{4.38}$$

$$H_{\mathrm{cav_{RC}-cav_R}} = g_{\mathrm{cav}} (c^{\dagger}_{\mathrm{R}} c_{\mathrm{RC}} + \mathrm{h.c.}), \tag{4.39}$$

$$H_{\mathrm{cav_R}} = \omega_{\mathrm{cav_R}} c^{\dagger}_{\mathrm{R}} c_{\mathrm{R}}, \tag{4.40}$$

where $a^{\dagger}_{x,i}$ ($a_{x,i}$) is the bosonic creation (annihilation) operator for an OH stretch excitation at the ith molecule of the $x = \mathrm{R}, \mathrm{RC}$ species, and $c^{\dagger}_{x}$ (c_x) is the bosonic creation (annihilation) operator for a photon in the cavity hosting x. Given that population of just RC (but not R) is assumed to be excited by the pump, only its anharmonicity is relevant [compare Eqs. (4.36) and (4.2)]. All energy and coupling parameters in Eqs. (4.36)-(4.40) are defined in Sec. 4.4. The latter two terms of H read

$$H_{\mathrm{bath}} = \sum_{x=\mathrm{RC}, \mathrm{cav_{RC}}, \mathrm{cav_R}, \mathrm{R}, \mathrm{P}} H_{\mathrm{bath},x}, \tag{4.41a}$$

$$H_{\mathrm{system-bath}} = \sum_{x=\mathrm{RC}, \mathrm{cav_{RC}}, \mathrm{cav_R}, \mathrm{R}, \mathrm{P}} H_{\mathrm{system-bath},x}. \tag{4.41b}$$

In particular,

$$H_{\text{bath},x} = \sum_{i=1}^{N_x} \int_{-\infty}^{\infty} d\omega\, \omega B_{x,i}^{\dagger}(\omega) B_{x,i}(\omega), \tag{4.42a}$$

$$H_{\text{bath,cav}_x} = \int_{-\infty}^{\infty} d\omega\, \omega B_{\text{cav}_x}^{\dagger}(\omega) B_{\text{cav}_x}(\omega), \tag{4.42b}$$

$$H_{\text{bath,P}} = \sum_{y=cis,trans} \sum_{i=1}^{N_{\text{R}}} \int_{-\infty}^{\infty} d\omega\, \omega |B_{y,i}(\omega)\rangle\langle B_{y,i}(\omega)|, \tag{4.42c}$$

and

$$H_{\text{system-bath},x} = \frac{\sqrt{\gamma_x}}{\sqrt{2\pi}} \sum_{i=1}^{N_z} \int_{-\infty}^{\infty} d\omega [a_{x,i}^{\dagger} B_{x,i}(\omega) + \text{h.c.}], \tag{4.43a}$$

$$H_{\text{system-bath,cav}_x} = \frac{\sqrt{\kappa_x}}{\sqrt{2\pi}} \int_{-\infty}^{\infty} d\omega [c_x^{\dagger} B_{\text{cav}_x}(\omega) + \text{h.c.}], \tag{4.43b}$$

$$H_{\text{system-bath,P}} = \sum_{y=cis,trans} \frac{\sqrt{\Gamma_y}}{\sqrt{2\pi}} \sum_{i=1}^{N_{\text{R}}} \int_{-\infty}^{\infty} d\omega [|\text{P}_i\rangle\langle B_{y,i}(\omega)| + \text{h.c.}] \tag{4.43c}$$

for $x = \text{RC}, \text{R}$. The various interactions between $|x_i\rangle = a_{x,i}^{\dagger}|\text{G}\rangle$, $|\text{cav}_x\rangle$, $|\text{P}_i\rangle$, and their baths are summarized in Fig. 4.4. Note that the bath modes for $|\text{R}\rangle$ only include the nonradiative degrees of freedom that induce its decay [cf. Eqs. (4.1b) and (4.42a)]. Since probe excitation of the polaritonic system would be carried out experimentally via laser impingement on the R cavity mirror, the radiative input is considered to couple only to the R cavity [56, 152]. The operator $B_{\text{RC},i}^{\dagger}(\omega)$ ($B_{\text{RC},i}(\omega)$) creates (annihilates) a nonradiative bath mode that has frequency ω, is coupled to RC molecule i, and satisfies the bosonic commutation relations $[B_{\text{RC},i}(\omega), B_{\text{RC},i'}^{\dagger}(\omega')] = \delta_{i,i'}\delta(\omega-\omega')$ and $[B_{\text{RC},i}(\omega), B_{\text{RC},i'}(\omega')] = 0$. Analogously, $B_{\text{cav}_x}^{\dagger}(\omega)$ ($B_{\text{cav}_x}(\omega)$) creates (annihilates) a x cavity radiative bath mode of frequency ω and satisfies $[B_{\text{cav}_x}(\omega), B_{\text{cav}_x}^{\dagger}(\omega')] = \delta(\omega-\omega')$ and $[B_{\text{cav}_x}(\omega), B_{\text{cav}_x}(\omega')] = 0$. The decay constants $\gamma_{\text{RC}} = \gamma_{\text{R}} = 5\ \text{cm}^{-1}$ approximate the absorption linewidth of the OH stretch excitation in R [140] and RC [141, 142]. The cavity photon lifetimes $\kappa_{\text{RC}} = \kappa_{\text{R}} = 9.5\ \text{cm}^{-1}$ are chosen such that $2\kappa_x/\omega_x$ (each cavity has only one mirror that couples to external photons, Fig. 4.1) approximately matches experimental parameters [55, 56]. We

have also defined the operator $P_{\mathrm{P}} = \sum_{i=1}^{N_{\mathrm{R}}} |\mathrm{G}\rangle\langle \mathrm{P}_i|/\sqrt{N_{\mathrm{R}}}$, which (through $P_{\mathrm{P}}^{\dagger} P_{\mathrm{P}}$) keeps track of the IVR-transferred population from $|\mathrm{R}\rangle$ to $|\mathrm{P}\rangle$. The remaining decay rates Γ_{cis} and Γ_{trans} (Sec. 4.2) represent relaxation of the HONO torsional state into the local R (*cis*) or P (*trans*) wells.

4.3.2 Input-output theory

In this section, we obtain expressions for the transient spectra and reaction efficiency using input-output theory for pump-probe spectroscopy of vibrational polaritons [56]. Besides the subtleties introduced by the inclusion of nonlinear effects, this derivation follows the same steps as those of the bare case (Sec. 4.2.2). In fact, the notation here is identical to that Sec. 4.2.2, unless otherwise noted.

To derive equations of motion for $|\mathrm{RC}\rangle$, RC cavity, R cavity, $|\mathrm{R}\rangle$, and $|\mathrm{P}\rangle$, we first carry out standard input-output theory, specifically the steps taken in Sec. 4.2.2 to obtain equations of motion (4.18) and (4.19) in the bare case. If we then account for the assumption made above that only the R cavity couples to an input field, we arrive at the Heisenberg-Langevin equations

$$\begin{aligned}
\frac{dP_{\mathrm{RC}}(t)}{dt} &= -i(\omega_{\mathrm{RC}} - i\gamma_{\mathrm{RC}}/2)P_{\mathrm{RC}}(t) \\
&\quad - ig_{\mathrm{RC}}\sqrt{N_{\mathrm{RC}}}c_{\mathrm{RC}}(t) - 2i\Delta P_{\mathrm{RC},3}(t), && \text{(4.44a)} \\
\frac{dc_{\mathrm{RC}}(t)}{dt} &= -i(\omega_{\mathrm{cav_{RC}}} - i\kappa_{\mathrm{RC}}/2)c_{\mathrm{RC}}(t) \\
&\quad - ig_{\mathrm{cav}}c_{\mathrm{R}}(t) - ig_{\mathrm{RC}}\sqrt{N_{\mathrm{RC}}}P_{\mathrm{RC}}(t), && \text{(4.44b)} \\
\frac{dc_{\mathrm{R}}(t)}{dt} &= -i(\omega_{\mathrm{cav_R}} - i\kappa_{\mathrm{R}}/2)c_{\mathrm{R}}(t) - ig_{\mathrm{cav}}c_{\mathrm{RC}}(t) \\
&\quad - ig_{\mathrm{R}}\sqrt{N_{\mathrm{R}}}P_{\mathrm{R}}(t) - \sqrt{\kappa_{\mathrm{R}}}c_{\mathrm{R,in}}(t), && \text{(4.44c)} \\
\frac{dP_{\mathrm{R}}(t)}{dt} &= -i(\omega_{\mathrm{R}} - i\gamma_{\mathrm{R}}/2)P_{\mathrm{R}}(t) \\
&\quad - ig_{\mathrm{R}}\sqrt{N_{\mathrm{R}}}c_{\mathrm{R}}(t) - iV_{\mathrm{R-P}}P_{\mathrm{P}}(t), && \text{(4.44d)} \\
\frac{dP_{\mathrm{P}}(t)}{dt} &= -i[\omega_{\mathrm{P}} - i(\Gamma_{cis} + \Gamma_{trans})/2]P_{\mathrm{P}}(t) \\
&\quad - iV_{\mathrm{R-P}}P_{\mathrm{R}}(t), && \text{(4.44e)}
\end{aligned}$$

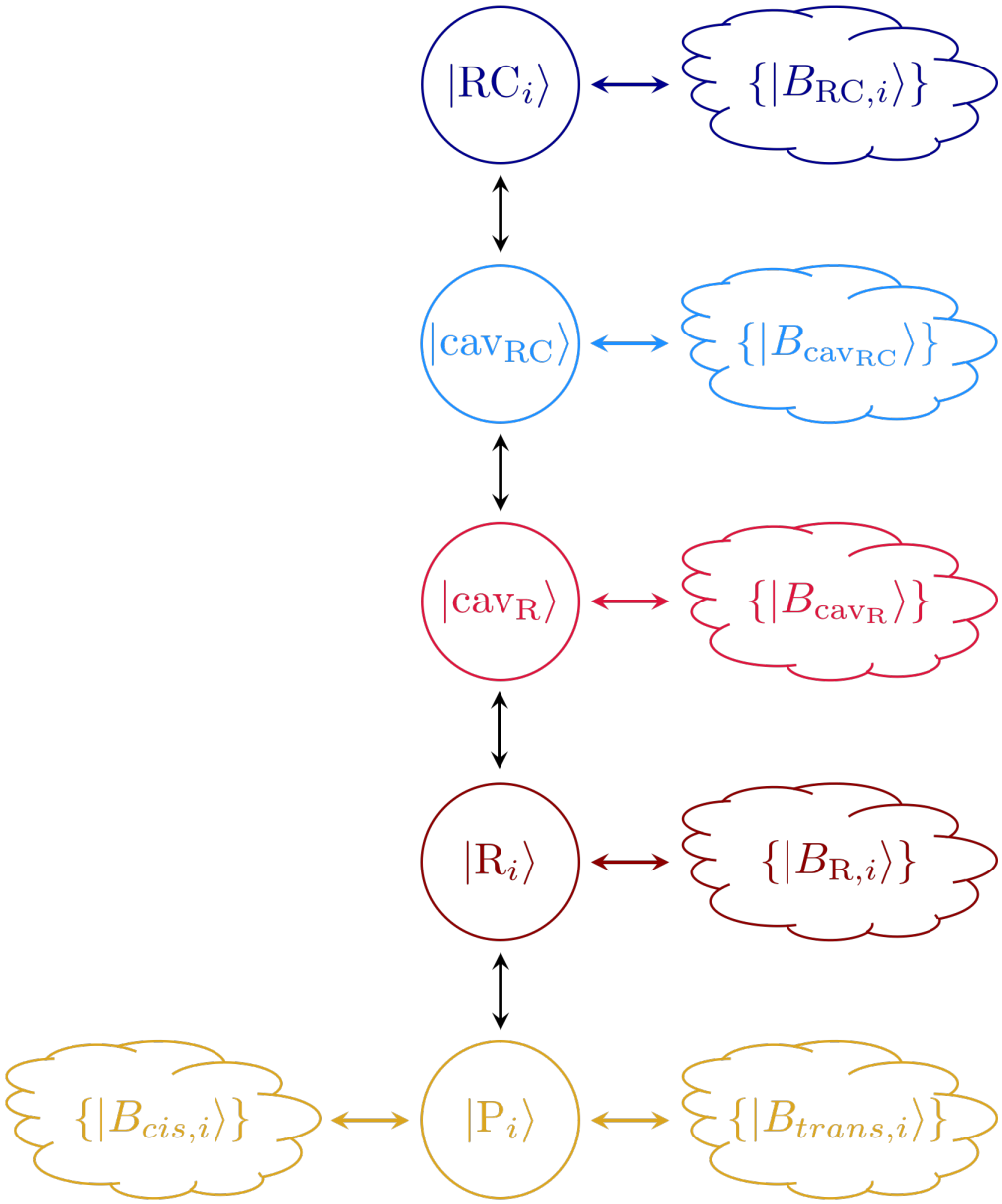

Figure 4.4: Schematic of the system and bath interactions of the R → P fast isomerization channel for the polaritonic device See Eqs. (4.35), (4.41), and those defining the terms therein, for Hamiltonian H. The ith molecule of compound $x = \mathrm{RC}, \mathrm{R}$ has an OH stretch excitation $|x_i\rangle$ (dark blue, dark red circle), which is coupled to a set $|B_x\rangle$ of nonradiative bath states (dark blue, dark red clouds) that contributes to its decay. $|x_i\rangle$ is also coupled to photon $|\mathrm{cav}_x\rangle$ of the cavity containing compound x. $|\mathrm{cav}_x\rangle$ interacts with a set $|B_{\mathrm{cav}_x}\rangle$ of radiative bath states, as well as with the other cavity state. For probe excitation of the polaritonic device, the states in $|B_{\mathrm{cav}_{\mathrm{RC}}}\rangle$ (light blue cloud) contribute to decay—in the form of transmission—of $|\mathrm{cav}_{\mathrm{RC}}\rangle$ (light blue circle), while the states in $|B_{\mathrm{cav}_{\mathrm{R}}}\rangle$ (light red cloud) contribute to decay—in the form of reflection—and excitation of $|\mathrm{cav}_{\mathrm{R}}\rangle$ (light red circle). Finally, $|\mathrm{R}_i\rangle$ is coupled to another state, the torsional overtone $|\mathrm{P}_i\rangle$ (yellow), which can concomitantly decay into either the *cis* or *trans* potential wells of HONO via coupling to $|B_{cis,i}\rangle$ or $|B_{trans,i}\rangle$, respectively.

where $P_x = \sum_{i=1}^{N_x} a_{x,i}/\sqrt{N_x}$ is the linear molecular polarization representing the collective bright molecular states $P_{\mathrm{R}}^{\dagger}|\mathrm{G}\rangle$ and $P_{\mathrm{RC}}^{\dagger}|\mathrm{G}\rangle$, P_x is coupled to cavity polarization $c_x^{\dagger}$, and $P_{\mathrm{RC},3} = \sum_{i=1}^{N_{\mathrm{RC}}} a_{\mathrm{RC},i}^{\dagger} a_{\mathrm{RC},i} a_{\mathrm{RC},i}/\sqrt{N_{\mathrm{RC}}}$ is the third-order polarization for RC that depends on the pump-induced excited-state fraction f_{pump}, a parameter that describes the extent of pumped RC population stored in the corresponding dark-state reservoir. The corresponding input-output relations are

$$c_{\mathrm{RC,out}}(t) = \sqrt{\kappa_{\mathrm{RC}}} c_{\mathrm{RC}}(t), \tag{4.45a}$$

$$c_{\mathrm{R,out}}(t) - c_{\mathrm{R,in}}(t) = \sqrt{\kappa_{\mathrm{R}}} c_{\mathrm{R}}(t), \tag{4.45b}$$

$$P_{z,\mathrm{out}}(t) = \sqrt{\gamma_z} P_z(t), \tag{4.45c}$$

$$P_{\mathrm{P,out},y}(t) = \sqrt{\Gamma_y} P_{\mathrm{P}}(t). \tag{4.45d}$$

where

$$c_{\mathrm{R,in}}(t) = \frac{i}{\sqrt{2\pi}} \int_{-\infty}^{\infty} d\omega B_{\mathrm{cav_R}}(\omega)(t_{\mathrm{in}}) e^{-i\omega(t-t_{\mathrm{in}})} \tag{4.46}$$

is the R cavity input field that excites the R cavity at time t_{in},

$$c_{x,\mathrm{out}}(t) = \frac{i}{\sqrt{2\pi}} \int_{-\infty}^{\infty} d\omega B_{\mathrm{cav}_x}(\omega)(t_{\mathrm{out}}) e^{-i\omega(t-t_{\mathrm{out}})}, \tag{4.47}$$

$$P_{u,\mathrm{out}}(t) = \frac{i}{\sqrt{2\pi}} \int_{-\infty}^{\infty} d\omega \beta_u(\omega)(t_{\mathrm{out}}) e^{-i\omega(t-t_{\mathrm{out}})} \tag{4.48}$$

annihilate output fields produced as energy is dissipated from the polaritonic system by bath modes at time $t_{\mathrm{out}} > t$, and the different β_u are defined as $\beta_u(\omega) = \sum_{i=1}^{N_u} B_{u,i}(\omega)/\sqrt{N_u}$ for $u = \mathrm{R}, \mathrm{RC}$ and $\beta_u(\omega) = \sum_{i=1}^{N_{\mathrm{R}}} |\mathrm{G}\rangle\langle B_{u,i}(\omega)|/\sqrt{N_{\mathrm{R}}}$ for $u = cis, trans$. Notice that for $|\mathrm{P}\rangle$, the Heisenberg-Langevin equations [cf. Eqs. (4.44e) and (4.21)], input-output relations [cf. Eqs. (4.45d) and (4.17)], and the associated notation are identical to those in the bare case (Sec. 4.2.2). In contrast, the Heisenberg-Langevin equation (4.44a) contains the third-order RC polarization $P_{\mathrm{RC},3}$, whose dynamics become relevant when the polaritonic device is pump-excited.

We now treat the dynamics of $P_{\mathrm{RC},3}$, beginning with evaluation of the exact Heisenberg-

Langevin equation for $a^{\dagger}_{\mathrm{RC},i}a_{\mathrm{RC},i}a_{\mathrm{RC},i}$:

$$\frac{d[a^{\dagger}_{\mathrm{RC},i}(t)a_{\mathrm{RC},i}(t)a_{\mathrm{RC},i}(t)]}{dt} = \frac{da^{\dagger}_{\mathrm{RC},i}(t)}{dt}a_{\mathrm{RC},i}(t)a_{\mathrm{RC},i}(t) + a^{\dagger}_{\mathrm{RC},i}(t)\frac{da_{\mathrm{RC},i}(t)}{dt}a_{\mathrm{RC},i}(t) + a^{\dagger}_{\mathrm{RC},i}(t)a_{\mathrm{RC},i}(t)\frac{da_{\mathrm{RC},i}(t)}{dt} \tag{4.49a}$$

$$= A_1 + A_2, \tag{4.49b}$$

where

$$A_1 = -i(\omega_{\mathrm{RC}} - i3\gamma_{\mathrm{RC}}/2 + 2\Delta)[a^{\dagger}_{\mathrm{RC},i}(t)a_{\mathrm{RC},i}(t)]a_{\mathrm{RC},i}(t) - 2ig_{\mathrm{RC}}[a^{\dagger}_{\mathrm{RC},i}(t)a_{\mathrm{RC},i}(t)]c_{\mathrm{RC}}(t), \tag{4.50a}$$

$$A_2 = ig_{\mathrm{RC}}[c^{\dagger}_{\mathrm{RC}}(t)a_{\mathrm{RC},i}(t)]a_{\mathrm{RC},j}(t) - 2i\Delta[a^{\dagger}_{\mathrm{RC},i}(t)a^{\dagger}_{\mathrm{RC},i}(t)a_{\mathrm{RC},i}(t)a_{\mathrm{RC},i}(t)]a_{\mathrm{RC},i}(t). \tag{4.50b}$$

In going from Eq. (4.49a) to Eq. (4.49b) [*i.e.*, the sum of Eqs. (4.50a) and (4.50b)] we have used

$$\frac{da_{\mathrm{RC},i}(t)}{dt} = -i(\omega_{\mathrm{RC}} - i\gamma_{\mathrm{RC}}/2)a_{\mathrm{RC},i}(t) - ig_{\mathrm{RC}}c_{\mathrm{RC}}(t) - 2i\Delta a^{\dagger}_{\mathrm{RC},i}(t)a_{\mathrm{RC},i}(t)a_{\mathrm{RC},i}(t), \tag{4.51}$$

obtainable by inspection of Eq. (4.44a). We now analyze the terms that contribute to the dynamics of the anharmonic-induced polarization. As written above, all terms in Eqs. (4.50a) and (4.50b) are proportional to the product of a quantity in square brackets and a creation operator. In particular, the first (second) term in Eq. (4.50a) is proportional to $[a^{\dagger}_{\mathrm{RC},i}a_{\mathrm{RC},i}]a_{\mathrm{RC},i}$ ($[a^{\dagger}_{\mathrm{RC},i}a_{\mathrm{RC},i}]c_{\mathrm{RC}}$) and interpretable as creation of a population in the first excited RC state followed by an RC (RC cavity) transition. On the other hand, the first (second) term in Eq. (4.50b) is proportional to $[c^{\dagger}_{\mathrm{RC}}a_{\mathrm{RC},i}]a_{\mathrm{RC},i}$ ($[a^{\dagger}_{\mathrm{RC},i}a^{\dagger}_{\mathrm{RC},i}a_{\mathrm{RC},i}a_{\mathrm{RC},i}]a_{\mathrm{RC},i}$) and interpretable as the creation of a RC-cavity coherence (population of the second excited RC state) followed by an RC transition. Because we supposed that the pump pulse only creates singly excited RC population (in the form of dark RC states), we neglect both terms in Eq. (4.50b) [56]. Moreover, we approximate the $a^{\dagger}_{\mathrm{RC},i}a_{\mathrm{RC},i}$ in the rightmost term of Eq. (4.50a) as $f_{\mathrm{pump}} = \sum_{i=1}^{N_{\mathrm{RC}}} a^{\dagger}_{\mathrm{RC},i}a_{\mathrm{RC},i}/N_{\mathrm{RC}}$, the effective fraction of total RC molecules populated via relaxation from polariton to RC dark states during the delay time [56].

With these steps, Eq. (4.49) becomes

$$\frac{dP_{\mathrm{RC},3}(t)}{dt} = -i(\omega_{\mathrm{RC}} + 2\Delta - i3\gamma_{\mathrm{RC}}/2)P_{\mathrm{RC},3}(t) - 2ig_{\mathrm{RC}}f_{\mathrm{pump}}\sqrt{N_{\mathrm{RC}}}c_{\mathrm{RC}}(t). \tag{4.52}$$

We associate absorbance into RC, absorbance into R, and reaction efficiency η with the fraction of the initial energy that is dissipated by the nonradiative bath of $|\mathrm{RC}\rangle$, nonradiative bath of $|\mathrm{R}\rangle$, and the bath inducing relaxation from $|\mathrm{P}\rangle$ into the *trans*-HONO well, respectively. In analogy to using input-output Eqs. (4.16) and (4.17) to obtain Eqs. (4.26) for R absorption and (4.27) for reaction efficiency η_0 in the bare case, we employ polaritonic input-output Eqs. (4.45c) and (4.45d) to write

$$\mathrm{absorbance}_{\mathrm{R}}(f_{\mathrm{pump}},\omega) = \gamma_{\mathrm{R}}|S_{\mathrm{R}}(f_{\mathrm{pump}},\omega)|^2 \tag{4.53}$$

$$\eta(f_{\mathrm{pump}},\omega) = \Gamma_{trans}|S_{\mathrm{P}}(f_{\mathrm{pump}},\omega)|^2. \tag{4.54}$$

The linear response functions S_{R} and S_{P} are defined such that each multiplied by $c_{\mathrm{R,in}}(\omega)$ yields $P_{\mathrm{R}}(\omega)$ and $P_{\mathrm{P}}(\omega)$, respectively. From the Heisenberg-Langevin equations (4.44), it is evident that calculation of Eqs. (4.53)-(4.54) requires knowledge of $V_{\mathrm{R-P}}$. As done in Sec. 4.2.2 for the bare case, we perturbatively treat the IVR coupling and neglect the terms containing $V_{\mathrm{R-P}}$ when evaluating Eqs. (4.53)-(4.54) in computations. In particular, the reaction efficiency can now be written as

$$\eta(f_{\mathrm{pump}},\omega) = \mathrm{absorbance}_{\mathrm{R}}(f_{\mathrm{pump}},\omega)\mathrm{QY}_{\mathrm{R}\to\mathrm{P}}(\omega), \tag{4.55}$$

where

$$\mathrm{QY}_{\mathrm{R}\to\mathrm{P}}(\omega) = \frac{\gamma_{\mathrm{R}\to\mathrm{P}}(\omega)}{\gamma_{\mathrm{R}}} \tag{4.56}$$

is an isomerization quantum yield, and

$$\gamma_{\mathrm{R}\to\mathrm{P}}(\omega) = \frac{V^2_{\mathrm{R}\to\mathrm{P}}\Gamma_{trans}}{(\omega-\omega_{\mathrm{P}})^2 + [(\Gamma_{cis}+\Gamma_{trans})/2]^2} \tag{4.57}$$

is the transition rate from $|\mathrm{R}\rangle$ to $|\mathrm{P}\rangle$. The validity of this perturbative treatment can be shown by noticing that

$$P_{\mathrm{R}}(\omega) = \frac{g_{\mathrm{R}}\sqrt{N_{\mathrm{R}}}[\omega - \omega_{\mathrm{P}} + i(\Gamma_{cis} + \Gamma_{trans})/2]}{(\omega - \omega_{\mathrm{R}} + i\gamma_{\mathrm{nonrad}}/2)[\omega - \omega_{\mathrm{P}} + i(\Gamma_{cis} + \Gamma_{trans})/2] - V_{\mathrm{R-P}}^2} c_{\mathrm{R}}(\omega), \tag{4.58}$$

recognizing that the fraction on the right-hand side is equal to $S_{\mathrm{R},0}(\omega)$ [Eq. (4.24)] up to a constant, and analyzing the roots of the denominator of this fraction as done in the last paragraph of Sec. 4.2.2. For later use, we define

$$\eta_{\mathrm{ON}} = \eta(0.3, \omega_{\mathrm{ON}}), \tag{4.59}$$

$$\eta_{\mathrm{OFF}} = \eta(0, \omega_{\mathrm{ON}}),$$

$$\eta_0 \equiv \eta_0(\omega_{\mathrm{R}}), \tag{4.60}$$

where ω_{ON} (see Fig. 4.5B, pink dashed line) is the frequency that maximizes $\eta(0.3, \omega)$ in the region $\omega \in [\omega_{\mathrm{P}} - 2\ \mathrm{cm}^{-1}, \omega_{\mathrm{R}} - g_{\mathrm{R}}\sqrt{N_{\mathrm{R}}} + 2\ \mathrm{cm}^{-1}]$ containing the lowest polariton lineshape for all coupling strengths explored in this work.

4.4 Results

Before proceeding to analyze the dynamics of the remote-control device, we investigate its spectral features. In the first excitation manifold, the Hamiltonian for the polariton states in the basis of the constituent species is ($\hbar = 1$)

$$H_{\mathrm{system}}^{(\mathrm{no\ pump})} = \begin{pmatrix} \omega_{\mathrm{RC}} & g_{\mathrm{RC}}\sqrt{N_{\mathrm{RC}}} & 0 & 0 \\ g_{\mathrm{RC}}\sqrt{N_{\mathrm{RC}}} & \omega_{\mathrm{cav_{RC}}} & g_{\mathrm{cav}} & 0 \\ 0 & g_{\mathrm{cav}} & \omega_{\mathrm{cav_R}} & g_{\mathrm{R}}\sqrt{N_{\mathrm{R}}} \\ 0 & 0 & g_{\mathrm{R}}\sqrt{N_{\mathrm{R}}} & \omega_{\mathrm{R}} \end{pmatrix}, \tag{4.61}$$

where the entries from left to right (top to bottom) represent $|\mathrm{RC}\rangle$, the cavity hosting RC, the cavity hosting R, and $|\mathrm{R}\rangle$, respectively. For simplicity, we take each cavity mode to be resonant with the hosted OH vibration: $\omega_{\mathrm{cav}_{\mathrm{RC}}} = \omega_{\mathrm{RC}} = 3455\ \mathrm{cm}^{-1}$ (the average frequency of the OH stretch of RC [141, 142]) and $\omega_{\mathrm{cav}_{\mathrm{R}}} = \omega_{\mathrm{R}} = 3402\ \mathrm{cm}^{-1}$ (the frequency of the OH stretch vibration of R [140]). Let the collective light-matter couplings [4] be $g_{\mathrm{RC}}\sqrt{N_{\mathrm{RC}}} = 57\ \mathrm{cm}^{-1}$ and $g_{\mathrm{R}}\sqrt{N_{\mathrm{R}}} = 11\ \mathrm{cm}^{-1}$ for numbers N_{RC} and N_{R} of RC and R molecules, respectively, per mode volume V of each cavity; we have incorporated V into the g values for notational convenience. These couplings correspond to $\sim 1.7\%$ and $\sim 0.3\%$ of the transition energy of each interacting species, comparable to experimental values (0.2-2.2%) for mid-infrared vibrational polaritons [19, 108, 157]. As will become clear, the particular polariton mixing fractions and energies endowed by the chosen light-matter interaction strengths are essential for realizing the proposed remote control. With no cavity-cavity coupling ($g_{\mathrm{cav}} = 0$; Fig. 4.2A, blue and red panels), one pair of polaritons has character of only RC and its cavity (blue), and the other pair only R and its cavity (red). Upon introduction of intercavity coupling $g_{\mathrm{cav}} = 27\ \mathrm{cm}^{-1}$ (Fig. 4.2A, purple panel)—corresponding to $\sim 0.8\%$ of the cavity photon energies [144]—the three lowest polaritons from the $g_{\mathrm{cav}} = 0$ case hybridize into three states delocalized across RC, R, and their host cavities. This mixing of states from both compounds enables pumping of RC to remotely tune the energy of polaritons with R character and thereby the isomerization efficiency. In contrast, the highest polariton for $g_{\mathrm{cav}} = 0$ is spectrally isolated and does not change much in energy or character when intercavity coupling is introduced (Fig. 4.2A, cf. blue and purple panels).

Thus, population of the dark RC states is achievable via excitation of this highest polariton with a pump pulse (Fig. 4.2B, left panel) impinging on the RC cavity (Fig. 4.1B, top panel). Because g_{RC} and $\omega_{\mathrm{RC}} - \omega_{\mathrm{R}}$ are sufficiently larger than g_{R}, this highest level is essentially half RC and half RC cavity in character. Furthermore, by conservation of the number of energy levels, there are $N_{\mathrm{RC}} - 1$ RC dark reservoir states, significantly larger than 4, the number of polaritons. Energy relaxation from the highest polariton is then most likely to occur into the relatively dense RC dark manifold [4, 5, 53]. For pumping a polariton that is half molecule and half cavity in character, a

previous study showed that changing the field intensity of the pump pulse can tune f_{pump} from zero to several tenths [108].

The resulting pump-dependent effective Hamiltonian is [56]

$$H_{\text{system}}^{(\text{pump})} = \begin{pmatrix} \omega_{\text{RC}} & 0 & g_{\text{RC}}\sqrt{(1-2f_{\text{pump}})N_{\text{RC}}} & 0 & 0 \\ 0 & \omega_{\text{RC}}+2\Delta & g_{\text{RC}}\sqrt{2f_{\text{pump}}N_{\text{RC}}} & 0 & 0 \\ g_{\text{RC}}\sqrt{(1-2f_{\text{pump}})N_{\text{RC}}} & g_{\text{RC}}\sqrt{2f_{\text{pump}}N_{\text{RC}}} & \omega_{\text{cav}_{\text{RC}}} & g_{\text{cav}} & 0 \\ 0 & 0 & g_{\text{cav}} & \omega_{\text{cav}_{\text{R}}} & g_{\text{R}}\sqrt{N_{\text{R}}} \\ 0 & 0 & 0 & g_{\text{R}}\sqrt{N_{\text{R}}} & \omega_{\text{R}} \end{pmatrix}. \tag{4.62}$$

Though not utilized in calculations of absorption or reaction efficiency, this matrix provides physical intuition in that it characterizes the polaritonic transitions in the absence of lineshape broadening (our calculations do account for dissipative effects): $|\text{RC}\rangle$, the $|\text{RC}\rangle$ $1 \rightarrow 2$ transition, the cavity with RC, the cavity with R, and $|\text{R}\rangle$, from left to right (top to bottom). $\Delta = -89$ cm^{-1} is the mechanical anharmonicity of the OH stretch of RC [141, 142]. It is evident from Eq. (4.62) that as the parameter f_{pump} representing the degree of population of RC dark reservoir states is increased, the coupling between RC and the cavity is reduced, formalizing the qualitative arguments provided above. Taking the perspective that the hybrid states for $g_{\text{cav}} \neq 0$ are formed by mixing the polariton states of the noninteracting cavities (Fig. 4.2A), pumping blueshifts the lower RC polariton away from the lower R polariton and reduces their mixing when $g_{\text{cav}} \neq 0$ (Fig. 4.2B). Indeed, the lowest polariton for $g_{\text{cav}} \neq 0$ becomes predominantly R and its corresponding cavity upon pumping (Fig. 4.2B, right).

The ability to shift its energy and increase its R character with pumping of RC renders this lowest polariton state promising for enhancing with greater pump strengths the energy that eventually dissipates into R molecules, and thus the isomerization triggered when a probe pulse impinges on the R cavity (Fig. 4.2, cf. A and B). Spectra (Fig. 4.5A) computed from input-output theory reveal that probe absorption of the lowest polariton into R, *i.e.*, due to R component, is blueshifted and stronger with more pumping. This trend is in agreement with the pump-induced

rise of its R and R-cavity mixing fractions (Fig. 4.2B, cf. left and right panels). Probe absorption into R scales not only with component of R but also with that of R cavity because the probe laser impinges on this cavity. As a consistency check, we note that the energies and intensities of the other absorption peaks (Fig. 4.5A) also agree with the energies and R/R-cavity characters (Fig. 4.2), respectively, of the higher polariton states. In particular, (for each f_{pump} explored in Fig. 4.5A) the lack of a detectable absorption peak between 3500 and 3520 cm^{-1} is consistent with < 5% character of the highest polariton being either R or R cavity (Fig. 4.2A).

Now we show that the efficiency η of the probe-initiated reaction is highly pump-tunable (Fig. 4.5B). Also calculated from input-output theory, η [Eq. (4.55)] is the product of the polariton probe absorbance into R and the quantum yield of isomerization, *i.e.*, efficiency of decay into $|\text{P}\rangle$, from the excited polariton. For our isomerization model, which is developed from previous experimental and theoretical studies (see Sec. 4.2), the quantum yield scales with the energy resonance between the excited polariton and $|\text{P}\rangle$ [Eqs. (4.56) and (4.57)]. Given that the peak absorption of the lowest polariton moves away in energy from $|\text{P}\rangle$ ($\omega_{\text{P}} = 3362\ \text{cm}^{-1}$ [140]; see Sec. 4.2.1) with pumping (Fig. 4.5A), it is somewhat counterintuitive that the corresponding peak value of η increases. This behavior arises because for all values of f_{pump}, spectral overlap between any polariton and $|\text{P}\rangle$ is small (Fig. 4.5A). Thus, the peak η is controlled by the position and intensity of the lowest-polariton absorption. It therefore makes sense that the maximum η blueshifts and rises with higher pumping (Fig. 4.5B). Relative to the experimental bare reaction efficiency η_0 [Eq. (4.60)], the peak η values are an order of magnitude greater (Fig. 4.5B), even for $f_{\text{pump}} = 0$. The reason for such high values is that the lowest polariton is (Fig. 4.5A) a more efficient absorber (into R) and nearer in resonance to $|\text{P}\rangle$ than the bare $|\text{R}\rangle$ (peak absorbance = 0.07 [140]). To realize remote tuning of reactivity, we focus on the probe frequency (Fig. 4.5B, pink dashed line) that corresponds to the peak η for the highest explored fraction $f_{\text{pump}} = 0.3$ of pump-excited RC molecules. Notably, pumping enhances the reaction efficiency η_{ON} for this choice of ω_{probe} by an order of magnitude compared to the efficiency η_{OFF} with no pumping (Fig. 4.5C). As an aside, while the model in this work only includes polariton relaxation to $|\text{P}\rangle$ and the (molecular

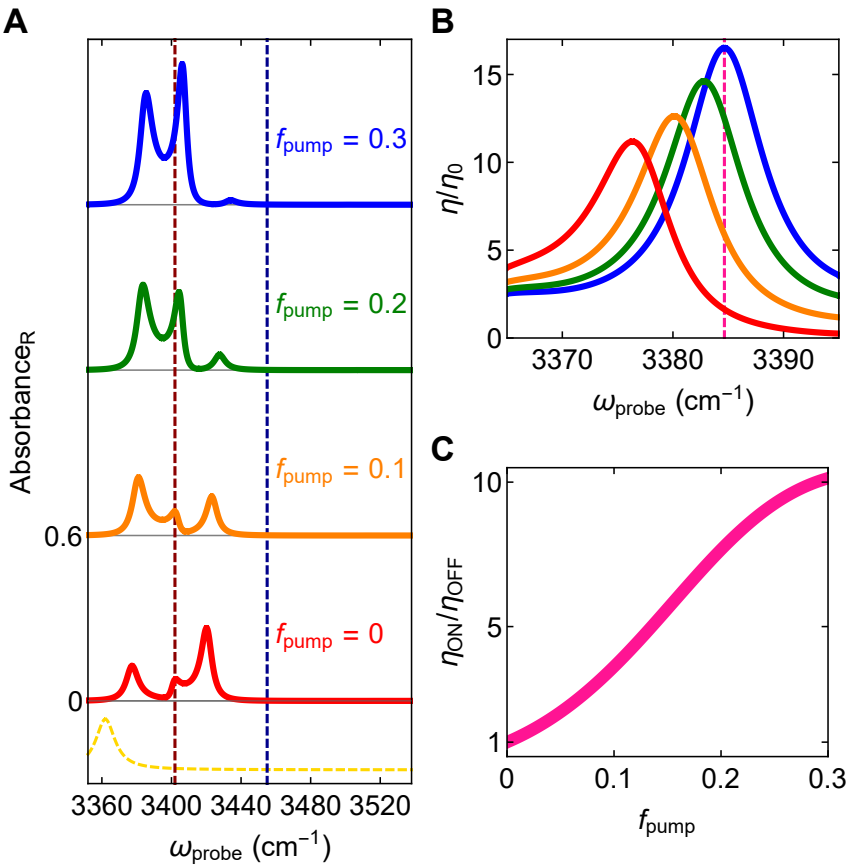

Figure 4.5: Pumping of the RC enhances probe-initiated reaction with high tunability (A) Probe energy absorption into reactant (R), *i.e.*, due to R component, given various fractions f_{pump} of pump-excited RC molecules. The dashed lines indicate the energies of the bare vibrations (*i.e.*, those without strong light-matter coupling) of RC (dark blue) and R (dark red), as well as the arbitrarily scaled energy spectrum of the non-absorbing quantum state $|\text{P}\rangle$ (yellow) that first receives population from the strongly coupled R vibration via IVR and then relaxes into product (P) states. (B) Relative reaction efficiency η/η_0 (*i.e.*, compared to the bare efficiency) as a function of the probe pulse energy. The color scheme for the solid lines follows that of (A). (C) Enhancement $\eta_{\text{ON}}/\eta_{\text{OFF}}$ of reaction efficiency (*i.e.*, compared to $f_{\text{pump}} = 0$, probe excitation only) as a function of f_{pump} at the probe energy $\omega_{\text{probe}} \approx 3385$ cm^{-1} associated with the maximum η for $f_{\text{pump}} = 0.3$ and indicated by the pink dashed line in (B).

and photonic) vacuum ground state, relaxation from the lowest polariton to dark (R or RC) or other polariton states is energetically uphill. Therefore, these uphill processes can be neglected if their respective transition energies are sufficiently larger than k_BT (k_B is the Boltzmann constant and T is the temperature).

So far, we have considered modifying a reaction by optical pumping of RC. We now briefly show further manipulation of the R $\rightarrow$ P isomerization efficiency via tuning of intercavity and

cavity-RC couplings, both adjustable without any direct alteration of R. Thus, we also show remote control of the reaction in the linear probe-excitation regime, *i.e.*, without pumping. For each g_{cav} or $g_{\mathrm{RC}}\sqrt{N_{\mathrm{RC}}}$, the probe frequency is fixed at that which affords peak reaction efficiency when $f_{\mathrm{pump}} = 0.3$ (Fig. 4.5B, pink dashed line). When the intercavity coupling is manipulated (Fig. 4.6A), *e.g.*, by varying the thickness of the middle mirror [158], the maximum boost in reaction efficiency with pumping (η_{ON}) over that without (η_{OFF}) reaches several 10-fold as g_{cav} goes from 0 to 30 cm^{-1}. Such an increase occurs because delocalization of the lowest polariton across RC, R, and their host cavities—and therefore potential for reactive modification—increases with intercavity coupling. Changing g_{cav} raises too the absolute η_{ON} (compared to bare efficiency η_0, Fig. 4.6B) by up to an order of magnitude for fixed f_{pump}. Intriguingly, as g_{cav} vanishes, the absolute efficiency without pumping climbs to an order of magnitude higher than in the bare case. This rise can occur because only for zero intercavity coupling does the (probe-excited) lowest polariton remain unchanged with pumping, and thus the fixed probe frequency corresponds to the maximum reaction efficiency in the linear probe-excitation regime. That the peak efficiency can exceed η_0 by an order of magnitude, even when $f_{\mathrm{pump}} = 0$, has been explained above. Alternatively, $g_{\mathrm{RC}}\sqrt{N_{\mathrm{RC}}}$ can be tuned (Fig. 4.6C), *e.g.*, by increasing the concentration of RC, to yield similar favorable pump-enhancements (Fig. 4.6, cf. A and C) and absolute efficiencies (Fig. 4.6, cf. B and D) for fixed pumping. Indeed, cavity-RC coupling can also regulate the efficiency of the single-pulse photoisomerization (Fig. 4.6, C and D, $f_{\mathrm{pump}} = 0$). Resemblance between the effects of varying g_{cav} and $g_{\mathrm{RC}}\sqrt{N_{\mathrm{RC}}}$ is understandable, given that pumping also has no effect on the lowest polariton as the latter coupling strength approaches zero. Notice though that $g_{\mathrm{RC}}\sqrt{N_{\mathrm{RC}}}$ must exceed ~ 40 cm^{-1} to appreciably influence $\eta_{\mathrm{ON}}/\eta_{\mathrm{OFF}}$ (Fig. 4.6C) and $\eta_{\mathrm{ON}}/\eta_0$ (Fig. 4.6D). The origin of this requirement is the same as that of the pump-induced modulation (with fixed cavity-RC coupling): adjusting $g_{\mathrm{RC}}\sqrt{N_{\mathrm{RC}}}$ changes the mixing between the polaritons of the noninteracting cavities; control of reactivity is realizable when the lowest polariton of the entire device is sufficiently delocalized across the photonic and vibrational species associated with both RC and R. Although pumping of RC provides a very versatile tuning mechanism, in the absence of ultrafast

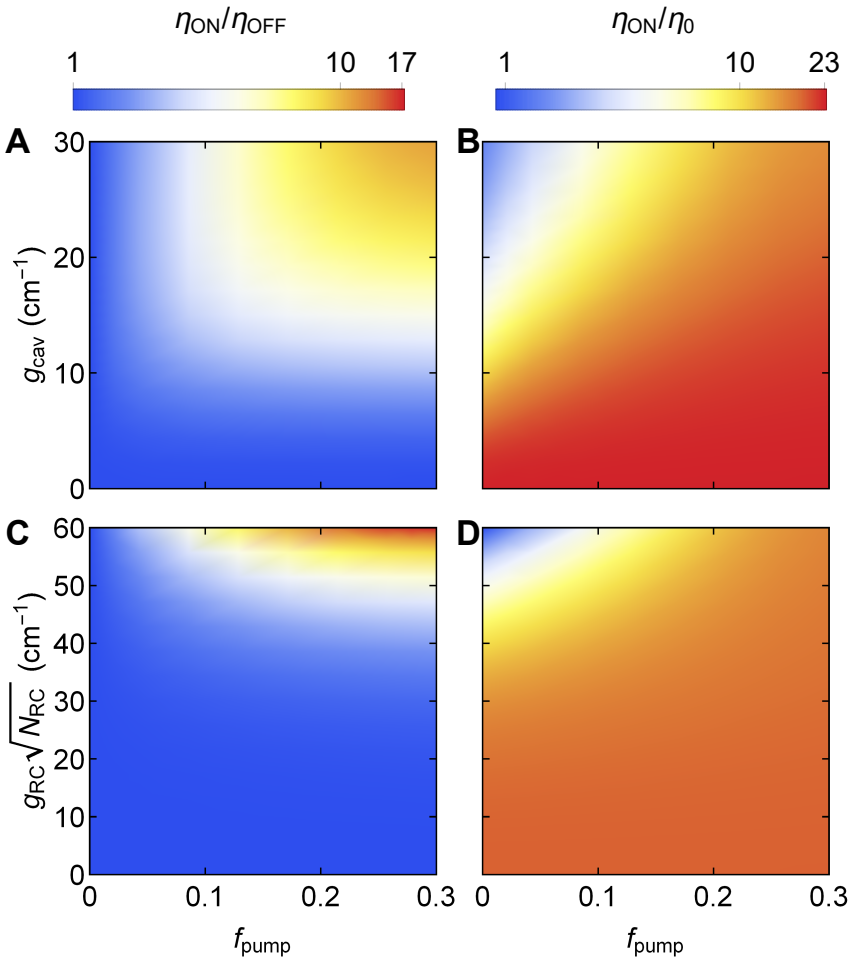

Figure 4.6: Pump-induced enhancement of probe-initiated reaction can be remotely tuned by varying properties of the cavities and RC Reaction efficiencies η_{ON} relative to those without pumping (η_{OFF}) or in the bare case (*i.e.*, without strong light-matter coupling, η_0) as a function of either intercavity coupling strength g_{cav} (A and B) or collective cavity-RC coupling $g_{RC}\sqrt{N_{RC}}$ (C and D) and fraction f_{pump} of pump-excited RC molecules. The probe frequency for each g_{cav} (A and B) or g_{RC} (C and D) is fixed at that leading to maximum reaction efficiency for $f_{pump} = 0.3$ (see Fig. 4.5B, pink dashed line). All other parameters are from the simulations shown in Fig. 4.5. In (B) and (D), notice the ability to control reaction efficiency even in the linear optical regime ($f_{pump} = 0$, probe excitation only).

equipment and so long as increasing the thickness of the intercavity mirror or the concentration of RC is feasible, the linear optical experiments suggested provide an interesting alternative to our

original proposal.

4.5 Conclusions

We have theoretically demonstrated ultrafast remote control of the isomerization of *cis*-HONO to *trans*-HONO using an infrared polaritonic device. The proposed setup consists of two strongly interacting microcavities containing separate ensembles of the RC and reactant. The polaritons of the hybrid system are delocalized across both molecular species and their host cavities. Acting on the RC cavity, a pump pulse excites the highest polariton, followed by picosecond-timescale relaxation to the dark-state reservoir of RC. Because of anharmonicity, the $1 \rightarrow 2$ vibrational transition of RC is significantly detuned from the RC cavity mode, hence inducing an effective weakening of the collective coupling (and hybridization) between RC and the remaining components of the device. The lowest polariton concomitantly blueshifts and acquires less character of RC and its respective cavity and more of reactant and its respective cavity. As a result, probe-pulse excitation acting on the reactant cavity yields enhanced efficiency of IVR into the product state compared to the no-pumping case. By raising the pump intensity, the reaction efficiency can be boosted by an order of magnitude. Remarkably, this tunability requires no spatial contact whatsoever between RC and reactant, challenging the paradigm of traditional chemical catalysis that the catalyst must bind its reactant. We emphasize that additional manipulation of reactivity can be achieved by varying the intercavity or RC-cavity coupling strengths, *e.g.*, by changing the distance between cavities or the concentration of RC, respectively. These adjustments extend remote control to the linear optical regime.

Although our results involve tuning a vibrational excited state that couples into the reaction coordinate, they can be generalized to electronic excited states, which feature a variety of photochemical reactions, some of which have been explored already in the polaritonic regime [3, 4, 7, 9]. Success of the proposed strategies relies essentially on (1) the ability to couple RC and R to interacting cavity modes and (2) a difference in coupling between the fundamental and anharmonic

transition of the former compound. Indeed, inorganic [159] and organic [160, 161] excitons are satisfactory platforms for realization of the polaritonic device and the pump-dependent modulation of light-matter coupling studied here. Furthermore, remote control of reactivity can be extended to include plasmonic nanostructures, which have been well-studied in the strong coupling regime [48, 162, 163] and also offer promising routes for ultrafast manipulation of nanoparticle-reactant [164], plasmon-plasmon [165], and photon-plasmon interactions [166]. In light of recent experimental reports in the literature where chemical reactions have been controlled with vibrational strong coupling [20, 21, 24], we also emphasize the following: our proposed scheme involves an infrared-photoinduced process, where the strongly coupled reactant mode (OH stretch) is different from the reaction coordinate (torsion). In contrast, the reported experiments are carried out under thermally activated conditions, and strong coupling is applied to the stretching mode of a reacting bond. It is currently unclear whether a thermally-activated analog of the proposal is feasible; we are currently exploring such possibility.

Beyond the application described here, the polaritonic device can be employed as a diagnostic tool for reaction mechanisms. For example, by strongly coupling different reactant excited states one at a time to the reactant cavity and comparing how their respective reaction efficiencies change with the intensity of the pump pulse, the relative importance of each state in the reaction and its position in a proposed pathway may be determined. Such functionality would be particularly attractive in IVR or IVR-driven reactions, such as the HONO isomerization studied here [167], where several possibly interacting excited states may participate in the dynamics. More broadly, the proposed remote control represents a new class of molecular quantum technologies featuring manipulation of chemical processes through coherent interactions [168]. In particular, this technique to control reactions without direct catalyst-reactant interaction paves way for novel and possibly greener approaches to catalytic and separations chemistry. One interesting prospect is the prevention of byproduct formation by spatially separating all reagents and coupling only their respective states necessary for the reaction by means of, for instance, optical cavities. Notably, the inherent separation of reagents also reduces chemical and energy waste generated in purification.

Chapter 4, in full, is adapted from the material as it appears in "Remote Control of Chemistry in Optical Cavities," M. Du, R. F. Ribeiro and J. Yuen-Zhou, *Chem* **5**, 1167 (2019). The dissertation author was the primary investigator and author of this paper.

Chapter 5

Remote energy transfer using electronic strong coupling

5.1 Introduction

Enhancement of excitation energy transfer (EET) remains an exciting subfield of the chemical sciences. Although Förster resonance energy transfer [169] (FRET) is one of the most extensively studied and well known forms of EET, its efficiency range is only at 1-10 nm [170]. As such, exploration of EET schemes beyond that of a traditional pair of donor and acceptor molecules has been a highly active area of research. For instance, the theory of multichromophoric FRET [171] has been applied to demonstrate the role of coherent exciton delocalization in photosynthetic light harvesting [172–176]. This coherence, which is due to excitonic coupling between molecular emitters, has also been argued to increase EET in mesoscopic multichromophoric assemblies [177], with recent studies even reporting micron-sized transfer ranges in H-aggregates [178, 179]. Along similar lines, a well-studied process is plasmon-coupled resonance energy transfer [180], where molecules which are separated several tens to hundreds of nanometers apart can efficiently transfer energy between themselves due to the enhanced electromagnetic fields provided by the

neighboring nanoparticles [181, 182]. Transfer between molecules across even longer distances can be mediated by the in-plane propagation of surface plasmons (SPs), with micron ranges reported in the literature [183, 184] (see Ref. [185] for an example of micron-range EET via other types of electromagnetic modes). Notably, the plasmonic effects in these last examples occur in the so-called weak-coupling regime, where the frequency of energy exchange between excitons and plasmons is much slower than their respective decays.

An intriguing advancement in polariton-assisted remote energy transfer (PARET) has recently been reported by the Ebbesen group for cyanine dye J-aggregates strongly coupled to a microcavity mode [90]. For spatially separated slabs of donor and acceptor dyes placed between two mirrors, it was found that increasing the interslab spacing from 10 to 75 nm led to no change in the relaxation rate between the hybrid light-matter states or *polaritons*, thus revealing a remarkable distance independence of the process. Importantly, such PARET phenomenon was already noted in an earlier work by the Lidzey group [89] with a different cyanine-dye system, although the interslab spacing was not systematically varied there; similar work was also previously reported for hybridization of Frenkel and Wannier-Mott excitons in an optical microcavity [186]. Motivated by these experiments, we hereby present a quantum-mechanical theory for polariton-assisted energy transfer which aims to characterize the various types of PARET afforded by these hybrid light-matter systems. To be concrete, we do so within a model where the "photonic modes" are SPs in a metal film and consider spatially separated slabs of donors and acceptor dyes which electrostatically couple to one another as well as to the SPs. We present a comprehensive formalism which encompasses the cases where either one or both types of chromophores are strongly coupled to the SPs. We apply our theory to a model system similar to those reported by the Ebbesen and Lidzey groups. Our work complements recent studies proposing schemes to enhance one-dimensional exciton conductance [68, 69]. In those studies, the delocalization afforded by strong coupling (SC) is exploited to overcome static disorder within the molecular aggregate. Here, the emphasis is not on disorder (surmountable also by polaritonic topological protection [187]), but rather on PARET between two different types of chromophores, where energy harvested by one chromophore can

be collected in another. This focus on long-range capabilities, as well as in-depth analyses of the rate contributions for the SC-induced states, provide fresh perspectives on PARET. In particular, we offer fascinating predictions for the experimentally unexplored scenario of "photonic modes" strongly coupled to one of donors or acceptors (the latter case was first theoretically investigated for the chromophores in a microcavity [188]).

As a preview, we highlight the structure and the main conclusions of this work (the latter are summarized in Table 5.1). We begin by introducing the general Hamiltonian for spatially separated slabs of donors and acceptor chromophores in Sec. 5.2. EET rates for a single or both types of chromophores strongly coupled to SPs are presented in Secs. 5.2.1 and 5.2.2, respectively. In the former case, the rates are "FRET-like" [169] and shown to be dependent on spectral overlap (of absorption and emission lineshapes) [189, 190]. For SC of donors, EET can be tuned for enhancement or suppression. This result is in stark contrast with that of acceptors-SPs SC where, surprisingly, EET to acceptor polariton states vanishes for large-enough samples. For the case when both chromophores strongly interact with SPs, transfer is instead mediated by vibrational relaxation in analogy [189, 190] with the theories of Davydov [191, 192] and Redfield [193]. Nevertheless, PARET is still achieved. In Sec. 5.3, we apply the formalism to study a model system resembling cyanine dye J-aggregates. Our numerical simulations demonstrate that applying SC exclusively to donors enables PARET up to 1 micron. We also show that sufficiently intense SC of acceptors induces a "carnival effect" that reverses the role of the donor and acceptor. Lastly, when both chromophores are strongly coupled to SPs, we obtain sizable PARET rates at chromophoric separations over hundreds of nanometers which are in good agreement with experiments.

5.2 Theory

We begin by describing the polaritonic (plexcitonic) setup that we theoretically investigate. Let the chromophore slabs lie above ($z > 0$) and parallel to the metal film ($z < 0$) that sustains

Table 5.1: Comparison of different cases of PARET arising from SC of donors and/or acceptors.

SC of	Features
Donors only	• PARET from donor polariton states; dominated by PRET contribution • Rate of EET from donor dark states $\approx$ bare (*i.e.*, no SPs) FRET rate. • "Förster regime" of PARET
Acceptors only	• Low EET to acceptor polariton states due to their low density of states (compared to dark states) and delocalized character • Rate of EET to acceptor dark states $\approx$ bare FRET rate • "Carnival effect": acceptor and donor reverse roles • "Förster regime" of PARET
Donors and Acceptors	• Polariton states are delocalized across donors *and* acceptors • Rate of PARET from polariton to dark states $\gg$ rate of PARET from dark/polariton to polariton states due to relative density of final states; dark-state manifolds are dense and act as traps • PARET mediated by vibrational relaxation • "Davydov/Redfield regime" of PARET

SP modes (example schematic diagrams are given in Figs. 5.1a, 5.2a, 5.4a, and 5.5a). We assume the metal film and the slabs are extended along the xy (longitudinal) plane. The slabs of $C = D,A$ (donor, acceptor) chromophores consist of $N_{xy,C}$, $N_{z,C}$, and $N_C = N_{xy,C}N_{z,C}$ molecules in the xy-plane, z-direction, and total, respectively. An effective Hamiltonian for this setup can be constructed as,

$$H = H_D + H_A + H_P + H_{DA} + H_{DP} + H_{AP}. \tag{5.1}$$

The term $H_C = H_C^{(sys)} + H_C^{(B)} + H_C^{(sys-B)}$ is the Hamiltonian for the slab with the C chromophores, where

$$H_C^{(sys)} = \hbar\omega_C \sum_{i,j} |C_{ij}\rangle\langle C_{ij}|, \tag{5.2a}$$

$$H_C^{(B)} = \sum_{i,j}\sum_{q} \hbar\omega_{q,C} b^\dagger_{q,C_{ij}} b_{q,C_{ij}}, \tag{5.2b}$$

$$H_C^{(sys-B)} = \sum_{i,j} |C_{ij}\rangle\langle C_{ij}| \sum_{q} \lambda_{q,C}\hbar\omega_{q,C}(b^\dagger_{q,C_{ij}} + \text{h.c.}), \tag{5.2c}$$

represent the system (excitonic), bath (phononic), and system-bath-coupling contributions, respectively. The label C_{ij} refers to a C exciton located at the (i,j)-th molecule of the corresponding slab [(i,j) indexes an (xy,z) coordinate]. We take every C_{ij} exciton to have energy $\hbar\omega_C$ and neglect inter-site coupling since the latter provides an insignificant dispersion to polaritons when compared to the SP dispersion. Specifically, within the wavevector range of interest, inter-site coupling only induces a constant energy shift (which we assume to be included in ω_C) to the exciton subsystem. Thus, the exciton dispersion is only relevant at much shorter wavelengths. $b^\dagger_{q,C_{ij}}(b_{q,C_{ij}})$ labels the creation (annihilation) of a phonon of energy $\hbar\omega_{q,C}$ at the q-th vibrational mode of the (i,j)-th molecule in the C slab. Given the molecular character of the problem, vibronic coupling is assumed to be local [194] (in contrast to that for relatively ordered materials such as crystals [195]): exciton C_{ij} couples linearly to $b^\dagger_{q,C_{ij}}$ and $b_{q,C_{ij}}$ but not to modes in other molecules [196]; these couplings are characterized by Huang-Rhys factors $\lambda^2_{q,C}$ [197]. The SP Hamiltonian

$H_P = H_P^{(sys)} + H_P^{(B)} + H_P^{(sys-B)}$ has similar form [198, 199]:

$$H_P^{(sys)} = \sum_{\vec{k}} \hbar\omega_{\vec{k}} a_{\vec{k}}^\dagger a_{\vec{k}}, \tag{5.3a}$$

$$H_P^{(B)} = \sum_{q} \hbar\omega_{q,P} b_{q,P}^\dagger b_{q,P}, \tag{5.3b}$$

$$H_P^{(sys-B)} = \sum_{\vec{k}} \sum_{q} g_{q,\vec{k}} (b_{q,P}^\dagger a_{\vec{k}} + \text{h.c.}), \tag{5.3c}$$

where $a_{\vec{k}}^\dagger (a_{\vec{k}})$ labels the creation (annihilation) of an SP of energy $\hbar\omega_{\vec{k}}$ and in-plane wavevector $\vec{k}$. Bath modes indexed by q, P with corresponding operator $b_{q,P}^\dagger$ ($b_{q,P}$) and energy $\hbar\omega_{q,P}$ are coupled to each SP mode $\vec{k}$ with strength $g_{q,\vec{k}}$. Specifically, these SP interactions occur with either electromagnetic or phonon modes and represent radiative and Ohmic losses, respectively [199]. The remaining rightmost terms in Eq. (5.1) represent the dipole-dipole interactions amongst donors, acceptors, and SP modes. The H_{DA} term is given by the electrostatic (near-field) dipole-dipole interactions between donors and acceptors,

$$H_{DA} = \sum_{i,j} \sum_{l,m} \frac{\mu_D \mu_A \kappa_{ijlm}}{r_{ijlm}^3} (|A_{lm}\rangle\langle D_{ij}| + \text{h.c.}), \tag{5.4}$$

where $\mu_C = |\vec{\mu}_{C_{ij}}|$ for transition dipole moment (TDM) $\vec{\mu}_{C_{ij}}$ corresponding to C_{ij}, r_{ijlm} is the distance between D_{ij} and A_{lm}, and $\kappa_{ijlm} = \hat{\mu}_{D_{ij}} \cdot \hat{\mu}_{A_{lm}} - 3(\hat{\mu}_{D_{ij}} \cdot \hat{r}_{ijlm})(\hat{\mu}_{A_{lm}} \cdot \hat{r}_{ijlm})$ is the orientational dependence of the interaction (we denote $\hat{v}$ as the unit vector corresponding to $\vec{v}$). We have ignored the corrections to κ_{ijlm} due to reflected waves from the metal—despite their prominent effects in phenomena such as photoluminescence [200]—since they are numerically involved and do not significantly change the order of magnitude of the bare dipole-dipole interaction;[201] furthermore their expected effects in H_{DA} will be overwhelmed by H_{CP}, as we shall explain in Secs. 5.2.1 and 5.3. For simplicity, we take the permittivity on top of the metal to be a real-valued positive dielectric constant ε_d. The light-matter interaction for species C in the rotating-wave approximation

[202] is also dipolar in nature and is described by [203]

$$H_{CP} = \sum_{i,j}\sum_{\vec{k}} \mu_C \kappa_{\vec{k}C_{ij}} \sqrt{\frac{\hbar\omega_{\vec{k}}}{2\varepsilon_0 S L_{\vec{k}}}} e^{-a_{d\vec{k}} z_{j,C}} e^{i\vec{k}\cdot\vec{R}_{i,C}} |C_{ij}\rangle\langle G| a_{\vec{k}} + \text{h.c.} \tag{5.5}$$

where $(\vec{R}_{i,C}, z_{j,C})$ are the position coordinates of C_{ij} and $|G\rangle$ is the electronic ground state (*i.e.*, with no excitons). Just like in H_{DA}, the interaction between an SP mode and a chromophore (indexed by $\vec{k}$ and C_{ij}, respectively) has an orientation-dependent parameter $\kappa_{\vec{k}C_{ij}} = -\hat{\mu}_{C_{ij}} \cdot (\hat{k} + i\frac{k}{a_{d\vec{k}}}\hat{z})$, where $a_{d\vec{k}} = \sqrt{|\vec{k}|^2 - \varepsilon_d(\omega_{\vec{k}}/c)^2}$ is the real-valued evanescent SP decay constant for the region above the metal. The light-matter coupling also includes the quantization length $L_{\vec{k}}$ [204] and area S of the SP.

The general Hamiltonian in Eq. (5.1) describes a complex many-body problem consisting of excitons, SPs, and vibrations, all coupled with each other. To obtain physical insight on the opportunities afforded by this physical setup, we consider in the next sections two limit cases where either one or both types of chromophores are strongly coupled to the SP. The study of these two situations already provides considerable perspective on the wealth of novel EET phenomena hosted by this polaritonic system.

5.2.1 Case *i*: strong coupling of only one chromophore

We consider the case where one of the chromophores C (D or A) is strongly coupled to an SP but the other, C', is not. This can happen when the concentration or thickness of the C slab is sufficiently high and that of the C' slab low. Under these circumstances, we write Eq. (5.1) as $H = H_0^{(i)} + V^{(i)}$, where we define the zeroth-order Hamiltonian as $H_0^{(i)} = H_{sys}^{(i)} + H_B + H_{sys-B}$. The system, bath, and their coupling are respectively characterized by $H_{sys}^{(i)} = H_D^{(sys)} + H_A^{(sys)} + H_P^{(sys)} + H_{CP}$, $H_B = H_D^{(B)} + H_A^{(B)} + H_P^{(B)}$, and $H_{sys-B} = H_D^{(sys-B)} + H_A^{(sys-B)} + H_P^{(sys-B)}$. The perturbation describing the weak interaction between chromophore C' and the SC species is $V^{(i)} = H_{DA} + H_{C'P}$, *i.e.*, the electrostatic interaction as in Förster [169] theory [189, 190]. To diagonalize $H_{sys}^{(i)}$, we introduce a collective exciton basis comprised of bright C states with in-plane momenta matching

those of the SP modes and ignore the very off-resonant SP-exciton couplings beyond the first Brillouin zone (FBZ) of the molecular system [203, 205]: $H_{sys}^{(i)} = H_{C'} + \sum_{\vec{k}\in\text{FBZ}} H_{bright,C}^{(\vec{k})} + H_{dark,C} + \sum_{\vec{k}\notin\text{FBZ}} \hbar\omega_{\vec{k}} a_{\vec{k}}^\dagger a_{\vec{k}}$, where

$$H_{bright,C}^{(\vec{k})} = \hbar\omega_C |C_{\vec{k}}\rangle\langle C_{\vec{k}}| + \hbar\omega_{\vec{k}} a_{\vec{k}}^\dagger a_{\vec{k}} + g_C(\vec{k})(|C_{\vec{k}}\rangle\langle G| a_{\vec{k}} + \text{h.c.}), \tag{5.6a}$$

$$H_{dark,C} = H_C^{(sys)} - \sum_{\vec{k}\in\text{FBZ}} \hbar\omega_C |C_{\vec{k}}\rangle\langle C_{\vec{k}}|. \tag{5.6b}$$

For each $\vec{k}$-mode in the FBZ, there is only one "bright" collective exciton state $|C_{\vec{k}}\rangle = \frac{1}{g_C(\vec{k})}\sum_{i,j}\mu_C \kappa_{\vec{k}C_{ij}} \sqrt{\frac{\hbar\omega_{\vec{k}}}{2\varepsilon_0 SL_{\vec{k}}}} e^{-a_{d\vec{k}} z_{j,C}} e^{i\vec{k}\cdot\vec{R}_{i,C}} |C_{ij}\rangle$ that couples to the $\vec{k}$-th SP mode $|\vec{k}\rangle = a_{\vec{k}}^\dagger|0\rangle$, where $g_C(\vec{k}) = \sqrt{\sum_{i,j}\left|\mu_C \kappa_{\vec{k}C_{ij}} \sqrt{\frac{\hbar\omega_{\vec{k}}}{2\varepsilon_0 SL_{\vec{k}}}} e^{-a_{d\vec{k}} z_{j,C}} e^{i\vec{k}\cdot\vec{R}_{i,C}}\right|^2}$. In addition to the weakly coupled C' states, $H_{sys}^{(i)}$ has two polariton eigenstates $|\alpha_{C,\vec{k}}\rangle = c_{C_{\vec{k}}\alpha_{C,\vec{k}}}|C_{\vec{k}}\rangle + c_{\vec{k}\alpha_{C,\vec{k}}}|\vec{k}\rangle$ for $\alpha = \text{UP}, \text{LP}$ (upper polariton and lower polariton, respectively), which are also eigenstates of $H_{bright,C}^{(\vec{k})}$ for each $\vec{k}\in\text{FBZ}$; throughout this work, $c_{mn} = \langle m|n\rangle$. Furthermore, there is a large reservoir of $N_C - N_{xy,C} = N_{xy,C}(N_{z,C}-1)$ "dark" (purely excitonic) eigenstates $|d_{C,\vec{k}}\rangle$ ($d = 0, 1, \cdots N_{z,C}-2$) which are also eigenstates of $H_{dark,C}$ with bare chromophore energy $\hbar\omega_C$.

EET rates between C and uncoupled C' states can be derived by applying Fermi's golden rule; the corresponding perturbation $V^{(i)}$ connects vibronic-polariton eigenstates of $H_0^{(i)}$ as in FRET and MC-FRET theories [171, 206–208]. For simplicity, we also invoke weak system-bath coupling H_{sys-B}, from which the following expression can be obtained [209, 210]:

$$\gamma_{F\leftarrow I} \approx \frac{2\pi}{\hbar} |\langle F|V^{(i)}|I\rangle|^2 J_{F,I}. \tag{5.7}$$

This is the rate of transfer between $H_{sys}^{(i)}$ eigenstates $|I\rangle$ and $|F\rangle$, where $J_{F,I}$ is the spectral overlap between absorption and emission spectra, which depend on H_B and H_{sys-B}. Since our focus is to understand the general timescales expected for the PARET problem, in Sec. 5.3 we treat the broadening of electronic/polaritonic levels due to H_{sys-B} as Lorentzian, although more sophisticated lineshape theories can be utilized if needed [197]. Furthermore, we can in principle also

refine Eq. (5.7) to consider the complexities of vibronic mixing between the various eigenstates of $H_{sys}^{(i)}$, as done in recent works by Jang and Cao [171, 206–208].

It follows from Eq. (5.7) that the rates from donor states—either polaritons with given wavevector $\vec{k}$ or a uniform mixture of dark states with occupation $p_{D_{\vec{k}}} = \frac{1}{N_D - N_{xy,D}}$ for all $d, \vec{k}$—to the incoherent set of all bare acceptor states are,

$$\gamma_{A \leftarrow \alpha_{D,\vec{k}}} = \frac{2\pi}{\hbar} \sum_{l,m} |\langle A_{lm}|H_{DA} + H_{AP}|\alpha_{D,\vec{k}}\rangle|^2 J_{A,\alpha_{D,\vec{k}}}, \tag{5.8a}$$

$$\gamma_{A \leftarrow dark_D} = \frac{2\pi}{\hbar(N_D - N_{xy,D})} \sum_{l,m} \sum_{\vec{k} \in \mathrm{FBZ}} \sum_{d} |\langle A_{lm}|H_{DA}|d_{D,\vec{k}}\rangle|^2 J_{A,d_{D,\vec{k}}}. \tag{5.8b}$$

Here, we notice that $\gamma_{A \leftarrow \alpha_{D,\vec{k}}}$ in Eq. (5.8a) can be enhanced or suppressed relative to bare (in the absence of metal) FRET due to additional SP-resonance energy transfer [211] (PRET) channel given by H_{AP}, as well as the spectral overlap $J_{A,\alpha_{D,\vec{k}}}$ that can be modified by tuning the energy of $|\alpha_{D,\vec{k}}\rangle$. Similar findings were obtained for electron transfer with only donors strongly coupled to a cavity mode [72]. Given that $|\alpha_{D,\vec{k}}\rangle$ corresponds to a delocalized state, one would expect a superradiant enhancement of the rate [173, 174]; in practice, this effect is minor due to the distance dependence of H_{DA} (see Sec. B.1.1). On the other hand, Eq. (5.8b) presents an average rate $\gamma_{A \leftarrow dark_D}$ from the dark states and hence does not feature a PRET term. In fact, it converges (see Sec. B.1.2 for derivation) to the bare FRET rate [Eq. (5.12b) below] in the limit of large $N_D \gg N_{xy,D}$ (when there are many layers of chromophores along z) and isotropically averaged and orientationally uncorrelated TDMs $\vec{\mu}_{C_{ij}}$ for both $C = D, A$.

In contrast, strongly coupling the acceptor states to SPs yields the following rates:

$$\gamma_{\alpha_A \leftarrow D} = \frac{2\pi}{\hbar N_D} \sum_{\vec{k} \in \mathrm{FBZ}} \sum_{i,j} |\langle \alpha_{A,\vec{k}}|H_{DA} + H_{DP}|D_{ij}\rangle|^2 J_{\alpha_{A,\vec{k}},D}, \tag{5.9a}$$

$$\gamma_{dark_A \leftarrow D} = \frac{2\pi}{\hbar N_D} \sum_{\vec{k} \in \mathrm{FBZ}} \sum_{d} \sum_{i,j} |\langle d_{A,\vec{k}}|H_{DA}|D_{ij}\rangle|^2 J_{d_{A,\vec{k}},D}. \tag{5.9b}$$

Here, we have calculated average rates over the N_D possible initial states at the D slab and summed over all final states for each polariton/dark band. Given the asymmetry of Fermi's golden rule with

respect to initial and final states (rates scale with the *probabilities* of occupation of *initial* states and with the *density* of *final* states) [173], the physical consequences of Eq. (5.9) are quite different to those of its counterpart in Eq. (5.8) when $N_A \gg N_{xy,A}$ and all TDMs are isotropically averaged and feature no orientational correlations amongst them. Seemingly counterintuitive in light of the various recently reported phenomena which are enhanced upon exciton delocalization, the rate of EET to polariton states is reduced substantially compared to the bare FRET rate (at short donor-acceptor separations; see Sec. B.1.3 for a formal derivation of this statement). Nevertheless, this statement is easily understood from a final-density-of-states argument [see Eq. (5.9a)]: only $N_{xy,A}$ bright acceptor collective modes contribute to $\gamma_{\alpha_A \leftarrow D}$, whereas N_A localized acceptor states contribute to the bare FRET rate. On the other hand, $\gamma_{dark_A \leftarrow D}$ behaves similarly to Eq. (5.8b) in that it converges [see Eqs. (5.13b) and (B.19c)] to the bare FRET rate. Thus, at donor-acceptor separations where the square of the FRET coupling exceeds on average that for PRET, the inequality $\gamma_{\alpha_A \leftarrow D} \ll \gamma_{dark_A \leftarrow D}$ is expected to hold.

Our analyses of Eqs. (5.8) and (5.9) reveal one of the main conclusions of this work: *while strong coupling of D but not A might yield a significant $D \rightarrow A$ EET rate change with respect to the bare case, strong coupling of A but not D will change that process in a negligible manner*. Interestingly, these trends have also been observed for transfer between layers of donor and acceptor quantum dots selectively coupled to metal nanoparticles in the weak-interaction regime [212]. However, polariton formation with A is not useless, for one may consider the intriguing prospect of converting A states into new donors. As we shall show in the next paragraphs, this role reversal or "carnival effect" can be achieved when the UP is higher in energy than the bare donor states. These findings are quite general and should apply to other molecular processes as long as the interactions between reactants and products (taking the roles of donors and acceptors) also decay at large distances, a scenario that is chemically ubiquitous [78].

5.2.2 Case *ii*: strong coupling of both donors and acceptors

We next consider the SC of SPs to both donors and acceptors. We rewrite Eq. (5.1) as

$H = H_0^{(ii)} + V^{(ii)}$, where $H_0^{(ii)} = H_{sys}^{(ii)} + H_B$ and the perturbation is $V^{(ii)} = H_{sys-B}$ for interslab distance large enough to neglect interaction H_{DA} in $V^{(ii)}$. Here, $H_{sys}^{(ii)} = H_D^{(sys)} + H_A^{(sys)} + H_{DP} + H_{AP} + H_{DA} + H_P$ is the polariton Hamiltonian. As in the Davydov model [191, 192], the EET pathways of interest become those where H_{sys-B} induces vibrationally mediated relaxation (faster than dipole-dipole coupling in typical organic chromophores separated by 1-10 nm [170]) among the delocalized states resulting from SC [189, 190]. The transfer rates describing these processes can be deduced by Fermi's golden rule too, the resulting expressions coinciding with those derived with Redfield [193] theory [99, 189, 190]. Although not necessary, we take $N_{xy,D} = N_{xy,A} = N_{xy}$ to avoid mathematical technicalities about working with two $\vec{k}$ grids of different sizes, a complication that does not give more insight into the physics of interest. As done in Sec. 5.2.1, we rewrite $H_{sys}^{(ii)}$ in $\vec{k}$-space: $H_{sys}^{(ii)} = \sum_{\vec{k}\in \mathrm{FBZ}} H_{bright}^{(\vec{k})} + H_{dark,D} + H_{dark,A} + H_{DA} + \sum_{\vec{k}\notin \mathrm{FBZ}} \hbar\omega_{\vec{k}} a_{\vec{k}}^\dagger a_{\vec{k}}$, where

$$\begin{aligned} H_{bright}^{(\vec{k})} = {} & \hbar\omega_D |D_{\vec{k}}\rangle\langle D_{\vec{k}}| + \hbar\omega_A |A_{\vec{k}}\rangle\langle A_{\vec{k}}| + \hbar\omega_{\vec{k}} a_{\vec{k}}^\dagger a_{\vec{k}} \\ & + g_D(\vec{k})(|D_{\vec{k}}\rangle\langle G| a_{\vec{k}} + \mathrm{h.c.}) + g_A(\vec{k})(|A_{\vec{k}}\rangle\langle G| a_{\vec{k}} + \mathrm{h.c.}), \end{aligned} \tag{5.10}$$

and the terms labeled *dark* are defined analogously to those in Eq. (5.6b). For each $\vec{k} \in$ FBZ, there are three polariton eigenstates of $H_{bright}^{(\vec{k})}$ that are linear combinations of $|D_{\vec{k}}\rangle$, $|A_{\vec{k}}\rangle$, and $|\vec{k}\rangle$, and we call them UP, middle polariton (MP), and LP, according to their energy ordering. In addition, the presence of $H_{dark,C}$ yields $N_C - N_{xy,C}$ dark C eigenstates.

The resulting expressions for the rates of transfer from a single polariton state or average

dark state to an entire polariton or dark state bands are

$$\gamma_{\beta\leftarrow\alpha_{\vec{k}}} = \sum_{\vec{k}'\in\mathrm{FBZ}}\sum_{C}|c_{C_{\vec{k}'}\beta_{\vec{k}'}}|^2|c_{C_{\vec{k}}\alpha_{\vec{k}}}|^2\sum_{i,j}|c_{C_{ij}C_{\vec{k}'}}|^2|c_{C_{ij}C_{\vec{k}}}|^2\mathcal{R}_C(\omega_{\beta_{\vec{k}'}\alpha_{\vec{k}}}), \tag{5.11a}$$

$$\gamma_{\alpha\leftarrow dark_C} = \frac{1}{N_C - N_{xy}}\sum_{\vec{k}'\in\mathrm{FBZ}}\sum_{\vec{k}\in\mathrm{FBZ}}\sum_{d}|c_{C_{\vec{k}'}\alpha_{\vec{k}'}}|^2 \times\sum_{i,j}|c_{C_{ij}C_{\vec{k}'}}|^2|c_{C_{ij}d_{C,\vec{k}}}|^2\mathcal{R}_C(\omega_{\alpha_{\vec{k}'}C}), \tag{5.11b}$$

$$\gamma_{dark_C\leftarrow\alpha_{\vec{k}}} = \sum_{\vec{k}'\in\mathrm{FBZ}}\sum_{d}|c_{C_{\vec{k}}\alpha_{\vec{k}}}|^2\sum_{i,j}|c_{C_{ij}d_{C,\vec{k}'}}|^2|c_{C_{ij}C_{\vec{k}}}|^2\mathcal{R}_C(\omega_{C\alpha_{\vec{k}}}), \tag{5.11c}$$

for $\alpha,\beta = \mathrm{UP},\mathrm{MP},\mathrm{LP}$ and $C = D,A$ [see Sec. B.2.1 for derivation of Eq. (5.11)]. To intuitively understand Eq. (5.11a), note that $|c_{C_{\vec{k}}\alpha_{\vec{k}}}|^2|c_{C_{ij}C_{\vec{k}}}|^2$ and $|c_{C_{\vec{k}'}\beta_{\vec{k}'}}|^2|c_{C_{ij}C_{\vec{k}'}}|^2$ are the fractions of exciton $|C_{ij}\rangle$ in the polariton states $|\alpha_{\vec{k}}\rangle$ and $|\beta_{\vec{k}'}\rangle$, respectively, while $\mathcal{R}_C(\omega_{\beta_{\vec{k}'}\alpha_{\vec{k}}})$ is the single-molecule rate of vibrational relaxation at the energy difference $\omega_{\beta_{\vec{k}'}} - \omega_{\alpha_{\vec{k}}}$. More specifically, $\mathcal{R}_C(\omega) = 2\pi\Theta(-\omega)[n(-\omega)+1]\mathcal{J}_C(-\omega)+2\pi\Theta(\omega)n(\omega)\mathcal{J}_C(\omega)$, where $\Theta(\omega)$ is the Heaviside step function, $n(\omega) = \frac{1}{e^{\hbar\omega/k_BT}-1}$ is the Bose-Einstein distribution function (k_B is the Boltzmann constant and T is temperature) for zero chemical potential $\mu = 0$, and $\mathcal{J}_C(\omega) = \sum_q \lambda_{q,C}^2\omega_{q,C}^2\delta(\omega-\omega_{q,C})$ is the spectral density for chromophore C [99]. Hence, one can interpret $\beta\leftarrow\alpha_{\vec{k}}$ as a sum of incoherent processes (over C and i,j) where the (local) vibrational modes in C_{ij} absorb or emit phonons concomittantly inducing population transfer between the various eigenstates of $H_{sys}^{(ii)}$. Eqs. (5.11b) and (5.11c) can be interpreted in a similar light. As an aside, we note that these transitions are analogous to the so-called intraband relaxation among collective exciton states in J-aggregates [213]. We now comment on some important qualitative trends in these rates while for simplicity assuming that $N_{z,D} = N_{z,A} = N_z$. First, EET from polariton or dark states to a polariton band [Eqs. (5.11a) and (5.11b)] scale as $\frac{\mathcal{R}_C}{N_z}$. To see this, note that both $|c_{C_{\vec{k}'}\beta_{\vec{k}'}}|^2$ and $|c_{C_{\vec{k}}\alpha_{\vec{k}}}|^2$ are $O(1)$, while $|c_{C_{ij}C_{\vec{k}'}}|^2$ and $|c_{C_{ij}C_{\vec{k}}}|^2$ are $O(\frac{1}{N_{xy}N_z})$, but the summations $\sum_{\vec{k}\in\mathrm{FBZ}}$ and$\sum_{i,j}$ are respectively carried over N_{xy} and $N_{xy}N_z$ terms. On the other hand, $\gamma_{dark_C\leftarrow\alpha_{\vec{k}}}$ takes values that are on the order of the single-molecule decay $\mathcal{R}_C(\omega_{C\alpha_{\vec{k}}})$. For sufficiently large N_z, these scalings are consistent with previous studies on relaxation dynamics of polaritons [51, 53, 126] and can be summarized as follows: the

dominant channels of relaxation are from the polariton states to a reservoir of dark states that share the same exciton character; their timescales are comparable to those of the corresponding single-chromophore vibrational relaxation; given the large density of states in this reservoir compared to the polariton bands, the dark states act as a population sink or trap from which population can only leak out very slowly [53, 214].

5.3 Application

The theory above is now applied to study EET kinetics associated with slabs of chromophores with $\hbar\omega_D = 2.1$ eV, $\hbar\omega_A = 1.88$ eV; these transition energies are chosen to match those of the J-aggregated cyanine dyes (TDBC and BRK5714, respectively) used in previous polariton experiments [90, 215]. For simplicity, this section assumes $T = 0$ and thus only considers downhill transfers to/from polariton and dark states. We describe the metal with Drude permittivity of silver ($\omega_p = 9.0$ eV, $\varepsilon_\infty = 1$ [216]) and all media at $z > 0$ (including molecular slabs) with $\varepsilon_d = 1$. We model spectral overlaps [Eqs. (5.8) and (5.9)] with Lorentzian functions $J_{F,I} = \frac{\frac{\Gamma_I+\Gamma_F}{2}}{\pi[(\frac{\Gamma_I+\Gamma_F}{2})^2+(\hbar\omega_{FI})^2]}$; we set $\Gamma_A \approx \Gamma_D = 47$ meV to represent observed values for absorption of TDBC [162] and $\Gamma_{P,\vec{k}} = \frac{v_g(\vec{k})}{L_{\vec{k}}}$ [203], where $v_g(\vec{k})$ is the SP group velocity. Rigorous treatments of lineshape functions have been previously reported in MC-FRET literature and could be applied to this problem as well [207, 208, 217, 218], although this effort is beyond the scope of our work. We also neglect differences in TDMs and assign $\mu_D = \mu_A = 10$ D, a typical number for cyanine dyes [219]. In addition, we assume that the dipoles are isotropically oriented and spatially uncorrelated.

5.3.1 Case *i*: strong coupling of only one chromophore

We now proceed to simulations for Case *i*, where only one of the molecular species forms polaritons. With the assumption of isotropically oriented and spatially uncorrelated dipoles, we find the interesting observation that the transfer rates in Eq. (5.8) can be approximately decomposed into incoherent sums of FRET and PRET rates (see Sec. B.1.2 for more explicit expressions,

derivations, and justification of validity),

$$\gamma_{A\leftarrow\alpha_{D,\vec{k}}} \approx \frac{2\pi}{\hbar}\sum_{l}\sum_{i,j}\Big(|c_{D_{\vec{k}}\alpha_{D,\vec{k}}}|^2|c_{D_{ij}D_{\vec{k}}}|^2|\langle A_{l0}|H_{DA}|D_{ij}\rangle|^2 + |c_{\vec{k}\alpha_{D,\vec{k}}}|^2|\langle A_{l0}|H_{AP}|\vec{k}\rangle|^2\Big) J_{A,\alpha_{D,\vec{k}}}, \tag{5.12a}$$

$$\gamma_{A\leftarrow dark_D} = \gamma_{\text{bare FRET}} = \frac{2\pi}{\hbar N_D}\sum_{l}\sum_{i,j}|\langle A_{l0}|H_{DA}|D_{ij}\rangle|^2 J_{A,D}, \tag{5.12b}$$

where, as explained above, only $\gamma_{A\leftarrow\alpha_{D,\vec{k}}}$ differs from $\gamma_{\text{bare FRET}}$. More concretely, we consider a 35-nm-thick slab of donors with 1×10^9 molecules/μm^3 on top of a 1 nm spacer placed on a plasmonic metal film. We set the monolayer slab of acceptors with 1×10^4 molecules/μm^2 at varying distances from the donors (Fig. 5.1a). Then the collective couplings of the donor-resonant SP mode ($|\vec{k}| = 1.1\times10^7$ m^{-1}) to donors and acceptors is $g_D(\vec{k}) = 155$ meV and $g_A(\vec{k}) \leq 2.5$ meV, respectively. When there is no separation between donor and acceptor slabs, rates > 1 ns^{-1} (Fig. 5.1b) are obtained for transfer to acceptors from the UP (~ 10 ns^{-1}), LP (~ 100 ns^{-1}), or the set of dark states (~ 10 ns^{-1}). As separation increases however, the rate from dark states decays much faster than those from either UP or LP. This difference stems from the slowly decaying PRET contribution of the polaritons, as well as the totally excitonic character of the dark states, which can only undergo FRET but not PRET (Fig. 5.1a,b). In fact, for large distances, the FRET contribution becomes significantly overwhelmed by PRET (Fig. 5.1c), in consistency with previous studies in the weak SP-coupling regime [220]. As the distance between slabs approaches 1 μm, it is fascinating that while transfer from dark states (and thus bare FRET) practically vanishes, the rate from either LP (~ 1 ns^{-1}) or UP (~ 0.01 ns^{-1}) is still at or above typical fluorescence decay rates (0.01-10 ns^{-1}) [221]. Roughly speaking (in FRET language), this PARET has a Förster distance in the μm range, or 1000-fold greater than the typical nm-range [222]. Interestingly, the LP rate exceeds the UP one by 1-2 orders of magnitude at all separations due to greater spectral overlap with the acceptor (Fig. 5.1a).

In contrast, strongly coupling the acceptors to a resonant SP mode does not lead to the aforementioned PARET from donors to acceptors (Fig. 5.2). Making the same assumptions as

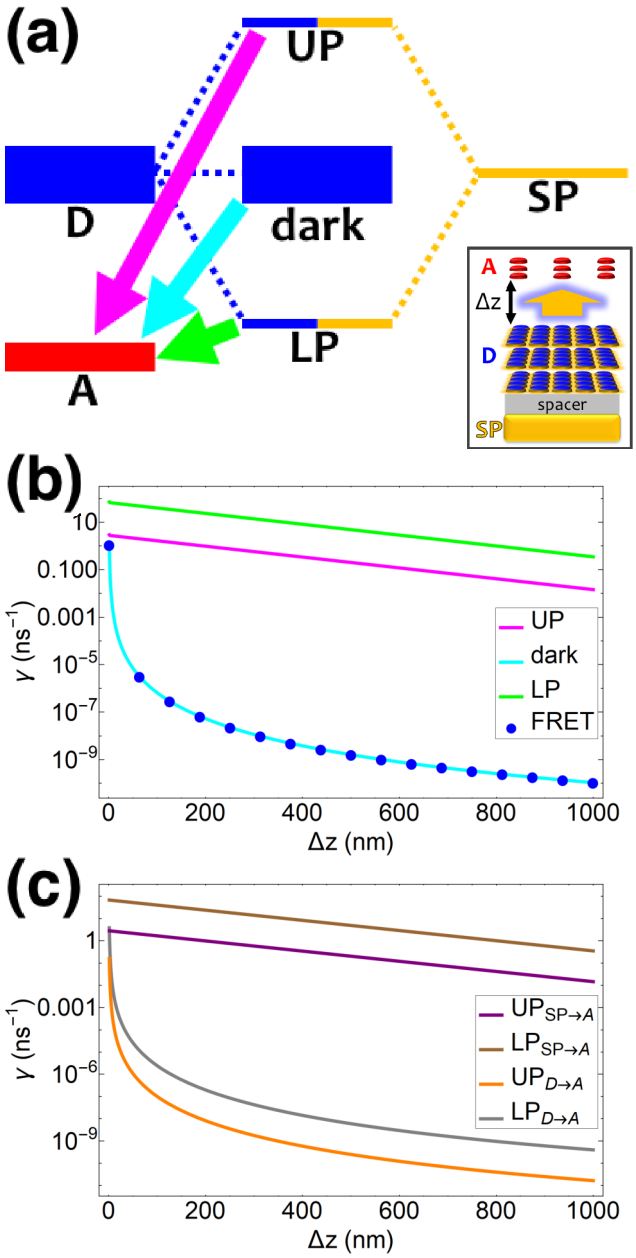

Figure 5.1: (a) Schematic energy-level diagram showing the EET transitions from donors strongly coupled to SPs to bare acceptors. The thickness of the horizonal lines denotes the density of states while the thickness of arrows corresponds to rate of transition (thicknesses not drawn to scale). Inset: representation of the EET process from a thick and dense slab of donors (featuring SC to SPs) to a dilute monolayer of acceptors. (b) Rates as a function of donor-acceptor separation Δz for EET from donor polariton and dark states to acceptors (lines). The rate from dark states and for the bare-donor FRET (dots), are calculated in the same manner. (c) Contributions of rates for transfer from donor UP and LP to acceptor states due to donor-acceptor (FRET) and SP-acceptor (PRET) interactions [see Eq. 5.12a and immediately preceding discussion].

above, *i.e.*, taking isotropically oriented and spatially uncorrelated dipoles, we obtain (Sec. B.1.3),

$$\gamma_{\alpha_A \leftarrow D} \approx \frac{2\pi}{\hbar N_D} \sum_{\vec{k}\in \mathrm{FBZ}} \sum_i \left(\sum_{l,m} |c_{A_{\vec{k}}\alpha_{A,\vec{k}}}|^2 |c_{A_{lm}A_{\vec{k}}}|^2 |\langle A_{lm}|H_{DA}|D_{i0}\rangle|^2 \right.$$
$$\left. + |c_{\vec{k}\alpha_{A,\vec{k}}}|^2 |\langle \vec{k}|H_{DP}|D_{i0}\rangle|^2 \right) J_{\alpha_{A,\vec{k}},D}, \tag{5.13a}$$

$$\gamma_{dark_A \leftarrow D} = \gamma'_{\text{bare FRET}} = \frac{2\pi}{\hbar N_D} \sum_i \sum_{l,m} |\langle A_{lm}|H_{DA}|D_{i0}\rangle|^2 J_{A,D}. \tag{5.13b}$$

We consider (Fig. 5.2a) a 50 nm-thick acceptor slab with a concentration of 1×10^9 molecules/μm^3 on top of the 1 nm spacer placed on the metal, and a monolayer of donors with concentration 1×10^4 molecules/μm^2 at varying distances from the acceptors. Notice that $\gamma_{dark_A \leftarrow D}$ becomes another bare FRET rate like in Eq. (5.12b). For $\gamma_{\alpha_A \leftarrow D}$, we see that PRET still dominates over FRET for long distances (Fig. 5.3). However, due to the suppression of $\gamma_{\alpha_A \leftarrow D}$ relative to $\gamma_{dark_A \leftarrow D}$ explained in Sec. 5.2.1, the limited spatial range of interactions of H_{DA} and H_{DP}, and the fact that the donor energy is lower than that of $|\mathrm{UP}_{A,\vec{k}}\rangle$for most $\vec{k} \in$ FBZ, the rates to the acceptor UP band fall below fluorescence timescales [221] and therefore offer no meaningful enhancements with respect to the bare FRET case (Fig. 5.2b). While the first two reasons also explain the similarly low rates to the LP band, the major factor is that most states $|\mathrm{LP}_{A,\vec{k}}\rangle$ essentially overlap only with acceptors that are closer to the metal—and thus farther from the donors—due to the evanesecent nature of the SP-exciton coupling [Eq. (5.5)].

Coupling SPs to acceptors need not, however, be a disappointment. Increasing the acceptor slab thickness to 140 nm affords for the acceptor-resonant SP mode ($|\vec{k}| = 9.8 \times 10^6$ m^{-1}) the collective coupling $g_A(\vec{k}) = 237$ meV while keeping $g_D(\vec{k}) = 1.7$ meV. Consequently, the acceptor UP energy $\hbar\omega_{UP_{A,\vec{k}}}$ is lifted higher than $\hbar\omega_D$ (Fig. 5.4a), thus allowing for the carnival effect where the donors and acceptors reverse roles. Due to sufficient spectral overlap between the acceptor UP and donor states (Fig. 5.4a), transfer *from* UP occurs at ~ 100 ns^{-1} for donor-acceptor separation of 1 nm and drops only to ~ 1 ns^{-1} when this separation approaches 1 μm (Fig. 5.4b). On the

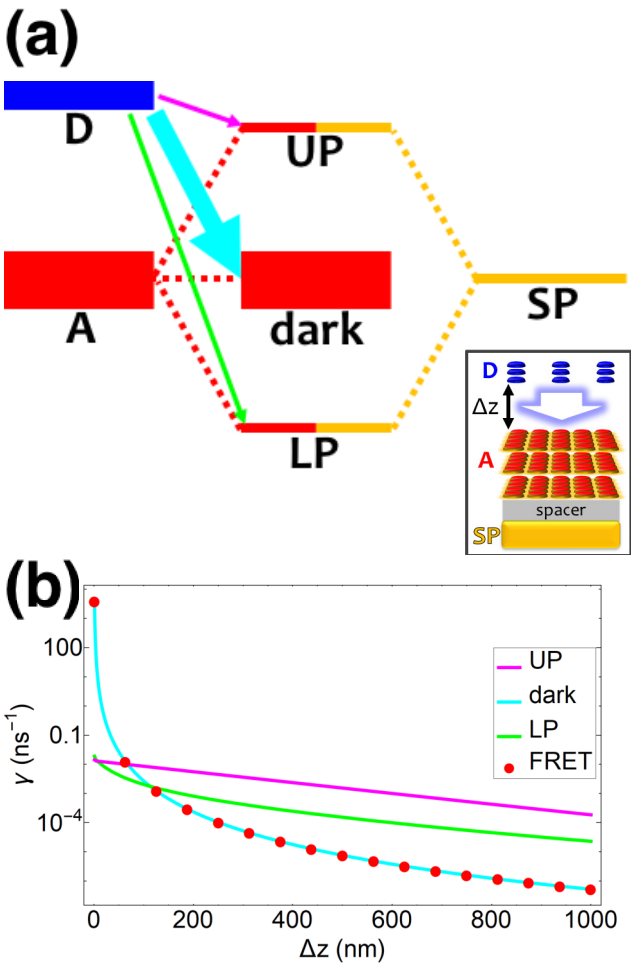

Figure 5.2: (a) Schematic energy-level diagram showing the EET transitions from bare donors to acceptors strongly coupled to SPs. The thickness of the horizonal lines denotes the density of states while the thickness of arrows corresponds to rate of transition (thicknesses not drawn to scale). Inset: representation of the EET process from a dilute monolayer of donors to a thick and dense slab of acceptors (featuring SC to SPs). (b) Rates as a function of donor-acceptor separation Δz for energy transfer from donors to acceptor polaritons and dark states (lines). The rate to dark states and for bare-acceptor FRET (dots), are calculated in the same manner.

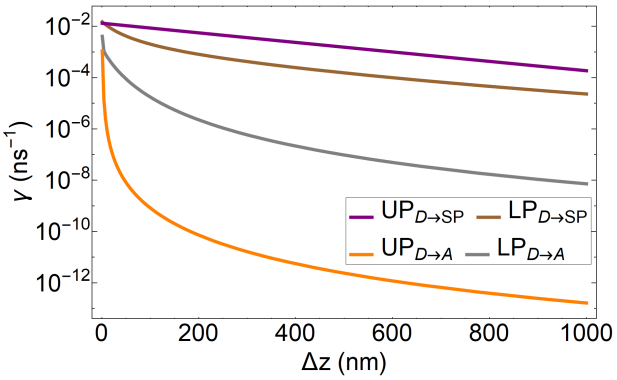

Figure 5.3: SC of SPs to acceptors. Contributions of EET rates from donors to acceptor UP and LP due to donor-acceptor (FRET) and SP-donor (PRET) interactions.

other hand, neither the acceptor dark nor LP states contribute to this reversed PARET given their lack of spectral overlap with the donors and detailed balance (especially at $T = 0$). This result provides the second main conclusion of our work: *polaritons offer great versatility to control spectral overlaps without actual chemical modifications to the molecules and can therefore endow them with new physical properties*. Before proceeding to simulations for Case *ii*, it should first be noted that while our model neglects intermediate- and far-field donor-acceptor dipole-dipole interactions that become relevant at $\sim \mu$m distances, these couplings are expected to be small compared to PRET couplings and therefore should not qualitatively change our results for Case *i*. The relative insignificance of the far-field, or radiative, contributions is consistent with their correspondence to emission followed by absorption (of a real photon) [223]. Regardless, these additional interactions can be modeled using a quantum electrodynamics treatment [224] of energy transfer in bulk media according to previous literature [225]. Second, we highlight that the PARET from polariton states for the donors-only and reversed cases of SC may not be efficient in experiments due to its competition with vibrational relaxation from UP to dark states (~10-100 fs for exciton-microcavity systems [51, 52, 226–228]) and/or radiative decay (dominated by fast cavity leakage ~10-100 fs for both microcavities [227–229] and SPs [230, 231]). However, conditions may be optimized to suppress these deleterious pathways by detuning the SP energy relative to that of the strongly coupled chromophore such that the polariton state is mostly excitonic and has an enhanced lifetime

[62].

5.3.2 Case *ii*: strong coupling of both donors and acceptors

Finally, when both chromophores are strongly coupled to SPs, we limit ourselves to donor-acceptor separations ≥ 10 nm to ignore H_{DA} terms (an approximation discussed in Section 5.2.2 and validated by the calculations above demonstrating that FRET coupling is significantly diminished at such distances). The thickness (35 nm) and density (1×10^9 molecules/μm^{-3}) of each slab is large enough to allow for SC of the donor-resonant SP mode ($|\vec{k}| = 1.1 \times 10^7$ m^{-1}, $g_D(\vec{k}) = 155$ meV, and $g_A(\vec{k}) = 142$ meV) to both chromophores separated up to ~ 400 nm. To evaluate the rates derived (Sec. B.2.2) from Eq. (5.11) under the condition $N_C \gg N_{xy,C}$ for $C = D, A$, we introduce a spectral density representing intramolecular exciton-phonon coupling of TDBC: $\mathcal{J}_A(\omega) \approx \mathcal{J}_D(\omega) = \mathcal{J}(\omega)$, where

$$\mathcal{J}(\omega) = \sum_{q \in B_{\mathrm{TDBC}}} \lambda_q^2 \omega_q^2 \frac{\frac{\Gamma/\hbar}{2}}{\pi[(\frac{\Gamma/\hbar}{2})^2 + (\omega - \omega_q)^2]}, \tag{5.14}$$

$\Gamma = 47$ meV is equal to the chromophore decay energy, and B_{TDBC} is the discrete set (Sec. B.2.2) of localized vibrational modes which significantly couple to each TDBC exciton. Such coupling has been experimentally [52, 226–228, 232] and theoretically [51, 126, 233–235] supported as the mechanism of vibrational relaxation for the dye; our spectral density has been reconstructed from the works of Agranovich and coworkers [51, 126]. By placing the donor slab on top of the spacer on the metal and varying the acceptor position above the donors (Fig. 5.5a), we find that for all donor-acceptor separations, the rates of PARET from UP to dark donors ($\sim 10^5$ ns^{-1}) and MP to dark acceptors ($\sim 10^4 - 10^5$ ns^{-1}) are substantially higher compared to those from dark donors to MP ($\sim 10^3$ ns^{-1}) and dark acceptors to LP ($\sim 10^3$ ns^{-1}) (Fig. 5.5b). These observations are in agreement with our discussion above, where the dark state manifolds act as population sinks due to their high density of states. Indeed, we also notice that the rates for UP $\rightarrow dark_D$ and MP $\rightarrow dark_A$ are enhanced (Fig. 5.5b) compared to those of UP $\rightarrow$ MP and MP $\rightarrow$ LP, respectively,

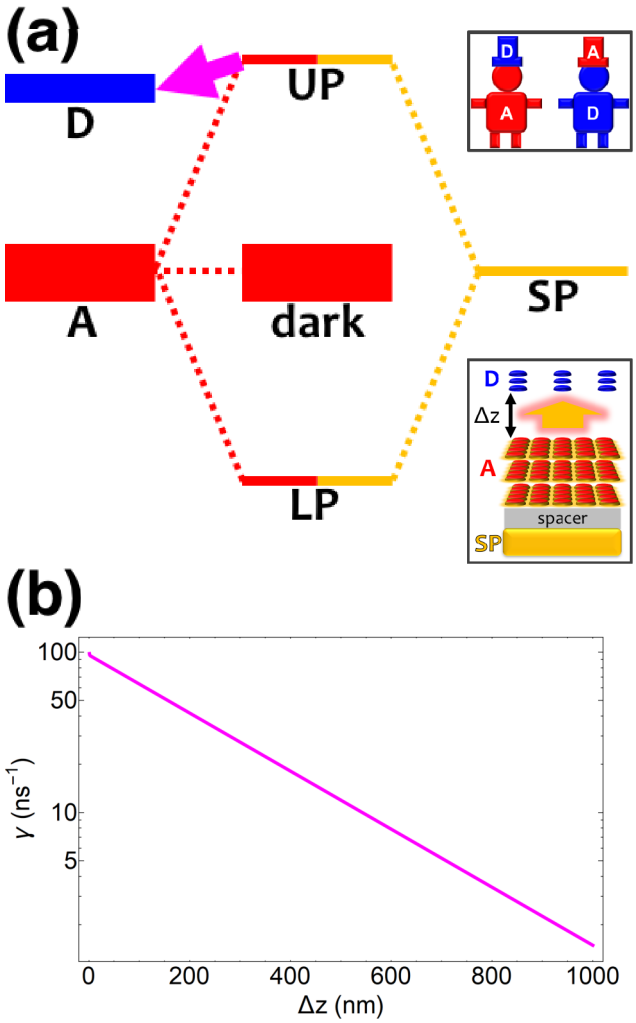

Figure 5.4: (a) Schematic energy-level diagram showing the "carnival-effect"-EET role-reversal process from acceptor UP state to bare donors. Insets: (top) cartoon illustrating the "carnival effect" between donors and acceptors and (bottom) representation of the reversed-role EET process from a thick and dense slab of acceptors (featuring SC to SPs) to a dilute monolayer of donors. (b) Rate as a function of donor-acceptor separation Δz for energy transfer from acceptor UP to bare donors.

by approximately $N_z = 35$, the analytically estimated ratio solely based on the associated density of final states. Another interesting detail seen from Fig. 5.5b is that the UP $\rightarrow$ MP (MP $\rightarrow$ LP) rate with respect to the interslab distance Δz is essentially parallel to that of UP $\rightarrow$ $dark_D$ (MP $\rightarrow$ $dark_A$). This is a consequence of the MP (LP) essentially having donor (acceptor) energy and character for most points in the FBZ. The UP $\rightarrow$ $dark_A$ and UP $\rightarrow$ LP processes behave similarly (Fig. 5.6).

These calculated rates establish consistency with a number of recent notable experiments. First, our results corroborate the experimental observation of efficient PARET for separated donor and acceptor slabs of cyanine dyes strongly coupled to a microcavity [89, 90]. While our SP model for the SC of both excitons cannot account for the exact distance-independent PARET [90] between donor and acceptor slabs in a microcavity, the rates are essentially constant over hundreds of nanometers due to the slowly decaying SP fields. Additional validation of our theory is obtained by defining rate parameters $\mathcal{C}$ (functions of the γ rates above, see Secs. B.2.3 and B.2.4) that can be directly compared to those experimentally reported (Table 5.2) [89]. Since experimental $\mathcal{C}$ have not been determined for the setup of our work, we instead use those describing a blend of two cyanine dyes where physical separation of the dyes did not significantly change the observed photoluminescence [89]. In our work, we obtained rates that assume zero temperature and sum across the whole polariton band in the FBZ; in practice, experiments occur at room temperature and probe polariton photoluminescence around a narrow window of wavevectors close to the anticrossings ($\sim 10^7$ m^{-1} in [236]). If we take these experimental details into account when calculating $\mathcal{C}$, we notice good agreements with our theory (see Table 5.2). As an aside, we reiterate that there are other experimental subtleties, notably competing processes such as radiative decay, that we have not considered but may compromise the longevity of the polariton states and thereby influence the observation of the EET phenomena predicted throughout this work for the two cases of SC.

Given the significant differences between the microcavity- [158, 237] and SP-based [48] systems, let alone experimental uncertainty, the accordance between our theory and the aforementioned experiments highlights the remarkable robustness of cavity SC of donor and acceptor

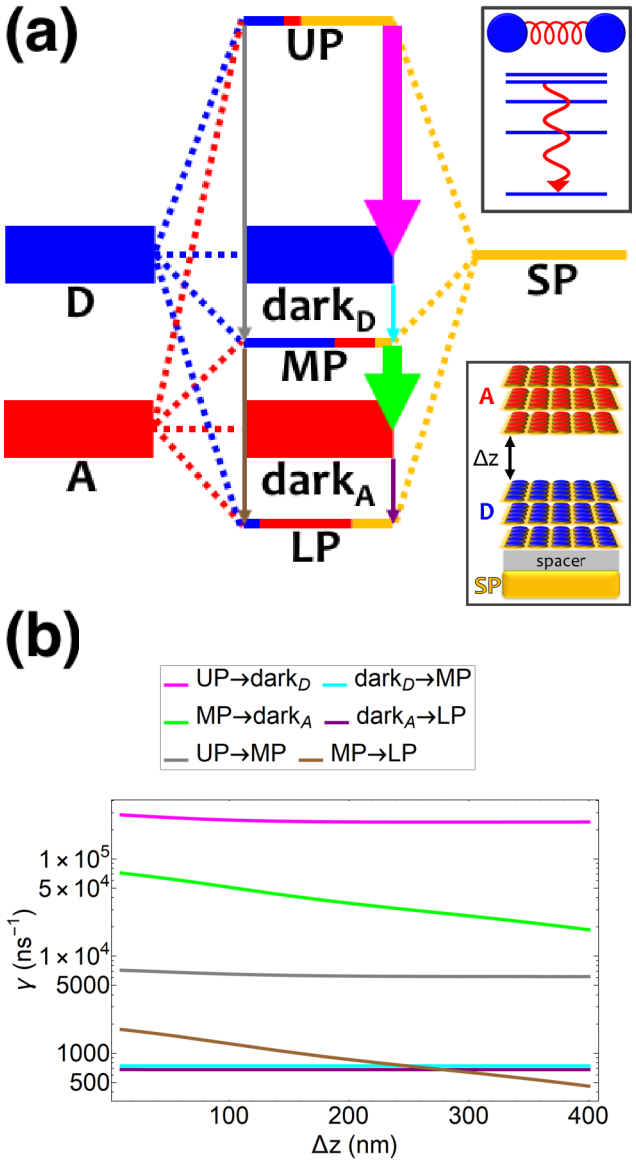

Figure 5.5: (a) Schematic energy-level diagram showing the EET transitions among polariton and dark states for both donors and acceptors strongly coupled to SPs. The SP mode is resonant with the donor transition (for polariton as initial state); the donor slab lies 1 nm above the metal and has fixed position ($z > 0$) while the acceptor slab is moved in the $+z$-direction to vary the donor-acceptor separation Δz. The thickness of the horizonal lines denotes the density of states while the thickness of arrows corresponds to rate of transition (thicknesses not drawn to scale). Insets: (top) cartoon illustrating vibrational relaxation, the EET mechanism for this case of SC, and (bottom) representation of the setup of thick and dense slabs for both types of chromophores (featuring SC to SPs). (b) Rates for selected downhill transitions as a function of Δz.

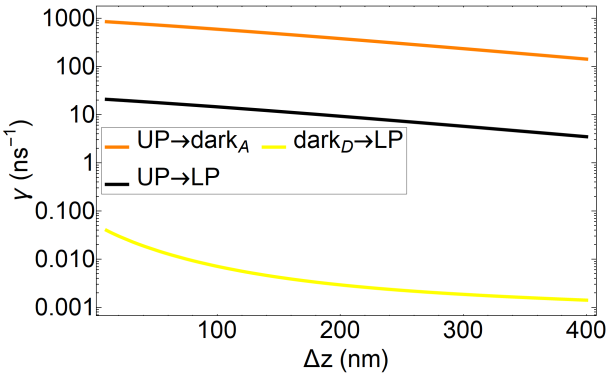

Figure 5.6: SC of SPs to both donors and acceptors. EET rates (that are not shown in Fig. 5.5) as a function of donor-acceptor separation Δz for downhill transtions among polariton and dark states. The SP mode is resonant with the donor transition, and the donor slab lies 1 nm from the metal and has fixed position while the acceptor slab is moved in the $+z$-direction to vary Δz.

excitons as a method for PARET. Moreover, we have arrived at the third main conclusion of this paper: *when donor and acceptors are both strongly coupled to a photonic mode, efficient energy exchange over hundreds of nm can occur via vibrational relaxation; more generally, local vibrational couplings can induce nonlocal transitions given sufficient delocalization of the polariton species—irrespective of spatial separation.* Seemingly "spooky", this action at a (far) distance is a manifestation of donor-acceptor entanglement resulting from strong light-matter coupling [238]. While this relaxation mechanism and entanglement is present in typical molecular aggregates [239, 240], the novelty in the polariton setup is the remarkable mesoscopic range of interactions that is effectively produced.

5.4 Conclusions

In summary, we have theoretically calculated experimentally consistent rates of PARET for various cases of SC. We employed a polariton (plexciton) setup consisting of a metal whose SP modes couple to donor and/or acceptor chromophores. For the case where a single type of chromophore is strongly coupled to SPs, we have demonstrated that energy transfer starting from delocalized states can be enhanced due to increased spectral overlap compared to the bare FRET

Table 5.2: Comparison between PARET rate parameters $\mathcal{C}$ for donor and acceptor cyanine dye J-aggregates strongly coupled to SP (theory) and microcavity (experiment) modes.[a]

$\mathcal{C}$	SP (theory)[b]	Microcavity (experiment)[c]
$\mathcal{C}_5^{\mathrm{UPB}}$	$(2.9\text{-}3.2\ \mathrm{fs})^{-1}$	$(34\ \mathrm{fs})^{-1}$
$\mathcal{C}_2$	$(177\text{-}259\ \mathrm{ps})^{-1}$	$(603\ \mathrm{ps})^{-1}$
$\mathcal{C}_5^{\mathrm{MPB}}$	$(6.9\text{-}12\ \mathrm{fs})^{-1}$	$(8.5\ \mathrm{fs})^{-1}$
$\mathcal{C}_1$	$(178\text{-}243\ \mathrm{ps})^{-1}$	$(228\ \mathrm{ps})^{-1}$

[a]See Secs. B.2.3 and B.2.4 for additional details. [b] Ranges of the rate parameters calculated from Eq. (B.34), plotted in Fig. 5.7, and accounting for the facts that typical polariton photoluminescence experiments occur at room temperature and probe only final polariton states near the anticrossings [236]. [c]Rate parameters that were obtained from experimental fitting of a kinetic model and that describe the PARET processes for a blend of J-aggregating NK-2707 (donors) and TDBC (acceptors) cyanine dyes both strongly coupled to a microcavity mode [89].

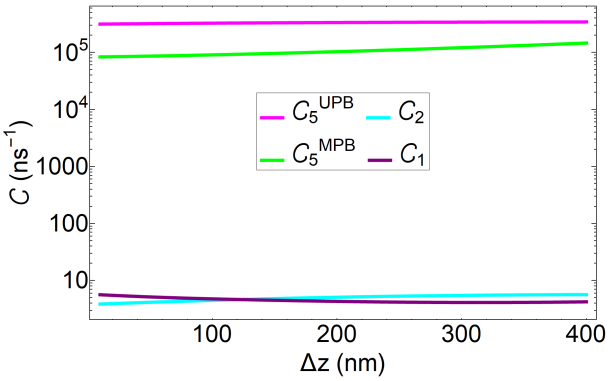

Figure 5.7: SC of SPs to both donors and acceptors. Rate parameters $\mathcal{C}$ as a function of donor-acceptor separation Δz for downhill transitions. The donor slab lies 1 nm from the metal and has fixed position while the acceptor slab is moved in the $+z$-direction to vary Δz.

case. Astonshingly, this transfer can remain fast up to 1 μm because the PRET coupling decays slowly with respect to metal-chromophore separation when compared to the faster decaying inter-chromophoric dipole-dipole coupling. Also, we have shown that delocalizing the acceptors is a poor strategy to enhance EET starting from the donors, but can lead to an intriguing and efficient role-reversed ("carnival effect") EET when starting from the acceptors. These observations shed new light on the timely debate of how to harness coherence to enhance molecular processes [241]. Given their generality, they can also be applied to guide the design of polaritonic systems to control other chemical processes that have similar donor-acceptor flavor (*e.g.*, charge transfer [242], electron transfer [72], singlet fission [62]) or reactant-product nature (*e.g.*, cis-trans isomerization [79, 205], dissociation [242]). Finally, our calculated rates support vibrational relaxation as the mechanism of PARET when both donors and acceptors are strongly coupled to a cavity mode. The results obtained in this work affirm light-matter SC as a promising and novel means to engineer novel interactions between molecular systems across mesoscopic lengthscales, thus opening doors to remote-controlled chemistry.

Chapter 5, in full, is adapted from the material as it appears in "Theory for polariton-assisted remote energy transfer," M. Du, L. A. Martínez-Martínez, R. F. Ribeiro, Z. Hu, V. M. Menon and J. Yuen-Zhou, *Chem. Sci.* **9**, 6659 (2018). The dissertation author was the primary investigator and author of this paper.

Chapter 6

Conclusions and outlook

6.1 Conclusions

In this dissertation, we provided insight on how VSC affects reactions where thermalization occurs on a similar or longer time scale compared to reactive events. In general, the rate of such reactions depends not only on the thermal-equilibrium properties (e.g., energies and populations) of the reacting molecules. The reaction rate can also depend on, for example, nonequilibrium populations, as well as the rates at which vibrational states dissipate and exchange energy. These additional factors provide a wide array of opportunities through which VSC can modify reactivity beyond changing thermal-equilibrium properties. Exploring these opportunities may help us understand the experimental observations of VSC-modified reaction kinetics, for which TST—a theory that assumes internal thermal equilibrium throughout the reaction—has not been able to explain.

We first studied thermally activated nonadiabatic electron transfer under VSC, specifically that where either $N = 2$ or $N \gg 1$ molecules are strongly coupled to an optical cavity mode. To do so, we developed a kinetic model, which combines Marcus-Levich-Jortner theory of electron transfer and theories of polariton relaxation, that explicitly includes both dissipative processes (i.e., thermalization) and reactive transitions.

For $N = 2$ molecules under VSC, the reaction can efficiently proceed through the polaritons.

The cavity decay of the polaritons can accelerate the thermalization of the reacting molecules and suppress nonequilibrium effects that influence the (bare) reaction rate. The reaction rate can be enhanced or suppressed due to cavity decay. However, this effect is less likely to happen for VSC of $N \gg 1$ molecules, since there are $N-1$ dark modes and thus a steep entropic penalty for the reaction to proceed through the 2 polaritons.

For $N \gg 1$ molecules under VSC, we considered a disordered ensemble of $N \gg 1$ molecules under VSC. Static disorder (i.e., inhomogeneous broadening) had not been rigorously accounted for in previous models of VSC reactions. In the presence of this energetic inhomogeneity, the average dark mode is delocalized across 2-3 molecules. We showed that an electron-transfer reaction proceeds primarily through the dark modes (instead of the polaritons), as expected by entropic considerations. Dark-mode delocalization reduces the rate of reactive transitions while leaving unchanged the rate of vibrational decay, thus changing the (net or apparent) reaction rate. This delocalization-modified kinetics can arise when the homogeneous linewidths of the the dark modes is smaller than their energy spacings.

We then turned our focus to photochemistry, where molecules are driven out of equilibrium by a laser. Specifically, we theoretically engineered a "remote control" of chemistry. This device contains two optical cavities with a shared middle mirror. One cavity contains a "remote catalyst" compound and the other cavity contains a reactant compound. Each compound undergoes VSC to its host cavity. Since the middle mirror is partially transparent, excitation of the remote catalyst can affect the reactivity of the reactant, even though the two compounds reside in different optical cavities. This idea goes beyond the textbook picture of a catalyst binding to its substrate to affect the reaction.

Finally, we developed a theory for a related phenomenon: polariton-assisted remote energy transfer. We considered the cases when one or both chromophores (i.e., donors and acceptors) undergo strong coupling between their electronic transitions and confined electromagnetic modes. In either case, we theoretically demonstrated energy transfer when the chromophores are spatially separated by as much as one micron. For one chromophore under strong coupling, this long-range

energy transfer occurs when the donors are strongly coupled. In general, when the acceptors are strong coupled, energy transfer is unchanged by strong coupling. However, we demonstrated an intriguing phenomenon which we called the "carnival effect": when the upper polariton is higher in energy than the donors, energy flows from this polariton to the donors, and thus the donors and acceptors have reversed roles. For both donors and acceptors under strong coupling, long-range energy transfer is mediated by a series of vibrational-relaxation transitions between dark states and polaritons.

6.2 Outlook

Here, we have paved the way towards understanding the role of nonequilibrium effects in thermally activated reactions under VSC. However, much work remains to elucidate the mechanism behind the experimentally observed VSC-modified reaction kinetics. For example, it is unclear whether the dark modes can affect chemical reactivity in typical experimental settings, where the homogeneous linewidths of the dark modes exceed their energy spacings.

In addition, the effects reported here pertain nonadiabatic reactions (which involve transitions between different electronic potential energy surfaces) whereas the experiments featured adiabatic reactions (which involve dynamics on a single electronic surface). Nevertheless, we believe that analogous effects can arise in adiabatic reactions. Indeed, the phenomena reported here rely crucially not on properties unique to nonadiabatic reactions but on the competition between reactive events and thermalization. Future studies may consider alkene hydroboration [93, 94] or ozonolysis [243], two adiabatic reactions where chemical species can react before they thermalize.

Another puzzle that remains in understanding the experiments is why the reaction rate is observed to change only when vibrational transitions are resonant with cavity modes having zero in-plane momentum (i.e., $k = 0$) [20, 22, 23]. According to recent theoretical work [244], if bulk polaritons [245] are accounted for, the polariton density of states is increased maximally by VSC when the resonance condition holds. It remains to be seen whether this enhancement is key to

understanding the experiments, since the polaritons are vastly outnumbered by the dark modes.

As suggested by [244], it is important for future theoretical models to more precisely represent the experimental systems. For example, the observed changes in reaction kinetics under VSC could be attributed to factors that appear in only some experimental setups supporting VSC. In fact, there have been unsuccessful attempts [246, 247] to reproduce initial findings [22, 24] of VSC-modified reactivity.

Chapter A

Appendix for Chapter 3

A.1 Numerically solving the master equation

State populations as a function of time are simulated by numerically solving master equation (3.4). We start by writing the equation as $d\mathbf{p}/dt = A\mathbf{p}$, where $\mathbf{p}$ is the vector of populations and A is the matrix of transition rates. Subsequently, we apply the following standard procedure to evaluate $\mathbf{p}(t) = \exp(At)\mathbf{p}(0)$ [248]. This method employs the symmetrization of A to avoid a numerically unstable matrix inversion. First, we compute the matrix $B = MAM^{-1}$, where M is the diagonal matrix with diagonal elements $M_{(X,\chi),(X,\chi)} = f_{(X,\chi)}^{-1/2}$, and $f_{(X,\chi)} = \exp(-\beta E_{(X,\chi)})/\sum_{(X,\chi)}\exp(-\beta E_{(X,\chi)})$. Since the transition rates [Eqs. (3.3), (3.7)-(3.8)] satisfy detailed balance, B is symmetric. After numerically diagonalizing B, the population at time t is evaluated as

$$\mathbf{p}(t) = M^{-1}Q\exp(Dt)Q^{\mathsf{T}}M\mathbf{p}(0), \tag{A.1}$$

where Q is a matrix whose columns are the eigenvectors of B, D is the diagonal matrix whose diagonal elements are the eigenvalues corresponding to said eigenvectors, and $Q^{\mathsf{T}} = Q^{-1}$ due to B being symmetric. Because we are interested in thermally activated reactivity, the vector of initial

populations, $\mathbf{p}(0)$, is taken to be a thermal distribution of reactant eigenstates:

$$p_{(R,\chi)}(0) = \frac{\exp(-\beta E_{(R,\chi)})}{\sum_{\chi} \exp(-\beta E_{(R,\chi)})}, \tag{A.2a}$$

$$p_{(P,\chi)}(0) = 0. \tag{A.2b}$$

We evaluate $\mathbf{p}(t)$ at $t = j\Delta t$, where $\Delta t = 0.2$ ns and $j = 0, \ldots, 100$.

A.2 Numerically fitting the reaction rate

The reaction rate is obtained by fitting the numerically determined values of reactant population,

$$p_R = \sum_{\chi} p_{(R,\chi)}, \tag{A.3}$$

and their respective values of t to the exponential function

$$p_R = \exp(-kt). \tag{A.4}$$

The fitting parameter k is the reaction rate. For all fits, the adjusted R^2 values have mean 0.99999 and standard deviation 7×10^{-6}. Such successful fitting reflects the reaction being first-order [134] in reactant. Here, first-order kinetics occurs because product excited states do not accumulate sufficiently (see Sec. 3.5.1) and the product ground state does not revert to reactant states at a fast enough rate (due to high activation energy).

A.3 Numerically fitting the thermodynamic parameters of activation

To determine the thermodynamic parameters of activation for a given reaction (*i.e.*, set of reaction parameters excluding temperature, T), we calculate the reaction rate, k, for $T = 278$, 283, 288, 293, 298 K. The rates are computed using numerical kinetic simulations, as described in Sec. A.2. We then fit the (k, T) values to the Eyring-Polanyi equation [249, 250],

$$k = \frac{k_B T}{h} \exp\left(-\frac{\Delta H^{\ddagger}}{RT} + \frac{\Delta S^{\ddagger}}{R}\right), \tag{A.5}$$

where R is the gas constant. The fitting parameters $\Delta H^{\ddagger}$ and $\Delta S^{\ddagger}$ are the enthalpy and entropy, respectively, of activation.

For all fits, the adjusted R^2 values have mean 0.9999996 and standard deviation 1×10^{-7}. This excellent agreement between the numerically obtained rates and the Eyring-Polanyi equation is attributed to a fortuitous choice of temperature range over which the fittings are performed. Sub-optimal goodness of fit is expected for general ranges of T because the transition rates [Eqs. (3.3), (3.7)-(3.8)] of our kinetic model have a different functional form (with respect to T) compared to Eq. (A.5).

Chapter B

Appendix for Chapter 5

B.1 Case *i*: strong coupling of only one chromophore

B.1.1 Lack of supertransfer enhancement

Here, we demonstrate that even though the donor polariton state is coherently delocalized, the superradiance enhancement of EET to bare acceptors that one could expect [173, 174] is negligible when taking into account the distance dependence and orientational correlation of the involved dipolar interactions. The essence of supertransfer is that a constructive interference of individual donor dipoles in an aggregate can lead to FRET rates that scale as N times a bare FRET rate. However, for this to happen, it is important to have a geometric arrangement where all donors are equally coupled to, *i.e.*, equidistantly spaced and identically oriented with respect to, all acceptors; this is not the case in our problem.

To show this point explicitly, we first evaluate the FRET rate associated with the delocalized donor $|D_{\vec{k}=0}\rangle$ transferring energy to bare acceptors,

$$\gamma^{FRET}_{A\leftarrow D_{\vec{k}=0}} \equiv \frac{2\pi}{\hbar}\sum_{l,m}|\langle A_{lm}|H_{DA}|D_{\vec{k}=\vec{0}}\rangle|^2 J_{A,D_{\vec{k}=\vec{0}}}$$
$$\approx \frac{2\pi}{\hbar}\mu_D^2\mu_A^2\sum_{l,m}\frac{1}{N_D}\left(\sum_{i,j}\frac{\kappa_{ijlm}}{r^3_{ijlm}}\right)^2 J_{A,D_{\vec{k}=\vec{0}}}, \tag{B.1}$$

where we have approximated $|D_{\vec{k}=0}\rangle$ as a totally symmetric state across all chromophores, $|c_{D_{i'j'}D_{\vec{k}=0}}|^2 = \frac{|\kappa_{\vec{k}D_{i'j'}}|^2}{\sum_{i,j}|\kappa_{\vec{k}D_{ij}}|^2} \approx \frac{1}{N_D}$ [see definition of $|C_{\vec{k}}\rangle$ for $C = D,A$ right after Eq. (5.6)].

Compare Eq. (B.1) to the corresponding supertransfer rate

$$\gamma_{\text{supertransfer}} = \frac{2\pi}{\hbar}\mu_D^2\mu_A^2\frac{1}{N_D}\sum_{l,m}\left|\sum_{i,j}V_{lm}\right|^2 J_{A,D}$$
$$= \frac{2\pi}{\hbar}\mu_D^2\mu_A^2\sum_{l,m}N_D V_{lm}^2 J_{A,D}, \tag{B.2}$$

where V_{lm} is the identical coupling between acceptor A_{lm} and any donor D_{ij} for all i,j and may take on any nonzero real value. Since the separations between the donors and any given acceptor are clearly different in the slab geometry of this work, the resulting rate is much less than that of Eq. (B.2).

We next show this more precisely. Consider $S^{(lm)}_{>}(\varepsilon) = \left\{(i,j)\,\middle|\,\frac{4}{r^6_{ijlm}} \geq \varepsilon^2 V_{lm}^2\right\}$ for positive $\varepsilon \to 0$, where this set has $N^{(lm)}_{>}$ elements. Then

$$\frac{1}{N_D}\left(\sum_{i,j}\frac{\kappa^2_{ijlm}}{r^3_{ijlm}}\right)^2 \leq \frac{1}{N_D}\left(\sum_{(i,j)\in S^{(lm)}_{>}(\varepsilon)}\frac{4}{r^3_{ijlm}}\right)^2 + \frac{2}{N_D}\left(\sum_{(i,j)\in S^{(lm)}_{>}(\varepsilon)}\frac{2}{r^3_{ijlm}}\right)\left(\sum_{(i,j)\notin S^{(lm)}_{>}(\varepsilon)}\frac{2}{r^3_{ijlm}}\right)$$
$$+\frac{1}{N_D}\left(\sum_{(i,j)\notin S^{(lm)}_{>}(\varepsilon)}\frac{4}{r^3_{ijlm}}\right)^2. \tag{B.3}$$

We have used the fact that the squared FRET orientation factor κ^2_{ijlm} ranges from 0 to 4 [222]. Since $S^{(lm)}_{>}(\varepsilon)$ is a finite set, the first term on the righthand side vanishes for sufficiently large N_D.

Thus,

$$\frac{1}{N_D}\left(\sum_{i,j}\frac{\kappa_{ijlm}^2}{r_{ijlm}^3}\right)^2 \leq \frac{2(N_D-N_>^{(lm)})\varepsilon|V_{lm}|}{N_D}\sum_{(i,j)\in S_>^{(lm)}(\varepsilon)}\frac{2}{r_{ijlm}^3}+\frac{(N_D-N_>^{(lm)})^2\varepsilon^2V_{lm}^2}{N_D}, \tag{B.4}$$

and so

$$\frac{\gamma_{A\leftarrow D_{\vec{k}=0}}^{FRET}}{\gamma_{\text{supertransfer}}} \leq \frac{J_{A,D_{\vec{k}=\vec{0}}}\sum_{l,m}\left[\frac{2(N_D-N_>^{(lm)})\varepsilon|V_{lm}|}{N_D}\sum_{(i,j)\in S_>^{(lm)}(\varepsilon)}\frac{2}{r_{ijlm}^3}+\frac{(N_D-N_>^{(lm)})^2\varepsilon^2V_{lm}^2}{N_D}\right]}{J_{A,D}N_D\sum_{l,m}V_{lm}^2}. \tag{B.5}$$

In the limit $N_D\to\infty$, we find

$$\frac{\gamma_{A\leftarrow D_{\vec{k}=0}}^{FRET}}{\gamma_{\text{supertransfer}}} \to \frac{J_{A,D_{\vec{k}=\vec{0}}}\varepsilon^2}{J_{A,D}} \to 0. \tag{B.6}$$

Therefore, we conclude that the decay of dipolar interactions with respect to distance precludes a supertransfer enhancement [173, 174] in our problem.

By noticing that $\left|\sum_{i,j}\frac{\kappa_{ijlm}}{r_{ijlm}^3}\right|^2 > \sum_{i,j}\frac{\kappa_{ijlm}^2}{r_{ijlm}^6}$ (at least when all $\kappa_{ijlm}\geq 0$), and for $J_{A,D}\approx J_{A,D_{\vec{k}=\vec{0}}}$, we still expect a coherence enhancement of EET: $\gamma_{A\leftarrow D_{\vec{k}=0}}^{FRET} > \frac{2\pi}{\hbar}\mu_D^2\mu_A^2\sum_{l,m}\frac{1}{N_D}\sum_{i,j}\frac{\kappa_{ijlm}^2}{r_{ijlm}^6}J_{A,D}$, the corresponding bare FRET rate. However, this enhancement is quite modest compared to all other effects that we consider in our problem (*e.g.*, PRET contributions).

B.1.2 Simulated rates: strong coupling of donors

Here, we derive expressions for the simulated rates of EET between a multi-layer slab of $N_D \gg N_{xy,D}$ donor molecules strongly coupled to a SP and a monolayer of acceptor molecules at $z = z_{0,A} > z_{j,D}$ for all j.

The polariton states $\alpha = \text{UP},\text{LP}$ are of the form $|\alpha_{D,\vec{k}}\rangle = c_{D_{\vec{k}}}\alpha_{D,\vec{k}}|D_{\vec{k}}\rangle + c_{\vec{k}}\alpha_{D,\vec{k}}|\vec{k}\rangle$, where

$|\vec{k}\rangle = a^{\dagger}_{\vec{k}}|0\rangle$ and

$$|D_{\vec{k}}\rangle = \frac{1}{\sqrt{\sum_{i,j}|\kappa_{\vec{k}D_{ij}}|^2 e^{-2a_{d\vec{k}}z_{j,D}}}}\sum_{i,j}\kappa_{\vec{k}D_{ij}}e^{-a_{d\vec{k}}z_{j,D}}e^{i\vec{k}\cdot\vec{R}_{i,D}}|D_{ij}\rangle. \tag{B.7}$$

Plugging Eq. (B.7) into Eq. (5.8a), the rate of transfer from donor polariton state $|\alpha_{D,\vec{k}}\rangle$ ($\alpha =$ UP, LP) to acceptors is

$$\begin{aligned}\gamma_{A\leftarrow\alpha_{D,\vec{k}}} &= \frac{2\pi}{\hbar}\sum_{l}\left|\langle A_{l0}|H_{DA}+H_{AP}|\alpha_{D,\vec{k}}\rangle\right|^2 J_{A\alpha_{D,\vec{k}}} \\ &= \frac{2\pi}{\hbar}\sum_{l}\left|\langle A_{l0}|H_{DA}+H_{AP}|\left(c_{D_{\vec{k}}\alpha_{D,\vec{k}}}\sum_{i,j}\frac{\kappa_{\vec{k}D_{ij}}e^{-a_{d\vec{k}}z_{j,D}}e^{i\vec{k}\cdot\vec{R}_{i,D}}}{\sqrt{\sum_{i,j}|\kappa_{\vec{k}D_{ij}}|^2e^{-2a_{d\vec{k}}z_{j,D}}}}|D_{ij}\rangle + c_{\vec{k}\alpha_{D,\vec{k}}}|\vec{k}\rangle\right)\right|^2 J_{A,\alpha_{D,\vec{k}}}.\end{aligned} \tag{B.8}$$

For simplicity, we next assume the chromophores lie in an infinitely extended and translationally invariant slab along the *xy* plane and their TDMs are isotropically distributed and orientationally uncorrelated:

$$\begin{aligned}\gamma_{A\leftarrow\alpha_{D,\vec{k}}} = |c_{D_{\vec{k}}\alpha_{D,\vec{k}}}|^2\frac{2\pi}{\hbar}N_A\sum_{i,j}\left(\frac{e^{-2a_{d\vec{k}}z_j}}{N_{xy,D}\sum_j e^{-2a_{d\vec{k}}z_{j,D}}}\right)\frac{\mu_D^2\mu_A^2\langle\kappa^2_{FRET}\rangle}{r_{ij}^6}J_{A\alpha_{D,\vec{k}}} \\ + |c_{\vec{k}\alpha_{D,\vec{k}}}|^2\frac{2\pi}{\hbar}\rho_A^{(2D)}\mu_A^2\langle|\kappa_{LM,\vec{k}}|^2\rangle\frac{\hbar\omega_{\vec{k}}}{2\varepsilon_0 L_{\vec{k}}}e^{-2a_{d\vec{k}}z_{0,A}}J_{A\alpha_{D,\vec{k}}},\end{aligned} \tag{B.9a}$$

where r_{ij} is distance between acceptor at $(0,0,z_{0,A})$ and donor ij, $\rho_A^{(2D)} = \frac{N_{xy,A}}{S}$ is the concentration of acceptors per unit area, the isotropically averaged orientation factors for FRET and light-matter interaction are $\langle\kappa^2_{FRET}\rangle = \langle\kappa^2_{ijl0}\rangle = \frac{2}{3}$ [222], and $\langle|\kappa_{LM,\vec{k}}|^2\rangle = \langle|\kappa_{\vec{k}D_{ij}}|^2\rangle = \frac{2}{3}+\frac{1}{3}\frac{|\vec{k}|^2}{a^2_{d\vec{k}}}$ [203]. Eq. (B.9a) shows that the isotropic distribution of dipoles and the lack of correlations amongst their orientations yields an incoherently averaged rate over the populations of exciton (first term) and SP (second term). Furthermore, Eq. (5.12a) is a less explicit form of Eq. (B.9a), which follows from using the approximation $\frac{e^{-2a_{d\vec{k}}z_{j,D}}}{N_{xy,D}\sum_j e^{-2a_{d\vec{k}}z_{j,D}}} \approx |c_{D_{ij}D_{\vec{k}}}|^2 = \frac{|\kappa_{\vec{k}D_{ij}}|^2e^{-2a_{d\vec{k}}z_{j,D}}}{\sum_{i,j}|\kappa_{\vec{k}D_{ij}}|^2e^{-2a_{d\vec{k}}z_{j,D}}}$ (*i.e.*, ignoring the orientational dependence of the exciton populations).

In obtaining Eq. (B.9a), we have utilized the following approximations which are valid for large N_D:

$$\left\langle \frac{\kappa_{\vec{k}D_{ij}} \kappa_{ijl0} \kappa^*_{\vec{k}D_{i'j'}} \kappa_{i'j'l0}}{\sum_{i,j} |\kappa_{\vec{k}D_{ij}}|^2 e^{-2a_{d\vec{k}} z_{j,D}}} \right\rangle \approx \frac{\langle \kappa_{\vec{k}D_{ij}} \kappa_{ijl0} \kappa^*_{\vec{k}D_{i'j'}} \kappa_{i'j'l0} \rangle}{\sum_{i,j} \langle |\kappa_{\vec{k}D_{ij}}|^2 \rangle e^{-2a_{d\vec{k}} z_{j,D}}} = \frac{\langle \kappa_{\vec{k}D_{ij}} \kappa_{ijl0} \kappa^*_{\vec{k}D_{i'j'}} \kappa_{i'j'l0} \rangle}{\langle |\kappa_{LM}|^2 \rangle N_{xy,D} \sum_j e^{-2a_{d\vec{k}} z_{j,D}}}, \tag{B.10a}$$

$$\left\langle \frac{\kappa_{\vec{k}D_{ij}} \kappa_{ijlm} \kappa^*_{\vec{k}A_{l0}}}{\sqrt{\sum_{i,j} |\kappa_{\vec{k}D_{ij}}|^2 e^{-2a_{d\vec{k}} z_{j,D}}}} \right\rangle \approx \frac{\langle \kappa_{\vec{k}D_{ij}} \kappa_{ijlm} \kappa^*_{\vec{k}A_{l0}} \rangle}{\langle \sqrt{\sum_{i,j} |\kappa_{\vec{k}D_{ij}}|^2 e^{-2a_{d\vec{k}} z_{j,D}}} \rangle}. \tag{B.10b}$$

In addition, we have applied a mean-field approach to the orientational factors,

$$\langle \kappa_{\vec{k}D_{ij}} \kappa_{ijl0} \kappa^*_{\vec{k}D_{i'j}} \kappa_{i'j'l0} \rangle \approx \langle \kappa_{\vec{k}D_{ij}} \kappa^*_{\vec{k}D_{i'j}} \rangle \langle \kappa_{ijl0} \kappa_{i'j'l0} \rangle = \langle |\kappa_{LM,\vec{k}}|^2 \rangle \langle \kappa^2_{FRET} \rangle \delta_{(i,j),(i'j')}, \tag{B.11a}$$

$$\langle \kappa_{\vec{k}D_{ij}} \kappa_{ijl0} \kappa^*_{\vec{k}A_{l0}} \rangle \approx \langle \kappa_{\vec{k}D_{ij}} \kappa^*_{\vec{k}A_{l0}} \rangle \langle \kappa_{ijl0} \rangle = 0. \tag{B.11b}$$

In the continuum limit, Eq. (B.9a) reads,

$$\gamma_{A \leftarrow \alpha_{D,\vec{k}}} = \frac{2\pi}{\hbar} \rho_A^{(2D)} \mathcal{S}_1 J_{A\alpha_{D,\vec{k}}}, \tag{B.12}$$

$$\mathcal{S}_1 = |c_{D_{\vec{k}} a_{D,\vec{k}}}|^2 \mu_D^2 \mu_A^2 \langle \kappa^2_{FRET} \rangle \frac{\int_s^{s+\mathcal{W}} dz e^{-2a_{d\vec{k}} z} \frac{\pi}{2(z_{0,A}-z)^4}}{\frac{e^{-2a_{d\vec{k}}(s+\mathcal{W})} - e^{-2a_{d\vec{k}} s}}{-2a_{d\vec{k}}}} + |c_{\vec{k}\alpha_{D,\vec{k}}}|^2 \mu_A^2 \langle |\kappa_{LM,\vec{k}}|^2 \rangle \frac{\hbar \omega_{\vec{k}}}{2\varepsilon_0 L_{\vec{k}}} e^{-2a_{d\vec{k}} z_{0,A}}, \tag{B.13}$$

where the base of the donor slab is located at $z = s$ and its thickness is $\mathcal{W}$ (while the integral over z has an analytical solution, it is complicated and does not shed much insight into the problem).

Next, we show that the rate [Eq. (5.8b)] of EET from donor dark states to a spatially separated monolayer of bare acceptors at $z = z_{0,A}$ converges to the bare FRET rate $\gamma_{\text{bare FRET}}$ in Eq. (5.12b) assuming that $N_D \gg N_{xy,D}$ and all donor and acceptor TDMs are isotropically oriented and uncorrelated. The steps applied in this subsection can be extended in a straightforward manner to establish this result for multiple layers in the acceptor slab. This result is intuitively expected given that the dark states are purely excitonic and centered at the original transition frequency ω_D; furthermore, the density of dark states is close to the original density of bare donor states. Our

derivation here relies on Lorentzian lineshapes for the dark donor and acceptor states; however, we anticipate the conclusions to hold for more general lineshapes under certain limits.

We assume that the lineshape of each dark state $|d_{D,\vec{k}}\rangle$ can be expressed as a Lorentzian with peak energy and linewidth identical to that of bare donors, leading to $J_{A,d_{D,\vec{k}}} = J_{A,D}$. Connecting this finding to the relevant rate expression, we can rewrite Eq. (5.8b) for an acceptor monolayer as

$$\gamma_{A\leftarrow dark_D} = \frac{2\pi}{\hbar}\frac{1}{N_D - N_{xy,D}}\sum_l \left[\sum_{i,j}|\langle A_{l0}|H_{DA}|D_{ij}\rangle|^2 - \sum_{\vec{k}\in \mathrm{FBZ}}|\langle A_{l0}|H_{DA}|D_{\vec{k}}\rangle|^2\right] J_{A,D}. \tag{B.14}$$

We have used the relation $\sum_{\vec{k}\in\mathrm{FBZ}}\sum_d |d_{\vec{k}}\rangle\langle d_{\vec{k}}| = 1_D^{(sys)} - \sum_{\vec{k}\in\mathrm{FBZ}}|D_{\vec{k}}\rangle\langle D_{\vec{k}}|$ for donor (electronic) identity $1_D^{(sys)}$. Assuming $N_{z,D} \gg 1$ (equivalent to $N_D \gg N_{xy,D}$), we have

$$\gamma_{A\leftarrow dark_D} = \frac{2\pi}{\hbar}\frac{1}{N_D}\sum_l\sum_{i,j}|\langle A_{l0}|H_{DA}|D_{ij}\rangle|^2 J_{A,D} - \frac{2\pi}{\hbar}\frac{1}{N_D}\sum_l\sum_{\vec{k}\in\mathrm{FBZ}}|\langle A_{l0}|H_{DA}|D_{\vec{k}}\rangle|^2 J_{A,D}. \tag{B.15}$$

We note that the first term is exactly $\gamma_{\text{bare FRET}}$. Applying the arguments from the derivation of the rate [Eq. (B.12)] of EET from donor polaritons to acceptors [including the orientational averaging approximations of Eqs. (B.10) and (B.11)], as well as the continuum approximation, we obtain

$$\gamma_{A\leftarrow dark_D} = \frac{2\pi}{\hbar}\rho_A^{(2D)}\mu_D^2\mu_A^2\langle\kappa_{FRET}^2\rangle\left[\frac{\int_s^{s+\mathcal{W}}dz\frac{\pi}{2(z_{0,A}-z)^4}}{\mathcal{W}} - \frac{1}{N_D}\sum_{\vec{k}\in\mathrm{FBZ}}\frac{\int_s^{s+\mathcal{W}}dze^{-2a_{d\vec{k}}z}\frac{\pi}{2(z_{0,A}-z)^4}}{\int_s^{s+\mathcal{W}}dze^{-2a_{d\vec{k}}z}}\right]J_{AD}. \tag{B.16}$$

Using $\sum_{\vec{k}\in\mathrm{FBZ}} = N_{xy,D}$ and $N_{z,D} \gg 1$, we arrive at

$$\begin{aligned}\frac{1}{N_D}\sum_{\vec{k}\in\mathrm{FBZ}}\frac{\int_s^{s+\mathcal{W}}dze^{-2a_{d\vec{k}}z}\frac{\pi}{2(z_{0,A}-z)^4}}{\int_s^{s+\mathcal{W}}dze^{-2a_{d\vec{k}}z}} &\leq \frac{1}{N_{z,D}}\max_{\vec{k}\in\mathrm{FBZ}}\frac{\int_s^{s+\mathcal{W}}dze^{-2a_{d\vec{k}}z}\frac{\pi}{2(z_{0,A}-z)^4}}{\int_s^{s+\mathcal{W}}dze^{-2a_{d\vec{k}}z}}\\ &\ll \frac{\int_s^{s+\mathcal{W}}dz\frac{\pi}{2(z_{0,A}-z)^4}}{\mathcal{W}},\end{aligned} \tag{B.17}$$

which yields

$$\gamma_{A\leftarrow dark_D} \approx \frac{2\pi}{\hbar}\rho_A^{(2D)}\mu_D^2\mu_A^2\langle\kappa_{FRET}^2\rangle\frac{\frac{\pi}{6}\left[\frac{1}{(z_{0,A}-s-\mathcal{W})^3}-\frac{1}{(z_{0,A}-s)^3}\right]}{\mathcal{W}}J_{AD}. \tag{B.18}$$

This expression is exactly the bare FRET rate $\gamma_{\text{bare FRET}}$ of Eq. (5.13b) under the aforementioned assumptions of infinitely extended slab along the *xy* plane, translational symmetry, orientational averaging, and the continuum limit.

B.1.3 Simulated rates: strong coupling of acceptors

The simulated rates for EET from a monolayer of bare donor at $z = z_{0,D} > z_{m,A}$ for all m to acceptor polariton/dark states asssuming a thick acceptor slab ($N_A \gg N_{xy,A}$), orientational averaging and no correlations for the TDMs $\vec{\mu}_{A_{lm}}$ are given by

$$\gamma_{\alpha_A\leftarrow D} = \frac{1}{\hbar}\int_0^{\pi/a} dk\, k\mathcal{S}_2(k)J_{\alpha_{A,\vec{k}}D}, \tag{B.19a}$$

$$\begin{aligned}\mathcal{S}_2(k) = {} & |c_{A_{\vec{k}}}\alpha_{A,\vec{k}}|^2\mu_D^2\mu_A^2\langle\kappa_{FRET}^2\rangle\frac{\int_s^{s+\mathcal{W}} dz e^{-2a_{d\vec{k}}z}\frac{\pi}{2(z_{0,D}-z)^4}}{\frac{e^{-2a_{d\vec{k}}(s+\mathcal{W})}-e^{-2a_{d\vec{k}}s}}{-2\alpha_{d\vec{k}}}} \\ & + |c_{\vec{k}}\alpha_{A,\vec{k}}|^2\mu_D^2\langle|\kappa_{LM,\vec{k}}|^2\rangle\frac{\hbar\omega_{\vec{k}}}{2\varepsilon_0 L_{\vec{k}}}e^{-2a_{d\vec{k}}z_{0,D}}\end{aligned} \tag{B.19b}$$

$$\gamma_{dark_A\leftarrow D} = \frac{2\pi}{\hbar}\rho_A\mu_D^2\mu_A^2\langle\kappa_{FRET}^2\rangle\frac{\pi}{6}\left[\frac{1}{(z_{0,D}-s-\mathcal{W})^3}-\frac{1}{(z_{0,D}-s)^3}\right]J_{AD} = \gamma'_{\text{bare FRET}}, \tag{B.19c}$$

where $\gamma'_{\text{bare FRET}}$ is the bare FRET rate. Here, the thickness of the acceptor slab is $\mathcal{W}$, its base is located at $z = s$, and its (three-dimensional) concentration is $\rho_A = \frac{N_A}{S\mathcal{W}}$. The derivation of Eq. (B.19) starts with the preliminary rate expression in Eq. (5.9) and proceeds analogously to those in Sec. B.1.2. In contrast to Eq. (B.12), Eq. (B.19a) also sums over the final polariton $\vec{k}$ modes, yielding a integral rate upon invoking the continuum-limit transformation $\sum_{\vec{k}\in\text{FBZ}} \rightarrow \frac{S}{(2\pi)^2}\int_0^{2\pi} d\phi \int_0^{\pi/a} dk\, k$ for acceptor lattice spacing a. Eq. (B.19) is a more explicit form of Eq. (5.13).

We now consider the case when

$$\frac{1}{N_{xy,A}}\sum_{\vec{k}\in\mathrm{FBZ}}|\langle\vec{k}|H_{DP}|D_{i0}\rangle|^2<\frac{1}{N_A}\sum_{l,m}|\langle A_{lm}|H_{DA}|D_{i0}\rangle|^2, \tag{B.20}$$

in other words, the average PRET coupling intensity is smaller than that of FRET; this happens when the donor-acceptor separation lies within the typical FRET range (1-10 nm). As we next show, the EET rate from a monolayer of bare donors to acceptor polariton band α_A is consequently much smaller than the bare FRET rate [$\gamma'_{\text{bare FRET}}$ in Eq. (5.13b)] as $N_A \gg N_{xy,A}$ (*i.e.*, $N_{z,A} \gg 1$), for isotropic and uncorrelated orientational distribution of TDMs $\vec{\mu}_{A_{lm}}, \vec{\mu}_{D_{i0}}$. The steps taken here resemble those employed in Sec. B.1.2. Starting from Eq. (5.13a), we utilize $|c_{A_{lm}A_{\vec{k}}}|^2 \approx \frac{1}{N_A}$ to obtain

$$\begin{aligned}
\gamma_{\alpha_A\leftarrow D} &\approx \frac{2\pi}{\hbar N_D}\sum_{\vec{k}\in\mathrm{FBZ}}\sum_i\left[|c_{A_{\vec{k}}\alpha_{A,\vec{k}}}|^2\sum_{l,m}\frac{1}{N_A}|\langle A_{lm}|H_{DA}|D_{i0}\rangle|^2+|c_{\vec{k}\alpha_{A,\vec{k}}}|^2|\langle\vec{k}|H_{DP}|D_{i0}\rangle|^2\right]J_{\alpha_{A,\vec{k}},D}\\
&\leq \frac{2\pi}{\hbar N_D}\sum_i\sum_{l,m}|\langle A_{lm}|H_{DA}|D_{i0}\rangle|^2\frac{1}{N_{z,A}}\max_{\vec{k}\in\mathrm{FBZ}}J_{\alpha_{A,\vec{k}},D}\\
&\quad+\frac{2\pi}{\hbar N_D}\sum_i\sum_{\vec{k}\in\mathrm{FBZ}}|\langle\vec{k}|H_{DP}|D_{i0}\rangle|^2\max_{\vec{k}\in\mathrm{FBZ}}J_{\alpha_{A,\vec{k}},D}\\
&\ll \frac{2\pi}{\hbar N_D}\sum_i\sum_{l,m}|\langle A_{lm}|H_{DA}|D_{i0}\rangle|^2J_{A,D}\\
&= \gamma'_{\text{bare FRET}},
\end{aligned} \tag{B.21}$$

where the second inequality holds for sufficiently large $N_{z,A}$ such that $\frac{2}{N_{z,A}}\max_{\vec{k}\in\mathrm{FBZ}}J_{\alpha_{A,\vec{k}},D} \ll J_{A,D}$. This result can be physically interpreted as follows: $\gamma'_{\text{bare FRET}}$ and $\gamma^{FRET}_{\alpha_A\leftarrow D}$ scale as the number of final states N_A and $N_{xy,A} \ll N_A$, respectively.

B.1.4 Additional simulation details

For simulations where the acceptors are under SC, the rates from donors to acceptor polariton bands [Eq. (B.19a)] were calculated numerically. In particular, the integrals over k were calculated via the trapezoidal rule using 2000 intervals.

For simulations of the "carnival effect" (*i.e.*, "reversed role" transfer from strongly coupled acceptors to donors) the coupling is strong enough such that the UP is higher in energy than the bare donors. Thus, the acceptor UP becomes a donor and the donors turn into acceptors. We use the rate Eq. (B.12) derived for the case of exclusive donor SC for transfer from a polariton state with the labels D and A interchanged.

B.2 Case *ii*: strong coupling of both donors and acceptors

B.2.1 Derivation of Eq. (5.11)

In this section, we show how to derive the EET rates in Eq. (5.11) between polariton/dark states when both donors and acceptors are strongly coupled to SP modes. While we only derive rate Eq. (5.11a) in significant detail, Eqs. (5.11b) and (5.11c) can be analogously obtained in essentially the same manner.

Excitons coupled to the $\vec{k}$-th SP mode produce polariton states of the form $|\alpha_{\vec{k}}\rangle = c_{D_{\vec{k}}\alpha_{\vec{k}}}|D_{\vec{k}}\rangle + c_{A_{\vec{k}}\alpha_{\vec{k}}}|A_{\vec{k}}\rangle + c_{\vec{k}\alpha_{\vec{k}}}|\vec{k}\rangle$. As discussed in Sec. 5.2.2, the perturbation $V^{(ii)}$ due to the chromophore and photon baths induces transitions between the UP, MP, LP and dark states of donors and acceptors,

$$V^{(ii)} = \sum_C \sum_{i,j} |C_{ij}\rangle\langle C_{ij}| \sum_q \lambda_{q,C}\hbar\omega_{q,C}(b^\dagger_{q,C_{ij}} + \text{h.c.}) + \sum_{\vec{k}}\sum_q g_{q,\vec{k}}(b^\dagger_{q,P}a_{\vec{k}} + \text{h.c.}), \tag{B.22}$$

where $C = D,A$. Given the locality of vibronic coupling, the first term only couples two states

that share the same chromophores. On the other hand, the second term does not couple different polariton/dark states because it represents radiative and Ohmic losses from the SP modes. The EET rate from a single polariton state $|\alpha_{\vec{k}}\rangle$ to the polariton band β can then be calculated by invoking Fermi's Golden Rule,

$$\gamma_{\beta\leftarrow\alpha_{\vec{k}}} = \sum_{\vec{k}'\in\mathrm{FBZ}}\sum_{C}|c_{C_{\vec{k}'}\beta_{\vec{k}'}}|^2|c_{C_{\vec{k}}\alpha_{\vec{k}}}|^2\sum_{i,j}|c_{C_{ij}C_{\vec{k}'}}|^2|c_{C_{ij}C_{\vec{k}}}|^2 \\ \times\frac{2\pi}{\hbar^2}\sum_{L'}\sum_{L}p_{L_{C_{ij}}}|\langle L'_{C_{ij}}|\sum_{q}\lambda_{q,C}\hbar\omega_{q,C}(b^{\dagger}_{q,C_{ij}}+b_{q,C_{ij}})|L_{C_{ij}}\rangle|^2\delta(\omega_{\beta_{\vec{k}'}\alpha_{\vec{k}}}+\omega_{L'_{C_{ij}}L_{C_{ij}}}). \tag{B.23}$$

$|L_{C_{ij}}\rangle$ refers to a local bath state of molecule C_{ij} and $p_{L_{C_{ij}}}$ is the thermal probability to populate it. Assuming that all molecules of the same type C (donor or acceptor) feature the same bath modes, we can associate the single-molecule rate

$$\frac{2\pi}{\hbar^2}\sum_{L'}\sum_{L}p_{L_{C_{ij}}}|\langle L'_{C_{ij}}|\sum_{q}\lambda_{q,C}\hbar\omega_{q,C}(b^{\dagger}_{q,C_{ij}}+b_{q,C_{ij}})|L_{C_{ij}}\rangle|^2\delta(\omega+\omega_{L'_{C_{ij}}L_{C_{ij}}})=\mathcal{R}_C(\omega) \tag{B.24}$$

which can be readily related to a spectral density. Then we arrive at the compact expression,

$$\gamma_{\beta\leftarrow\alpha_{\vec{k}}} = \sum_{\vec{k}'\in\mathrm{FBZ}}\sum_{C}|c_{C_{\vec{k}'}\beta_{\vec{k}'}}|^2|c_{C_{\vec{k}}\alpha_{\vec{k}}}|^2\sum_{i,j}|c_{C_{ij}C_{\vec{k}'}}|^2|c_{C_{ij}C_{\vec{k}}}|^2\mathcal{R}_C(\omega_{\beta_{\vec{k}'}\alpha_{\vec{k}}}), \tag{B.25}$$

which is exactly Eq. (5.11a).

To derive the average rate Eq. (5.11b) from dark states of chromophore C to the polariton band α, we begin with

$$\gamma_{\alpha\leftarrow dark_C} = \frac{2\pi}{\hbar^2}\sum_{\vec{k}'\in\mathrm{FBZ}}\frac{1}{N_C-N_{xy,C}}\sum_{\vec{k}\in\mathrm{FBZ}}\sum_{d}\sum_{i'j'}\sum_{L'}\sum_{i''j''}\sum_{L}\Big[p_{L_{C_{i''j''}}}|\langle\alpha_{\vec{k}'},L'_{C_{i'j'}}|V^{(ii)}|d_{C,\vec{k}},L_{C_{i''j''}}\rangle|^2 \\ \times\delta(\omega_{\alpha_{\vec{k}'}C}+\omega_{L'_{C_{i'j'}}L_{C_{i''j''}}})\Big]. \tag{B.26}$$

Similarly, the derivation of rate Eq. (5.11c) from polariton state $|\alpha_{\vec{k}}\rangle$ to the same dark states starts

at

$$\gamma_{dark_C \leftarrow \alpha_{\vec{k}}} = \frac{2\pi}{\hbar^2} \sum_{\vec{k} \in \mathrm{FBZ}} \sum_{d} \sum_{i'j'} \sum_{L'} \sum_{i''j''} \sum_{L} p_{L_{C_{i''j''}}} |\langle d_{C,\vec{k}'}, L'_{C_{i'j'}} | V^{(ii)} | \alpha_{\vec{k}}, L_{C_{i''j''}} \rangle|^2 \delta(\omega_{C\alpha_{\vec{k}}} + \omega_{L'_{C_{i'j'}} L_{C_{i''j''}}}). \tag{B.27}$$

We note that the presence of the prefactor $\frac{1}{N_C - N_{xy,C}}$ in Eq. (B.26) and lack thereof in Eq. (B.27) is due to the asymmetry of Fermi's Golden Rule: in the former equation, dark states serve as the initial state and thus the term for each state is weighted by its occupation probability, which we have assumed to be uniform at $\frac{1}{N_C - N_{xy,C}}$ given their degeneracy.

B.2.2 Simulated rates

In this section, we present the rates used in our simulations for both donors and acceptors strongly coupled to SPs assuming orientationally averaged TDMs $\vec{\mu}_{C_{ij}}$, $N_{xy,D} = N_{xy,A} = N_{xy}$, and $N_{z,C} \gg 1$ for $C = D, A$.

The overlap between $|C_{ij}\rangle$ and the collective mode $|C_{\vec{k}}\rangle$ can be written as $|c_{C_{ij}C_{\vec{k}}}| = \frac{\kappa_{\vec{k}C_{ij}} e^{-a_{d\vec{k}} z_{j,C}}}{\sqrt{\sum_{i,j} |\kappa_{\vec{k}C_{ij}}|^2 e^{-2a_{d\vec{k}} z_{j,C}}}}$ and plugged into Eq. (5.11a) to obtain the rate for EET from polariton state $|\alpha_{\vec{k}}\rangle$ to band β:

$$\gamma_{\beta \leftarrow \alpha_{\vec{k}}} = \frac{1}{2\pi} \sum_{C} \left[\frac{|c_{C_{\vec{k}}\alpha}|^2}{\rho_C \frac{e^{-2a_{d\vec{k}}(s_C + \mathcal{W}_C)} - e^{-2a_{d\vec{k}} s_C}}{-2a_{d\vec{k}}}} \right.$$
$$\left. \times \int_0^{\pi/a} dk'\, k' |c_{C_{\vec{k}}\beta}|^2 \frac{\frac{e^{-2(a_{d\vec{k}} + a_{d\vec{k}'})(s_D + \mathcal{W}_D)} - e^{-2(a_{d\vec{k}} + a_{d\vec{k}'})s_D}}{-4a_{d\vec{k}'}}}{\frac{e^{-2a_{d\vec{k}'}(s_D + \mathcal{W}_D)} - e^{-2a_{d\vec{k}'} s_D}}{-2a_{d\vec{k}'}}} \mathcal{R}_C(\omega_{\beta_{\vec{k}'}\alpha_{\vec{k}}}) \right], \tag{B.28}$$

where we have applied orientational averaging of the TDMs under the approximation $\langle |c_{C_{ij}C_{\vec{k}}}|^2 \rangle \approx \frac{e^{-2a_{d\vec{k}} z_{j,C}}}{N_{xy} \sum_j e^{-2a_{d\vec{k}} z_{j,C}}}$ (Sec. B.1.2) and the $\vec{k}$-space continuum-limit transformation (Sec. B.1.3).

The derivation of the EET rate from polariton $|\alpha_{\vec{k}}\rangle$ to dark states is similar to that of Eq.

(B.18) (Sec. B.1.2). We can write Eq. (5.11c) as

$$\gamma_{dark_C \leftarrow \alpha_{\vec{k}}} = |c_{C_{\vec{k}}\alpha_{\vec{k}}}|^2 \mathcal{R}_C(\omega_{C\alpha_{\vec{k}}}) \sum_{i,j} |c_{C_{ij}C_{\vec{k}}}|^2 \sum_{\vec{k}' \in \mathrm{FBZ}} \sum_{d} |\langle C_{ij}|d_{C,\vec{k}'}\rangle|^2. \tag{B.29}$$

Inserting the relation $\sum_{\vec{k}\in\mathrm{FBZ}} \sum_d |d_{C,\vec{k}}\rangle\langle d_{C,\vec{k}}| = 1_C^{(sys)} - \sum_{\vec{k}\in\mathrm{FBZ}} |C_{\vec{k}}\rangle\langle C_{\vec{k}}|$, we obtain

$$\gamma_{dark_C \leftarrow \alpha_{\vec{k}}} = |c_{C_{\vec{k}}\alpha_{\vec{k}}}|^2 \mathcal{R}_C(\omega_{C\alpha_{\vec{k}}}) \sum_{i,j} |c_{C_{ij}C_{\vec{k}}}|^2 \left(1 - \sum_{\vec{k}' \in \mathrm{FBZ}} |c_{C_{ij}C_{\vec{k}'}}|^2\right). \tag{B.30}$$

Noting that $|c_{C_{ij}C_{\vec{k}'}}|^2 \sim \frac{1}{N_{xy}N_{z,C}}$ and $\sum_{\vec{k}\in\mathrm{FBZ}}$ sums over N_{xy} terms, we utilize $N_{z,C} \gg 1$ and $\sum_{i,j} |c_{C_{ij}C_{\vec{k}}}|^2 = 1$ to write

$$\gamma_{dark_C \leftarrow \alpha_{\vec{k}}} = |c_{C_{\vec{k}}\alpha_{\vec{k}}}|^2 \mathcal{R}_C(\omega_{C\alpha_{\vec{k}}}). \tag{B.31}$$

This same logic can be applied to arrive at

$$\gamma_{\alpha \leftarrow dark_C} = \frac{1}{2\pi\rho_C \mathcal{W}_C} \int_0^{\pi/a} dk'\, k' |c_{C_{\vec{k}'}\alpha_{\vec{k}'}}|^2 \mathcal{R}_C(\omega_{\alpha_{\vec{k}'}C}) \tag{B.32}$$

for a continuum of $\vec{k}$ states.

In summary, the simulated equations for the case where both donors and acceptors are strongly coupled are

$$\gamma_{\beta \leftarrow \alpha_{\vec{k}}} = \frac{1}{2\pi} \sum_C \left[\frac{|c_{C_{\vec{k}}\alpha}|^2}{\rho_C \frac{e^{-2a_{d\vec{k}}(s_C+\mathcal{W}_C)} - e^{-2a_{d\vec{k}}s_C}}{-2a_{d\vec{k}}}} \right.$$
$$\left. \times \int_0^{\pi/a} dk'\, k' |c_{C_{\vec{k}}\beta}|^2 \frac{\frac{e^{-2(a_{d\vec{k}}+a_{d\vec{k}'})(s_D+\mathcal{W}_D)} - e^{-2(a_{d\vec{k}}+a_{d\vec{k}'})s_D}}{-4a_{d\vec{k}'}}}{\frac{e^{-2a_{d\vec{k}'}(s_D+\mathcal{W}_D)} - e^{-2a_{d\vec{k}'}s_D}}{-2a_{d\vec{k}'}}} \mathcal{R}_C(\omega_{\beta_{\vec{k}'}\alpha_{\vec{k}}}) \right], \tag{B.33a}$$

$$\gamma_{\alpha \leftarrow dark_C} = \frac{1}{2\pi\rho_C \mathcal{W}_C} \int_0^{\pi/a} dk'\, k' |c_{C_{\vec{k}'}\alpha_{\vec{k}'}}|^2 \mathcal{R}_C(\omega_{\alpha_{\vec{k}'}C}), \tag{B.33b}$$

$$\gamma_{dark_C \leftarrow \alpha_{\vec{k}}} = |c_{C_{\vec{k}}\alpha_{\vec{k}}}|^2 \mathcal{R}_C(\omega_{C\alpha_{\vec{k}}}). \tag{B.33c}$$

From these expressions, it can be seen that the rates to polariton bands [Eqs. (B.33a) and (B.33b)]

scale as $\sim \frac{1}{N_{z,C}}$ relative to the rate to dark states [Eq. (B.33c)], which scales as a single-molecule rate $\mathcal{R}_C$. This is because there are N_{xy} states in each polariton band as opposed to $N_C - N_{xy}$ in the band of dark states.

The spectral density [Eq. (5.14)] that governs $\mathcal{R}_C(\omega)$ depends on the energies $\hbar\omega_q$ and coupling strengths $\lambda_q\hbar\omega_q$ of representative localized vibrational modes B_{TDBC}, reproduced below from literature [226]:

$\hbar\omega_q$ (meV)	40	80	120	150	185	197
$\lambda_q\hbar\omega_q$ (meV)	14	18	25	43	42	67

B.2.3 Rate parameters for comparison to experiments

Here, we present closed-form expressions for certain rate parameters characterizing downhill vibrational-relaxation transitions between polariton and dark states. Specifically, these rate parameters were first introduced as empirical constants fitted to the data of Coles et al. [89]. For spatially separated slabs of donors and acceptors—the setup studied in our work—such experimental values are not available in the literature. Instead, we compare to those of Coles et al. for a blend of donors and acceptors. This comparison is supported by qualitatively similar photoluminescence for both setups, as reported by the same authors [89].

Based on their fitting model [Eqs. (3)-(5) of Ref. [89]], we express their rate parameters $\{\mathcal{C}_5^{\mathrm{UPB}} = (34\text{ fs})^{-1}, \mathcal{C}_2 = (603\text{ ps})^{-1}, \mathcal{C}_5^{\mathrm{MPB}} = (8.5\text{ fs})^{-1}, \mathcal{C}_1 = (228\text{ ps})^{-1}\}$ (Table 1 of Ref. [89]) in terms of our theoretical framework as follows (throughout this section we use the convention

$c_{a,b} = \langle a|b\rangle$ and $\omega_{f,i} = \omega_f - \omega_i$):

$$\mathcal{C}_5^{\mathrm{UPB}} \equiv \max_{\vec{k}}\{\gamma_{dark_D \leftarrow \mathrm{UP}_{\vec{k}}}\}, \tag{B.34a}$$

$$\mathcal{C}_2 \equiv N_{dark_D}\left\langle 2\pi \mathcal{J}_D(-\omega_{\mathrm{MP}_{\vec{k}},D})\frac{\pi k^2}{(2\pi)^2/S}\frac{1}{N_D}\right\rangle_{\vec{k}} \tag{B.34b}$$

$$= \frac{N_{dark_D}}{2\rho_D \mathcal{W}_D}\frac{\int_{k_{\min}}^{k_{\max}} dk'\,(k')^3 \mathcal{J}_D(-\omega_{\mathrm{MP}_{\vec{k}'},D})}{\frac{1}{2}(k_{\max}^2 - k_{\min}^2)}, \tag{B.34c}$$

$$\mathcal{C}_5^{\mathrm{MPB}} \equiv \max_{\vec{k}}\{\gamma_{dark_A \leftarrow \mathrm{MP}_{\vec{k}}}\}, \tag{B.34d}$$

$$\mathcal{C}_1 \equiv N_{dark_A}\left\langle 2\pi \mathcal{J}_A(\omega_{-\mathrm{LP}_{\vec{k}},A})\frac{\pi k^2}{(2\pi)^2/S}\frac{1}{N_A}\right\rangle_{\vec{k}} \tag{B.34e}$$

$$= \frac{N_{dark_A}}{2\rho_A \mathcal{W}_A}\frac{\int_{k_{\min}}^{k_{\max}} dk'\,(k')^3 \mathcal{J}_A(-\omega_{\mathrm{LP}_{\vec{k}'},A})}{\frac{1}{2}(k_{\max}^2 - k_{\min}^2)}, \tag{B.34f}$$

where the relations in Eqs. (B.34b) and (B.34e) were obtained by comparing the first terms on the right-hand sides of Eqs. (4) and (3) of Ref. [89], respectively, with Eq. (15) of the theoretical work by Michetti and La Rocca [234]. The particular $k_{\min}, k_{\max}$ used in calculation of $\mathcal{C}_2$ and $\mathcal{C}_1$ in Table 5.2 are given in the next section. $\mathcal{J}_C(\omega)$ is the spectral density [defined after Eq. (5.11)] for chromophore $C = D, A$. N_{dark_C} is a fitting constant proportional to the steady-state population—assumed to be invariant with respect to wavevector by Coles et al. Notice that $\mathcal{C}_5^{\mathrm{UPB}}$ and $\mathcal{C}_5^{\mathrm{MPB}}$ can be numerically evaluated using theory presented above [Eq. (B.33c)]. However, numerical computation of $\mathcal{C}_2$ and $\mathcal{C}_1$ requires the values of N_{dark_C}, which are not actually defined by Coles et al. [89]. Given that the precise values $\mathcal{C}$ were determined by Michetti and La Rocca [234] (as well as other references; see first three sentences of footnotes of Table 1 in Ref. [89]), we next estimate N_{dark_C} using a combination of experimental results from Ref. [89] and the theoretical results from Ref. [234].

The first step is to relate $\mathcal{C}_2$ and $\mathcal{C}_1$ to FGR rates $\gamma_{\mathrm{MP}_{\vec{k}} \leftarrow dark_D}$ and $\gamma_{\mathrm{LP}_{\vec{k}} \leftarrow dark_A}$ [Eq. (B.33b)]

using Eqs. (4) and (3) of Ref. [89]:[2]

$$N_{dark_D} \approx \frac{(603\text{ ps})^{-1}\left\langle |c_{D,\mathrm{MP}_\theta}|^2[n(-\omega_{\mathrm{MP}_\theta,D})+1]\right\rangle_\theta}{\left\langle \gamma_{\mathrm{MP}_\theta \leftarrow dark_D}\right\rangle_\theta}, \tag{B.35a}$$

$$N_{dark_A} \approx \frac{(228\text{ ps})^{-1}\left\langle |c_{A,\mathrm{LP}_\theta}|^2[n(-\omega_{\mathrm{LP}_\theta,A})+1]\left(\frac{|\omega_{\mathrm{LP}_\theta,A}|}{75\text{ meV}/\hbar}\right)^{1.93}\right\rangle_\theta}{\left\langle \gamma_{\mathrm{LP}_\theta \leftarrow dark_A}\right\rangle_\theta}, \tag{B.35b}$$

where $|c_{C,\alpha_\theta}|^2$ is the fraction of exciton C in polariton state α_θ for $(C,\alpha) = (D,\mathrm{MP}),(A,\mathrm{LP})$ and $n(\omega) = \frac{1}{e^{\hbar\omega/k_BT}-1}$ is the Bose-Einstein distribution function. We have replaced $\vec{k}$ with θ to indicate quantities that are either experimentally determined for a polariton state excited by a laser with this incident angle (see Coles et al. [89] for further experimental details) or estimated from Michetti and La Rocca [234]. We carry out the averages $\langle\cdot\rangle_\theta$ above over the θ-interval $[\theta_{\min} = 17^\circ, \theta_{\max} = 56^\circ]$ by making the following assumptions:

- $$|c_{D,\mathrm{MP}_\theta}|^2 = \begin{cases} 0 & \theta \in [\theta_{\min}, 27^\circ] \\ \frac{0.8}{\theta_{\max}-27^\circ}(\theta-\theta_{\max})+0.8 & \theta \in [27^\circ, \theta_{\max}] \end{cases} \tag{B.36}$$

  (Fig. 3d of Coles et al. [89])

- $n(-\omega_{\mathrm{MP}_\theta,D}) \approx 0$ because $|\omega_{\mathrm{MP}_\theta,D}| \gg k_BT$ (Figs. 4a-4c of Coles et al. [89])

- $$|c_{A,\mathrm{LP}_\theta}|^2 = \begin{cases} \frac{0.9}{47^\circ-\theta_{\min}}(\theta-47^\circ)+0.9 & \theta \in [\theta_{\min}, 47^\circ] \\ 0.9 & \theta \in [47^\circ, \theta_{\max}] \end{cases} \tag{B.37}$$

  (Fig. 3e of Coles et al. [89]),

[2] We associate the nomenclature of Coles et al. to ours to minimize the introduction of new names and variables: upper polariton band (UPB) $\rightarrow$ UP, middle polariton band (MPB) $\rightarrow$ MP, and lower polariton band (LPB) $\rightarrow$ LP, ex2 $\rightarrow$ donors (D), exciton reservoir ex2 $\rightarrow$ dark donors ($dark_D$), ex1 $\rightarrow$ acceptors (A), exciton reservoir ex1 $\rightarrow$ dark acceptors ($dark_A$).

- $$\omega_{\mathrm{LP}_\theta,A}(\mathrm{nm}^{-1}) = \frac{1}{\frac{-30\ \mathrm{nm}}{\theta_{\max}-\theta_{\min}}(\theta-\theta_{\max})+640\ \mathrm{nm}} - \frac{1}{636.4\ \mathrm{nm}} \tag{B.38}$$

  (Figs. 4a-4c of Coles et al. [89]),

- $\langle \gamma_{\mathrm{MP}_\theta \leftarrow dark_D} \rangle_\theta \approx \langle \gamma_{\mathrm{LP}_\theta \leftarrow dark_A} \rangle_\theta \approx 10^7\ \mathrm{s}^{-1}$ (roughly the average rate of scattering from the dark states to states in the LP close to the anticrossing for microcavity with a single strongly coupled J-aggregate cyanine dye, Fig. 6 of Michetti and La Rocca [89]).

Then we arrive at $N_{dark_D} \approx 49$ and $N_{dark_A} \approx 112$.

Using these quantities, numerical values for Eq. (B.34) can be calculated, as discussed in the next section. Comparison of the values to the rate parameters of Coles et al. is summarized in Table 5.2.

B.2.4 Additional simulation details

We note that the rates in Eqs. (B.33a) and (B.33b) from polariton and dark states, respectively, to polariton bands were calculated numerically: as for the case of exclusive SC of acceptors to SPs (Sec. B.1.4), the k-integrals were computed with the trapezoidal rule using 2000 intervals.

For the downhill energy transfer processes between polariton and dark states, we also compared (Table 5.2) rate parameters $\mathcal{C}$ that were experimentally determined by Coles et al. [89] to analogous theoretical rate parameters that we presented in Sec. B.2.3. The latter values, shown in the second column of Table 5.2, were calculated by computing the $\mathcal{C}$ in Eq. (B.34) with the same simulation conditions as for Fig. 5.5b, except considering $T = 300$ K and polariton k-interval $[k_{\min} = 0.8k_A, k_{\max} = 1.1k_D]$ (instead of $T = 0$ K and the entire FBZ, respectively; see next paragraph for justification). $k_A = 9.8 \times 10^6\ \mathrm{m}^{-1}$ and $k_D = 1.1 \times 10^7\ \mathrm{m}^{-1}$ are the anticrossing wavevectors for acceptors and donors, respectively. Given the reduced k-interval, the numerical integrals

[Eqs. (B.34c) and (B.34f)] were evaluated using only 200 intervals (instead of 2000). The results are plotted in Fig. 5.7.

The above changes in temperature and k-interval were chosen to allow for a more direct comparison with the experiments of Coles et al. Their experiments were carried out at room temperature and only probed polariton states near the anticrossings. Our choice of $[k_{\min}, k_{\max}]$ comes from the paper of Hakala et al. [236]. To the best of our knowledge, this is the only work that studies a system with SPs strongly coupled to two organic-exciton bands and reports the concentration of the chromophore *after* it has been deposited on the metal and becomes strongly coupled to SPs. Specifically, the three polariton bands formed from hybridization of SPs and two exciton bands of Rhodamine 6G dye afforded absorption signal detectable in the window$\sim$ $[1.2\times10^7\ \mathrm{m}^{-1}, 1.8\times10^7\ \mathrm{m}^{-1}]$, or between ~ 0.8 of the smaller anticrossing wavevector and ~ 1.1 of the bigger. This result stayed essentially the same for a wide range of concentrations, ranging from 0.1-10% of that used in this work for strongly coupled chromophores. So we employed $[k_{\min}, k_{\max}]$ for our calculation of $\mathcal{C}$ (without changing the concentration we assumed for Fig. 5.5b).

It should be noted that between the systems of our work and Coles et al., there are differences in setup (physically separated slabs vs. blend) and electromagnetic modes (SP vs. microcavity). We argue that these differences do not preclude good agreement with respect to order of magnitude:

- The validity of comparing physically separated slabs and a blend of donors and acceptors has been explained in Sec. B.2.3, as well as Sec. 5.3.

- Energy-transfer rates [Eq. (5.11)] are dictated by energy gaps between polariton and dark states, exciton fractions of polariton states, and the spectral densities, regardless of the nature of the electromagnetic modes.

Bibliography

[1] K. Hirai, J. A. Hutchison, and H. Uji-i. Recent progress in vibropolaritonic chemistry. *ChemPlusChem*, 85(9):1981–1988, 2020.

[2] A. V. Kavokin, J. J. Baumberg, G. Malpuech, and F. P. Laussy. *Microcavities*. Series on Semiconductor Science and Technology. Oxford University Press, 2017.

[3] T. W. Ebbesen. Hybrid light–matter states in a molecular and material science perspective. *Acc. Chem. Res.*, 49(11):2403–2412, 2016.

[4] R. F. Ribeiro, L. A. Martínez-Martínez, M. Du, J. Campos-Gonzalez-Angulo, and J. Yuen-Zhou. Polariton chemistry: controlling molecular dynamics with optical cavities. *Chem. Sci.*, 9(30):6325–6339, 2018.

[5] V. M. Agranovich, Y. N. Gartstein, and M. Litinskaya. Hybrid resonant organic–inorganic nanostructures for optoelectronic applications. *Chem. Rev.*, 111(9):5179–5214, 2011.

[6] M. Hertzog, M. Wang, J. Mony, and K. Börjesson. Strong light–matter interactions: a new direction within chemistry. *Chem. Soc. Rev.*, 48(3):937–961, 2019.

[7] J. Feist, J. Galego, and F. J. Garcia-Vidal. Polaritonic chemistry with organic molecules. *ACS Photonics*, 5(1):205–216, 2018.

[8] F. Herrera and F. C. Spano. Theory of nanoscale organic cavities: The essential role of vibration-photon dressed states. *ACS Photonics*, 5(1):65–79, 2018.

[9] J. Flick, N. Rivera, and P. Narang. Strong light-matter coupling in quantum chemistry and quantum photonics. *Nanophotonics*, 7(9):1479–1501, 2018.

[10] F. Herrera and J. Owrutsky. Molecular polaritons for controlling chemistry with quantum optics. *J. Chem. Phys.*, 152(10):100902, 2020.

[11] E. Coccia, J. Fregoni, C. A. Guido, M. Marsili, S. Pipolo, and S. Corni. Hybrid theoretical models for molecular nanoplasmonics. *J. Chem. Phys.*, 153(20):200901, 2020.

[12] T. E. Li, B. Cui, J. E. Subotnik, and A. Nitzan. Molecular polaritonics: Chemical dynamics under strong light–matter coupling. *Annu. Rev. Phys. Chem.*, 2021.

[13] D. S. Wang and S. F. Yelin. A roadmap toward the theory of vibrational polariton chemistry. *ACS Photonics*, 8(10):2818–2826, 2021.

[14] B. Xiang and W. Xiong. Molecular vibrational polariton: Its dynamics and potentials in novel chemistry and quantum technology. *J. Chem. Phys.*, 155(5):050901, 2021.

[15] D. Sidler, M. Ruggenthaler, C. Schäfer, E. Ronca, and A. Rubio. A perspective on ab initio modeling of polaritonic chemistry: The role of non-equilibrium effects and quantum collectivity. *arXiv preprint arXiv:2108.12244*, 2021.

[16] A. D. Dunkelberger, B. S. Simpkins, I. Vurgaftman, and J. C. Owrutsky. Vibration-cavity polariton chemistry and dynamics. *Annu. Rev. Phys. Chem.*, 2022.

[17] A. Shalabney, J. George, J. Hutchison, G. Pupillo, C. Genet, and T. W. Ebbesen. Coherent coupling of molecular resonators with a microcavity mode. *Nat. Commun.*, 6(1):5981, 2015.

[18] J. P. Long and B. S. Simpkins. Coherent coupling between a molecular vibration and Fabry–Perot optical cavity to give hybridized states in the strong coupling limit. *ACS Photonics*, 2 (1):130–136, 2015.

[19] S. R. Casey and J. R. Sparks. Vibrational strong coupling of organometallic complexes. *J. Phys. Chem. C*, 120(49):28138–28143, 2016.

[20] A. Thomas, J. George, A. Shalabney, M. Dryzhakov, S. J. Varma, J. Moran, T. Chervy, X. Zhong, E. Devaux, C. Genet, J. A. Hutchison, and T. W. Ebbesen. Ground-state chemical reactivity under vibrational coupling to the vacuum electromagnetic field. *Angew. Chem., Int. Ed.*, 128(38):11634–11638, 2016.

[21] A. Thomas, L. Lethuillier-Karl, K. Nagarajan, R. M. A. Vergauwe, J. George, T. Chervy, A. Shalabney, E. Devaux, C. Genet, J. Moran, and T. W. Ebbesen. Tilting a ground-state reactivity landscape by vibrational strong coupling. *Science*, 363(6427):615–619, 2019.

[22] J. Lather, P. Bhatt, A. Thomas, T. W. Ebbesen, and J. George. Cavity catalysis by cooperative vibrational strong coupling of reactant and solvent molecules. *Angew. Chem., Int. Ed.*, 58 (31):10635–10638, 2019.

[23] K. Hirai, R. Takeda, J. A. Hutchison, and H. Uji-i. Modulation of Prins cyclization by vibrational strong coupling. *Angew. Chem., Int. Ed.*, 132(13):5370–5373, 2020.

[24] H. Hiura and A. Shalabney. Vacuum-field catalysis: Accelerated reactions by vibrational ultra strong coupling. *ChemRxiv*, 2021.

[25] R. M. A. Vergauwe, A. Thomas, K. Nagarajan, A. Shalabney, J. George, T. Chervy, M. Seidel, E. Devaux, V. Torbeev, and T. W. Ebbesen. Modification of enzyme activity by vibrational strong coupling of water. *Angew. Chem., Int. Ed.*, 58(43):15324–15328, 2019.

[26] J. Lather and J. George. Improving enzyme catalytic efficiency by co-operative vibrational strong coupling of water. *J. Phys. Chem. Lett.*, 12(1):379–384, 2021.

[27] J. Galego, C. Climent, F. J. Garcia-Vidal, and J. Feist. Cavity Casimir-Polder forces and their effects in ground-state chemical reactivity. *Phys. Rev. X*, 9(2):021057, 2019.

[28] J. A. Campos-Gonzalez-Angulo and J. Yuen-Zhou. Polaritonic normal modes in transition state theory. *J. Chem. Phys.*, 152(16):161101, 2020.

[29] T. E. Li, A. Nitzan, and J. E. Subotnik. On the origin of ground-state vacuum-field catalysis: Equilibrium consideration. *J. Chem. Phys.*, 152(23):234107, 2020.

[30] V. P. Zhdanov. Vacuum field in a cavity, light-mediated vibrational coupling, and chemical reactivity. *Chem. Phys.*, 535:110767, 2020.

[31] P. Hänggi, P. Talkner, and M. Borkovec. Reaction-rate theory: fifty years after Kramers. *Rev. Mod. Phys.*, 62(2):251–341, 1990.

[32] E. W. Fischer and P. Saalfrank. Ground state properties and infrared spectra of anharmonic vibrational polaritons of small molecules in cavities. *J. Chem. Phys.*, 154(10):104311, 2021.

[33] X. Li, A. Mandal, and P. Huo. Cavity frequency-dependent theory for vibrational polariton chemistry. *Nat. Commun.*, 12(1):1315, 2021.

[34] X. Li, A. Mandal, and P. Huo. Theory of mode-selective chemistry through polaritonic vibrational strong coupling. *J. Phys. Chem. Lett.*, 12(29):6974–6982, 2021.

[35] P.-Y. Yang and J. Cao. Quantum effects in chemical reactions under polaritonic vibrational strong coupling. *J. Phys. Chem. Lett.*, 12(39):9531–9538, 2021.

[36] C. Schäfer, J. Flick, E. Ronca, P. Narang, and A. Rubio. Shining light on the microscopic resonant mechanism responsible for cavity-mediated chemical reactivity. *arXiv preprint arXiv:2104.12429*, 2021.

[37] A. Mandal, X. Li, and P. Huo. Theory of vibrational polariton chemistry in the collective coupling regime. *J. Chem. Phys.*, 156(1):014101, 2021.

[38] J. A. Campos-Gonzalez-Angulo, R. F. Ribeiro, and J. Yuen-Zhou. Resonant catalysis of thermally activated chemical reactions with vibrational polaritons. *Nat. Commun.*, 10(1): 4685, 2019.

[39] N. T. Phuc, P. Q. Trung, and A. Ishizaki. Controlling the nonadiabatic electron-transfer reaction rate through molecular-vibration polaritons in the ultrastrong coupling regime. *Sci. Rep.*, 10(1):7318, 2020.

[40] B. S. Simpkins, A. D. Dunkelberger, and J. C. Owrutsky. Mode-specific chemistry through vibrational strong coupling (or a wish come true). *J. Phys. Chem. C*, 125(35):19081–19087, 2021.

[41] M. Du, J. A. Campos-Gonzalez-Angulo, and J. Yuen-Zhou. Nonequilibrium effects of cavity leakage and vibrational dissipation in thermally activated polariton chemistry. *J. Chem. Phys.*, 154(8):084108, 2021.

[42] M. Du and J. Yuen-Zhou. Catalysis by dark states in vibropolaritonic chemistry. *Phys. Rev. Lett.*, 128(9):096001, 2022.

[43] M. Du, R. F. Ribeiro, and J. Yuen-Zhou. Remote control of chemistry in optical cavities. *Chem*, 5(5):1167–1181, 2019.

[44] M. Du, L. A. Martínez-Martínez, R. F. Ribeiro, Z. Hu, V. M. Menon, and J. Yuen-Zhou. Theory for polariton-assisted remote energy transfer. *Chem. Sci.*, 9(32):6659–6669, 2018.

[45] R. A. Marcus. Chemical and electrochemical electron-transfer theory. *Annu. Rev. Phys. Chem.*, 15(1):155–196, 1964.

[46] V. G. Levich. Present state of the theory of oxidation-reduction in solution (bulk and electrode reactions). *Adv. Electrochem. Electrochem. Eng*, 4:249–371, 1966.

[47] J. Jortner. Temperature dependent activation energy for electron transfer between biological molecules. *J. Chem. Phys.*, 64(12):4860–4867, 1976.

[48] P. Törmä and W. L. Barnes. Strong coupling between surface plasmon polaritons and emitters: a review. *Rep. Prog. Phys.*, 78(1):013901, 2015.

[49] O. Bitton, S. N. Gupta, and G. Haran. Quantum dot plasmonics: from weak to strong coupling. *Nanophotonics*, 8(4):559–575, 2019.

[50] N. S. Mueller, Y. Okamura, B. G. M. Vieira, S. Juergensen, H. Lange, E. B. Barros, F. Schulz, and S. Reich. Deep strong light–matter coupling in plasmonic nanoparticle crystals. *Nature*, 583(7818):780–784, 2020.

[51] V. M. Agranovich, M. Litinskaia, and D. G. Lidzey. Cavity polaritons in microcavities containing disordered organic semiconductors. *Phys. Rev. B*, 67(8):085311, 2003.

[52] T. Virgili, D. Coles, A. M. Adawi, C. Clark, P. Michetti, S. K. Rajendran, D. Brida, D. Polli, G. Cerullo, and D. G. Lidzey. Ultrafast polariton relaxation dynamics in an organic semiconductor microcavity. *Phys. Rev. B*, 83(24):245309, 2011.

[53] J. del Pino, J. Feist, and F. J. Garcia-Vidal. Quantum theory of collective strong coupling of molecular vibrations with a microcavity mode. *New J. Phys.*, 17(5):053040, 2015.

[54] T. Neuman and J. Aizpurua. Origin of the asymmetric light emission from molecular exciton–polaritons. *Optica*, 5(10):1247–1255, 2018.

[55] B. Xiang, R. F. Ribeiro, A. D. Dunkelberger, J. Wang, Y. Li, B. S. Simpkins, J. C. Owrutsky, J. Yuen-Zhou, and W. Xiong. Two-dimensional infrared spectroscopy of vibrational polaritons. *Proc. Natl. Acad. Sci. U. S. A.*, 115(19):4845–4850, 2018.

[56] R. F. Ribeiro, A. D. Dunkelberger, B. Xiang, W. Xiong, B. S. Simpkins, J. C. Owrutsky, and J. Yuen-Zhou. Theory for nonlinear spectroscopy of vibrational polaritons. *J. Phys. Chem. Lett.*, 9(13):3766–3771, 2018.

[57] G. D. Scholes, C. A. DelPo, and B. Kudisch. Entropy reorders polariton states. *J. Phys. Chem. Lett.*, 11(15):6389–6395, 2020.

[58] J. Galego, F. J. Garcia-Vidal, and J. Feist. Cavity-induced modifications of molecular structure in the strong-coupling regime. *Phys. Rev. X*, 5(4):041022, 2015.

[59] M. Kowalewski, K. Bennett, and S. Mukamel. Cavity femtochemistry: Manipulating nonadiabatic dynamics at avoided crossings. *J. Phys. Chem. Lett.*, 7(11):2050–2054, 2016.

[60] T. Szidarovszky, G. J. Halász, A. G. Császár, L. S. Cederbaum, and Á. Vibók. Conical intersections induced by quantum light: Field-dressed spectra from the weak to the ultrastrong coupling regimes. *J. Phys. Chem. Lett.*, 9(21):6215–6223, 2018.

[61] T. S. Haugland, E. Ronca, E. F. Kjønstad, A. Rubio, and H. Koch. Coupled cluster theory for molecular polaritons: Changing ground and excited states. *Phys. Rev. X*, 10(4):041043, 2020.

[62] L. A. Martínez-Martínez, M. Du, R. F. Ribeiro, S. Kéna-Cohen, and J. Yuen-Zhou. Polariton-assisted singlet fission in acene aggregates. *J. Phys. Chem. Lett.*, 9(8):1951–1957, 2018.

[63] K. Stranius, M. Hertzog, and K. Börjesson. Selective manipulation of electronically excited states through strong light–matter interactions. *Nat. Commun.*, 9(1):2273, 2018.

[64] L. A. Martínez-Martínez, E. Eizner, S. Kéna-Cohen, and J. Yuen-Zhou. Triplet harvesting in the polaritonic regime: A variational polaron approach. *J. Chem. Phys.*, 151(5):054106, 2019.

[65] Y. Yu, S. Mallick, M. Wang, and K. Börjesson. Barrier-free reverse-intersystem crossing in organic molecules by strong light-matter coupling. *Nat. Commun.*, 12(1):3255, 2021.

[66] C. Ye, S. Mallick, M. Hertzog, M. Kowalewski, and K. Börjesson. Direct transition from triplet excitons to hybrid light–matter states via triplet–triplet annihilation. *J. Am. Chem. Soc.*, 143(19):7501–7508, 2021.

[67] E. Orgiu, J. George, J. A. Hutchison, E. Devaux, J. F. Dayen, B. Doudin, F. Stellacci, C. Genet, J. Schachenmayer, C. Genes, G. Pupillo, P. Samorì, and T. W. Ebbesen. Conductivity in organic semiconductors hybridized with the vacuum field. *Nat. Mater.*, 14(11): 1123–1129, 2015.

[68] J. Schachenmayer, C. Genes, E. Tignone, and G. Pupillo. Cavity-enhanced transport of excitons. *Phys. Rev. Lett.*, 114(19):196403, 2015.

[69] J. Feist and F. J. Garcia-Vidal. Extraordinary exciton conductance induced by strong coupling. *Phys. Rev. Lett.*, 114(19):196402, 2015.

[70] J. Liu, Q. Zhao, and N. Wu. Vibration-assisted exciton transfer in molecular aggregates strongly coupled to confined light fields. *J. Chem. Phys.*, 150(10):105102, 2019.

[71] N. Krainova, A. J. Grede, D. Tsokkou, N. Banerji, and N. C. Giebink. Polaron photoconductivity in the weak and strong light-matter coupling regime. *Phys. Rev. Lett.*, 124(17): 177401, 2020.

[72] F. Herrera and F. C. Spano. Cavity-controlled chemistry in molecular ensembles. *Phys. Rev. Lett.*, 116(23):238301, 2016.

[73] G. Groenhof and J. J. Toppari. Coherent light harvesting through strong coupling to confined light. *J. Phys. Chem. Lett.*, 9(17):4848–4851, 2018.

[74] M. Wang, M. Hertzog, and K. B orjesson. Polariton-assisted excitation energy channeling in organic heterojunctions. *Nat. Commun.*, 12(1):1874, 2021.

[75] A. Mandal, T. D. Krauss, and P. Huo. Polariton-mediated electron transfer via cavity quantum electrodynamics. *J. Phys. Chem. B*, 124(29):6321–6340, 2020.

[76] N. M. Hoffmann, L. Lacombe, A. Rubio, and N. T. Maitra. Effect of many modes on self-polarization and photochemical suppression in cavities. *J. Chem. Phys.*, 153(10):104103, 2020.

[77] L. Mauro, K. Caicedo, G. Jonusauskas, and R. Avriller. Charge-transfer chemical reactions in nanofluidic Fabry-Pérot cavities. *Phys. Rev. B*, 103(16):165412, 2021.

[78] J. A. Hutchison, T. Schwartz, C. Genet, E. Devaux, and T. W. Ebbesen. Modifying chemical landscapes by coupling to vacuum fields. *Angew. Chem., Int. Ed.*, 51(7):1592–1596, 2012.

[79] J. Galego, F. J. Garcia-Vidal, and J. Feist. Suppressing photochemical reactions with quantized light fields. *Nat. Commun.*, 7(1):13841, 2016.

[80] J. Fregoni, G. Granucci, E. Coccia, M. Persico, and S. Corni. Manipulating azobenzene photoisomerization through strong light–molecule coupling. *Nat. Commun.*, 9(1):4688, 2018.

[81] A. Mandal and P. Huo. Investigating new reactivities enabled by polariton photochemistry. *J. Phys. Chem. Lett.*, 10(18):5519–5529, 2019.

[82] J. Fregoni, G. Granucci, M. Persico, and S. Corni. Strong coupling with light enhances the photoisomerization quantum yield of azobenzene. *Chem*, 6(1):250–265, 2020.

[83] P. Antoniou, F. Suchanek, J. F. Varner, and J. J. Foley. Role of cavity losses on nonadiabatic couplings and dynamics in polaritonic chemistry. *J. Phys. Chem. Lett.*, 11(21):9063–9069, 2020.

[84] B. Munkhbat, M. Wersäll, D. G. Baranov, T. J. Antosiewicz, and T. Shegai. Suppression of photo-oxidation of organic chromophores by strong coupling to plasmonic nanoantennas. *Sci. Adv.*, 4(7), 2018.

[85] S. Felicetti, J. Fregoni, T. Schnappinger, S. Reiter, R. de Vivie-Riedle, and J. Feist. Photoprotecting uracil by coupling with lossy nanocavities. *J. Phys. Chem. Lett.*, pages 8810–8818, 2020.

[86] N. Nefedkin, E. Andrianov, and A. Vinogradov. The role of strong coupling in the process of photobleaching suppression. *J. Phys. Chem. C*, 124(33):18234–18242, 2020.

[87] I. S. Ulusoy and O. Vendrell. Dynamics and spectroscopy of molecular ensembles in a lossy microcavity. *J. Chem. Phys.*, 153(4):044108, 2020.

[88] E. Davidsson and M. Kowalewski. Simulating photodissociation reactions in bad cavities with the lindblad equation. *J. Chem. Phys.*, 153(23):234304, 2020.

[89] D. M. Coles, N. Somaschi, P. Michetti, C. Clark, P. G. Lagoudakis, P. G. Savvidis, and D. G. Lidzey. Polariton-mediated energy transfer between organic dyes in a strongly coupled optical microcavity. *Nat. Mater.*, 13(7):712–719, 2014.

[90] X. Zhong, T. Chervy, L. Zhang, A. Thomas, J. George, C. Genet, J. A. Hutchison, and T. W. Ebbesen. Energy transfer between spatially separated entangled molecules. *Angew. Chem., Int. Ed.*, 56(31):9034–9038, 2017.

[91] R. Sáez-Blázquez, J. Feist, A. I. Fernández-Domínguez, and F. J. García-Vidal. Organic polaritons enable local vibrations to drive long-range energy transfer. *Phys. Rev. B*, 97: 241407, 2018.

[92] B. Xiang, R. F. Ribeiro, M. Du, L. Chen, Z. Yang, J. Wang, J. Yuen-Zhou, and W. Xiong. Intermolecular vibrational energy transfer enabled by microcavity strong light–matter coupling. *Science*, 368(6491):665–667, 2020.

[93] Y. Oyola and D. A. Singleton. Dynamics and the failure of transition state theory in alkene hydroboration. *J. Am. Chem. Soc.*, 131(9):3130–3131, 2009.

[94] D. R. Glowacki, C. H. Liang, S. P. Marsden, J. N. Harvey, and M. J. Pilling. Alkene hydroboration: Hot intermediates that react while they are cooling. *J. Am. Chem. Soc.*, 132(39): 13621–13623, 2010.

[95] B. K. Carpenter. Energy disposition in reactive intermediates. *Chem. Rev.*, 113(9):7265–7286, 2013.

[96] C. Climent and J. Feist. On the S_N2 reactions modified in vibrational strong coupling experiments: reaction mechanisms and vibrational mode assignments. *Phys. Chem. Chem. Phys.*, 22:23545–23552, 2020.

[97] A. Thomas, A. Jayachandran, L. Lethuillier-Karl, R. M. Vergauwe, K. Nagarajan, E. Devaux, C. Genet, J. Moran, and T. W. Ebbesen. Ground state chemistry under vibrational strong coupling: dependence of thermodynamic parameters on the Rabi splitting energy. *Nanophotonics*, 9(2):249–255, 2020.

[98] A. Strashko and J. Keeling. Raman scattering with strongly coupled vibron-polaritons. *Phys. Rev. A*, 94(2):023843, 2016.

[99] V. May and O. Kühn. *Charge and Energy Transfer Dynamics in Molecular Systems*. Wiley, 2011.

[100] G. S. Agarwal. *Quantum Optics*. Cambridge University Press, 2013.

[101] A. D. Dunkelberger, B. T. Spann, K. P. Fears, B. S. Simpkins, and J. C. Owrutsky. Modified relaxation dynamics and coherent energy exchange in coupled vibration-cavity polaritons. *Nat. Commun.*, 7:13504, 2016.

[102] T. Hümmer, F. J. García-Vidal, L. Martín-Moreno, and D. Zueco. Weak and strong coupling regimes in plasmonic QED. *Phys. Rev. B*, 87(11):115419, 2013.

[103] B. Metzger, E. Muller, J. Nishida, B. Pollard, M. Hentschel, and M. B. Raschke. Purcell-enhanced spontaneous emission of molecular vibrations. *Phys. Rev. Lett.*, 123(15):153001, 2019.

[104] M. Pelton. Modified spontaneous emission in nanophotonic structures. *Nat. Photonics*, 9 (7):427–435, 2015.

[105] A. Semenov and A. Nitzan. Electron transfer in confined electromagnetic fields. *J. Chem. Phys.*, 150(17):174122, 2019.

[106] I. Vurgaftman, B. S. Simpkins, A. D. Dunkelberger, and J. C. Owrutsky. Negligible effect of vibrational polaritons on chemical reaction rates via the density of states pathway. *J. Phys. Chem. Lett.*, 11(9):3557–3562, 2020.

[107] B. Xiang, R. F. Ribeiro, L. Chen, J. Wang, M. Du, J. Yuen-Zhou, and W. Xiong. State-selective polariton to dark state relaxation dynamics. *J. Phys. Chem. A*, 123(28):5918–5927, 2019.

[108] A. D. Dunkelberger, R. B. Davidson II, W. Ahn, B. S. Simpkins, and J. C. Owrutsky. Ultrafast transmission modulation and recovery via vibrational strong coupling. *J. Phys. Chem. A*, 122(4):965–971, 2018.

[109] D. Polak, R. Jayaprakash, T. P. Lyons, L. Á. Martínez-Martínez, A. Leventis, K. J. Fallon, H. Coulthard, D. G. Bossanyi, K. Georgiou, I. I. A. J. Petty, J. Anthony, H. Bronstein, J. Yuen-Zhou, A. I. Tartakovskii, J. Clark, and A. J. Musser. Manipulating molecules with strong coupling: harvesting triplet excitons in organic exciton microcavities. *Chem. Sci.*, 11 (2):343–354, 2020.

[110] D. M. Leitner and P. G. Wolynes. Quantum energy flow during molecular isomerization. *Chem. Phys. Lett.*, 280(5):411–418, 1997.

[111] R. Chikkaraddy, B. de Nijs, F. Benz, S. J. Barrow, O. A. Scherman, E. Rosta, A. Demetriadou, P. Fox, O. Hess, and J. J. Baumberg. Single-molecule strong coupling at room temperature in plasmonic nanocavities. *Nature*, 535(7610):127–130, 2016.

[112] B. Barnes, F. García Vidal, and J. Aizpurua. Special issue on "Strong Coupling of Molecules to Cavities". *ACS Photonics*, 5(1):1–1, 2018.

[113] O. Vendrell. Collective Jahn-Teller interactions through light-matter coupling in a cavity. *Phys. Rev. Lett.*, 121(25):253001, 2018.

[114] D. G. Baranov, M. Wersäll, J. Cuadra, T. J. Antosiewicz, and T. Shegai. Novel nanostructures and materials for strong light–matter interactions. *ACS Photonics*, 5(1):24–42, 2018.

[115] K. Hirai, H. Ishikawa, T. Chervy, J. A. Hutchison, and H. Uji-i. Selective crystallization via vibrational strong coupling. *Chem. Sci.*, 12(36):11986–11994, 2021.

[116] T. Botzung, D. Hagenmüller, S. Schütz, J. Dubail, G. Pupillo, and J. Schachenmayer. Dark state semilocalization of quantum emitters in a cavity. *Phys. Rev. B*, 102(14):144202, 2020.

[117] G. D. Scholes. Polaritons and excitons: Hamiltonian design for enhanced coherence. *Proc. R. Soc. A*, 476(2242):20200278, 2020.

[118] N. C. Chávez, F. Mattiotti, J. A. Méndez-Bermúdez, F. Borgonovi, and G. L. Celardo. Disorder-enhanced and disorder-independent transport with long-range hopping: Application to molecular chains in optical cavities. *Phys. Rev. Lett.*, 126(15):153201, 2021.

[119] D. Sidler, C. Schäfer, M. Ruggenthaler, and A. Rubio. Polaritonic chemistry: Collective strong coupling implies strong local modification of chemical properties. *J. Phys. Chem. Lett.*, 12(1):508–516, 2021.

[120] R. Houdré, R. P. Stanley, and M. Ilegems. Vacuum-field Rabi splitting in the presence of inhomogeneous broadening: Resolution of a homogeneous linewidth in an inhomogeneously broadened system. *Phys. Rev. A*, 53(4):2711–2715, 1996.

[121] J. Galego, F. J. Garcia-Vidal, and J. Feist. Many-molecule reaction triggered by a single photon in polaritonic chemistry. *Phys. Rev. Lett.*, 119(13):136001, 2017.

[122] B. Kramer and A. MacKinnon. Localization: theory and experiment. *Rep. Prog. Phys.*, 56 (12):1469–1564, 1993.

[123] S. Schütz, J. Schachenmayer, D. Hagenmüller, G. K. Brennen, T. Volz, V. Sandoghdar, T. W. Ebbesen, C. Genes, and G. Pupillo. Ensemble-induced strong light-matter coupling of a single quantum emitter. *Phys. Rev. Lett.*, 124(11):113602, 2020.

[124] T. Szidarovszky, G. J. Halász, and A. Vibók. Three-player polaritons: nonadiabatic fingerprints in an entangled atom–molecule–photon system. *New J. Phys.*, 22(5):053001, 2020.

[125] E. Davidsson and M. Kowalewski. Atom assisted photochemistry in optical cavities. *J. Phys. Chem. A*, 124(23):4672–4677, 2020.

[126] M. Litinskaya, P. Reineker, and V. M. Agranovich. Fast polariton relaxation in strongly coupled organic microcavities. *J. Lumin.*, 110(4):364–372, 2004.

[127] A. B. Grafton, A. D. Dunkelberger, B. S. Simpkins, J. F. Triana, F. J. Hernández, F. Herrera, and J. C. Owrutsky. Excited-state vibration-polariton transitions and dynamics in nitroprusside. *Nat. Commun.*, 12(1):214, 2021.

[128] C. Duan, Q. Wang, Z. Tang, and J. Wu. The study of an extended hierarchy equation of motion in the spin-boson model: The cutoff function of the sub-Ohmic spectral density. *J. Chem. Phys.*, 147(16):164112, 2017.

[129] O. Kühn and H. Naundorf. Dissipative wave packet dynamics of the intramolecular hydrogen bond in *o*-phthalic acid monomethylester. *Phys. Chem. Chem. Phys.*, 5(1):79–86, 2003.

[130] P. Vöhringer, D. C. Arnett, R. A. Westervelt, M. J. Feldstein, and N. F. Scherer. Optical dephasing on femtosecond time scales: Direct measurement and calculation from solvent spectral densities. *J. Chem. Phys.*, 102(10):4027–4036, 1995.

[131] Y. J. Chang and E. W. Castner. Fast responses from "slowly relaxing" liquids: A comparative study of the femtosecond dynamics of triacetin, ethylene glycol, and water. *J. Chem. Phys.*, 99(10):7289–7299, 1993.

[132] B. Xiang, R. F. Ribeiro, Y. Li, A. D. Dunkelberger, B. B. Simpkins, J. Yuen-Zhou, and W. Xiong. Manipulating optical nonlinearities of molecular polaritons by delocalization. *Sci. Adv.*, 5(9):eaax5196, 2019.

[133] H. P. Breuer and F. Petruccione. *The Theory of Open Quantum Systems*. Oxford University Press, 2002.

[134] P. Atkins and J. de Paula. *Physical Chemistry*. Oxford University Press, 9th edition, 2010.

[135] A. Canales, D. G. Baranov, T. J. Antosiewicz, and T. Shegai. Abundance of cavity-free polaritonic states in resonant materials and nanostructures. *J. Chem. Phys.*, 154(2):024701, 2021.

[136] C. Schäfer, M. Ruggenthaler, and A. Rubio. Ab initio nonrelativistic quantum electrodynamics: Bridging quantum chemistry and quantum optics from weak to strong coupling. *Phys. Rev. A*, 98(4):043801, 2018.

[137] X. Shi, K. Ueno, T. Oshikiri, Q. Sun, K. Sasaki, and H. Misawa. Enhanced water splitting under modal strong coupling conditions. *Nat. Nanotechnol.*, 13(10):953–958, 2018.

[138] O. Vendrell. Coherent dynamics in cavity femtochemistry: Application of the multiconfiguration time-dependent Hartree method. *Chem. Phys.*, 509:55–65, 2018.

[139] M. Reitz, F. Mineo, and C. Genes. Energy transfer and correlations in cavity-embedded donor-acceptor configurations. *Sci. Rep.*, 8(1):9050, 2018.

[140] R. Schanz, V. Boţan, and P. Hamm. A femtosecond study of the infrared-driven *cis-trans* isomerization of nitrous acid (HONO). *J. Chem. Phys.*, 122(4):044509, 2005.

[141] A. Olbert-Majkut, M. Wierzejewska, and J. Lundell. Light-induced, site-selective isomerization of glyoxylic acid in solid xenon. *Chem. Phys. Lett.*, 616-617:91–97, 2014.

[142] A. Olbert-Majkut, J. Lundell, and M. Wierzejewska. Light-induced opening and closing of the intramolecular hydrogen bond in glyoxylic acid. *J. Phys. Chem. A*, 118(2):350–357, 2014.

[143] A. Armitage, M. S. Skolnick, V. N. Astratov, D. M. Whittaker, G. Panzarini, L. C. Andreani, T. A. Fisher, J. S. Roberts, A. V. Kavokin, M. A. Kaliteevski, and M. R. Vladimirova. Optically induced splitting of bright excitonic states in coupled quantum microcavities. *Phys. Rev. B*, 57(23):14877–14881, 1998.

[144] R. P. Stanley, R. Houdré, U. Oesterle, M. Ilegems, and C. Weisbuch. Coupled semiconductor microcavities. *Appl. Phys. Lett.*, 65(16):2093–2095, 1994.

[145] D. G. Lidzey, D. D. C. Bradley, A. Armitage, S. Walker, and M. S. Skolnick. Photon-mediated hybridization of Frenkel excitons in organic semiconductor microcavities. *Science*, 288(5471):1620–1623, 2000.

[146] D. J. Nesbitt and R. W. Field. Vibrational energy flow in highly excited molecules: Role of intramolecular vibrational redistribution. *J. Phys. Chem.*, 100(31):12735–12756, 1996.

[147] R. T. Hall and G. C. Pimentel. Isomerization of nitrous acid: An infrared photochemical reaction. *J. Chem. Phys.*, 38(8):1889–1897, 1963.

[148] P. Hamm. The infrared-driven *cis–trans* isomerization of nitrous acid HONO III: A mixed quantum–classical simulation. *Chem. Phys.*, 347(1):503–513, 2008.

[149] A. Nitzan. *Chemical Dynamics in Condensed Phases: Relaxation, Transfer and Reactions in Condensed Molecular Systems*. Oxford University Press, 2006.

[150] D. A. Steck. *Quantum and Atom Optics*, volume 47. Oregon Center for Optics and Department of Physics, University of Oregon, Eugene, Oregon, 2007.

[151] C. W. Gardiner and M. J. Collett. Input and output in damped quantum systems: Quantum stochastic differential equations and the master equation. *Phys. Rev. A*, 31(6):3761–3774, 1985.

[152] C. Ciuti and I. Carusotto. Input-output theory of cavities in the ultrastrong coupling regime: The case of time-independent cavity parameters. *Phys. Rev. A*, 74(3):033811, 2006.

[153] D. Segal and A. Nitzan. Steady-state quantum mechanics of thermally relaxing systems. *Chem. Phys.*, 268(1):315–335, 2001.

[154] L. Khriachtchev, J. Lundell, E. Isoniemi, and M. Räsänen. HONO in solid Kr: Site-selective *trans–cis* isomerization with narrow-band infrared radiation. *J. Chem. Phys.*, 113(10):4265–4273, 2000.

[155] H. Li, A. Piryatinski, J. Jerke, A. R. S. Kandada, C. Silva, and E. R. Bittner. Probing dynamical symmetry breaking using quantum-entangled photons. *Quantum Sci. Technol.*, 3 (1):015003, 2017.

[156] J. A. Ćwik, P. Kirton, S. De Liberato, and J. Keeling. Excitonic spectral features in strongly coupled organic polaritons. *Phys. Rev. A*, 93(3):033840, 2016.

[157] W. Ahn, I. Vurgaftman, A. D. Dunkelberger, J. C. Owrutsky, and B. S. Simpkins. Vibrational strong coupling controlled by spatial distribution of molecules within the optical cavity. *ACS Photonics*, 5(1):158–166, 2018.

[158] M. S. Skolnick, T. A. Fisher, and D. M. Whittaker. Strong coupling phenomena in quantum microcavity structures. *Semicond. Sci. Technol.*, 13(7):645, 1998.

[159] G. Khitrova, H. M. Gibbs, F. Jahnke, M. Kira, and S. W. Koch. Nonlinear optics of normal-mode-coupling semiconductor microcavities. *Rev. Mod. Phys.*, 71(5):1591–1639, 1999.

[160] P. Vasa, W. Wang, R. Pomraenke, M. Lammers, M. Maiuri, C. Manzoni, G. Cerullo, and C. Lienau. Real-time observation of ultrafast Rabi oscillations between excitons and plasmons in metal nanostructures with J-aggregates. *Nat. Photonics*, 7:128, 2013.

[161] B. Liu, P. Rai, J. Grezmak, R. J. Twieg, and K. D. Singer. Coupling of exciton-polaritons in low $-Q$ coupled microcavities beyond the rotating wave approximation. *Phys. Rev. B*, 92 (15):155301, 2015.

[162] J. Bellessa, C. Bonnand, J. C. Plenet, and J. Mugnier. Strong coupling between surface plasmons and excitons in an organic semiconductor. *Phys. Rev. Lett.*, 93(3):036404, 2004.

[163] S. Maxim and N. Abraham. Optics of exciton-plasmon nanomaterials. *J. Phys.: Condens. Matter*, 29(44):443003, 2017.

[164] N. T. Fofang, N. K. Grady, Z. Fan, A. O. Govorov, and N. J. Halas. Plexciton dynamics: Exciton–plasmon coupling in a J-aggregate–Au nanoshell complex provides a mechanism for nonlinearity. *Nano Lett.*, 11(4):1556–1560, 2011.

[165] E. Prodan, C. Radloff, N. J. Halas, and P. Nordlander. A hybridization model for the plasmon response of complex nanostructures. *Science*, 302(5644):419, 2003.

[166] N. Thakkar, M. T. Rea, K. C. Smith, K. D. Heylman, S. C. Quillin, K. A. Knapper, E. H. Horak, D. J. Masiello, and R. H. Goldsmith. Sculpting Fano resonances to control photonic–plasmonic hybridization. *Nano Lett.*, 17(11):6927–6934, 2017.

[167] F. Richter, P. Rosmus, F. Gatti, and H.-D. Meyer. Time-dependent wave packet study on *trans-cis* isomerization of HONO. *J. Chem. Phys.*, 120(13):6072–6084, 2004.

[168] M. Shapiro and P. Brumer. *Quantum Control of Molecular Processes*. Wiley, 2012.

[169] T. Förster. Zwischenmolekulare energiewanderung und fluoreszenz. *Ann. Phys.*, 2(1-2): 55–75, 1948.

[170] A. Govorov, P. L. H. Martínez, and H. V. Demir. *Understanding and Modeling Förster-type Resonance Energy Transfer (FRET): Introduction to FRET*. Springer Singapore, 2016.

[171] S. Jang, M. D. Newton, and R. J. Silbey. Multichromophoric Förster resonance energy transfer. *Phys. Rev. Lett.*, 92(21):218301, 2004.

[172] S. Jang, M. D. Newton, and R. J. Silbey. Multichromophoric Förster resonance energy transfer from B800 to B850 in the light harvesting complex 2: Evidence for subtle energetic optimization by purple bacteria. *J. Phys. Chem. B*, 111(24):6807–6814, 2007.

[173] I. Kassal, J. Yuen-Zhou, and S. Rahimi-Keshari. Does coherence enhance transport in photosynthesis? *J. Phys. Chem. Lett.*, 4(3):362–367, 2013.

[174] S. Lloyd and M. Mohseni. Symmetry-enhanced supertransfer of delocalized quantum states. *New J. Phys.*, 12(7):075020, 2010.

[175] G. S. Engel, T. R. Calhoun, E. L. Read, T.-K. Ahn, T. Mančal, Y.-C. Cheng, R. E. Blankenship, and G. R. Fleming. Evidence for wavelike energy transfer through quantum coherence in photosynthetic systems. *Nature*, 446:782, 2007.

[176] S. Duque, P. Brumer, and L. A. Pachón. Classical approach to multichromophoric resonance energy transfer. *Phys. Rev. Lett.*, 115:110402, 2015.

[177] G. D. Scholes. Long-range resonance energy transfer in molecular systems. *Annu. Rev. Phys. Chem.*, 54(1):57–87, 2003.

[178] A. T. Haedler, K. Kreger, A. Issac, B. Wittmann, M. Kivala, N. Hammer, J. Kohler, H.-W. Schmidt, and R. Hildner. Long-range energy transport in single supramolecular nanofibres at room temperature. *Nature*, 523(7559):196–199, 2015.

[179] S. K. Saikin, M. A. Shakirov, C. Kreisbeck, U. Peskin, Y. N. Proshin, and A. Aspuru-Guzik. On the long-range exciton transport in molecular systems: The application to H-aggregated heterotriangulene chains. *J. Phys. Chem. C*, 121(45):24994–25002, 2017.

[180] L.-Y. Hsu, W. Ding, and G. C. Schatz. Plasmon-coupled resonance energy transfer. *J. Phys. Chem. Lett.*, 8(10):2357–2367, 2017.

[181] X. Zhang, C. A. Marocico, M. Lunz, V. A. Gerard, Y. K. Gunâko, V. Lesnyak, N. Gaponik, A. S. Susha, A. L. Rogach, and A. L. Bradley. Experimental and theoretical investigation of the distance dependence of localized surface plasmon coupled Förster resonance energy transfer. *ACS Nano*, 8(2):1273–1283, 2014.

[182] W. Ding, L.-Y. Hsu, and G. C. Schatz. Plasmon-coupled resonance energy transfer: A real-time electrodynamics approach. *J. Chem. Phys.*, 146(6):064109, 2017.

[183] D. Bouchet, D. Cao, R. Carminati, Y. De Wilde, and V. Krachmalnicoff. Long-range plasmon-assisted energy transfer between fluorescent emitters. *Phys. Rev. Lett.*, 116(3): 037401, 2016.

[184] J. de Torres, P. Ferrand, G. Colas des Francs, and J. Wenger. Coupling emitters and silver nanowires to achieve long-range plasmon-mediated fluorescence energy transfer. *ACS Nano*, 10(4):3968–3976, 2016.

[185] S. Götzinger, L. de S. Menezes, A. Mazzei, S. Kühn, V. Sandoghdar, and O. Benson. Controlled photon transfer between two individual nanoemitters via shared high-Q modes of a microsphere resonator. *Nano Lett.*, 6(6):1151–1154, 2006.

[186] M. Slootsky, X. Liu, V. M. Menon, and S. R. Forrest. Room temperature Frenkel-Wannier-Mott hybridization of degenerate excitons in a strongly coupled microcavity. *Phys. Rev. Lett.*, 112(7):076401, 2014.

[187] J. Yuen-Zhou, S. K. Saikin, T. Zhu, M. C. Onbasli, C. A. Ross, V. Bulovic, and M. A. Baldo. Plexciton Dirac points and topological modes. *Nat. Commun.*, 7:11783, 2016.

[188] D. M. Basko, F. Bassani, G. C. La Rocca, and V. M. Agranovich. Electronic energy transfer in a microcavity. *Phys. Rev. B*, 62(23):15962–15977, 2000.

[189] M. Yang and G. R. Fleming. Influence of phonons on exciton transfer dynamics: comparison of the Redfield, Förster, and modified Redfield equations. *Chem. Phys.*, 282(1):163–180, 2002.

[190] E. N. Zimanyi and R. J. Silbey. Theoretical description of quantum effects in multi-chromophoric aggregates. *Philos. Trans. R. Soc., A*, 370(1972):3620–3637, 2012.

[191] A. S. Davydov. Teoriya spektrov pogloshcheniya molekulyarnykh kristallov. *Zhur. Eksptl. Teoret. Fiz.*, 18(2):210–218, 1948.

[192] A. S. Davydov. *Theory of Molecular Excitons*. McGraw-Hill, New York, 1962.

[193] A. G. Redfield. The theory of relaxation processes. In *Advances in Magnetic and Optical Resonance*, volume 1, pages 1–32. Elsevier, 1965.

[194] M. R. Philpott. Theory of vibronic coupling in the polariton states of molecular crystals. *J. Chem. Phys.*, 52(11):5842–5850, 1970.

[195] T. F. Soules and C. B. Duke. Resonant energy transfer between localized electronic states in a crystal. *Phys. Rev. B*, 3(2):262–274, 1971.

[196] T. Holstein. Studies of polaron motion: Part I. The molecular-crystal model. *Ann. Phys.*, 8 (3):325–342, 1959.

[197] S. Mukamel. *Principles of Nonlinear Optical Spectroscopy*. Oxford University Press, 1995.

[198] D. F. Walls and G. J. Milburn. *Quantum Optics*. Springer-Verlag, 1994.

[199] E. Waks and D. Sridharan. Cavity QED treatment of interactions between a metal nanoparticle and a dipole emitter. *Phys. Rev. A*, 82(4):043845, 2010.

[200] J. Yuen-Zhou, S. K. Saikin, and V. M. Menon. Molecular emission near metal interfaces: The polaritonic regime. *J. Phys. Chem. Lett.*, 9(22):6511–6516, 2018.

[201] F. Zhou, Y. Liu, and Z.-Y. Li. Surface-plasmon-polariton-assisted dipole–dipole interaction near metal surfaces. *Opt. Lett.*, 36(11):1969–1971, 2011.

[202] M. O. Scully and M. S. Zubairy. *Quantum Optics*. Cambridge University Press, New York, New York, 1997.

[203] A. González-Tudela, P. A. Huidobro, L. Martín-Moreno, C. Tejedor, and F. J. García-Vidal. Theory of strong coupling between quantum emitters and propagating surface plasmons. *Phys. Rev. Lett.*, 110(12):126801, 2013.

[204] A. Archambault, F. Marquier, J.-J. Greffet, and C. Arnold. Quantum theory of spontaneous and stimulated emission of surface plasmons. *Phys. Rev. B*, 82(3):035411, 2010.

[205] L. A. Martínez-Martínez, R. F. Ribeiro, J. Campos-González-Angulo, and J. Yuen-Zhou. Can ultrastrong coupling change ground-state chemical reactions? *ACS Photonics*, 5(1): 167–176, 2017.

[206] S. Jang, Y. Jung, and R. J. Silbey. Nonequilibrium generalization of Förster–Dexter theory for excitation energy transfer. *Chem. Phys.*, 275(1):319–332, 2002.

[207] S. Jang and R. J. Silbey. Theory of single molecule line shapes of multichromophoric macromolecules. *J. Chem. Phys.*, 118(20):9312–9323, 2003.

[208] J. Ma and J. Cao. Förster resonance energy transfer, absorption and emission spectra in multichromophoric systems. I. Full cumulant expansions and system-bath entanglement. *J. Chem. Phys.*, 142(9):094106, 2015.

[209] S. Baghbanzadeh and I. Kassal. Distinguishing the roles of energy funnelling and delocalization in photosynthetic light harvesting. *Phys. Chem. Chem. Phys.*, 18(10):7459–7467, 2016.

[210] S. Baghbanzadeh and I. Kassal. Geometry, supertransfer, and optimality in the light harvesting of purple bacteria. *J. Phys. Chem. Lett.*, 7(19):3804–3811, 2016.

[211] G. L. Liu, Y.-T. Long, Y. Choi, T. Kang, and L. P. Lee. Quantized plasmon quenching dips nanospectroscopy via plasmon resonance energy transfer. *Nat. Methods*, 4:1015, 2007.

[212] T. Ozel, P. L. Hernandez-Martinez, E. Mutlugun, O. Akin, S. Nizamoglu, I. O. Ozel, Q. Zhang, Q. Xiong, and H. V. Demir. Observation of selective plasmon-exciton coupling in nonradiative energy transfer: Donor-selective versus acceptor-selective plexcitons. *Nano Lett.*, 13(7):3065–3072, 2013.

[213] M. Bednarz, V. A. Malyshev, and J. Knoester. Intraband relaxation and temperature dependence of the fluorescence decay time of one-dimensional Frenkel excitons: The Pauli master equation approach. *J. Chem. Phys.*, 117(13):6200–6213, 2002.

[214] A. Canaguier-Durand, C. Genet, A. Lambrecht, T. W. Ebbesen, and S. Reynaud. Non-Markovian polariton dynamics in organic strong coupling. *Eur. Phys. J. D*, 69(1):24, 2015.

[215] X. Zhong, T. Chervy, S. Wang, J. George, A. Thomas, J. A. Hutchison, E. Devaux, C. Genet, and T. W. Ebbesen. Non-radiative energy transfer mediated by hybrid light-matter states. *Angew. Chem., Int. Ed.*, 55(21):6202–6206, 2016.

[216] E. D. Palik. *Handbook of Optical Constants of Solids II*. Academic Press, 1985.

[217] J. Ma, J. Moix, and J. Cao. Förster resonance energy transfer, absorption and emission spectra in multichromophoric systems. II. Hybrid cumulant expansion. *J. Chem. Phys.*, 142 (9):094107, 2015.

[218] J. M. Moix, J. Ma, and J. Cao. Förster resonance energy transfer, absorption and emission spectra in multichromophoric systems. III. Exact stochastic path integral evaluation. *J. Chem. Phys.*, 142(9):094108, 2015.

[219] S. Valleau, S. K. Saikin, M.-H. Yung, and A. A. Guzik. Exciton transport in thin-film cyanine dye J-aggregates. *J. Chem. Phys.*, 137(3):034109, 2012.

[220] A. O. Govorov, J. Lee, and N. A. Kotov. Theory of plasmon-enhanced Förster energy transfer in optically excited semiconductor and metal nanoparticles. *Phys. Rev. B*, 76(12): 125308, 2007.

[221] B. Valeur and M. N. Berberan-Santos. *Molecular Fluorescence: Principles and Applications*. Wiley, 2nd edition, 2012.

[222] I. L. Medintz and N. Hildebrandt. *FRET - Förster Resonance Energy Transfer: From Theory to Applications*. Wiley, 2013.

[223] D. L. Andrews. A unified theory of radiative and radiationless molecular energy transfer. *Chem. Phys.*, 135(2):195–201, 1989.

[224] G. Juzeliūnas and D. L. Andrews. Quantum electrodynamics of resonant energy transfer in condensed matter. *Phys. Rev. B*, 49(13):8751–8763, 1994.

[225] H. T. Dung, L. Knöll, and D.-G. Welsch. Resonant dipole-dipole interaction in the presence of dispersing and absorbing surroundings. *Phys. Rev. A*, 66(6):063810, 2002.

[226] D. M. Coles, P. Michetti, C. Clark, W. C. Tsoi, A. M. Adawi, J.-S. Kim, and D. G. Lidzey. Vibrationally assisted polariton-relaxation processes in strongly coupled organic-semiconductor microcavities. *Adv. Funct. Mater.*, 21(19):3691–3696, 2011.

[227] D. M. Coles, P. Michetti, C. Clark, A. M. Adawi, and D. G. Lidzey. Temperature dependence of the upper-branch polariton population in an organic semiconductor microcavity. *Phys. Rev. B*, 84(20):205214, 2011.

[228] N. Somaschi, L. Mouchliadis, D. Coles, I. E. Perakis, D. G. Lidzey, P. G. Lagoudakis, and P. G. Savvidis. Ultrafast polariton population build-up mediated by molecular phonons in organic microcavities. *Appl. Phys. Lett.*, 99(14):143303, 2011.

[229] D. G. Lidzey, A. M. Fox, M. D. Rahn, M. S. Skolnick, V. M. Agranovich, and S. Walker. Experimental study of light emission from strongly coupled organic semiconductor microcavities following nonresonant laser excitation. *Phys. Rev. B*, 65(19):195312, 2002.

[230] M. van Exter and A. Lagendijk. Ultrashort surface-plasmon and phonon dynamics. *Phys. Rev. Lett.*, 60(1):49–52, 1988.

[231] C. Sönnichsen, T. Franzl, T. Wilk, G. von Plessen, J. Feldmann, O. Wilson, and P. Mulvaney. Drastic reduction of plasmon damping in gold nanorods. *Phys. Rev. Lett.*, 88(7):077402, 2002.

[232] D. M. Coles, R. T. Grant, D. G. Lidzey, C. Clark, and P. G. Lagoudakis. Imaging the polariton relaxation bottleneck in strongly coupled organic semiconductor microcavities. *Phys. Rev. B*, 88(12):121303, 2013.

[233] J. Chovan, I. E. Perakis, S. Ceccarelli, and D. G. Lidzey. Controlling the interactions between polaritons and molecular vibrations in strongly coupled organic semiconductor microcavities. *Phys. Rev. B*, 78(4):045320, 2008.

[234] P. Michetti and G. C. La Rocca. Simulation of J-aggregate microcavity photoluminescence. *Phys. Rev. B*, 77(19):195301, 2008.

[235] P. Michetti and G. C. La Rocca. Exciton-phonon scattering and photoexcitation dynamics in *J*-aggregate microcavities. *Phys. Rev. B*, 79(3):035325, 2009.

[236] T. K. Hakala, J. J. Toppari, A. Kuzyk, M. Pettersson, H. Tikkanen, H. Kunttu, and P. Törmä. Vacuum Rabi splitting and strong-coupling dynamics for surface-plasmon polaritons and rhodamine 6G molecules. *Phys. Rev. Lett.*, 103(5):053602, 2009.

[237] R. J. Holmes and S. R. Forrest. Strong exciton–photon coupling in organic materials. *Org. Electron.*, 8(2):77–93, 2007.

[238] F. J. Garcia-Vidal and J. Feist. Long-distance operator for energy transfer. *Science*, 357 (6358):1357–1358, 2017.

[239] V. M. Kenkre and P. Reineker. *Exciton Dynamics in Molecular Crystals and Aggregates*. Springer-Verlag, 1982.

[240] M. Sarovar, A. Ishizaki, G. R. Fleming, and K. B. Whaley. Quantum entanglement in photosynthetic light-harvesting complexes. *Nat. Phys.*, 6(6):462–467, 2010.

[241] G. D. Scholes, G. R. Fleming, L. X. Chen, A. Aspuru-Guzik, A. Buchleitner, D. F. Coker, G. S. Engel, R. van Grondelle, A. Ishizaki, D. M. Jonas, J. S. Lundeen, J. K. McCusker, S. Mukamel, J. P. Ogilvie, A. Olaya-Castro, M. A. Ratner, F. C. Spano, K. B. Whaley, and X. Zhu. Using coherence to enhance function in chemical and biophysical systems. *Nature*, 543:647, 2017.

[242] J. Flick, M. Ruggenthaler, H. Appel, and A. Rubio. Atoms and molecules in cavities, from weak to strong coupling in quantum-electrodynamics (QED) chemistry. *Proc. Natl. Acad. Sci. U. S. A.*, 114(12):3026–3034, 2017.

[243] L. M. M. Quijano and D. A. Singleton. Competition between reaction and intramolecular energy redistribution in solution: Observation and nature of nonstatistical dynamics in the ozonolysis of vinyl ethers. *J. Am. Chem. Soc.*, 133(35):13824–13827, 2011.

[244] I. Vurgaftman, B. S. Simpkins, A. D. Dunkelberger, and J. C. Owrutsky. Comparative analysis of polaritons in bulk, dielectric slabs, and planar cavities with implications for cavity-modified reactivity. *J. Chem. Phys.*, 156(3):034110, 2022.

[245] D. L. Mills and E. Burstein. Polaritons: the electromagnetic modes of media. *Rep. Prog. Phys.*, 37(7):817–926, 1974.

[246] M. V. Imperatore, J. B. Asbury, and N. C. Giebink. Reproducibility of cavity-enhanced chemical reaction rates in the vibrational strong coupling regime. *J. Chem. Phys.*, 154(19): 191103, 2021.

[247] G. D. Wiesehan and W. Xiong. Negligible rate enhancement from reported cooperative vibrational strong coupling catalysis. *J. Chem. Phys.*, 155(24):241103, 2021.

[248] T. J. Frankcombe and S. C. Smith. Time evolution in the unimolecular master equation at low temperatures: full spectral solution with scalable iterative methods and high precision. *Comput. Phys. Commun.*, 141(1):39–54, 2001.

[249] H. Eyring. The activated complex in chemical reactions. *J. Chem. Phys.*, 3(2):107–115, 1935.

[250] M. G. Evans and M. Polanyi. Some applications of the transition state method to the calculation of reaction velocities, especially in solution. *Trans. Faraday Soc.*, 31(0):875–894, 1935.